Organ-on-Silicon

Gaio, Nikolas

DOI
10.4233/uuid:ceba7976-a4b0-469e-bdd0-70f0a14dc275

Publication date
2019

Document Version
Final published version

Citation (APA)
Gaio, N. (2019). *Organ-on-Silicon*. [Dissertation (TU Delft), Delft University of Technology].
https://doi.org/10.4233/uuid:ceba7976-a4b0-469e-bdd0-70f0a14dc275

ORGAN-ON-SILICON

ORGAN-ON-SILICON

Proefschrift

ter verkrijging van de graad van doctor
aan de Technische Universiteit Delft,
op gezag van de Rector Magnificus Prof. dr. ir. T. H. J. J. van der Hagen,
voorzitter van het College voor Promoties,
in het openbaar te verdedigen op vrijdag 12 juli 2019 om 12:30 uur

door

Nikolas GAIO

Master of Science in Biomedical Engineering, Delft University of Technology
geboren te Feltre, Italy.

Dit proefschrift is goedgekeurd door de

promotor: Prof. dr. ir. R. Dekker

Samenstelling promotiecommissie:

Rector Magnificus	voorzitter
Prof. dr. ir. R. Dekker	Technische Universiteit Delft, promotor
Onafhankelijke leden:	
Prof. dr. ir. A. van den Berg	Technische Universiteit Twente
Prof. dr. ir. J. den Toonder	Technische Universiteit Eindhoven
Dr. A. J. M. van den Eijnden - van Raaij	Human Organ and Disease Model Technologies
Prof. dr. P.J. French	Technische Universiteit Delft
Dr. C. Silvestri	BIOND Solutions B.V.
Prof. dr. ir. P. M. Sarro	Technische Universiteit Delft
Prof. dr. ir. W. van Driel	Technische Universiteit Delft, reservelid

Keywords: *Organ-on-Chip, Organ-on-Silicon, polymers, silicon, platform, microelectrode array, packaging, system, iPSC, cardiomyocytes, neurons, organoid, brain, heart*

Printed by: Ipskamp drukkers

Cover design by: Nina Verduin - Bananina Studios,

http://bananina.nl

ISBN: 978-94-028-1575-7

An electronic version of this dissertation is available at
http://repository.tudelft.nl/.

To my stressed, loud, and grumpy family

CONTENTS

1

INTRODUCTION

1.1. FROM PETRI DISHES TO ORGAN-ON-CHIP

Research and development (R&D) expenditure by the pharmaceutical industry has increased exponentially since the 1970s, and has become a large share of their overall cost structure. However, this has not led to an increase in the number of drugs entering the market, explaining in part why the average development costs per drug is now around $ 2.6 B, while the average development time takes a lengthly 13.5 years [1]. Only in the EU, € 32.5B were spent on drug R&D in 2017, involving 115.000 scientists and in total 750.000 jobs [2].

One of the biggest challenges facing the pharmaceutical industry is the high attrition rate in drug development. The product failing rates in the United States, Europe, and Japan between 1990 and 2004 have drastically increased, to approximately 75% at the preclinical phase, 70% while testing the product on healthy volunteers to determine safety and dosing (phase I), and 55% while testing the safety and efficacy of the product on small and large numbers of patients (phase II and phase III, respectively) [3]. As a consequence there is an urgent need for new technologies to identify and validate reliable new human therapeutic targets, and more effective drug development [4].

In current preclinical drug R&D, cell cultures and animal models are often used to predict the drug response of compounds in humans. However, these models do not always capture human physiology and pathology sufficiently to be used as good surrogates, often failing to recapitulate diseases and to predict human responses to new medicines [5, 6]. One alternative under investigation is the use of primary human cells or stem cell in culture. However it is clear that to be true substitutes, other aspects of

their *in situ* (patho) physiology need to be considered. This may include cell and tissue geometries, electrical activity, flow and substrate mechanics.

Organ-on-Chips (OOCs) are models that take these considerations into account by combining sophisticated chip technology with biology. This enables human responses to be recapitulated *in vitro* more accurately than in other systems developed so far [4, 5]. A common definition of OOC is reported in the text-box aside [7]. OOCs make it possible to culture complex tissue structures at a small scale [8]. The cultured cells, often different cell types, interact *in vitro* to create a tissue model of functional units of an organ. These may, for example, be nephrons of the kidney, alveoli of the lungs, or the blood-brain barrier of the vascular system. Growth, proliferation, differentiation, maturation and controlled interactions between different cell types in the model are facilitated in the controlled environment of the OOC chip device [8].

"human 'organs on chips' (organ chips) are microfluidic cell culture devices with separate parenchymal and vascular compartments lined by living human cells that mimic the multicellular architecture, tissue-tissue interfaces and relevant physical microenvironment of key functional units of living organs, while providing dynamic vascular perfusion in vitro..."

Donald E. Ingber

Even though Organ-on-Chip devices have specific structures, functionalities, shapes and dimensions according to the application and/or the tissues analyzed, they all share four main key elements (summarized in Figure 1.1) [9]:

- a microchip;
- a 2D and/or 3D cell culture;
- components for stimulus loading and/or to apply drugs; and
- sensors.

1.2. TOWARDS THE TROUGH OF DISILLUSIONMENT

1.2.1. BEFORE THE "LUNG-ON-CHIP"

The attempt to improve drug R&D by culturing cells in a device that mimics organs or a body-specific microenvironment is not a new concept. Already in 1995, Sweeney et

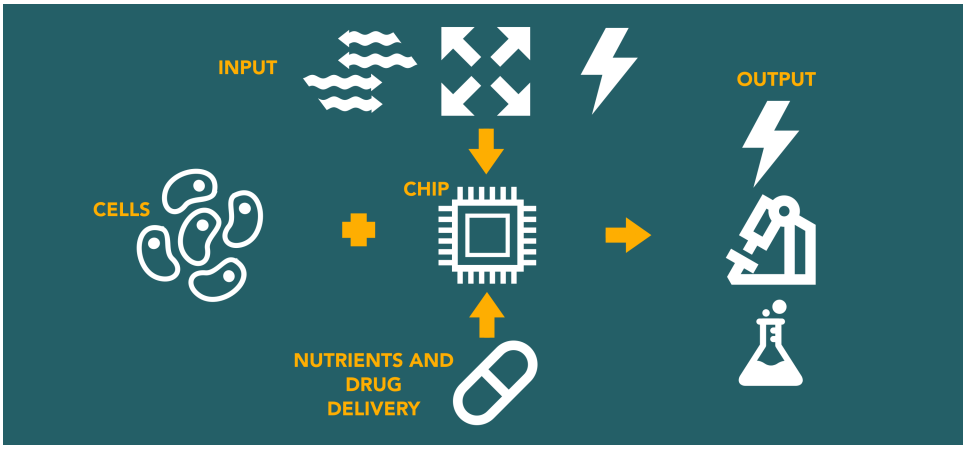

Figure 1.1: Schematic drawing presenting the different elements of an OOC device: (i) a microchip combined with (ii) a 2D and/or 3D cell culture, (iii) components for stimulus loading and/or to apply drugs, and (iv) sensors and optical windows for microscopy.

al. [10], presented a multi-bioreactor system, known as cell culture analogue (CCA), with the aim of mimicking the interactions among different tissues in the body. The model was developed in an attempt to obtain an *in vitro* parallel of a purely mathematical physiologically based pharmacokinetic (PBPK) model commonly used to predict adsorption, distribution, metabolism and excretion (ADME) in the human body.

The system included two or more compartments, containing rat's liver and lung cells. The chambers were connected together by a fluidic system. A proof of concept of the system functionality was given by including naphthalene in the liver compartment. The naphthalene was converted in reactive metabolites (naphthalene oxide) by the cells, and was then injected into the lung compartment causing lung injuries. Even though the system was not representing body physiology very well, the recirculation of the metabolites from the liver compartment caused cytotoxicity in the lung one. Using naphthalene as a toxicity model compound, it was demonstrated that a bioreactor system compartmentalizing liver and lung functionality, could indeed replicate the *in vivo* cytochrome P-450 (CYP)-dependent naphthalene lung cytotoxicity.

CCAs provided a first proof of concept of how a device in combination with tissues can mimic physiologically relevant phenomena. The emergence of microfabrication techniques and the rise of the Lab-on-Chip (LOC) field enabled the miniaturization of this concept and resulted in a drastic reduction of the dimensions of the devices. An optimized version of the CCA presented by Sin et al. [11] in 2004 is shown in Figure 1.2a. The microfluidic approach allowed to bring the values of important parameters, such

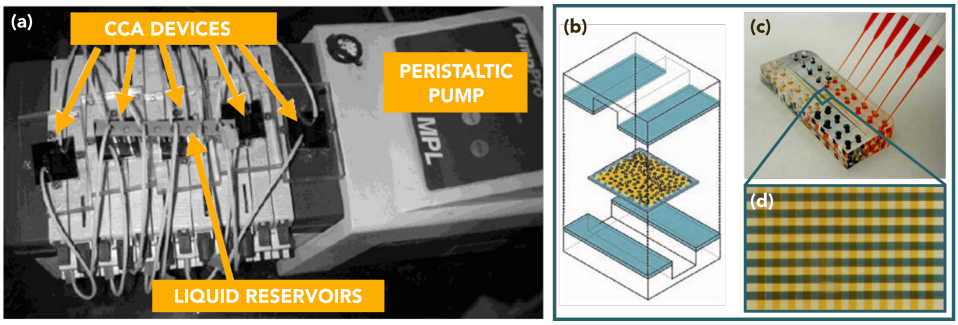

Figure 1.2: (a) Photograph of the CCA presented in [11]. (b) 3D schematic of the microfluidic chip presented by Sin et al. [12] composed of two microfluidic channels separated by a porous membrane where cells can be cultured. (c) Photograph of one of the chips presented in [12] and (d) an optical image of multiple overlapping channels separated by the porous membrane. Figures adapted from [11, 12].

as the shear stress and the fluid-cell ratio, much closer to physiological values. In parallel with these advancements, the importance of three-dimensional cellular interactions and cues given by their microenvironment gained a growing recognition [13, 14].

CCAs were followed by several LOCs designed to stimulate cells cultures with physiologically relevant cues. For example, soft-lithography based tools were used to pattern cell cultures by means of compartments and grooves [15], or to induce cell migration via the generation of soluble chemoattractant gradients [16]. These kind of devices have been used to locally stimulate a section of a single cell grown in a channel with a reagent, exploiting the interface between multiple laminar flows [4, 17]. During those years, polydimethylsiloxane (PDMS) became the mostly used material for microfluidic applications due to its unique properties. As the LOC field and the use of soft-lithography and PDMS became more popular, the complexity of the chips increased, eventually resulting in the development of microfluidic chips including multiple channels separated by porous membranes, as the device presented by Cheung et al. [12] in 2007, and shown in Figure 1.2b,c,d.

The OOC field, as we know it today, originated in 2010 from the Wyss Institute. Hu et al. [18] pioneered the development of the first Lung-on-Chip: a microfluidic chip, including two microchannels running in parallel and separated by a thin porous membrane (Figure 1.3a). Endothelial and epithelial cells are grown on the two sides of the membrane and are stimulated with hemodynamic shear stress and mechanical strain by using the integrated pneumatic and microfluidic system to mimic the physiologically relevant cues of the lungs (Figure 1.3b,c). This publication is usually referred as the first OOC and the one that conceived and divulged the term Organ-on-Chip.

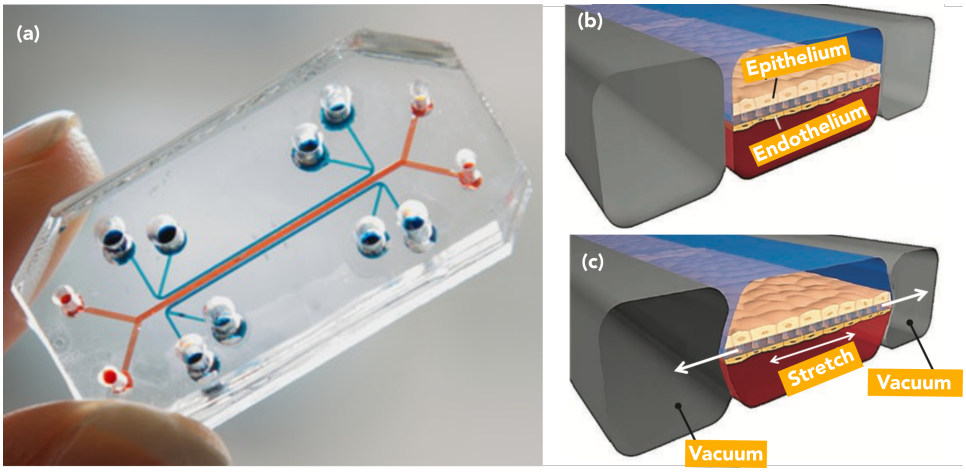

Figure 1.3: (a) Photograph of the Lung-on-Chip presented by Hu et al. [18]. 3D rendering of the main functionalities of the device. In (b) the co-culture composed of a monolayer of epithelium and endothelium cells is seeded inside the microfluidic channels. The channels can be used to apply hemodynamic shear stress and to stretch the co-culture by applying vacuum on the chamber on the sides of the microfluidic channels as shown in (c). Figure adapted from [18].

1.2.2. THE ORGAN-ON-CHIP AGE

Since its first appearance in 2010, the OOC technology has attracted increasing interest and activity in the academic field (with more than 15000 academic publications in 2016 [19] - as shown in Figure 1.4), giving rise to a very diversified field of applications encompassing: disease models, drug discovery, cell biology, etc [8, 18, 20]. Research to date has focused on the development of devices that represent a single functional unit of an organ. There are well-described OOCs for liver [21], kidney [22], lung [18], gut [23], and multiple other [4]. Most of this devices are variations on the format and fabrication process used by Hu et al. [18] in 2010.

The field has successfully attracted the interest of private and public funding agencies. For example, in 2012 the USA's National Center for Advancing Translational Sciences (NCATS), and National Institutes of Health (NIH) commonly invested $ 70 M over a 5-year period for an Organs-on-Chips Program. While in 2017 in the Netherlands, around € 18 M was invested by NWO in the Netherlands OoC initiative (NOCI), lasting 10 years [6]. Meanwhile, OOC companies have attracted the interest of private investors as well. Emulate Inc., a company that was spun out from the Wyss Center, collected more than $ 95 M [24]. Meanwhile Mimetas B.V., in the Netherlands, attracted a total of $ 37 M in four rounds of investments [25].

Since its beginning in 2010, the field has quickly caught the attention of world-wide

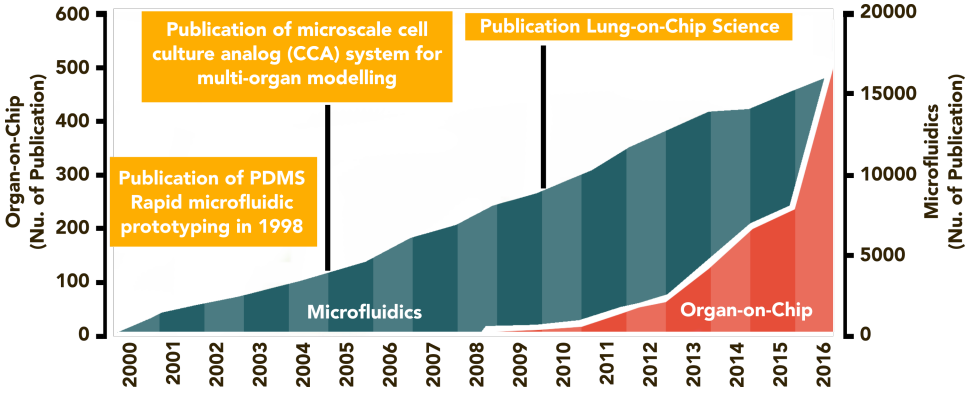

Figure 1.4: Graph reporting the number of publications published from 2000 to 2015 with the keywords "Microfluidics" and "Organ-on-a-Chip". Figure adapted from [19].

media outlets [6]. The general public seems to easily grasp the idea that an Organ-on-Chip is an avatar of a human organ composed of cells and a computer chip. Moreover, they seem attracted by the potential that they could have in reducing and replacing animal testing in the future, even though they often do not fully understand their precise working [6]. The expectations on the OOC field are also shown by the fact that, in 2016 this technology was included in the Top 10 Emerging Technologies list defined by the World Economic Forum's Meta-Council on Emerging Technologies [26].

1.2.3. THE UPCOMING DISILLUSION

As the OOC field attracted more and more attention, the expectations drastically increased with an irrational trend to a point where they are no longer aligned with the results achieved. In order to persuade investors, several overstatements were made by companies [6]. Additionally, popular media has often covered the field with sensational stories, associating the OOC with a quick way to reduce replace animals during drug R&D. In contrast to this "hype", the reality is that pharma companies have not integrated any of these tools into their R&D yet [6].

As reported by Yole' in their Market Analysis report on the OOC field, the failure of the pioneering and well-funded OOC companies to fulfil these high expectations, could have avalanche effects on the whole industry reducing the confidence [6, 27]. Even though this might happen, it does not necessarily imply the end nor the downsizing of OOC field as might be inferred from the Gartner Hype Cycle represented in Figure 1.5.

Technologies often go through different phases before they are fully mature and

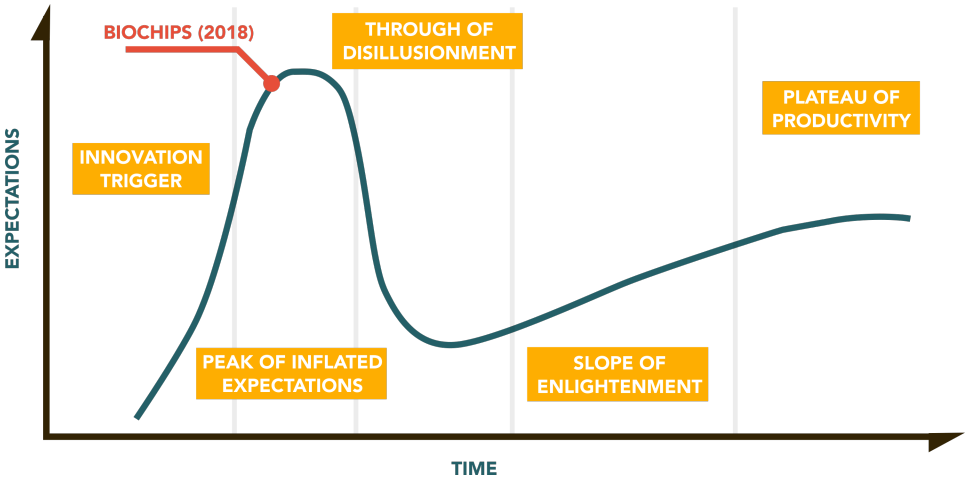

Figure 1.5: Gartner Hype Cycle representing the different phases of a new technology before reaching a mainstream adoption. Figure adapted from [28].

ready for a mainstream adoption [29, 30]. Emerging technologies usually start from an **innovation trigger**, where an early proof-of-concept is developed. In this phase no commercial product is available yet. This is also the moment when the media and investors start getting interested in the technology. The product then moves on towards a second phase: the **peak of inflated expectations**. In 2018, Gartner Inc. included the Biochips field in this phase [31]. Even though the definition of Biochips provided by Gartner Inc. is quite broad, this phase has several points in common with the current state of the OOC field described by Mastrangeli et al. [6]. Next, the technology moves towards the through of **disillusionment**. In this phase the interest in the field wanes, and part of the companies and startups working in this field might pivot towards other technologies or even fail. Even though this phase might sound like a negative moment for companies, investments are not completely over. Usually, companies that focus on early adopter satisfaction have more chances to attract private investments during this phase. After the through, the technology and its advantages are better defined in the **slope of enlightenment**. Second and third generation of the products are developed in this phase. Only at product maturation, in the **plateau of productivity**, real adoption takes off and mainstream sales are achieved. Even though this graphical representation of the life-cycle of a new technology does not guarantee the success of the field, it shows how common the high expectations of the OOC field are. Other technologies [32, 33], such as virtual assistants and social network analysis were considered in a through of disillusionment in 2009 and 2010, before becoming mainstream few years after.

1

1.3. COMMERCIALLY AVAILABLE ORGAN-ON-CHIPS

As a result of the enthusiasm of researchers over the past 10 years, many biologists' start-ups ventures entered into the OOC field (more than 30 worldwide) [19]. Companies such as Draper Inc., CN Bio Innovations Ltd, TissUse GmbH, Emulate Inc., Mimetas B.V., Nortis Inc. among others are reported in the Yole' market analysis [27]. None of the ventures have gained considerable market volume yet, because all of them are still in the technological validation phase, and very few have recurring revenues. Moreover, many startups claim collaboration with big pharma companies but none of them is exclusive.
Here, three main OOC devices on the market will be discussed: Emulate Inc., Mimetas B.V. and Tissuse GmbH products.

As mentioned in Section 1.2.2, Emulate Inc. provides a device based on PDMS and soft-lithography which has a similar design as the Lung-on-Chip presented by Hu et al. [18, 34]. These chips are used in combination with an external system to provide perfusion and mechanical stimulation [35]. The Emulate chips have been used in multiple applications (lungs [18], guts [36], blood-brain barriers [37] among others) and their potential was also proven by the fact that multiple academia perform their studies with similar chips. The Emulate chips are mainly used for tissue-tissue interface models. The high functionality, provided by the design and the use of PDMS, allows to replicate physiologically relevant conditions, such as unidirectional fluid flow similar to microvasculature, gas flow and mechanical strain stimulations [4].

Mimetas B.V. is located in the Netherlands and was founded in 2013. Instead of providing a single chip model, Mimetas' OOC uses a standard well plate format called the Organoplate® (shown in Figure 1.6a,b,c). This product can be used without external pumps and the flow is driven by gravity by means of a rocker that tilts the plate thereby moving the medium back and forth [19]. The unique properties of this plate and the fact that it can be used without a pump, makes this device compatible with medium-high throughput assays. The company claims high usability and easy pipetting of the cells into the device [38]. This device is also designed for tissue-tissue studies, however, compared to Emulate, the shear stress provided by the flow in the microfluidic channel is 2-3 times lower than the physiological conditions [19]. The Organoplate® does not include PDMS and is compatible and with high-volume production technologies. The device is being used to model different organs, using different cell types including: neurons, hepatocytes, endothelial cells, kidney proximal tubular cells, and cancer cells among others [19].

TissUse GmbH and its product differentiate themselves from the previous two companies and the rest of the field because they combine several organs in one chip, result-

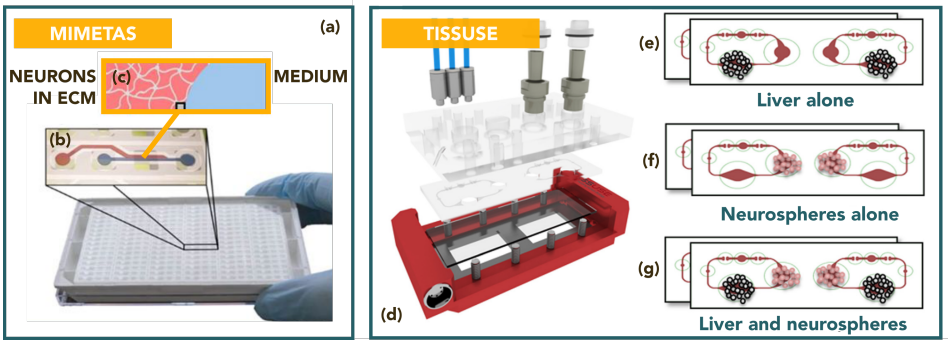

Figure 1.6: (a) Photograph of the Organoplate®. This includes 96 microfluidic chips as shown in (b). The chips includes two channels represented in blue and red. One of the two channels can be used to culture neurons in an extracellular matrix (ECM) and the other channel is used to provide nutrients to the cell culture (c). The ECM gel is restricted in the gel channel thanks to a phase guide which works as capillary pressure barrier. (d) Photograph of the TissUse plate, and (e,f,g) showing the multiple chambers where the different cell cultures can be seeded. Figures adapted from [40, 41].

ing in a Human-on-Chip model. TissUse GmbH provides a plate that can host 2 or 4 tissues in multiple chambers connected by a microfluidic system (Figure 1.6d-g). The flow is regulated by an embedded pump that is used in combination with an external controller. The plate has been used for example with a liver and skin biopsies combination, and intestine, liver, skin, and kidney combination [19]. The company is now focusing on models including more than 4 organs, trying to continue the path towards a whole human body on a chip [39].

This work focuses on devices with a high functionality, capable of reproducing physiologically relevant cues such as those presented by Hu et al. [18] and commercialized by Emulate Inc. Even though this class of devices have a huge potential to reproduce with precision multiple human organ parameters, their future commercialization is currently hindered by their fabrication. The soft-lithography process employed poses major technical hurdles towards large-scale manufacturing, higher throughput and robustness, which are important steps for industrial adoption. As highlighted by the market analysis of the OOC field performed by Yole' in 2017, most of the companies working with these "Emulate-type" devices are not fully aware of these manufacturing limitations even though they might slow down their mainstream commercialization [27]. In order to address this problem, a new class of manufacturable OOC devices at least including the functionalities of the Emulate devices needs to be developed.

1

1.4. ORGAN-ON-SILICON

The future of high-functionality OOCs, such as those supplied by Emulate Inc., might enormously benefit from the use of conventional cleanroom-compatible microfabrication processes. Standard fabrication process, are based on the use silicon wafers and are easier to scale-up in production volumes compared to soft-lithography. Moreover, silicon and other materials often used to fabricate microelectromechanical systems (MEMS) devices (e.g. silicon dioxide and silicon nitride) are biocompatible, meaning that they do not induce any toxic reaction when in contact with a tissue [42, 43]. Last but not the least, silicon allows for a larger level of integration of sensors [44–47], actuators and if needed electronic circuits [48] in the Organ-on-Chip itself.

As already mentioned, other system such as the Mimetas' device can be fabricated without the use of PDMS and soft-lithography. However, this usually comes at expense of a reduced functionality. It is strongly believed that combining highly functional OOCs with robust fabrication methods will enable the success of the OOC field in the years to come. Here, for the first time a new subclass of OOCs, the Organ-on-Silicon (OOS), is defined. Organ-on-Silicon includes all the OOCs fabricated on substrates and with technologies that are compatible with the standard (MEMS) microfabrication industrial base. The need for a new name is necessary to differentiate and clarify the way how these chips are made: with automated and reproducible steps that are also used to fabricate silicon MEMS devices. In the past, key opinion leaders have been misleading with the respect to the fabrication processes employed for OOCs when they stated that soft-lithography is an adaption of fabrication methods used in the computer microchip industry [7, 34].

To enable the fabrication of Organ-on-Chip devices with standard microfabrication technique, while guaranteeing a wide range of functionalities, it is necessary to define protocols to process stretchable polymers (such as PMDS) on silicon wafers and in a standard microfabrication environment. The definition of this protocol was already started by the Electronic Components, Technology and Materials (ECTM) group in TU Delft during the development of other medical devices such as catheters and other stretchable electronics [44, 49–51]. However, a structured and complete protocol for PDMS processing on silicon was not available yet. To promote the use of OOS, it is also necessary to develop some relevant show cases, to prove that this kind of approach does not pose any technological limitation.

1.5. MOTIVATION AND OUTLINE OF THIS THESIS

1.5.1. SCOPE OF THE THESIS

The research presented in this thesis was partly carried out with the ECSEL Joint Undertaking InForMed Project[1]. One of the aims of this multidisciplinary project was to bridge technologies from academia to the market through a pilot line. The InForMed project goal and activities perfectly matched with the challenges that slow down the development of OOC field mentioned in Section 1.3. The OOC activities in the InForMed project were the result of an intense collaboration involving academia, packaging companies, silicon fabs and contractors among others. Consequently, this work is the result of a project constantly balancing between academia and industry.

The goal of this research is to combine polymer processing with standard microfabrication and then employ the results in the OOC field. In particular, this work aims to prove that a material such as PDMS can be processed with standard silicon based fabrication techniques. In order to achieve this, a set of guidelines for PDMS processing on silicon, called here PDMS on Silicon (POS) guidelines, was defined. These guidelines were then employed for the development of two OOS platforms: Cytostretch and the BI/OND platform. For each platform, one prototype product was demonstrated. This work is not aimed at developing and validating a novel OOC model (composed of chip and cells), but it focuses instead on the development of a novel and robust technology to facilitate the development of new cell models based on scalable devices.

The thesis is divided into three parts. **In the first part**, the developed POS guidelines are described. This was done by performing and optimizing PDMS deposition, lithography, etching and releasing technique, to obtain an automatic and scalable process. **The second part** of this work presents the first OOC platform obtained with the POS process: Cytostretch. This OOC platform was partially developed before this work and employed for an Heart-on-Chip model [44]. The original platform was tested to identify its strength and weaknesses. Under the InForMed umbrella, the original Cytostretch Heart-on-Chip device was re-designed, packaged and integrated into a new system. Moreover, its suitability to apply mechanical strain to cell monolayers was demonstrated. The new Heart-on-Chip was designed taking into consideration fabrication compatibility, performances and ease of use. **The third part** is the development of a new microfluidic OOS platform: the BI/OND platform. As previously, the platform was used to fabricate a first prototype product: a microfluidic OOC compatible with 3D cell cultures such as organoids. The basic functionalities of the device were tested with midbrain organoids.

[1] InForMed project: grant no. 2014-2-662155 - ECSEL JU project.

1

1.5.2. OUTLINE OF THE THESIS

Chapter 2 comprises the first part of this thesis, the development of the POS guidelines. This chapter starts with introducing PDMS as a structural material for OOCs and soft-lithography as a fabrication process. The guidelines to deposit and pattern POS wafers are then presented. The chapter also presents the integration of PDMS in a MEMS device. Moreover, it is shown how PDMS contamination of a clean room (CR) environment can be avoided.

The second part of this thesis starts in Chapter 3 and ends in Chapter 7. Chapter 3 introduces the first OOS platform, Cytostretch. One by one the available modules of the Cytostretch platform are introduced and tested: the porous membranes, the microelectrode array (MEA), microgrooves and strain gauges.

Chapter 4 presents the limitations of the platform, and in particular of the the Heart-on-Chip device developed with it. Manufacturability, performance and ease of use are the key points that this thesis focuses on. This chapter also address the first issue: manufacturability. The fabrication of the device is optimized by replacing parylene with polyimide for the insulation of the interconnects. Moreover, a new fabrication process to deposit and simultaneosly pattern PDMS is reported.

Chapter 5 focuses on the performance of the micro electrode array embedded in the Heart-on-Chip. The TiN electrodes integrated in the original Cytostretch device showed a high electrochemical impedance. This problem was addressed by incorporating carbon nanotube (CNT) and poly(3,4-ethylenedioxythiophene) polystyrene sulfonate (PEDOT:PSS) coated electrodes into the platform.

In Chapter 6 the ease of use of the Cytostretch Heart-on-Chip was addressed. The chips presented in Chapter 4 were diced, assembled and packaged with standard techniques used in the silicon chip industry. An easy and complete system around the chips was developed. This system is composed of a conditioning box, a pump, and software. The chapter also introduces a set of tests to validate the packaged chip and the system.

In Chapter 7 the new Cytostretch Heart-on-Chip is tested with induced pluripotent stem cells (iPSC)-derived cardiomyocytes. A protocol to seed these cells is developed and optimized. The application of strain through the membrane with iPSC-derived cardiomyocytes is then tested.

Chapter 8 presents the second platform, a microfluidic OOS known as the BI/OND platform. The device is especially developed to combine organoids with microfluidics. Also in this case, the fabrication process of the chips is described. Moreover, the system de-

veloped to use them is presented. Finally, the chip and the system are tested to demonstrate the basic functionalities of the device.

General conclusions are presented and further research recommendations are provided in Chapter 9.

REFERENCES

[1] O. Gassmann, G. Reepmeyer, and M. Von Zedtwitz, *Leading pharmaceutical innovation* (Springer-Verlag Berlin Heidelberg, 2008).

[2] European Federation of Pharmaceutical Industries and Associations, *The pharmaceutical industry in figures,* (accessed: 01.09.2018).

[3] H. Ledford, *Translational research: 4 ways to fix the clinical trial,* Nature News **477**, 526 (2011).

[4] N. Beißner, T. Lorenz, and S. Reichl, *Microsystems for Pharmatechnology* (Springer International Publishing, 2016).

[5] A. D. van der Meer and A. van den Berg, *Organs-on-chips: breaking the in vitro impasse,* Integrative Biology **4**, 461 (2012).

[6] M. Mastrangeli, S. Millet, and J. van den Eijnden-van Raaij, *Organ-on-chip in development: Towards a roadmap for organs-on-chip,* (2019).

[7] D. E. Ingber, *Developmentally inspired human 'organs on chips',* Development **145**, dev156125 (2018).

[8] A. van de Stolpe and J. den Toonder, *Workshop meeting report organs-on-chips: human disease models,* Lab on a chip **13**, 3449 (2013).

[9] Q. Yang, Q. Lian, and F. Xu, *Perspective: Fabrication of integrated organ-on-a-chip via bioprinting,* Biomicrofluidics **11**, 031301 (2017).

[10] L. M. Sweeney, M. L. Shuler, J. G. Babish, and A. Ghanem, *A cell culture analogue of rodent physiology: Application to naphthalene toxicology,* Toxicology in vitro **9**, 307 (1995).

[11] A. Sin, K. C. Chin, M. F. Jamil, Y. Kostov, G. Rao, and M. L. Shuler, *The design and fabrication of three-chamber microscale cell culture analog devices with integrated dissolved oxygen sensors,* Biotechnology progress **20**, 338 (2004).

[12] B.-h. Chueh, D. Huh, C. R. Kyrtsos, T. Houssin, N. Futai, and S. Takayama, *Leakage-free bonding of porous membranes into layered microfluidic array systems,* Analytical chemistry **79**, 3504 (2007).

[13] J. B. Kim, R. Stein, and M. J. O'hare, *Three-dimensional in vitro tissue culture models of breast cancer—a review,* Breast cancer research and treatment **85**, 281 (2004).

[14] B. M. Baker and C. S. Chen, *Deconstructing the third dimension–how 3d culture microenvironments alter cellular cues,* J Cell Sci **125**, 3015 (2012).

[15] A. M. Taylor, S. W. Rhee, C. H. Tu, D. H. Cribbs, C. W. Cotman, and N. L. Jeon, *Microfluidic multicompartment device for neuroscience research,* Langmuir **19**, 1551 (2003).

[16] N. L. Jeon, H. Baskaran, S. K. Dertinger, G. M. Whitesides, L. Van De Water, and M. Toner, *Neutrophil chemotaxis in linear and complex gradients of interleukin-8 formed in a microfabricated device,* Nature biotechnology **20**, 826 (2002).

[17] S. Takayama, E. Ostuni, P. LeDuc, K. Naruse, D. E. Ingber, and G. M. Whitesides, *Selective chemical treatment of cellular microdomains using multiple laminar streams,* Chemistry & biology **10**, 123 (2003).

[18] D. Huh, B. D. Matthews, A. Mammoto, M. Montoya-Zavala, H. Y. Hsin, and D. E. Ingber, *Reconstituting organ-level lung functions on a chip,* Science **328**, 1662 (2010).

[19] B. Zhang and M. Radisic, *Organ-on-a-chip devices advance to market,* Lab on a Chip **17**, 2395 (2017).

[20] E. W. Esch, A. Bahinski, and D. Huh, *Organs-on-chips at the frontiers of drug discovery,* Nature reviews Drug discovery **14**, 248 (2015).

[21] S. S. Bale, L. Vernetti, N. Senutovitch, R. Jindal, M. Hegde, A. Gough, W. J. McCarty, A. Bakan, A. Bhushan, T. Y. Shun, *et al., In vitro platforms for evaluating liver toxicity,* Experimental biology and medicine **239**, 1180 (2014).

[22] K. Jang, A. P. Mehr, G. A. Hamilton, L. A. McPartlin, S. Chung, K.-Y. Suh, and D. E. Ingber, *Human kidney proximal tubule-on-a-chip for drug transport and nephrotoxicity assessment,* Integrative Biology **5**, 1119 (2013).

[23] H. J. Kim, D. Huh, G. Hamilton, and D. E. Ingber, *Human gut-on-a-chip inhabited by microbial flora that experiences intestinal peristalsis-like motions and flow,* Lab on a Chip **12**, 2165 (2012).

[24] Crunchbase, *Emulate,* (accessed: 06.03.2019).

[25] Crunchbase, *Mimetas,* (accessed: 06.03.2019).

[26] World Economic Forum, *Top 10 emerging technologies of 2016,* (accessed: 01.09.2018).

[27] Yole Développement, *Organs-on-chips 2017 report,* (accessed: 01.09.2018).

[28] D. E. O'Leary, *Gartner's hype cycle and information system research issues,* International Journal of Accounting Information Systems **9**, 240 (2008).

[29] Gartner Inc., *Gartner hype cycle,* (accessed: 06.03.2019).

[30] A. Linden and J. Fenn, *Understanding gartner's hype cycles,* Strategic Analysis Report Nº R-20-1971. Gartner, Inc (2003).

[31] Gartner Inc., *5 trends emerge in the gartner hype cycle for emerging technologies, 2018,* (accessed: 06.03.2019).

[32] Gartner Inc., *Gartner's hype cycle special report for 2009,* (accessed: 06.03.2019).

[33] Gartner Inc., *2010 emerging technologies hype cycle is here,* (accessed: 06.03.2019).

[34] D. Huh, H. J. Kim, J. P. Fraser, D. E. Shea, M. Khan, A. Bahinski, G. A. Hamilton, and D. E.

Ingber, *Microfabrication of human organs-on-chips,* Nature protocols **8**, 2135 (2013).

[35] Emulate Inc., *Platform & products,* (accessed: 01.01.2018).

[36] H. J. Kim, D. Huh, G. Hamilton, and D. E. Ingber, *Human gut-on-a-chip inhabited by microbial flora that experiences intestinal peristalsis-like motions and flow,* Lab on a Chip **12**, 2165 (2012).

[37] M. W. van Der Helm, A. D. Van Der Meer, J. C. Eijkel, A. van den Berg, and L. I. Segerink, *Microfluidic organ-on-chip technology for blood-brain barrier research,* Tissue barriers **4**, e1142493 (2016).

[38] Mimetas BV, *Easy-to-use,* (accessed: 06.03.2019).

[39] TissUse GmbH, *Tissuse website,* (accessed: 06.03.2019).

[40] N. R. Wevers, R. Van Vught, K. J. Wilschut, A. Nicolas, C. Chiang, H. L. Lanz, S. J. Trietsch, J. Joore, and P. Vulto, *High-throughput compound evaluation on 3d networks of neurons and glia in a microfluidic platform,* Scientific reports **6**, 38856 (2016).

[41] E.-M. Materne, A. P. Ramme, A. P. Terrasso, M. Serra, P. M. Alves, C. Brito, D. A. Sakharov, A. G. Tonevitsky, R. Lauster, and U. Marx, *A multi-organ chip co-culture of neurospheres and liver equivalents for long-term substance testing,* Journal of biotechnology **205**, 36 (2015).

[42] G. Voskerician, M. S. Shive, R. S. Shawgo, H. Von Recum, J. M. Anderson, M. J. Cima, and R. Langer, *Biocompatibility and biofouling of mems drug delivery devices,* Biomaterials **24**, 1959 (2003).

[43] B. W. Kristensen, J. Noraberg, P. Thiébaud, M. Koudelka-Hep, and J. Zimmer, *Biocompatibility of silicon-based arrays of electrodes coupled to organotypic hippocampal brain slice cultures,* Brain research **896**, 1 (2001).

[44] S. K. Pakazad, A. Savov, A. Van de Stolpe, and R. Dekker, *A novel stretchable micro-electrode array (smea) design for directional stretching of cells,* Journal of Micromechanics and Microengineering **24**, 034003 (2014).

[45] S. Khoshfetrat Pakazad, *Stretchable micro-electrode arrays for electrophysiology,* (2015).

[46] W. Quiros-Solano, N. Gaio, C. Silvestri, G. Pandraud, and P. Sarro, *Pedot: Pss: a conductive and flexible polymer for sensor integration in organ-on-chip platforms,* Procedia Engineering **168**, 1184 (2016).

[47] W. Quiros-Solano, N. Gaio, C. Silvestri, G. Pandraud, and P. Sarro, *Polymeric strain gauges as pressure sensors for microfabricated organ-on-chips,* in *2017 19th International Conference on Solid-State Sensors, Actuators and Microsystems (TRANSDUCERS)* (IEEE, 2017) pp. 1296–1299.

[48] R. Ponte, V. Giagka, and W. A. Serdijn, *Design and custom fabrication of a smart temperature sensor for an organ-on-a-chip platform,* in *2018 IEEE Biomedical Circuits and Systems Conference (BioCAS)* (IEEE, 2018) pp. 1–4.

[49] B. Mimoun, V. Henneken, A. van der Horst, and R. Dekker, *Flex-to-rigid (f2r): A generic plat-*

form for the fabrication and assembly of flexible sensors for minimally invasive instruments, IEEE Sensors Journal **13**, 3873 (2013).

[50] W. Quirós-Solano, N. Gaio, O. Stassen, Y. Arik, C. Silvestri, N. Van Engeland, A. Van der Meer, R. Passier, C. Sahlgren, C. Bouten, *et al.*, *Microfabricated tuneable and transferable porous pdms membranes for organs-on-chips,* Scientific reports **8**, 13524 (2018).

[51] S. Joshi, A. Savov, S. Shafqat, and R. Dekker, *Investigation of "fur-like" residues post dry etching of polyimide using aluminum hard etch mask,* Materials Science in Semiconductor Processing **75**, 130 (2018).

2

PDMS ON SILICON (POS) GUIDELINES

2.1. INTRODUCTION

As mentioned in Chapter 1, the commercialization of OOC devices in the upcoming years might be hindered by the materials and the fabrication processes currently employed [1]. To address this problem, this chapter focuses on the novel fabrication technique developed to facilitate the upscaling of OOC manufacturability. This chapter is divided into two parts. In the first part, an overview of the technology behind standard OOC devices is provided. In particular, it focuses on the most commonly used material - PDMS - and the most commonly used fabrication process - soft-lithography. In order to exploit the unique properties of PDMS without resorting to the poorly-scalable soft-lithography, the PDMS on Silicon (POS) guidelines were developed and they will be presented in the second part of this chapter. The procedures for the deposition and patterning of PDMS on silicon (Si) wafers, while guaranteeing the wafers process compatibility with standard microfabrication processes, are discussed. This was done to be able to transfer the fabrication of PDMS based OOCs from soft-lithography towards standard silicon-based microfabrication technologies, enabling the large-scale fabrication of these devices.

2.2. PDMS AND SOFT-LITHOGRAPHY

In the past ten years, OOC technology has been reliant on a single material, PDMS, and the most commonly used fabrication process, soft-lithography [2]. The first and biggest

discoveries and advancements in the OOC field were made through PDMS-based devices [3, 4], and at the same time the biggest technical issues and challenges with OOCs have often been related to this material and the way it is processed [1]. Section 2.2.1 of this chapter gives an overview of PDMS, highlighting the advantages and disadvantages of this material. Moreover, the soft-lithography process will be presented in Section 2.2.2, emphasizing the limitations of this technology.

2.2.1. PDMS

PDMS is a polymeric organosilicon compound (also known as silicone) with the chemical formula: $(CH_3[Si(CH_3)_2O]_nSi(CH_3)_3)$. The material is characterized by its inorganic siloxane (Si–O–Si) backbone to which organic methyl (CH_3) groups are attached. PDMS became the mostly used material for microfluidic applications in general, and for OOC devices in particular [2].

The polymerization of PDMS occurs when two components, a siloxane oligomer, and a curing agent, are mixed together in a specific mixing ratio. The two components are usually provided together in a kit, such as the Sylgard 184 formulation from Dow Corning Inc. [5]. Although PMDS polymerisation takes place at room temperature, it can be also accelerated by placing the sample at a higher temperature (usually 90 °C), as used throughout the thesis. During the polymerisation, the vinyl groups ($CH_2 = CH^-$) of the siloxane oligomers and the hydrosilane (SiH) groups in the curing agent form covalent bonds [2]. In the particular case of Sylgard 184, the cross-linking reaction is catalysed by a platinum-catalyst present in the curing agent, although other kits employ different catalysts [2, 6, 7]. The mixing ratio between the two components can be tuned to modify the properties of PDMS, such as the pre-polymerization viscosity, the elastic modulus [8], and liquid absorption [9]. Nevertheless, the 10:1 ratio is most commonly used.

The polarity of the siloxane backbone of the PDMS molecule is shielded by the non-polar methyl groups [10, 11], making the PDMS molecule highly hydrophobic, and less prone to creating intermolecular reactions [12]. Consequently, structures and tools fabricated from, or coated with PDMS exhibit a low surface energy and low chemical reactivity [11], resulting in a high level of biocompatibility. Additionally, PDMS has a high chemical and thermal stability (Sylgard 184 by Dow Corning Inc. can up to 186 °C in air) as a result of the strong chemical bonds and the polarity of Si–O backbone structure [11, 12]. The siloxane bonds have nearly zero energy of rotation about the Si–O groups [12]. This makes PDMS suitable for highly flexible and stretchable structures [2].

PDMS is optically transparent (down to 300 nm wavelength), and is permeable to

non-polar gasses [2]. In the particular case of OOC applications, the optical transparency of PDMS has been extremely useful to allow the alignment of the individual elements that compose a microfluidic device. Moreover, it provides the possibility to monitor cells cultured inside 3D PDMS structures using the standard optical microscopes used in the day-to-day routine in biological labs [13]. Additionally, the permeability to gasses guarantees the exchange of oxygen between the closed cell culture environment inside the chip, and the controlled environment provided by the incubator in which they are stored [2].

Another property that made PDMS so popular in this field is that it is commercially available and relatively inexpensive compared to other polymers such as polyimide (PI) and poly(3,4-ethylenedioxythiophene) polystyrene sulfonate (PEDOT:PSS). However, as every material PDMS also has some limitations that have negatively influenced the wide adoption in the microfluidic field. The porosity of PDMS causes small molecules, like chemokines, cytokines, growth factors or drugs, to diffuse into, or bind onto free (not cell-covered) polymer. This may reduce the effective free concentration of these molecules, and may affect dose-dependent outcomes of experiments [14]. However, several solutions have been identified to prevent this biochemical uptake, such as coating the PDMS with titanium dioxide, lipophilic coatings or cells [15, 16].

From a fabrication point of view, PDMS tends to swell when exposed to non-polar organic solvents such as chloroform or hexane [17]. This swelling, in combination with the high thermal coefficient of expansion and the elasticity of PDMS, have proven to be limiting factors during lithographical processes on PDMS, and the deposition of PDMS on PDMS or the deposition of PDMS on another materials (such as metals) [18]. Since PDMS is often used in combination with soft-lithography, the above mentioned limitations have often been disregarded. Soft-lithography does not require any photo lithography and/or deposition steps on PDMS, as presented in Section 2.2.2.

2.2.2. SOFT-LITHOGRAPHY

Soft-lithography quickly spread in academia since it allows for rapid and cheap fabrication of new OOC devices [2]. Unlike what the name suggests, soft-lithography is a non-photolithographic method for replicating a pattern without expensive photolithographic tools [2].

A 3D sketch of the fabrication steps to develop a soft-lithography based OOC (similar to those shown in Figure 1.3 and 1.2) are shown in Figure 2.1. This starts with a previously fabricated, re-usable mold (Figure 2.1a). Usually this consists of a patterned SU8 photoresist (PR) layer on a Si wafer. Uncured PDMS is dispensed onto the mold, trans-

ferring its pattern into the PDMS layer when it is cured (Figure 2.1b). Subsequently, the elastomer is detached from the mold by simply peeling it off (Figure 2.1c,d). The basic molding process described above can be used to form channels, cavities, porous membranes (Figure 2.1e-i) etc. Substantial pressure needs to be applied to the PDMS for the accurate transfer of small features, such as in the case of porous membranes with holes with sizes in the order of a few microns [4].

The channels and the membranes can then be sealed together to compose the chip as shown in Section 1.2.2 (Figure 2.1j-l). Before bringing together all the chip components, an oxygen plasma treatment is necessary to increase the hydrophilicity of the PDMS surface. The oxygen plasma breaks some of the Si–CH_3 junctions turning the PDMS from hydrophobic to hydrophilic. The PDMS elements are sealed together by

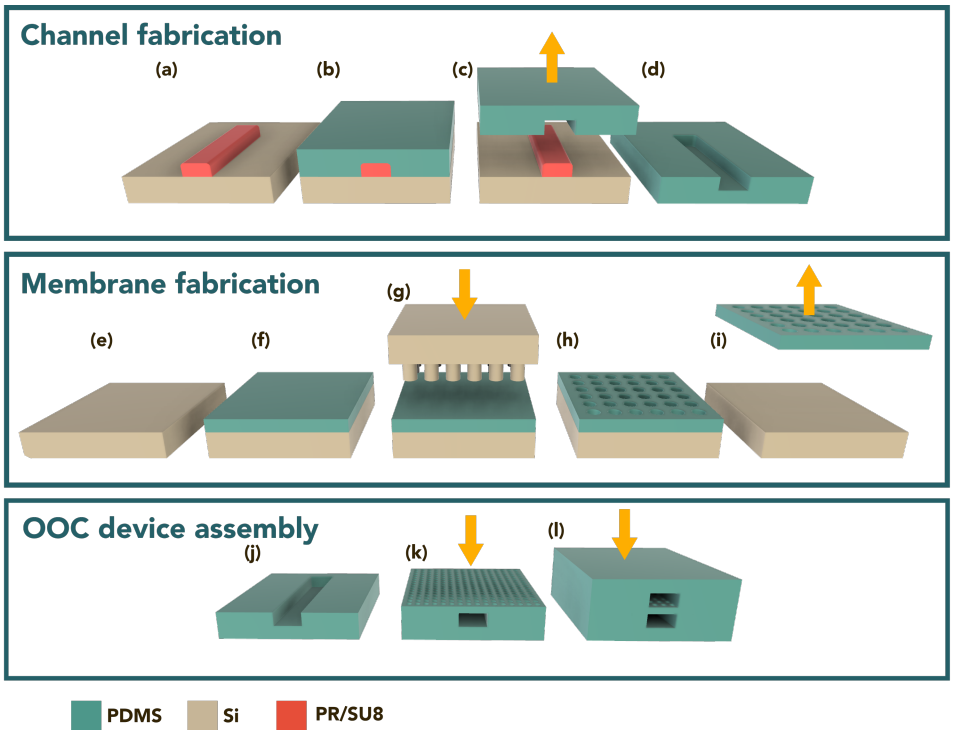

Figure 2.1: 3D rendering of the the fabrication steps for fabricating soft-lithography based microfluidic channels. Channel fabrication: (a) a mold is prepared spin coating and patterning a layer of SU8; (b) PDMS is spin coated on the mold; (c,d) the PDMS is manually peeled off from the mold. Membrane fabrication: (e,f) PDMS is spin coated on a pristine wafer; (g) a Si mold is brought in contact with the PDMS and pressed against the first Si wafer till curing; (h,i) the mold is removed and the PDMS membrane is manually peeled off. OOC device assembly: (j,k,l) the two elements fabricated in the previous steps are manually brought together after an oxygen plasma treatment, and then kept under a constant pressure to promote mechanical bonding. The figures are not drawn to scale.

manual alignment. The assembled device then needs to be stored at 60 °C overnight, under the application of uniform pressure to ensure a reliable bonding.

In literature several issues and limitations have been identified and reported with respect to soft-lithography. The fabrication of devices with small features is strongly limited by the manual steps required [4]. Moreover, soft-lithography is a labor-intensive procedure that reduces device throughput and yield, which is a hurdle towards large-scale fabrication. Steps such as dispensing, peeling-off and alignments are mostly performed manually. Moreover, the bonding of cured PDMS structures promoted by oxygen plasma and pressure has shown to be inconsistent [19], affecting the reliability of microfluidic systems embedded in the devices. These limitations conflict with the need for low-cost and reliable OOCs for cell culture, which is conventionally based on the extensive use of disposables.

2.3. PDMS ON SILICON (POS) GUIDELINES

Despite the obvious limitations of soft-lithography mentioned in Section 2.2.2 and the consequent incompatibility with any economy of scale, little to no effort has been done to fabricate 3D devices in PDMS without soft-lithography. The low cost and the limited number of devices necessary for a test have not stimulated the academic community to investigate into more manufacturable alternative technologies. Because of this lack and to circumvent the patent by Wyss [20], several companies have abandoned PDMS despite its unique properties such as stretchability and oxygen and optical transparency.

Unlike other groups, TU Delft and in particular the ECTM group, took a different approach. The ECTM group aims at providing highly reliable, repeatable and precise micromachining techniques to deposit, pattern and use PDMS and other polymers in conventional cleanroom-compatible microfabrication processes. The goal of these efforts is to replicate what has been done in the micro-electro-mechanical system (MEMS) field, where the standardization of surface patterning techniques, using lithography and etching, showed to be the major driver for its success [21].

Multiple commercially-available polymers such as PI, parylene, PEDOT:PSS and in particular PDMS were introduced in the Class-100 clean room of the TU Delft - Else Kooi Laboratory (TUD-EKL), and processing protocols were defined targeting three goals: (i) the deposition and patterning of polymers on Si wafers (Section 2.3.1, 2.3.2 and 2.3.3), (ii) the integration of polymer structures in a complete process including standard microfabrication steps, such as depositions and etching of insulators and conductive materials (Section 2.3.4); (iii) achieving the first two goals without affecting the CR environment with respect to contamination nor the generation of particles (Section 2.3.4).

In an effort to achieve these goals, a set of rules and procedures were developed. In this work, these will be referred as **PDMS on Silicon (POS)** guidelines. As most of the polymers have multiple properties, deposition, curing and etching steps in common, these guidelines can be also applied for the use of other polymers in standard microfabrication.

2.3.1. DEPOSITION

First, the siloxane oligomer and the curing agent are mixed together. This step is performed with a planetary centrifugal mixer (Thinky Speedmixer) to prevent bubble formation and to have a uniform mixing of the two components. In the case of a 10:1 mixture ratio, 6-7 grams of PDMS for a 4-inch wafer need to be prepared.

The deposition itself is performed on a single-wafer spin coater (Brewer Sience Manual Spinner). PDMS can not be dispensed using the automatic coater available in TUDEKL, since the polymerization reaction also happens at room temperature. This would result in the formation of cured PDMS particles, and eventually in the clogging of the tubes that deliver the PDMS onto the wafer.

The PMDS is directly dispensed on the centre of the wafer placed on the coater. The coating is performed with a two-step spin coating recipe. The first spreading step, usually performed at 300 RPM, is used to spread the PDMS to cover the whole wafer. In the second step both the spin speed and the time can be tuned to define the thickness of the layer. Thickness values ranging from 9 to 4 µm can be achieved with spinning times in the range of 30 to 90 s at 6000 RPM. Table 2.1 lists the recipes (second step) and the corresponding thickness obtained by tuning the time. Thinner layers can be obtained with different curing agent-siloxane oligomer ratios. For example, a 4.7 µm can be easily obtained in 45 s with a 1:5 ratio. Moreover, the thickness can be tuned by changing the rotation speed as reported in the Table 2.1. The maximum thickness is limited by difficulties in the handling of wafers covered with a very thick uncured PDMS layer. A layer thicker than 200 µm is rather unfeasible.

After spin coating, a manual edge bead removal (EBR) step is performed with a square rectangle foam cleaning swab stick soaked in acetone. This is used to remove the uncured PMDS from the side and the edges of the wafer. The EBR is performed by placing the stick in contact with the edge of the wafer while the wafer is rotated a 10 RPM. After the EBR, the wafers are placed horizontally in an open cassette, preventing the uncured PDMS to touch the slits of the cassette. The cassette with the wafers is then placed in a convection oven for curing in air at 90 °C for 1 hour.

Despite the fact that the deposition includes a number of manual steps (such as

Rotation Speed (RPM)	Time (s)	Ratio	Thickness (µm)
6000	30	1:10	9.2
6000	45	1:10	7.2
6000	60	1:10	5.7
6000	90	1:10	4.2
6000	45	1:5	4.7
4000	45	1:5	8.3
300	60	1:10	200

Table 2.1: Example of PDMS spin-coating recipes and the corresponding achieved thicknesses.

PDMS dispensing and the EBR), the deposition parameters are not influenced by the operator, resulting in a good reproducibility. Moreover, the manual steps do not affect the fabrication yield and throughput. An experienced operator can deposit a 7 µm-thick PDMS layer on a batch of 25 wafers in no more than 2 hours (including material preparation, spinning, EBR, and single wafer coater cleaning) with a yield of 100%. The deposition provides layers of 7 µm in thickness with a standard deviation of 0.1 µm over a single wafer and 0.2 µm from wafer to wafers. These observations were obtained by tracking time, yield, throughput and thickness on three different batches of 25 wafers. Finally, the steps of deposition and EBR could be readily automated in a full production environment with a dedicated tool.

2.3.2. LITHOGRAPHY

Till now, PDMS is generally considered to be incompatible with conventional lithography. One of the reasons is the low surface energy of PDMS which results in the dewetting of Novolak-based PRs when dispensed on PDMS as can be seen in Figure 2.2a [19]. This problem can be easily solved by applying an oxygen plasma treatment to the PDMS surface, to strip the methyl groups from the surface of the PDMS group and form Si–OH groups (Figure 2.2b,c) [22]. The oxygen plasma treatment is performed in a Trikon Omega 201 ICP plasma etcher with an isotropic oxygen plasma recipe (O_2, P: 50 mTorr, RIE Bias: 0 W, ICP Power: 500W). The treatment is not permanent, as the hydrophobicity of PDMS returns within a few hours since the unbound siloxane chains can migrate to the surface and restore the hydrophobicity [17, 19]. This problem was not critical during our fabrication process. Right after oxygen treatment, the wafers are loaded onto an automatic coater EVG 201 and a 1.4 µm thick PR layer is spin coated on top of the PDMS. Despite the fact that the deposition of the PR takes about one hour for

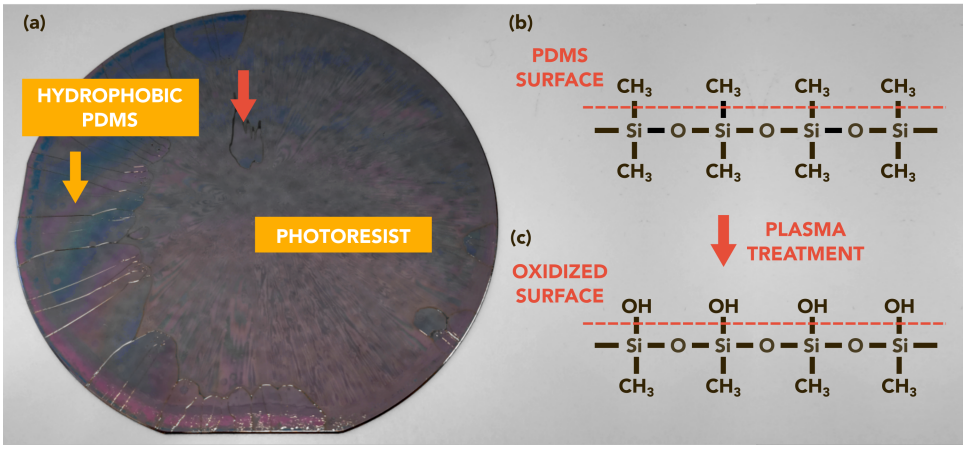

Figure 2.2: (a) Dewetting of Novolak-based PR on a PDMS surface. PR gaps indicated by arrows. Backbone structure of PDMS: (b) intrinsically hydrophobic surface and (c) hydrophilic surface after oxygen plasma treatment.

a complete batch, no relevant differences were detected between the first and the last wafer coated with PR, showing that the restoration of the PDMS hydrophobicity is not fast enough to affect PR coating of a complete batch.

Another issue that hinders lithography on PDMS is the high thermal expansion coefficient of PDMS [19]. The mismatch between the resist and the PMDS during PR baking results in cracking of the resist as shown in Figure 2.3a. In order to avoid this issue, the PDMS can be covered with a 250 nm thick aluminum (Al) layer to create a buffer layer between the PR and the PDMS. This layer, besides reducing the PR cracking, can be used as a hard etch mask. Often the depositon of Al on PDMS results in groove like topographies that can eventually create a permanent and undesirable alteration of the PDMS surface, and affect the lithography [19]. In our case, sputter deposition, using a Trikon Sigma 204 sputter machine, was used. The sputter deposition is performed at low power (1 kW) and the temperature of the wafer is kept at 25 °C. Even though the deposition seems to generate looking like grooves topography, as can be seen in Figure 2.3b, they do not affect the lithography performed right after the Al depositon. Moreover, after Al removal, no topography was seen on the PDMS, unlike previously reported [21]. The integration of the Al interlayer made the oxygen plasma treatment obsolete. Additionally, in an effort to reduce the risk of PR cracking, the temperature of the soft and hard bake of the resist was reduced to 80 °C. A 1 µm thick layer of PR was deposited and patterned with proximity exposure on multiple 25-wafers batches. Features down to 2 µm were achieved without critical issues [23].

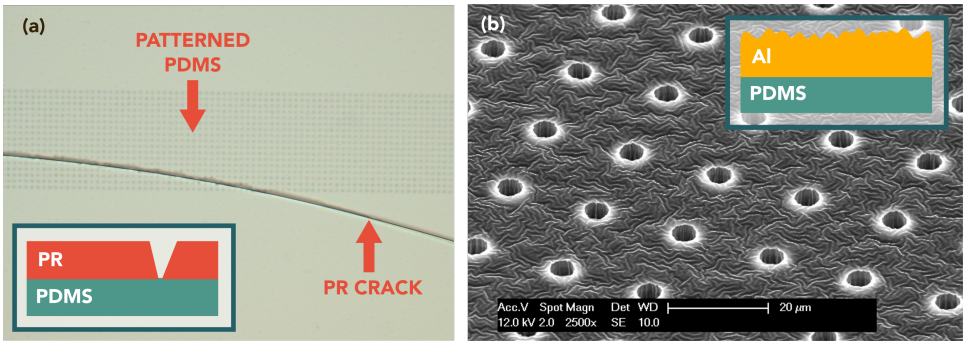

Figure 2.3: (a) Cracked PR layer on top of a PDMS layer. (b) Wrinkled Al on top of a PDMS layer.

2.3.3. ETCHING

Unlike most of the polymers that are solely composed of carbon and hydrogen, PDMS is a silicon-based polymer. Oxygen plasma etching, commonly used for polymers such as parylene and PI, does not generate any volatile products when applied to Si–O bonds, therefore a different etching chemestry is necessary. Moreover, the bond energy of Si–O (107 kcal) is higher than that of C–C (83 kcal) and C–O (85 kcal), consequently requiring higher etching powers [11]. Dry fluorine based chemistries, such as based on CF_4 and SF_6, are often used for PDMS etching since they generate volatile compounds when they react with the Si in PDMS [11]. Consequently, an SF_6 based recipe was developed in the Trikon Omega 201 etcher available in TUD-EKL.

Before etching the PDMS, it is necessary to pattern the Al maks interlayer. This is also performed in the Trikon Omega 201 etcher with a standard Al etching recipe (Cl:HB,1:1.3, P: 5 mTorr, RIE Bias: 50 W, ICP Power: 500W). As observed by Joshi et al. [24], the Al needs to be over-etched to avoid any micromasking effects originating from Al particles embedded in the PDMS during the sputter deposition. Subsequently, the PDMS is etched using the remaining PR and the patterned Al layer as a mask with a reactive-ion etch consisting of the following recipe: $CH_4 : SF_6 : O_2$,1:1:1, P: 20 mTorr, RIE Bias: 20 W, ICP Power: 500W. The recipe results in an etching rate of 0.4 µm/min while etching features 4 µm wide (for a 6% loading). After PDMS etching, the Al hard mask is removed by wet etching using a buffered solution of acetic acid, nitric acid (HNO_3), and hydrofluoric acid (PES etch) at room temperature for 10 minutes.

The profile of an 8.5 µm wide hole etched with the presented recipe is shown in Figure 2.4a. As can be seen, the recipe is isotropic and results in a rounded profile. The etching conditions were not further optimised to obtain a higher anisotropy, to control even more accurately shape and size of the cavities etched in the PDMS, since

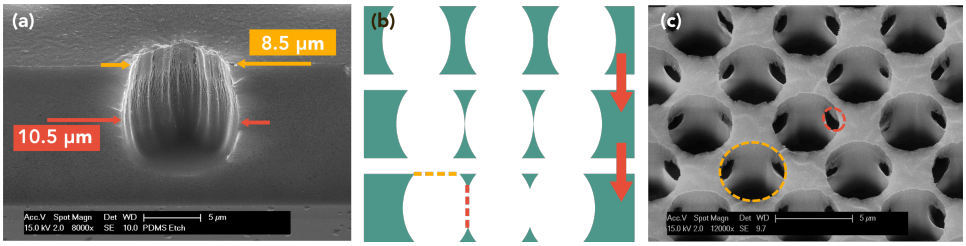

Figure 2.4: Scanning electron microscope (SEM) cross-section of a hole etched in PDMS with the etching process presented in Section 2.3.3. Bringing the rounded pores closer and closer, as shown in (b), it is possible to obtain the 3D scaffold in (c). Scale bars: 5 µm.

this rounded profile did not seem to affect the fabrication of the devices. Instead, the rounded profile can be exploited to create new structures, and in particular 3D scaffolds. If the holes are designed closed enough (Figure 2.4b), the rounded profile of the two holes merge creating a 3D structure resembling a scaffold as can be seen in Figure 2.4c.

2.3.4. INTEGRATION OF PDMS IN A STANDARD SILICON-BASED MICROFABRICATION PROCESS

Next to deposition and patterning, PDMS structures need to be integrated in a standard microfabrication process. This requires that the wafers with the PDMS structures can be further processed in standard CR tools, such as etchers, depositon and lithographic tools ect., without damaging or altering the PDMS structures or contaminating the machines used.

PDMS STRUCTURE INTEGRITY

One of the main issues with respect to integrating PDMS structures in a standard fabrication process is related to the fact that PDMS swells in contact with nonpolar solvents (e.g., hydrocarbons, toluene, and dichloromethane) [25]. Even for solvents like acetone and isopropanol, which have highly polar molecules, we opted to replace them with dimethyl sulfoxide (DMSO), since this results in less swelling [25].

Only strong acid and bases can affect PDMS, causing its depolymerization. This is due to the high bond energy and polarity of the polysiloxane chain [6]. Etchants often used in a CR evnironment, such as acetic acid, HNO_3, hydrofluoric acid and buffered hydrofluoric, have little to no effect on PDMS as confirmed by our tests. Moreover, the above-mentioned acids all have polar molecules, implying a little degree of PDMS swelling. This means that materials such as silicon oxide (SiO_2), titanium (Ti), and Al can be easily wet etched when PDMS structures are present on the wafer. In order to break

the polymer down into smaller subunits, certain acids (such as sulfuric acid - H_2SO_4 and trifluoroacetic acid [26]) or organic reagents (such as M tetrabutylammonium fluoride (TBAF) solution in N-methyl-2-pyrrolidone (NMP) [27]) have been used. Pure and diluted HNO_3 is often used to clean metallic and organic residues on silicon wafers in a standard microfabrication protocol. However, HNO_3 based solutions alter the PDMS surface [28], limiting the cleaning procedure of a wafer with PDMS structures. For this reason, the cleaning of wafers with PDMS structures needs to be performed only with an oxygen plasma. PDMS structures can be placed in a standard plasma stripper, such as the TEPLA Plasma 300, when protected with a metallic layer such as the Al hard mask.

In case of multilayer PDMS structures, swelling of the PDMS can result in detachment of two bonded PDMS layers as shown by Koh et al. [28]. To guarantee a strong adhesion between two layers of PDMS, two surface treatments are used: oxygen plasma and corona discharge [29, 30]. Several groups are still relying on these methods even after their reliability and repeatability have been proven to be quite low with variations of 50 and 20% in the bonding strength using oxygen plasma and corona discharge, respectively [28]. With the POS, when a multilayer device needs to be fabricated, a layer of uncured PDMS is deposited on top of a cured PDMS, instead of bonding together two cured PDMS layers. This has shown to provide a substantial higher bonding strength when compared to oxygen plasma or corona discharge [28].

The number of materials that can be deposited on top of a PDMS structure on silicon is quite limited. As already mentioned in Section 2.3.2, it is possible to sputter coat metals such as Al, Ti and titanium nitride (TiN) on condition that the power and the temperature of the deposition are kept low enough to avoid undesired PDMS expansion, etching and/or burning. High-temperature depositions such as plasma-enhanced chemical vapor deposition (PECVD) and low pressure chemical vapor deposition (LPCVD) are not allowed after the PDMS is deposited. This aspect can limit the range of feasible structures. However, it can be circumvented by means of a technique, previously referred to as polymer-last approach [31]. Following this approach, the process sequence of the chip is modified to move the fabrication of every high-thermal budget component before the deposition of the PDMS layer. This approach was used for the integration of CNTs structures [32, 33] and integrated circuits in a chip with PDMS structures [34].

PDMS IN A CR ENVIRONMENT

The deposition, lithography and etching of PDMS and its integration in standard microfabrication processes needs to be compatible with a CR environment, therefore implemented in such a way to prevent particles or any other form of contamination.

Wafers with PDMS are often prone to generate particles. The source of these parti-

cles can be subdivided into two categories. The first source of particles is the edge and the side of the wafers. They are generated by handling the wafers with tweezers, and/or loading and unloading a wafer in a cassette. In order to avoid these, the EBR presented in Section 2.3.1 was introduced. The second source of particles is on the backside of the wafer. These are generated while spinning PDMS at high rotation speeds. They usually detach while loading and unloading the wafers from the chuck of a machine. In the past, a manual cleaning of the backside of the wafer was performed before curing the wafers with a manual cleaning procedure using a CR-compatible tissue soaked in acetone (named **manual-tissue cleaning**). This procedure does not guarantee a clean backside as reported by the particle counts performed with a Nanophotonics Reflex 300 (Figure 2.5). To avoid this problem, an easy and quick way to clean the backside of the wafers was developed (named **auto-PR cleaning**). Before depositing the PDMS, a thin PR layer is spin coated on the backside of the wafer. Then, after PDMS deposition and curing, the wafer is loaded upside down on a single wafer coater and cleaned with an acetone spray while being rotated. The PDMS particles are carried away by the acetone while the resist is dissolved.

The two cleaning methods were compared using a particle counter. The results of these tests are shown in Table 2.2. The initial number of particles on the backside of the wafers before the deposition of PDMS were 257 ±19 and 411 ±10 for particles with diameter (d) between 0.218 and 0.240 µm and particles with diameter larger than 0.240 µm, respectively. After the PDMS deposition and the two cleaning processes, the particle counts showed a drastic difference in the amount of particles on the backside. In particular, the number of particles with $0.218 < d < 0.240$ µm increased to 780 ± 110 with the **auto-PR cleaning**, while they increased to 11205 ± 6599 with the **manual-tissue cleaning**. Moreover, the number of particles with $d > 0.240$ µm increased to 677 ±72 and 37452 ± 23209 with the **auto-PR** and the **manual-tissue cleaning**, respectively. These results show that the presented cleaning process provides a cleaner backside surface. A particle count measurement of a wafer before and after the **manual-tissue cleaning** is

Particle Count	0.218 < d < 0.240 µm	d > 0.240 µm
Before cleaning step	257 ±19	411 ±10
After auto-PR cleaning	780 ± 1100	677 ±72
After manual-tissue cleaning	11205 ± 6599	37452 ± 23209

Table 2.2: Particle counts on the backside of the wafers coated with PDMS, before and after the two presented cleaning steps: **manual-tissue** and **auto-PR cleaning.**

shown in Figure 2.5.

Besides the particles, another source of contamination of CR equipment can be caused by curing agent degassing and the re-deposition of PDMS during etching. The first problem occurs when the PDMS layer is not sufficiently cured. The problem can be identified by means of a Leak-up-Rate test. This test is usually performed to identify leakages in vacuum equipment, and can be performed to quantify the change of pressure in the chamber following the loading of a PDMS wafer. This test is usually performed in one of the chambers of the Trikon SigmaEVG 204. If the leak rate is higher than $2*10^{-6}$ Torr*L/sec, measured 10 minutes after loading the wafer in the chamber, the wafers are considered to be not compatible with sputtering or other vacuum equipment. This check is performed on one of the wafers for every batch, before any critical step (such as plasma etching and plasma deposition), to verify whether or not the wafer will degas excessively.

The re-deposition of material can occur during etching and/or during any high power sputtering on PDMS. This phenomenon happens for every material exposed to a directive plasma, but the extensive etching time of PDMS might result in an accumulation of PDMS on the surface around the chuck and create particles. In order to limit this problem several preventive actions can be taken. After every batch, the machine should be

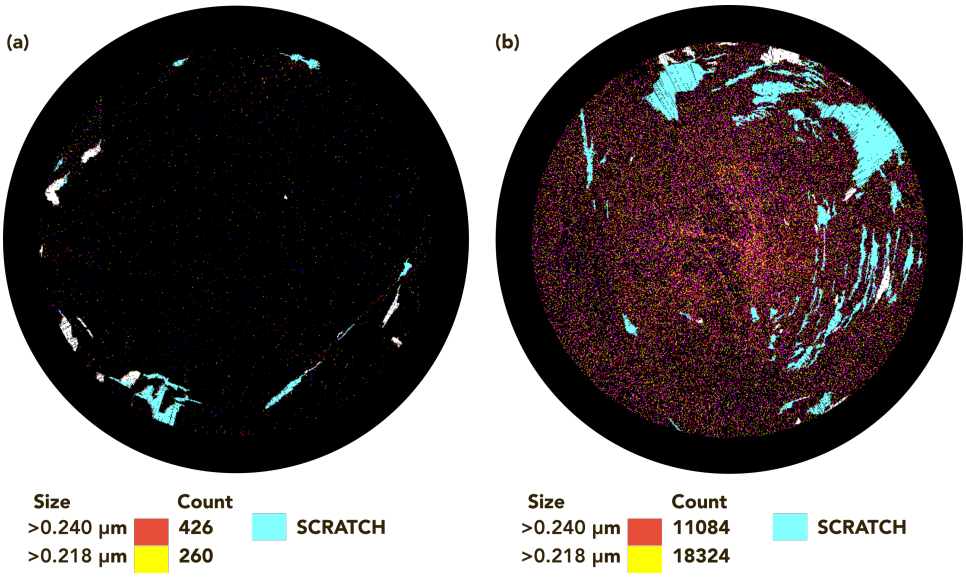

Figure 2.5: Particle count on the backside of a wafer before and after the **manual-tissue cleaning** performed to remove the PDMS residues, showing a drastic increase in the number of particle on the backside of the wafer and not visible under the microscope.

cleaned with a suitable isotropic plasma etching recipe. A frequent and periodic wet-cleaning of the machine is suggested to avoid accumulation of PDMS. Each machine user should run pre-conditioning recipes before etching any other material to avoid any influence of the PDMS on the chamber.

PDMS STRUCTURES RELEASING

The silicon support, on top of which these PDMS structures are fabricated, is not oxygen and light-transparent [35]. In order to exploit the optical transparency of PDMS, the silicon wafer can be replaced with a glass one. However, this choice limits the functionalities that could be integrated into the device, as glass is not a semiconductor and cannot be easily etched with deep-reactive ion etching (DRIE). To exploit the optical properties of PDMS, the Si underneath is completely or partially removed by means of DRIE, creating a freestanding PDMS membrane. The etching is performed in a Rapier Omega i2L DRIE etcher. To make sure that the PDMS is not etched by the recipe itself, a 2 µm thick layer of SiO_2 is usually deposited underneath the PDMS and used as landing layer for the etching. In this step, the PDMS layer might enter in contact with the chuck. Therefore, to avoid any PDMS residues on the chuck, we suggest to preventively sputter a thin layer of Al on top of the PDMS before the DRIE step. The SiO_2 underneath the PDMS can be easily removed by means of buffered hydrofluoric acid (BHF). This technique results in a membrane supported by a silicon frame. Membranes with an area smaller than 0.7 cm^2 were released with a success rate of 100%.

The second way to remove the silicon is by simply transferring the PDMS structures from the wafer to another device. Our group presented a novel and highly reproducible process to transfer porous PDMS layers fabricated with the POS technology [23, 36].

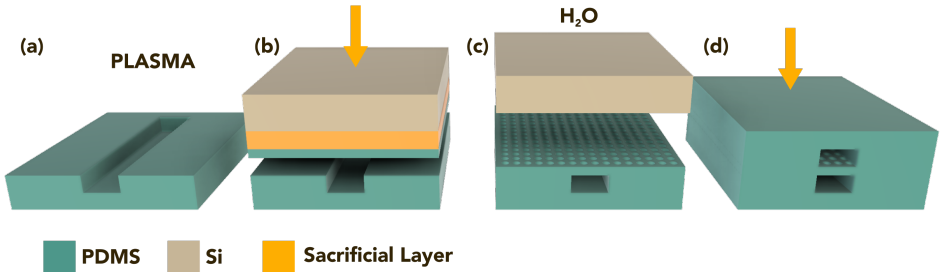

Figure 2.6: (a) Oxygen plasma treatment on the PDMS membrane on the bottom surface of the channel. (b) The porous membranes, carried by the silicon substrate, is placed in contact with the activated surfaces of the OOCs and then kept under a constant pressure to promote mechanical bonding. (c) The porous membrane is released by dissolving the sacricial layer in water in an ultrasonic bath. (d) Final assembly of the OOC by attaching the top part of the microfluidic chip. The figures are not drawn to scale. Figure adapted from [23].

To overcome issues normally encountered with soft-lithography, the process includes a sacrificial layer (poly(acrylic acid) - PAA) underneath the PDMS to easily transfer the membranes from the silicon carrier to any PDMS or glass substrate. The highly reliable fabrication and transfer method, shown in Figure 2.6, allows for very thin (smaller than 10 µm) functional membranes to be transferred at chip level with a high yield (80%).

2.4. CONCLUSIONS

In conclusion, to avoid the use of soft-lithography during the fabrication of PDMS-based OOC devices, a new set of process modules has been developed. In this work, these process steps are referred as POS guidelines. These include robust and reproducible techniques to deposit, pattern, and transfer PDMS layers on silicon. Moreover, they guarantee that the wafers can be further process in standard CR tools, without damaging or altering the PDMS structures or contaminating the equipment.

A PDMS deposition process was developed and characterized. The different parameters to tune the thickness of the layer were listed and tested. Moreover, the deposition uniformity was assessed. On a 7 µm-thick PDMS layer, variations of only ±0.1 and ±0.2 µm were measured across wafer to wafer and batch to batch, respectively. Next, an automated lithography process on PDMS was presented. This step does not require any plasma treatment to avoid de-wetting of the PDMS surface and it does not result in cracks of the PR layers. Features down to 2 µm were achieved without critical issues.

A dry etching recipe to pattern PDMS was presented and tested. The recipe results in an etching rate of approximately 0.4 µm/min and it was used to pattern standard porous membranes with a wide range of porosity and features, and 3D scaffolds.

The above mentioned steps were optimized to be compatible with a CR-environment. This was achieved by taking in consideration two main requirements: (a) making sure to preserve PDMS integrity and (b) avoiding particles generation.

The POS guidelines provide the foundations for the development of Organ-on-Silicon devices. The Cytostretch platform (presented in Chapter 3 and optimized and tested in Chapter 4-7) and the BI/OND platform (presented in Chapter 8) were designed and fabricated following the POS guidelines. The definition of the POS guidelines and their application for the fabrication of these two devices is a first step towards large-scale manufacturing, higher throughput and robustness of OOC fabrication. However, in order to transfer this fabrication process to a large-scale foundry, some of the steps need to be automated and optimized even further. In particular, the dispensing of the PDMS and part of the wafer cleaning need to be replaced by automated process steps.

REFERENCES

[1] Yole Développement, *Organs-on-chips 2017 report,* (accessed: 01.09.2018).

[2] N. Beißner, T. Lorenz, and S. Reichl, *Microsystems for Pharmatechnology* (Springer International Publishing, 2016).

[3] D. Huh, B. D. Matthews, A. Mammoto, M. Montoya-Zavala, H. Y. Hsin, and D. E. Ingber, *Reconstituting organ-level lung functions on a chip,* Science **328**, 1662 (2010).

[4] D. Huh, H. J. Kim, J. P. Fraser, D. E. Shea, M. Khan, A. Bahinski, G. A. Hamilton, and D. E. Ingber, *Microfabrication of human organs-on-chips,* Nature protocols **8**, 2135 (2013).

[5] The Dow Chemical Company, *Sylgard 184 silicone elastomer kit,* (accessed: 06.03.2019).

[6] G. K. Schalau II, A. Bobenrieth, R. O. Huber, L. S. Nartker, and X. Thomas, *Silicone adhesives in medical applications,* in *Applied Adhesive Bonding in Science and Technology* (IntechOpen, 2017).

[7] A. G. Bejenariu, J. Ø. Poulsen, A. L. Skov, and L. C. Henriksen, *A comparative study on the influence of the platinum catalyst in poly (dimethylsiloxane) based networks synthesis,* Chalmers tekniska högskola , 269 (2009).

[8] Z. Wang, A. A. Volinsky, and N. D. Gallant, *Crosslinking effect on polydimethylsiloxane elastic modulus measured by custom-built compression instrument,* Journal of Applied Polymer Science **131** (2014).

[9] W.-J. Chang, D. Akin, M. Sedlak, M. R. Ladisch, and R. Bashir, *Poly (dimethylsiloxane)(pdms) and silicon hybrid biochip for bacterial culture,* Biomedical Microdevices **5**, 281 (2003).

[10] J. E. Mark, H. R. Allcock, H. R. Allcock, and R. West, *Inorganic polymers* (Oxford University Press on Demand, 2005).

[11] S. J. Hwang, D. J. Oh, P. G. Jung, S. M. Lee, J. S. Go, J.-H. Kim, K.-Y. Hwang, and J. S. Ko, *Dry etching of polydimethylsiloxane using microwave plasma,* Journal of Micromechanics and Microengineering **19**, 095010 (2009).

[12] X. Thomas, *Silicone adhesives in healthcare applications,* Dow Corning Healthcare Industry , 1 (2003).

[13] J. Garra, T. Long, J. Currie, T. Schneider, R. White, and M. Paranjape, *Dry etching of polydimethylsiloxane for microfluidic systems,* Journal of Vacuum Science & Technology A: Vacuum, Surfaces, and Films **20**, 975 (2002).

[14] M. W. Toepke and D. J. Beebe, *Pdms absorption of small molecules and consequences in microfluidic applications,* Lab on a Chip **6**, 1484 (2006).

[15] B. Van Meer, H. De Vries, K. Firth, J. van Weerd, L. Tertoolen, H. Karperien, P. Jonkheijm, C. Denning, A. IJzerman, and C. Mummery, *Small molecule absorption by pdms in the context of drug response bioassays,* Biochemical and biophysical research communications **482**, 323 (2017).

[16] J. D. Wang, N. J. Douville, S. Takayama, and M. ElSayed, *Quantitative analysis of molecu-*

lar absorption into pdms microfluidic channels, Annals of biomedical engineering **40**, 1862 (2012).

[17] T. Honda, M. Miyazaki, H. Nakamura, and H. Maeda, *Controllable polymerization of biopolymers in a microreaction system,* in *World Congress of Medical Physics and Biomedical Engineering,* Vol. 1 (2006) p. 234.

[18] S. Khoshfetrat Pakazad, *Stretchable micro-electrode arrays for electrophysiology,* (2015).

[19] R. M. Diebold and D. R. Clarke, *Lithographic patterning on polydimethylsiloxane surfaces using polydimethylglutarimide,* Lab on a Chip **11**, 1694 (2011).

[20] D. E. Ingber, K. K. Parker, G. A. Hamilton, and A. Bahinski, *Organ chips and uses thereof,* (2014), US Patent App. 14/363,105.

[21] W. Chen, R. H. Lam, and J. Fu, *Photolithographic surface micromachining of polydimethylsiloxane (pdms),* Lab on a Chip **12**, 391 (2012).

[22] S. Bhattacharya, A. Datta, J. M. Berg, and S. Gangopadhyay, *Studies on surface wettability of poly (dimethyl) siloxane (pdms) and glass under oxygen-plasma treatment and correlation with bond strength,* Journal of microelectromechanical systems **14**, 590 (2005).

[23] W. Quirós-Solano, N. Gaio, O. Stassen, Y. Arik, C. Silvestri, N. Van Engeland, A. Van der Meer, R. Passier, C. Sahlgren, C. Bouten, *et al.*, *Microfabricated tuneable and transferable porous pdms membranes for organs-on-chips,* Scientific reports **8**, 13524 (2018).

[24] S. Joshi, A. Savov, S. Shafqat, and R. Dekker, *Investigation of "fur-like" residues post dry etching of polyimide using aluminum hard etch mask,* Materials Science in Semiconductor Processing **75**, 130 (2018).

[25] J. N. Lee, C. Park, and G. M. Whitesides, *Solvent compatibility of poly (dimethylsiloxane)-based microfluidic devices,* Analytical chemistry **75**, 6544 (2003).

[26] J. N. Lee, C. Park, and G. M. Whitesides, *Solvent compatibility of poly (dimethylsiloxane)-based microfluidic devices,* Analytical chemistry **75**, 6544 (2003).

[27] B. Balakrisnan, S. Patil, and E. Smela, *Patterning pdms using a combination of wet and dry etching,* Journal of Micromechanics and Microengineering **19**, 047002 (2009).

[28] K.-S. Koh, J. Chin, J. Chia, and C.-L. Chiang, *Quantitative studies on pdms-pdms interface bonding with piranha solution and its swelling effect,* Micromachines **3**, 427 (2012).

[29] M. A. Eddings, M. A. Johnson, and B. K. Gale, *Determining the optimal pdms–pdms bonding technique for microfluidic devices,* Journal of Micromechanics and Microengineering **18**, 067001 (2008).

[30] P. Rezai, P. R. Selvaganapathy, and G. R. Wohl, *Plasma enhanced bonding of polydimethylsiloxane with parylene and its optimization,* Journal of Micromechanics and Microengineering **21**, 065024 (2011).

[31] S. K. Pakazad, A. Savov, A. Van de Stolpe, and R. Dekker, *A novel stretchable micro-electrode array (smea) design for directional stretching of cells,* Journal of Micromechanics and Micro-

engineering **24**, 034003 (2014).

[32] N. Gaio, B. van Meer, C. Silvestri, S. Pakazad, S. Vollebregt, C. Mummery, and R. Dekker, *Upside-down carbon nanotube (cnt) micro-electrode array (mea),* in *2015 IEEE SENSORS* (IEEE, 2015) pp. 1–4.

[33] N. Gaio, C. Silvestri, B. van Meer, S. Vollebregt, C. L. Mummery, and R. Dekker, *Fabrication and characterization of an upside-down carbon nanotube microelectrode array,* IEEE Sensors Journal **16**, 8685 (2016).

[34] R. Ponte, V. Giagka, and W. A. Serdijn, *Design and custom fabrication of a smart temperature sensor for an organ-on-a-chip platform,* in *2018 IEEE Biomedical Circuits and Systems Conference (BioCAS)* (IEEE, 2018) pp. 1–4.

[35] W. O'Mara, R. B. Herring, and L. P. Hunt, *Handbook of semiconductor silicon technology* (Crest Publishing House, 2007).

[36] W. Quiros-Solano, N. Gaio, C. Silvestri, Y. Arik, O. Stassen, A. Van Der Meer, C. Bouten, A. Van Den Berg, R. Dekker, and P. Sarro, *A novel method to transfer porous pdms membranes for high throughput organ-on-chip and lab-on-chip assembly,* in *2018 IEEE Micro Electro Mechanical Systems (MEMS)* (IEEE, 2018) pp. 318–321.

3

THE CYTOSTRETCH PLATFORM

This chapter is based on:

- N. Gaio, B. van Meer, W. Quirós-Solano, L. Bergers, A. van de Stolpe, C. Mummery, P.M. Sarro, R. Dekker. "Cytostretch, an organ-on-chip platform". Micromachines, 7, n.7 (2017): 120. [1].
- W.F. Quirós-Solano, N. Gaio, O.M.J.A. Stassen, Y.B. Arik, C. Silvestri, N.C.A. Van Engeland, A. Van der Meer, R. Passier, C.M. Sahlgren, C.V.C. Bouten, A. van den Berg, R. Dekker, P.M. Sarro. "Microfabricated tuneable and transferable porous PDMS membranes for Organs-on-Chips".Scientific reports, 8, no. 1 (2018): 13524 [2].

3.1. INTRODUCTION

Following the POS guidelines, the first OOC fabricated with only standard microfabrication steps (OOS) was developed: the Cytostretch platform. Cytostretch is a customizable platform that can be used to realize a variety of different OOCs for different cell culture applications, by adding or removing one or more features during fabrication. The platform presented here builds on the technology originally developed for a Heart-on-Chip model developed by Pakazad et al. [3]. A platform-based design ensures fast time-to-market and the possibility of repurposing it with minor layout changes [3]. Hence, different chips built on the Cytostretch platform may serve different OOC market niches.

In the following sections, we describe the platform concept and the modules developed to date. Chip variants include membranes with (i) through-membrane pores

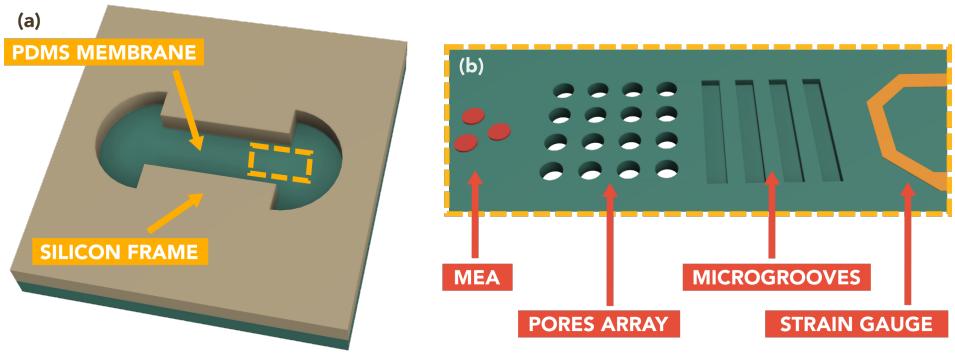

Figure 3.1: (a) 3D rendering of a chip fabricated with the Cytostretch platform equipped with the available modules (b). The figures are not drawn to scale.

that allow biological signalling molecules to pass between two different tissue compartments (Section 3.2.2), (ii) stretchable microelectrode array (MEA) for electrical monitoring and stimulation (Section 3.2.3), (iii) micropatterning to promote cell alignment (Section 3.2.4), and (iv) strain gauges to measure changes in substrate stress (Section 3.2.5). A 3D rendering of the chip fabricated with the Cytostretch platform and the above mentioned modules is shown in Figure 3.1. The fabrication of the Cytostretch platform and the modules was performed following the POS guidelines, even though they will not be mentioned again in the following fabrication descriptions.

3.2. CYTOSTRETCH PLATFORM

3.2.1. BASIC COMPONENT

The basic element of the Cytostretch platform is a freestanding PDMS membrane fabricated on a silicon chip. The cell culture medium can be contained in a plastic cylinder attached to the silicon die. Furthermore, the device can be fabricated in different shapes and dimensions as, for example, the dog-bone shaped membrane proposed by Pakazad et al. [3]. As presented in [3], this design allows for the integration of electrodes and other metallic structure in the PDMS membrane, by preventing their rupture [3].

The Cytostretch platform was designed in order to provide a set of OOCs that could guarantee mechanical stimulation of cell cultures by means of a stretchable membrane [3]. Moreover, it can be equipped with MEAs [4] and other sensors [5–8] to monitor the electrical activity of cells during and after the mechanical stimulation.

PDMS as the material of choice for the membrane of Cytostretch has two main advantages as substrate for cell cultures. In the first place, the substrate stiffness can be

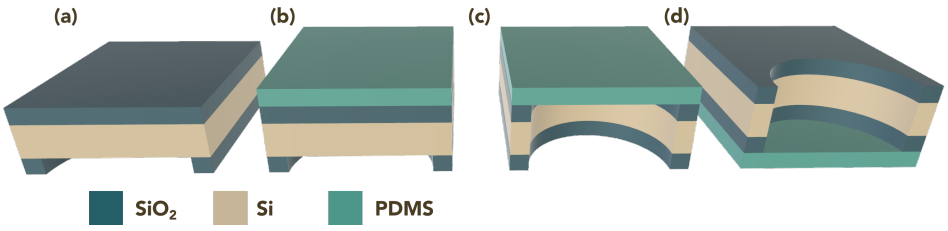

Figure 3.2: Process flow for the Cytostretch platform: (a) 2 and 6 µm of PECVD SiO_2 are deposited on the backside and the frontside of the wafer; the backside of the wafer is then patterned; (b) PDMS is spin coated on the wafer; (c) the Si and the SiO_2 underneath the membrane are etched with DRIE and BHF. The figures are not drawn to scale.

tuned by altering the ratio between elastomer and crosslinker [9]; this can modulate cell morphology, function, and fate [10]. Previous work suggests that matching the substrate elasticity with *in vivo* tissue elasticity can induce and direct stem cell differentiation [9]. For example, soft substrates promote neuronal differentiation, while substrates with bone-like stiffness promote osteogenic differentiation [9].

Secondly, the elasticity of PDMS allows the membrane to be inflated using a pneumatic system, thus exerting physical forces on cells cultured on the membrane. Hemodynamic shear stress or physical forces have been reported to affect the developmental fate of human induced pluripotent stem cells (hiPSC) in culture [9, 11], and stress induced by mechanical deformation might reveal disease-related functional changes.

FABRICATION OF THE CYTOSTRETCH PLATFORM

Si wafers are used as starting substrate for the fabrication of the Cytostretch platform. Processing starts with the deposition of a 2 µm and 6 µm thick SiO_2 layer by PECVD on the front and backside of the wafer, respectively. The SiO_2 layer on the backside is patterned by dry-etching to define the membrane area (Figure 3.2a). Subsequently, a 15 µm thick PDMS layer is spin coated onto the frontside of the wafer at 3500 RPM for 30 seconds and cured for one hour at 90 °C (Figure 3.2b). Finally, the membrane is released by removing the Si and the SiO_2 layers from underneath the membrane using DRIE and buffered hydrofluoric acid (BHF), respectively (Figure 3.2c,d).

3.2.2. POROUS MEMBRANE

A Cytostretch chip with through-membrane micropores of defined size may be useful for applications where a cell layer or 3D tissue needs to be supported while allowing the exchange of biological signals through the membrane. An example of signaling is immune cell migration from blood vessels to a wound in the skin [12, 13]. Convention-

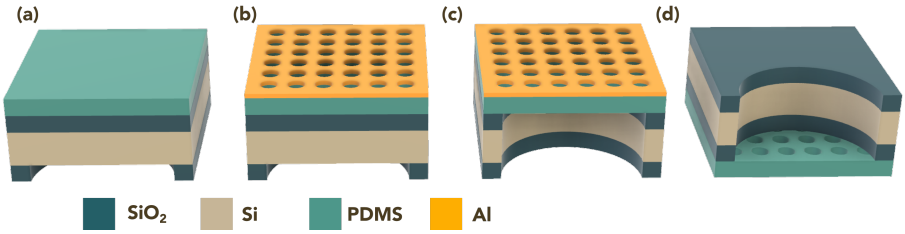

Figure 3.3: Process flow for the through-membrane micropore array: (a) a PDMS layer is spin coated on the wafer; (b) the Al hard mask is patterned and then used to pattern the PDMS with a dry etching step; (c) the membrane is released; (d) the Al layer is then removed with PES etch. The figures are not drawn to scale..

ally, commercially available low-porosity non-stretchable thin film (t: 10–20 µm) are used [2]. However, a highly porous support is preferred in this type of applications so that the membrane is optimally permeable for the signal. Stretchability might be useful for investigating the role of mechanical load in skin scarring [14]. The utility of a Cytostretch chip with a defined pore size is illustrated in this section by the migration of THP-1 monocytes (an immune cell-line) in a chemotactic essay.

FABRICATION

This porous membrane module consists of an array of through-membrane micropores patterned in the PDMS layer. This module is inserted into the fabrication flow immediately after PDMS spinning and curing and before the release of the membrane (Figure 3.3a). To pattern the PDMS, an aluminum (Al) layer is sputter coated onto the PDMS at room temperature. The Al is patterned by a 1.4 µm thick positive photoresist and dry-etched (Figure 3.3b). Next, the pattern in the Al is transferred in the PDMS followed by the removal of the hard mask by means of wet-etching (Figure 3.3c,d). The fabrication ends by releasing the membrane as discussed in Section 3.2.1.

Quirós-Solano et al. [2] used this process to fabricate porous PDMS membranes with pore sizes down to 2 µm in diameter and a wide porosity range (2-65%). The scanning electron microscope (SEM) pictures of membranes patterned with pores with different dimensions and porosities are shown in Figure 3.4.

APPLICATIONS

Recently these membranes have been used in multiple applications. In particular, Quirós-Solano et al. [2] studied the effect of the pore dimensions and porosity on the transmigration of MDA (MDA-MB-231) and HUVEC (human umbilical endothelial cells) cells from one side of the membrane to the side. Moreover, he studied how MDA morphology is altered by the dimensions of the pores [2]. Among others, he demonstrated that it

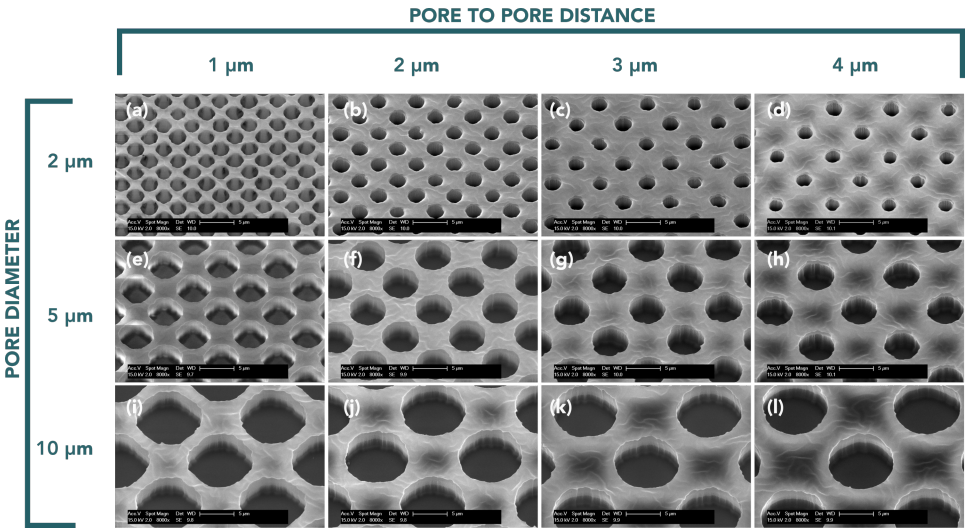

Figure 3.4: SEM images of different porous PDMS membranes with various pore diameters and pore-to-pore distances, taken at a fixed magnification (8000X) and tilting angle of 26 °. Scale bars: 5 µm. Figure adapted from [2].

is possible to prevent MDA cells transmigration and protrusions by reducing the dimensions of the pores down to 2 µm. In this thesis, we demonstrate the migration of THP-1 immune cells through the porous Cytostretch membrane.

THP-1 cells were cultured in RPMI-1640 medium. A basic test similar to a standard Boyden chamber experiment [15] was performed (Figure 3.5). The membrane was placed between two PDMS slabs with a center hole of 5 mm to create two fluidic chambers. The bottom chamber was filled with culture medium that was enriched with monocyte chemoattractant protein 1 (MCP-1), while the immune cells were seeded in the top chamber. The MCP-1 provided a strong stimulus to attract the monocytes. Images of the membrane and the volume below the membrane were recorded with a Leica

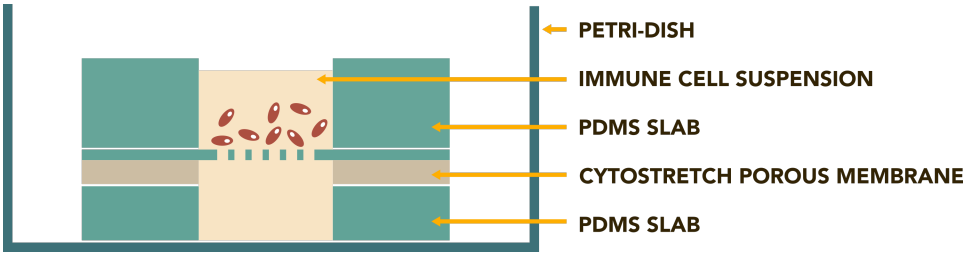

Figure 3.5: Schematic of setup for simple migration experiment. The figure is not drawn to scale.

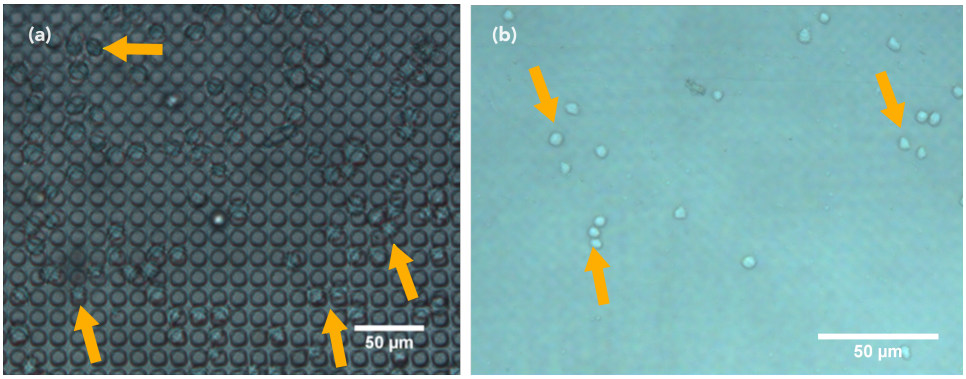

Figure 3.6: Phase contrast images of the cell migration experiment. (a) The top of the microporous membrane 5 min after seeding shows immune cells resting on the pores. (b) The volume below the membrane 3.5 hours after seeding shows immune cells in the cavity under the membrane. Cells indicated by yellow arrows.

inverted phase microscope, 20× objective, at 5 min and 3.5 hours after seeding of the membrane. For the migration experiment, membranes with 8 µm pores were used. After 5 min, cells were observed on top of the membranes, settling on/near the pores (Figure 3.6a). At that time, cells were not observed in the reservoir underneath the membrane. After 3.5 hours, however, the immune cells were visible in the fluid below the membrane (Figure 3.6b) and had virtually disappeared from the top of the membrane. This shows that the membrane did not restrict migration to the opposite side.

3.2.3. MICROELECTRODE ARRAY

The activity of electrically active cells, such as heart, muscle, and neural cells, can be recorded with MEAs. Changes in the electrical response due to drugs have shown to be predictive for their pharmacological safety profile [16]. MEAs can also be used to stimulate electrogenic cells and modulate their behavior by means of electrical impulses [17]. Furthermore, electrical stimulation might play a role in the cardiac differentiation of human embryonic stem cells [18].

A stretchable MEA, based on the Cytostretch platform, consists of an array of 12 TiN electrodes embedded in the PDMS membrane. In order to demonstrate the functionality of the electrode module, the stretchable MEA was tested, by recording the electrical activity of hiPSC-derived cardiomyocytes (hiPSC-CMs).

FABRICATION

This electrode module is fabricated before PDMS deposition following the polymer-last approach proposed in Section 2.3.4. The processing starts by depositing and pattern-

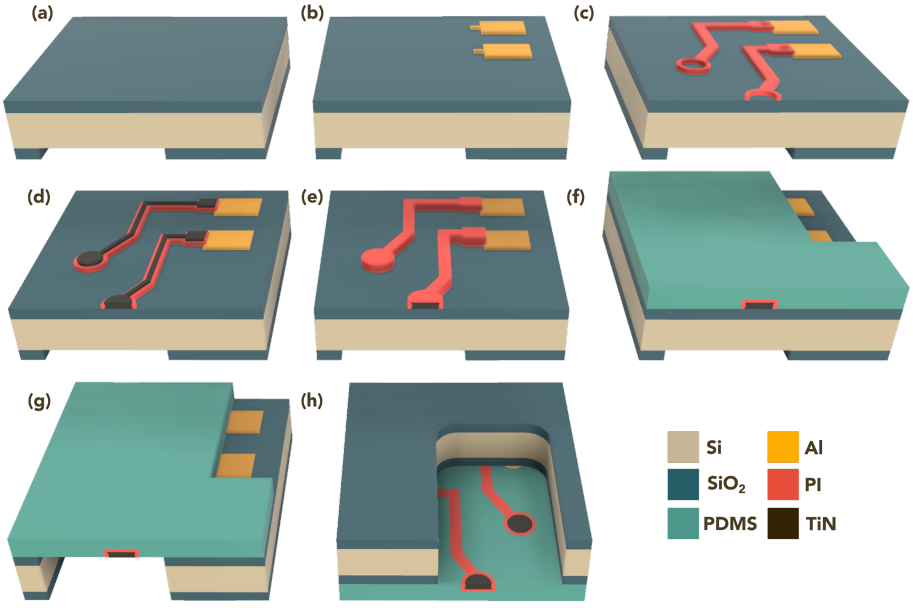

Figure 3.7: Process flow for the MEA module: (a,b) Al deposition and patterning; (c) the first layer of parylene is deposited and patterned; (d) TiN deposition and patterning; (e) the second layer of parylene is deposited and patterned; (f) PDMS deposition and patterning; (g,h) membrane releasing. The figures are not drawn to scale.

ing 500 nm of Al on the frontside of the wafer (Figure 3.7b). This metal layer is used for the contact pads and the electrical interconnects outside the membrane area. Next, the metal lines extending from the contact pads to the electrodes are fabricated. These consist of a 100-nm-thick layer of sputtered TiN, sandwiched between two layers of parylene (Figure 3.7c,d,e).

PDMS is then spin coated and cured, and openings to the bond pads are etched through the PDMS layer (Figure 3.7f), using an Al layer as a hard mask. The process flow again ends with the release of the membrane as previously described (Figure 3.7g,h). The Cytostretch chip is then loaded on the adaptor presented by Pakazad et al. [3, 4] and described in Chapter 4, which allows for electrical read out using Multi-Channel Systems GmbH (MCS) equipment.

SEM images of the Cytostretch device including both the MEA are shown in Figure 3.8. Twelve circular electrodes with a diameter of 12 µm were included into the membrane.

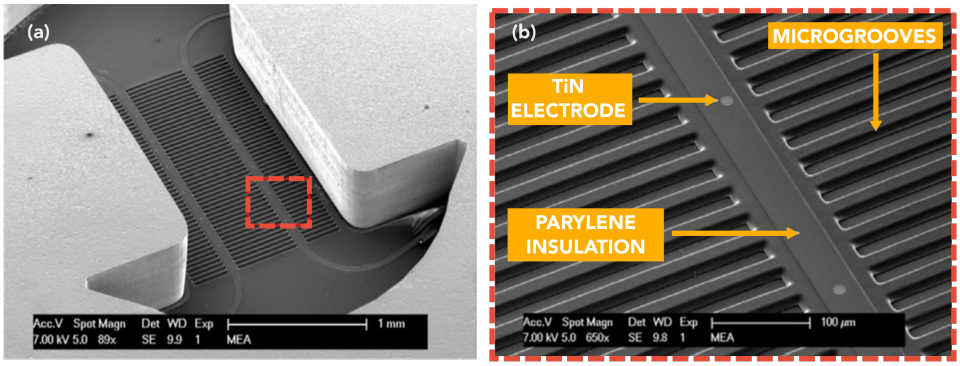

Figure 3.8: (a) SEM image of the Cytostretch chip from the back. (b) Close-up of the area highlighted in (a) depicting transversal microgrooves, the exposed TiN electrodes and parylene insulation of the metal tracks. Figure adapted from [4]. Scale bars: (a) 1 mm and (b) 100 µm.

APPLICATION

To investigate the electrical recording capability of the electrodes, hiPSC-CMs were plated onto the stretchable Cytostretch MEA device. First, the devices were sterilized in ethanol and coated with matrigel (Invitrogen, Carlsbad, CA, USA). Next, the cells were plated and cultured on the device for 36 hours in a CO_2 incubator at 37 °C. The readout of the field potential of the hiPSC-CMs is performed with a MCS USB-MEA-System. Cytostretch interfaces with this system through a printed circuit board adaptor as presented in [3, 4].

The maximum number of electrodes included in the Cytostretch membrane is defined by the width of the interconnect tracks in the dog-bone-shaped membrane, as presented by Pakazad et al. [3, 4]. The hiPSC-CMs plated on the Cytostretch started beating spontaneously within three days, demonstrating their viability and functionality. Figure 3.9a shows the Cytostretch MEA with hiPSC-CMs after three days of culturing.

The recorded signal shows the electric field potential of the hiPSC-CMs on top of the electrode. The signal was filtered with Matlab using a bandpass filter (2–200 Hz) and a cut-off filter (50 Hz) to remove motion artifacts. The spikes in the electric field potential seen in Figure 3.9b correspond to the depolarization phase of the action potential [4]. Typically recorded signals are in the order of 100 µV. The signal has a relatively low signal-to-noise ratio (SNR) compared to other work [19, 20], due to the high electrochemical impedance of the flat and subcellular electrodes [3, 4].

3.2.4. MICROGROOVES

Organ tissues are highly organized and layered structures that incorporate multiple cell types to simulate complex organ-specific functions, including organ repair by cell re-

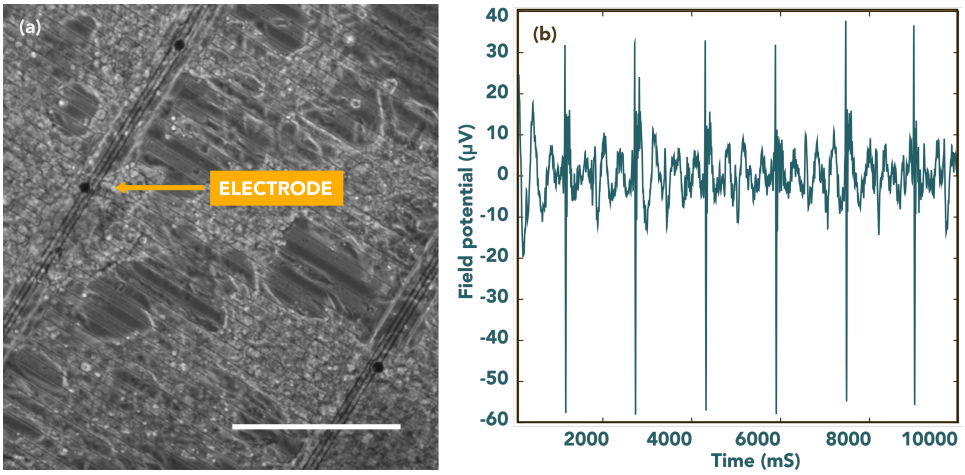

Figure 3.9: (a) Optical images of cardiac hiPSC on the Cytostretch device. Scale bar: 250 μm. (b) The field potential recording from one of the electrodes.

newal, vascularization and inflammatory responses. Both macroscopic and microscopic organization of cells takes place, generating a physiologically relevant tissue. Stem cells of the intestine can orient themselves in the intact tissue and smooth muscle cells can generate peristaltic contractions. In striated muscles, the anisotropic orientation of cells is crucial, since it determines the direction in which the muscle shortens. Feinberg et al. [21] showed anisotropic cardiac myocyte alignment by microcontact printing of an extracellular matrix (ECM) protein. However, this manual technique is not suitable for microfabrication and is cumbersome in a cell lab.

The Cytostretch membrane can be patterned to create microgrooves to control the orientation of cells in the culture. This module was employed to provide topological cues to hiPSC-CMs and assess their anisotropic alignment after seven days in culture.

FABRICATION

The microgrooves are fabricated on the same side of the Cytostretch membrane as the MEA electrodes. Therefore, the microgroove module is fabricated before deposition of the PDMS. After fabrication of the electrodes, a 4-μm-thick layer of photoresist (PR) is spin coated and patterned (Figure 3.10c). The PR will serve as a mold for the microgrooves in the PDMS membrane. Next, PDMS is spin coated onto the wafer and cured (Figure 3.10d) and the membrane is released (Figure 3.10e,f). To prevent the UV light generated during the DRIE etching from deep cross linking the PR, a layer of titanium (Ti) is embedded in the SiO_2 etch-stop layer (Figure 3.10a). The Ti layer is removed at the same time with the wet etching of the SiO_2 etch-stop layer. Finally, the PR mold is

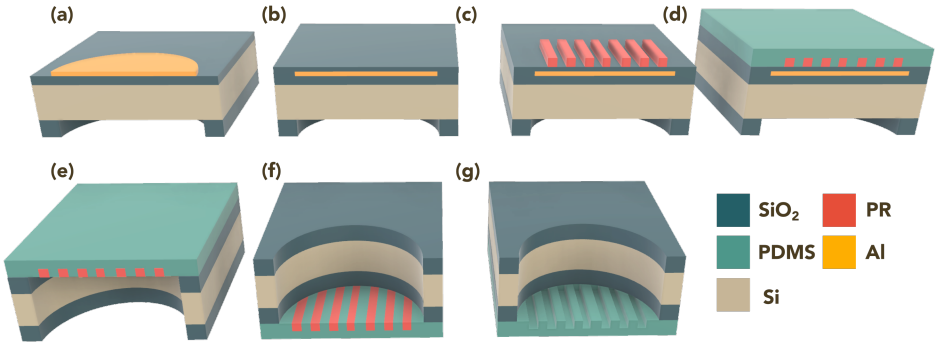

Figure 3.10: Process flow for the microgroove module: (a,b) substrate with Ti mask embedded in the front-side SiO_2 layer; (c) PR spinning and patterning; (d) PDMS deposition; (e,f) membrane releasing; (g) PR stripping. The figures are not drawn to scale.

dissolved in acetone (Figure 3.10).

The microgrooves were characterized using SEM. A SEM image of the microgrooves embedded in the Cytostretch membrane is shown in Figure 3.8. Therefore, the width and the height of the microgrooves are determined by the lithography step shown in Figure 3.10c. With this fabrication technique, microgrooves with arbitrary shape, width and height can be easily fabricated.

APPLICATIONS

In order to assess how well cells align to the microgrooves, the micropatterned PDMS was sterilized by UV treatment and coated with Matrigel (Invitrogen). Commercially available human induced pluripotent stem cell (hiPSC)-derived cardiomyocytes (Ncardia B.V., Galileiweg, The Netherlands) were thawed and after seven days replated onto the microgrooved PDMS. Cells were cultured in Ncardia Cardiomyocyte Medium.

After seven days in culture on the micropatterned substrate, the cells were fixed with 2% paraformaldehyde and stained with an anti-alpha-actinin antibody, anti-troponin-I antibody and DAPI (4',6-diamidino-2-phenylindole) to reveal the sarcomeric structures and the cell nucleus.

hiPSC-CMs plated on standard culture substrates such as culture plastic or glass coverslips show a more isotropically orientated sarcomeric organization compared to cardiomyocytes *in vivo*, which is partially regulated by their shape [22]. hiPSC-CMs are less mature than adult myocardium and this is evident in several of their physiological properties, among which cardiomyocyte elongation: adult cardiomyocytes have a

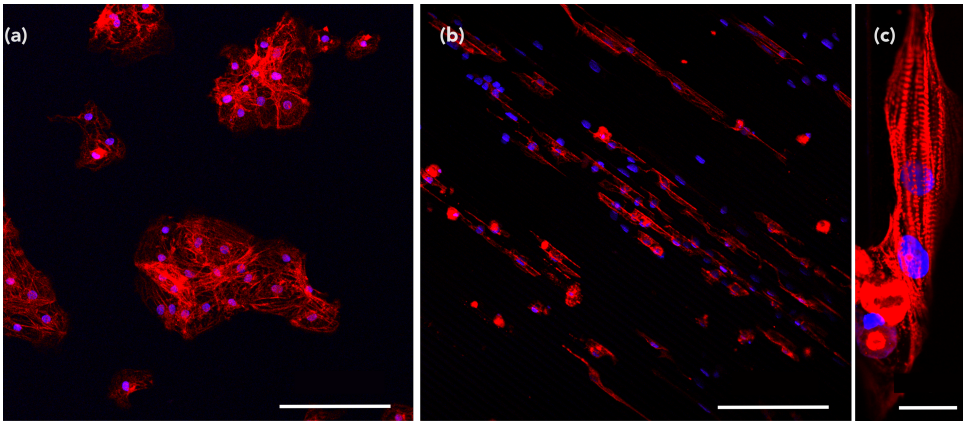

Figure 3.11: Confocal images of hiPSC-CMs stained for anti-alpha-actinin (red) and DAPI (blue) to reveal the sarcomeric structure and cell nucleus. (a) hiPSC-CM on plain PDMS. (b,c) hiPSC-CM on micropatterned PDMS. Scale bars: (a,b) 150 µm and (c) 20 µm.

length-to-width ratio of 5–9.5 to 1 whereas hiPSC-CMs are limited to a ratio of 3 to 1 [23].

Compared to hiPSC-CMs cultured onto plain PDMS-coated coverslips (Figure 3.11a), the topological cues of the micropatterned PDMS increase the aspect ratio of hiPSC-CMs and induce a more rectangular shape, possibly by limiting the cell width. Figure 3.11b,c show, respectively, a large-field view of the cell culture grown on the microgrooves and a representative hiPSC-CM cultured on microgrooved PDMS with an aspect ratio of 7:1, indicating a more physiological cardiomyocyte elongation.

3.2.5. STRAIN GAUGES

To date, most OOCs have used static optical techniques (immunofluorescence endpoint detection, microscope cell imaging) to measure the deformation of PDMS membranes during inflation [24]. We presented a novel Cytostretch module that integrates sensing structures into the membrane to quantify the strain applied to heart or muscle cells [5], or exerted by them during contraction. Ti strain gauges were integrated into the Cytostretch PDMS membrane and characterized by measuring the resistance change as a result of the applied strain. The strain gauges were characterized in a custom-made setup to mesure their resistance under mechanical strain. The setup consists of a probe station, a custom-made holder for the Cytostretch device and a pressure source (Figure 3.12).

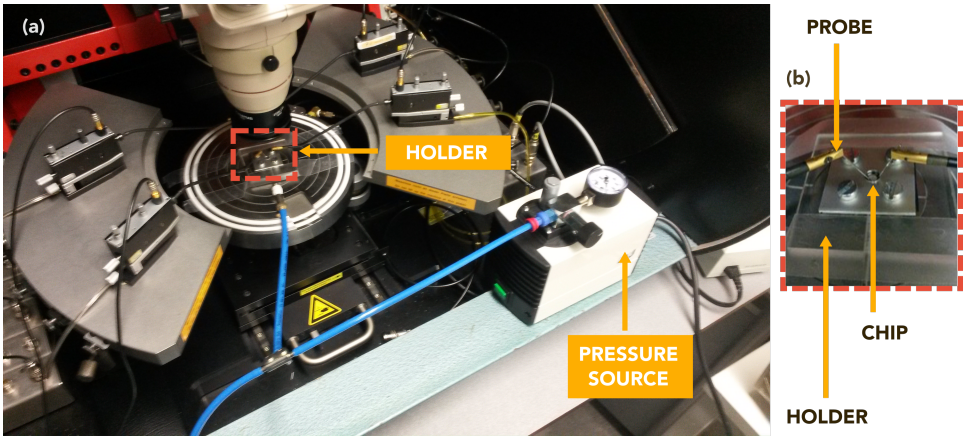

Figure 3.12: Measurement setup (a) and custom-made holder (b) used to measure the resistance change of the Ti strain gauges in the Cytostretch membrane platform.

FABRICATION

A 100-nm-thick layer of Ti is deposited by sputter coating onto the PDMS layer at room temperature to avoid any cracking. The Ti layer is patterned to form strain gauges with different geometries by dry etching with 3-µm-thick positive PR as the masking layer (Figure 3.13b). To protect the strain gauges during the release etch from the backside, the frontside of the wafer is temporarily covered with a 200-nm-thick layer of Al (Figure 3.13c). After the membrane is released, the Al layer is selectively removed in PES solution without damaging the strain gauges (Figure 3.13d). Figure 3.14a shows a Ti strain gauge fabricated on the edge of the Cytostretch PDMS membrane.

APPLICATION

To verify the change in resistance of the gauge when the membrane is deformed, the probe station is configured to continuously record the I-V characteristics of the device.

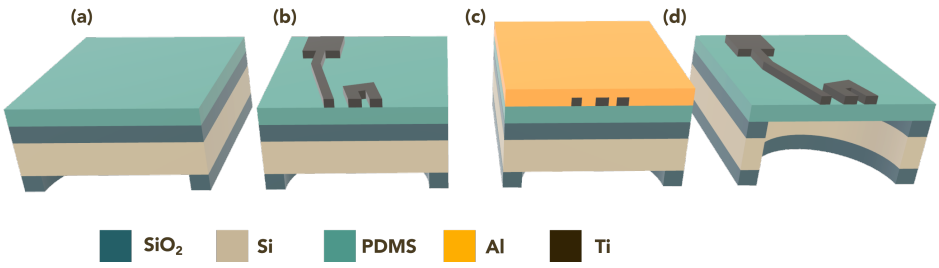

Figure 3.13: Process flow for the strain gauges: (a,b) Ti deposition and patterning on PDMS; (c) Al deposition; (d) membrane releasing and Al etching. The figures are not drawn to scale.

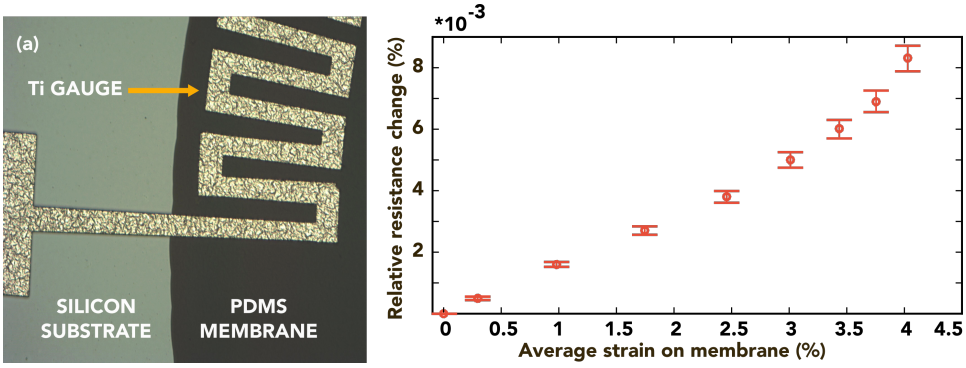

Figure 3.14: (a) Optical image from the front side showing a close-up of the Ti gauges at the interface between the Si substrate and the PDMS membrane. As presented in [5], the strain gauges were fabricated on circular membranes. (b) Relative resistance change of a strain gauge as function of the strain on the membrane.

The deformation of the membrane is induced by applying a positive pressure (from 0 to 3 kPa) to the membrane through the cavity formed in the Si substrate and the bottom of the holder. The pressure change is monitored using a standard manometer capable of measuring pressures down to 100 Pa. The correspondent strain in the membrane was geometrically calculated, by simply measuring the vertical displacement of the membrane for multiple pressures applied on the backside of the chip, as previously done in [3, 25]. This method is described in more details in Chapter 6. The resistance variations for different strain values were recorded with a probe station.

The relation between the applied strain and the resulting resistance variations is reported in Figure 3.14b. When the membranes are stretched with a 2.5% strain (1.5 kPa), the relative resistance change is approximately 0.004% $\pm 0.27 * 10^{3}$. As mentioned in Section 3.2.1, strain can be used to induce specific stem cell fate. Hence, the membrane acts as the tunable substrate for cell culture and the strain gauges make it possible to continuously monitor the strain applied to the Cytostretch membrane. The characterization of the device demonstrates the feasibility of sensor integration in the Cytostretch platform.

3.3. CONCLUSIONS

In this chapter, a modular and customizable platform for OOCs fabricated following the POS guidelines is presented. The platform consists of a microfabricated PDMS membrane, with four different modules that can be independently inserted into the main fabrication flow to add functionality depending on the application requirements. The modules have been described in detail and their fabrication processes have been discussed. Moreover, the functionality of the modules has been demonstrated in typical

OOC applications.

The first technology module produces an array of through-membrane pores in order to create a PDMS membrane with pores of a defined size that enables signal exchange through the membrane. The membrane was tested by studying the migration of immune cells through the pores. The second module consists of an integrated stretchable MEA. The electrode array was tested by measuring the electric field potential of cardiomyocytes cultured on the device's membrane under cyclic stretch. The third technology module adds microgrooves, molded into PDMS membrane. The grooves are used to align cells and improve the orientation and sarcomeric organization of hiPSC-CMs cultured on the membrane. The last module adds strain gauges that are used as a feedback sensor in order to enable real-time measurement of the membrane strain.

The modular character of the Cytostretch membrane platform makes it highly suitable for realizing various functions in OOCs and should eventually reduce design and fabrication costs. As the Cytostretch platform was designed taking in account the POS guidelines, every Cytostretch OOC device complies with the POS guidelines and benefits from the their advantages: large-scale manufacturing, higher throughput and robustness (Chapter 2).

While characterizing the Cytostretch platform, multiple limitations that could eventually hinder its large scale use were identified. First, part of the MEA module is made of parylene. This material and its deposition process are known to be incompatible with standard thin-film technology. Secondly, as it can be seen in the characterization of the MEA module (Section 3.2.3 - Figure 3.9b), the detection of cell action potentials with the presented MEA is characterized by a low signal-to-noise ratio. This issue could prevent the use of Cytostretch devices in studies where the extracellular field potential generated by the cells' action potential needs to be studied in details (such as in cardiotoxicity studies). Thirdly, the Cytostretch platform was packaged in such a way that end-user were required to perform several manual steps that can negatively affect the reproducibility and robustness of the results. These limitations will be addressed in the next chapters (Chapter 4-7).

REFERENCES

[1] N. Gaio, B. van Meer, W. Quirós Solano, L. Bergers, A. van de Stolpe, C. Mummery, P. Sarro, and R. Dekker, *Cytostretch, an organ-on-chip platform,* Micromachines **7**, 120 (2016).

[2] W. Quirós-Solano, N. Gaio, O. Stassen, Y. Arik, C. Silvestri, N. Van Engeland, A. Van der Meer, R. Passier, C. Sahlgren, C. Bouten, *et al., Microfabricated tuneable and transferable porous pdms membranes for organs-on-chips,* Scientific reports **8**, 13524 (2018).

[3] S. K. Pakazad, A. Savov, A. Van de Stolpe, and R. Dekker, *A novel stretchable micro-electrode array (smea) design for directional stretching of cells,* Journal of Micromechanics and Microengineering **24**, 034003 (2014).

[4] S. Khoshfetrat Pakazad, *Stretchable micro-electrode arrays for electrophysiology,* (2015).

[5] W. Quiros-Solano, G. Pandraud, and P. Sarro, *Wafer-level fabrication of strain gauges on pdms membranes for low-pressure sensing,* in *2015 IEEE SENSORS* (IEEE, 2015) pp. 1–4.

[6] W. Quiros-Solano, N. Gaio, C. Silvestri, G. Pandraud, and P. Sarro, *Pedot: Pss: a conductive and flexible polymer for sensor integration in organ-on-chip platforms,* Procedia Engineering **168**, 1184 (2016).

[7] W. Quiros-Solano, N. Gaio, C. Silvestri, G. Pandraud, and P. Sarro, *Polymeric strain gauges as pressure sensors for microfabricated organ-on-chips,* in *2017 19th International Conference on Solid-State Sensors, Actuators and Microsystems (TRANSDUCERS)* (IEEE, 2017) pp. 1296–1299.

[8] R. Ponte, V. Giagka, and W. A. Serdijn, *Design and custom fabrication of a smart temperature sensor for an organ-on-a-chip platform,* in *2018 IEEE Biomedical Circuits and Systems Conference (BioCAS)* (IEEE, 2018) pp. 1–4.

[9] A. I. Teixeira, S. Ilkhanizadeh, J. A. Wigenius, J. K. Duckworth, O. Inganäs, and O. Hermanson, *The promotion of neuronal maturation on soft substrates,* Biomaterials **30**, 4567 (2009).

[10] J. Park, P. Kim, W. Helen, A. J. Engler, A. Levchenko, and D.-H. Kim, *Control of stem cell fate and function by engineering physical microenvironments,* Integrative biology **4**, 1008 (2012).

[11] D. E. Discher, D. J. Mooney, and P. W. Zandstra, *Growth factors, matrices, and forces combine and control stem cells,* Science **324**, 1673 (2009).

[12] L. J. van den Broek, G. C. Limandjaja, F. B. Niessen, and S. Gibbs, *Human hypertrophic and keloid scar models: principles, limitations and future challenges from a tissue engineering perspective,* Experimental dermatology **23**, 382 (2014).

[13] L. Bergers, T. Waaijman, T. De Gruijl, A. Van De Stolpe, R. Dekker, and S. Gibbs, *Skin-on-chip: Integrating skin-tissue and microsystems engineering,* in *TISSUE ENGINEERING PART A*, Vol. 21 (MARY ANN LIEBERT, INC 140 HUGUENOT STREET, 3RD FL, NEW ROCHELLE, NY 10801 USA, 2015) pp. S337–S338.

[14] R. Ogawa, K. Okai, F. Tokumura, K. Mori, Y. Ohmori, C. Huang, H. Hyakusoku, and S. Akaishi, *The relationship between skin stretching/contraction and pathologic scarring: the important role of mechanical forces in keloid generation,* Wound Repair and Regeneration **20**, 149 (2012).

[15] S. Boyden, *The chemotactic effect of mixtures of antibody and antigen on polymorphonuclear leucocytes,* Journal of Experimental Medicine **115**, 453 (1962).

[16] S. R. Braam, L. Tertoolen, A. van de Stolpe, T. Meyer, R. Passier, and C. L. Mummery, *Prediction of drug-induced cardiotoxicity using human embryonic stem cell-derived cardiomyocytes,* Stem cell research **4**, 107 (2010).

[17] K. Wang, H. A. Fishman, H. Dai, and J. S. Harris, *Neural stimulation with a carbon nanotube microelectrode array,* Nano letters **6**, 2043 (2006).

[18] M. Yamada, K. Tanemura, S. Okada, A. Iwanami, M. Nakamura, H. Mizuno, M. Ozawa, R. Ohyama-Goto, N. Kitamura, M. Kawano, *et al.*, *Electrical stimulation modulates fate determination of differentiating embryonic stem cells,* Stem cells **25**, 562 (2007).

[19] R. Gerwig, K. Fuchsberger, B. Schroeppel, G. S. Link, G. Heusel, U. Kraushaar, W. Schuhmann, A. Stett, and M. Stelzle, *Pedot–cnt composite microelectrodes for recording and electrostimulation applications: Fabrication, morphology, and electrical properties,* Frontiers in neuroengineering **5**, 8 (2012).

[20] T. Gabay, M. Ben-David, I. Kalifa, R. Sorkin, R. A. Ze'ev, E. Ben-Jacob, and Y. Hanein, *Electrochemical and biological properties of carbon nanotube based multi-electrode arrays,* Nanotechnology **18**, 035201 (2007).

[21] A. W. Feinberg, A. Feigel, S. S. Shevkoplyas, S. Sheehy, G. M. Whitesides, and K. K. Parker, *Muscular thin films for building actuators and powering devices,* Science **317**, 1366 (2007).

[22] M.-A. Bray, S. P. Sheehy, and K. K. Parker, *Sarcomere alignment is regulated by myocyte shape,* Cell motility and the cytoskeleton **65**, 641 (2008).

[23] C. Denning, V. Borgdorff, J. Crutchley, K. S. Firth, V. George, S. Kalra, A. Kondrashov, M. D. Hoang, D. Mosqueira, A. Patel, *et al.*, *Cardiomyocytes from human pluripotent stem cells: from laboratory curiosity to industrial biomedical platform,* Biochimica et Biophysica Acta (BBA)-Molecular Cell Research **1863**, 1728 (2016).

[24] W. K. Schomburg, *Introduction to microsystem design* (Springer, 2015).

[25] S. Rosset, M. Niklaus, P. Dubois, and H. R. Shea, *Metal ion implantation for the fabrication of stretchable electrodes on elastomers,* Advanced Functional Materials **19**, 470 (2009).

4

TOWARD LARGE-SCALE FABRICATION OF A HEART-ON-CHIP

This chapter is based on:

- N. Gaio, S. Kersjes, W.F. Quirós-Solano, P.M. Sarro, R. Dekker. "Versatile and Automated 3D Polydimethylsiloxane (PDMS) Patterning for Large-Scale Fabrication of Organ-on-Chip (OOC) Components". In Eurosensors 2018, Graz, Austria, pp. 873, 2018. [1]

4.1. INTRODUCTION

A crucial need of pharmaceutical companies during their development process is to assess drug safety at an early stage of the development pipeline to identify and eliminate compounds that exhibit a potential for adverse drug reactions. At least 462 medicines were withdrawn from the market between 1953 and 2014, with consequences for patients, regulatory systems and pharma companies [2].

Since cardiac complications are among the leading causes of drug withdrawals, cardiotoxicity tests play a critical role in the toxicity and safety assessment of new medicines [2, 3]. Cardiac and non-cardiac drugs can cause unexpected drug-induced ventricular arrhythmias, which can easily develop into ventricular fibrillation or cardiac deaths. These particular complications are usually related to the interface between the drug and cardiomyocyte ion channels which affects polarization and depolarization of cell mem-

branes [4].

Under these circumstances, the development of efficient and low cost cardiac *in vitro* tests to screen drugs to avoid life-threatening drug reactions is necessary. OOCs and, in this particular case, Heart-on-Chips can satisfy this demand by providing an environment that promotes the viability and the differentiation of human derived stem cells into cardiac cells. Moreover, they can increase the reliability of *in vitro* testing by including model dependent conditions that reproduce the *in vivo* environment. The Heart-on-Chip Cytostretch device, developed by Pakazad et al. [5] can be used for this particular purpose.

The key features of Cytostretch are its capability to provide mechanical stimulation to cell cultures by means of a stretchable membrane and the possibility to monitor the electrical signals generated by the cells by means of an integrated MEA [5, 6]. These two properties combined, make Cytostretch a suitable platform to create a Heart-on-Chip that can be used for more predictive cardiotoxicity assays.

Previous work has shown that the mechanical stimulation of induced pluripotent stem cell derived cardiomyocytes (iPSC-CM) promotes their differentiation and alignment, as well as their electrical and mechanical coupling [7, 8]. At the same time, MEA technologies have attracted an increasing interest in cardiotoxicity screening [9–11]. MEA technology has been applied in multiple cardiotoxicity tests, as an *in vitro* tool for monitoring the effects of drugs [9]. Cytostrech is so far the only device that allows for mechanical stimulation of iPSC-CM to promote their maturation while observing the effect of compounds on their electrical response.

4.2. LIMITATIONS OF THE CYTOSTRETCH HEART-ON-CHIP

Cytostretch has shown to be a versatile platform for several applications. However, the Heart-on-Chip model obtained from the platform showed multiple limitations that could eventually hinder its large scale use. Issues in three main areas were identified and are addressed in this work: manufacturability, performance, and ease of use.

4.2.1. MANUFACTURABILITY

Even though the fabrication of the chip was designed following the POS guidelines, one of the main issues related to the Cytostretch chip was the use of parylene for the insulation of the metal lines.

The deposition of parylene polymer coatings is performed via vapor deposition, allowing for precise control of the coating thickness. This polymer is an inert and biocompatible coating, which provides excellent moisture, chemical, and dielectric barrier

properties [12–15]. However, this technique is known to be incompatible with standard thin-film technology [6]. For this reason, in this work, the parylene was replaced with a photosensitive polyimide (PI) that can be easily deposited and patterned like a photoresist (PR).

As explained in Chapter 2, also the processing of PDMS in a standard microfabrication environment can be cumbersome. For this reason, we developed an alternative for the deposition and patterning of PDMS without the use of spin coaters and dry etching equipment in the form of an automated and versatile molding process to deposit and pattern PDMS on Si wafers in one step. The process was employed for the fabrication of the Cytostretch chip but can be also applied in the fabrication of other OOC and Lab-on-Chip (LOC) devices. This part will be covered in this chapter (Section 4.3).

4.2.2. ELECTRODE PERFORMANCE

The Cytostretch chip is equipped with a TiN microelectrode array (MEA). However, due to the fabrication process, the electrodes have a smooth surface, which significantly reduces the double layer capacitance of the MEA, resulting in a high electrochemical impedance. We investigated two approaches to improve the electrochemical performance of the Cytostretch MEA by integrating advanced materials such as Poly (3,4 - ethylene dioxythiophene) (PEDOT) and Carbon-Nanotubes (CNT) as electrode coatings. Both materials are known to exhibit a low electrochemical impedance due to their porous film surfaces. This topic will be covered in detail in Chapter 5.

4.2.3. EASE OF USE

Last but not the least, for practical use, the Cytostretch chip was packaged as shown in Figure 4.1. This allows the signals detected by the MEA to be read by the standard MCS readout equipment and it can be used to inflate the PDMS membrane. Even though this adaptor was successfully used to demonstrate the Cytostretch Heart-on-Chip, it has the disadvantage that it requires the end-user (i.e. biologists) to perform several manual steps that can negatively affect the reproducibility and robustness of the results. In this thesis, the Cytostretch adaptor package was redesigned to improve ease of use. This part will be covered in Chapter 6.

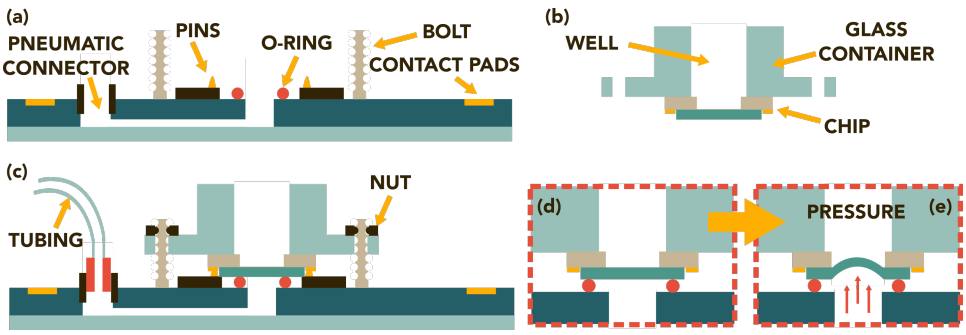

Figure 4.1: (a) Schematic cross-section of the PCB used in combination with the original Cytostretch chip to stretch the PDMS membrane and adapt the chip to a MCS read-out system. (b) In order to be used, the chip is glued to a glass container. (c) The chip and the glass container are then mounted on the PCB to read the electrical signals generated by the cells cultured on the chip membrane and to stimulate them with pneumatic actuation as shown in (d,e). The figures are not drawn to scale.

4.3. MANUFACTURABILITY CHALLENGES: PARYLENE AND PDMS

Even though Cytostretch was designed and fabricated following the POS guidelines, two main fabrication issues were identified in the fabrication of the device during our discussions: the use of parylene and the need to dry etch PDMS.

In the original process flow, parylene was chosen for its attractive properties as structural material, such as optical transparency, good dielectric properties, chemical and biological inertness, compatible Young's modulus of 2.7 - 4.75 GPa and tensile strength of 40 - 110 MPa, low gas permeability and low intrinsic film stress [12, 14, 16, 17]. In particular, parylene C was chosen, for its fast deposition rate compared to parylene N. Moreover, the biocompatbility of parylene C has promoted its use in medical devices such as implantables and as the structural material in MEA for neural applications [12].

The deposition process of parylene is performed with a room-temperature and low-pressure CVD process [12]. Even though this process guarantees pinhole-free and highly-conformal deposition [12], it requires frequent cleanings of the deposition chamber and other parts of the tool. This process generates particles, making the tool incompatible with a standard CR environment. Moreover, the conformal deposition of parylene is performed on both sides of the wafer. Consequently, after parylene deposition, the backside of the wafer needs to be cleaned by removing the layer of parylene by dry etching, complicating the fabrication process. Last but not the least, without an extensive optimization of the etching recipe, the parylene structures result in nearly vertical etching profiles. This may eventually hinder the conformal metallization of these structures

and cause detachment of the electrodes as identified by Pakazaad et al. [6].

For the above mentioned reasons, Pakazad suggested to replace parylene with PI. Unlike parylene, the deposition of PI only involves a spin-coating process and curing in a nitrogen environment. Moreover, PI has the desired mechanical stiffness to maintain the structural integrity of MEAs [6].

At the same time, PDMS etching is considered to be a critical step to include in a silicon fab as mentioned in Section 2.3.4. Even though this could be performed in a CR environment, the frequent cleaning of etching equipment might discourage a MEMS fab to accept such a process, in particular if a limited number of etching tools are available.

These two limitations were addressed, trying to replace parylene with a more suitable polymer and finding an alternative to deposit and pattern PDMS. To address these two issues, the Cytostretch Heart-on-Chip device was fabricated employing the mask designs shown in Figure 4.2. The Si chips (7x7 mm^2) are equipped with 12 circular TiN electrodes that can be reached via Al metal lines (width: 50 µm) and contact pads located around the membrane (Figure 4.2a,b). The TiN electrodes (diameter: 30 µm) are connected to the Al metal lines (Figure 4.2c,d,e) and are insulated by two layers of PI located underneath and on top of the TiN (Figure 4.2f,g,h and Figure 4.2i). The TiN electrodes and the PI insulation layers are embedded in a PDMS membrane located at the centre of the chip (Figure 4.2j). The designs shown in Figure 4.2 are combined following the fabrication sequence presented in Figure 4.3.

4.4. ELECTRICAL INSULATION: FROM PARYLENE TO POLYIMIDE

In order to remove the issues related to parylene, the TiN interconnects were insulated with polyimide. PI is often used in microelectronics, aerospace and medical devices for its thermal resistance [18], chemical resistance [19], good mechanical properties [20], and low dielectric constant [21]. In the particular case of medical devices, PI has been studied as an insulation layer in neural implants [22], intravascular ultrasound (IVUS) catheters [23] and flexible body patches [24].

In thin-film technology, PI layers can be deposited by means of vapor deposition polymerization [25], lamination (with Kapton- type PI) [26] or spin-coating [27]. In this work the PI is deposited with spin-coating since it is the most suitable process for the desired layer thicknesses. In particular, the FUJIFILM 9305 Polyimide was chosen. This PI is photosensitive, and it can be easily deposited and patterned like a standard PR. Moreover, it is NMP free and thus, environment, health and safety (EHS) compatible [15].

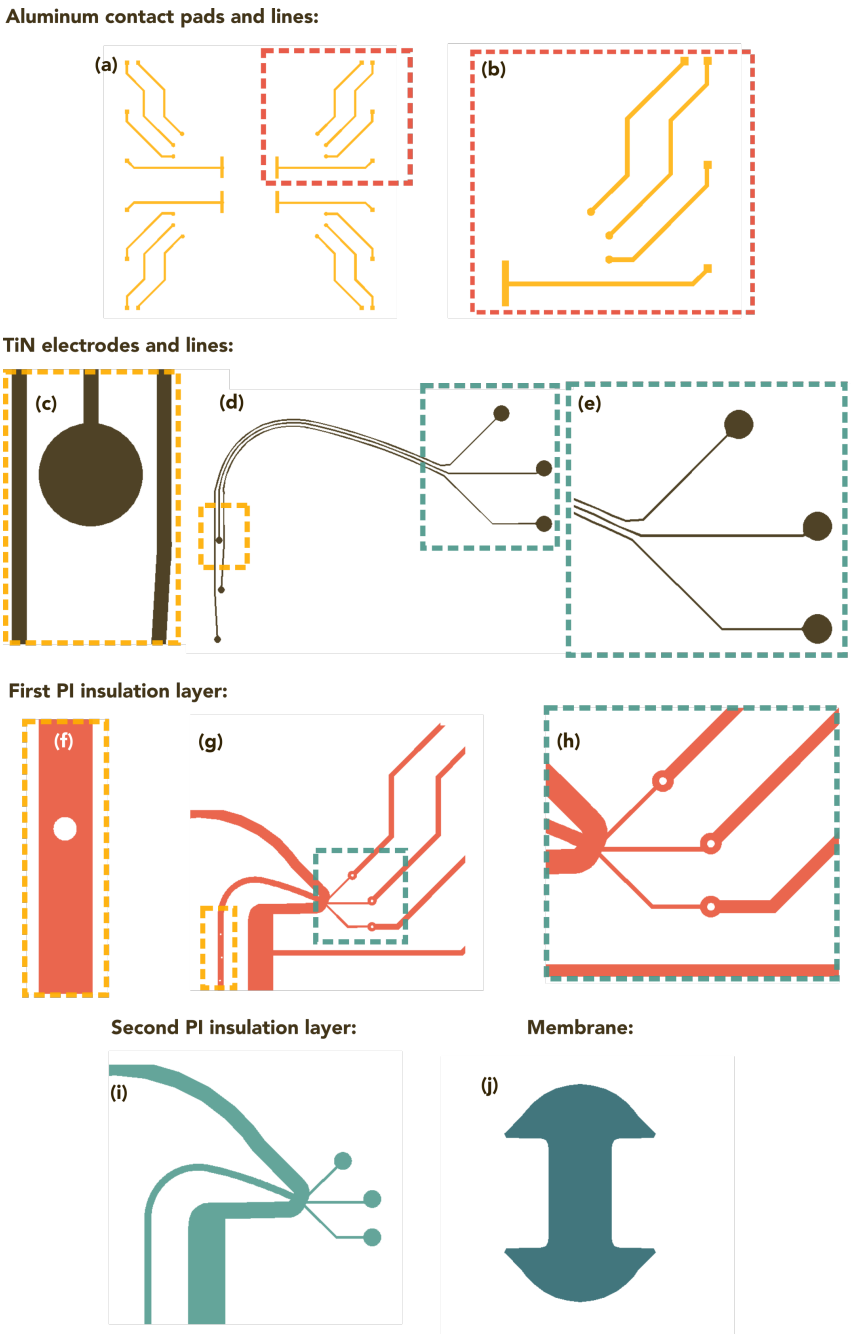

Figure 4.2: Mask designs for the Cytostretch Heart-on-Chip device: (a,b) design of the Al lines and contact pads; (c,d,e) design of the TiN lines and electrodes; (f,g,h) design of the first PI layer - (f) close-up of an electrode opening and (h) close-up of the contact spot between the TiN and Al lines; (i) design of the second layer of PI insulating the TiN lines; (j) design of the membrane.

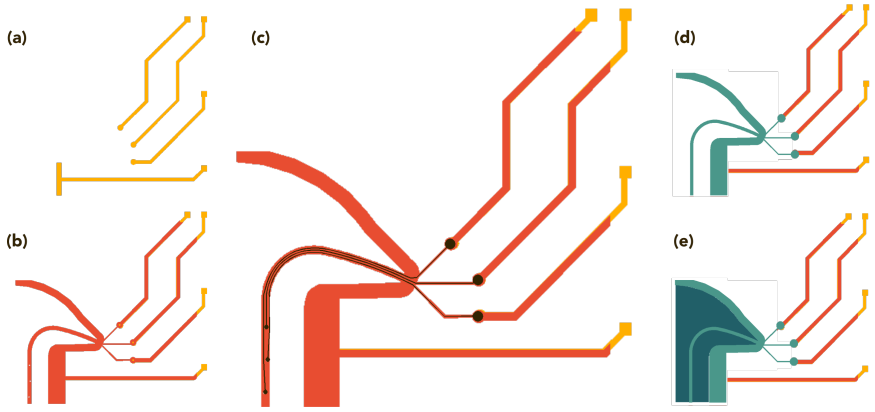

Figure 4.3: Mask designs (one quarter of a die) shown one on top of each other following the fabrication sequence: (a) fabrication of Al lines and contact pads; (b) deposition of first layer of PI, insulating the Al lines; (c) fabrication of the TiN lines and electrodes; (d) insulation of the TiN lines with a second layer of PI; (e) releasing of PDMS membrane.

In our experiments, the precursor of the PI is dispensed. The backside and the edges of the wafers are cleaned using the HTRD2 developer as presented in Section 2.3.1. Next, the wafer is moved to a hotplate and pre-baked to dry the solvent. The precursor layer is then exposed on a wafer stepper ASML PAS 5500/80 waferstepper and then developed in HTRD2. The deposition ends by curing the wafers at 350 °C in N_2 gas environment to complete the imidization process (Koyo). The change from parylene to PI made the fabrication of the chip more compatible with standard thin-film technology since the deposition and development can be automated.

In contrast to the highly conformal parylene deposition, the spin coating of the PI imposes the risk that some of the Al structures are only partially covered and after the coating some of the Al tracks may not be fully insulated. This issue, beside hindering the electrical insulation of the metal lines, might eventually results in corrosion of the Al structures when the device is placed in a humid environment. In order guarantee the full coverage of the Al, a re-tuning of thickness of the PI-Al-PI stack was performed. This was done taking into account that the Al contact pads should not be too thin (> 1 µm) to allow for the deposition of an under-bump metallization, and the PI should be as thin as possible to guarantee an easy step coverage of the TiN interconnects.

To achieve this multiple PI and Al thicknesses were tested. Figure 4.4 shows two examples of a non-conformal and a conformal PI coating. The final thicknesses chosen for the fabrication were an Al thickness of 1.5 µm and a PI thickness of 0.7 µm.

The thickness of the TiN had to be tuned based on the selected PI thickness to guar-

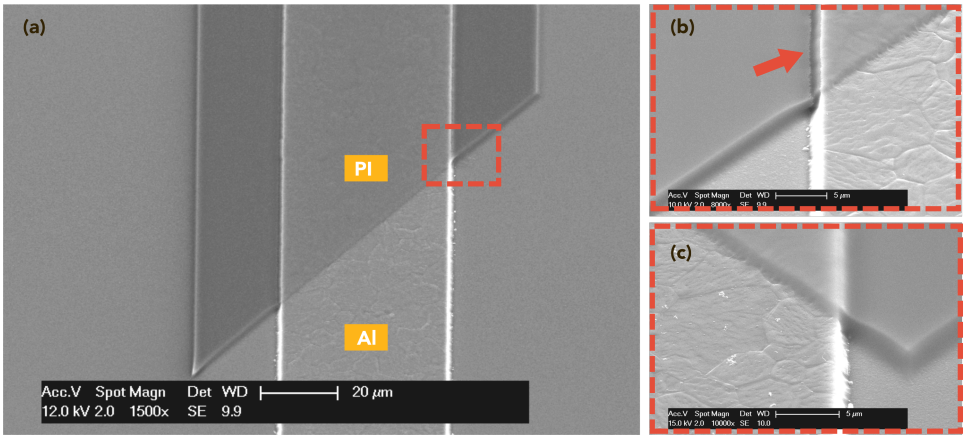

Figure 4.4: (a) SEM image of the first layer of PI layer spin coated on the Al. A non-conformal (b) and a conformal (c) PI coating on an Al structure. Non-conformal PI layer on Al step indicated by red arrow. Scale bars: (a) 20 µm and (b,c) 5 µm.

antee a conformal TiN layer over the PI topography. This was guaranteed by developing the PI with an horizontal immersion technique that, as presented by Joshi et al. [15], provides profiles with positive angles. The optimization resulted in a TiN layer thickness of 0.2 µm (Figure 4.5). A thicker layer of TiN will result in a higher initial stress after release of the membrane. The TiN lines were cleaned from PR residues after the etching with NMP at 70 °C. However, the cleaning process did not completely remove the PR as shown in Figure 4.6.

The thickness of the second layer of PI was also optimized to guarantee conformal coverage of the topography on the wafer. The final thickness selected was 1 µm. The optimized layer stack, allowed for the deposition and patterning of a 4 µm thick PR layer

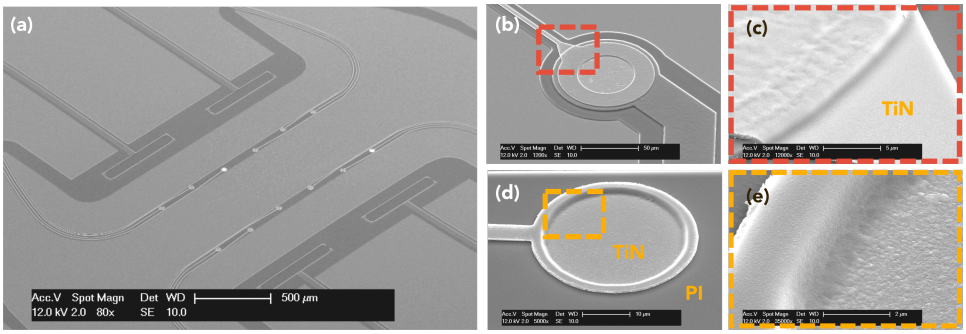

Figure 4.5: (a) SEM images of the TiN layer on top of the PI. (b-e) SEM images of the TiN layer conformally coating the patterned PI layer. Scale bars: (a) 500 µm, (b) 50 µm, (c) 5 µm, (d) 10 µm and (e) 2 µm.

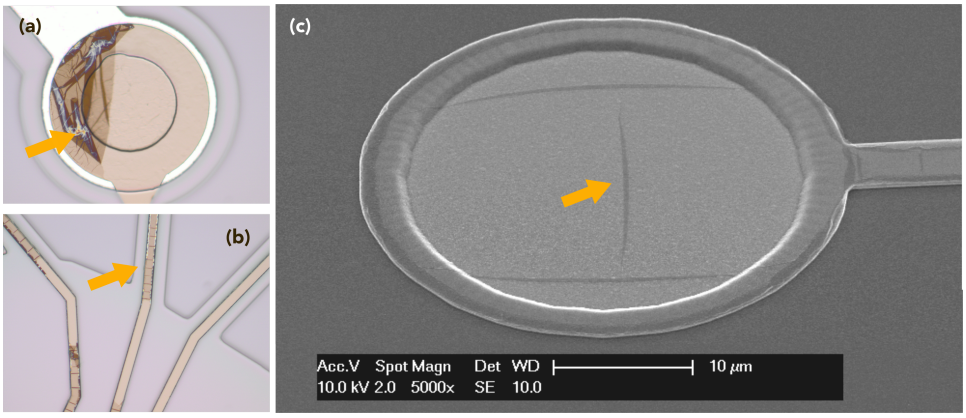

Figure 4.6: Optical (a,b) and SEM (c) images of the PR residues on the TiN layer after the dry etching and the NMP cleaning. PR residues indicated by yellow arrows.

for the fabrication of the microgrooves presented in Section 3.2.4.
During integration of the PI in the Cytostretch process two main issues were identified and addressed:

- poor adhesion between the two layers of PI compromising the insulation of the TiN metal lines; and
- poor adhesion between the PI and PDMS caused detachment of the PI-TiN-PI sandwich from the PDMS layer.

4.4.1. PI-PI ADHESION

To improve the adhesion, an oxygen plasma treatment was introduced after TiN metal lines were patterned (TEPLA Plasma 300 (Power: 600 Watt, Time: 60 s, O_2: 250 ml/min)).

This oxygen plasma treatment alters the wettability of the polymide, making the polymeric surface hydrophilic. Nakamura et al. [28] suggested that the increase of hydrophilicity of the treated surface is mainly induced by the increase of hydrophilic groups (C–O bond) on the polyamide surface. It is suggested that the chemical and mechanical bonding between PI layers can be improved with the increase in hydrophilicity of the first PI film [28].

To prove the efficacy of the treatment, the hydrophilicity of the PI surface before and after the oxygen plasma treatment was determined by a contact angle measurement (shown in Figure 4.7a,b). From the measurements, it can be observed that the hydrophilicity of PI surface is increased after the oxygen plasma treatment. The average

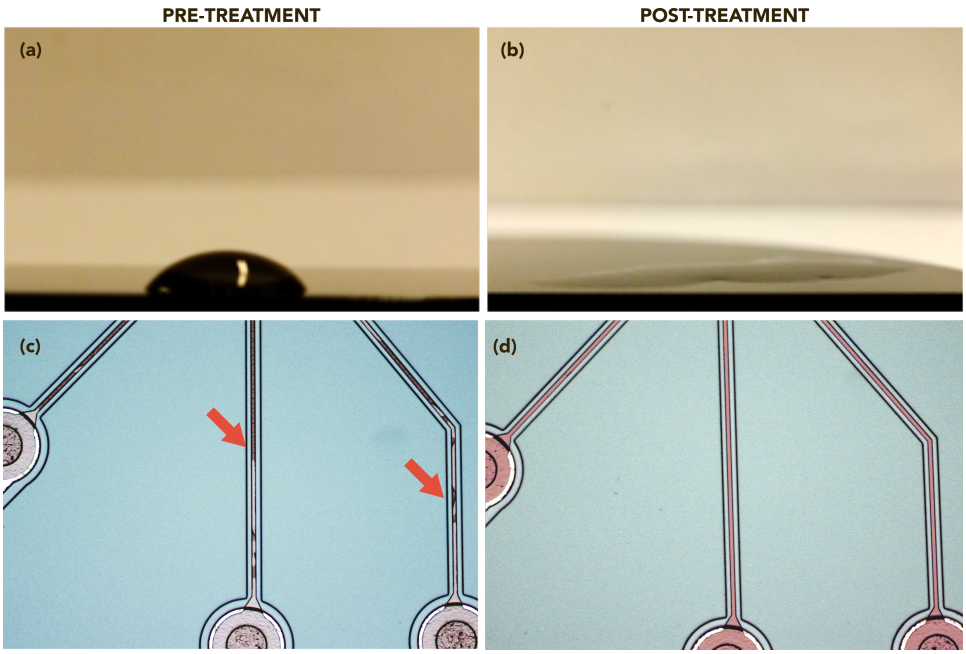

Figure 4.7: Contact angle measurement on PI surface, prior (a) and after (b) the oxygen plasma treatment. (c,d) The plasma treatment resulted in the removal of the PR residues indicated by the red arrows. PR residues indicated by red arrows.

contact angle of a pristine PI film is 57.6 °, while after the treatment the contact angle is close to 0 °. This result confirms the increase in hydrophilicity. With the introduction of the oxygen plasma treatment, no delamination of the PI layer during PEDOT:PSS deposition was observed (Chapter 5). The process not only provides an improved adhesion between the two layers of PI, but also cleans the TiN from the resist residues left after metal lines etching as can be seen in Figure 4.7c,d.

4.4.2. PI-PDMS ADHESION

Additionally, an adhesion issues between the PI insulation layers (deposited in the step shown in Figure 3.7e) and PDMS layer (deposited in the step shown in Figure 3.7f) was identified. Delamination of the PI film from PDMS membrane was observed after the immersion of the device in acetone (Figure 4.8). The reduced adhesion may result in delamination of the PI structures during the application of strain to the membrane. Several methods have been suggested to improve the PI-PDMS adhesion, such as the deposition of an intermediate layer [22, 29] and surface modification of the PI [30]. In this work, plasma etching treatment was tested to improve the adhesion.

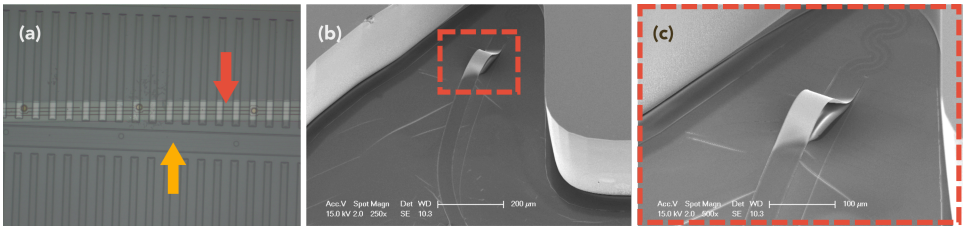

Figure 4.8: (a-c) The delamination of the PI film from PDMS after immersion in acetone at room temperature for 10 minutes during the fabrication of a Cytostretch chip equipped with a MEA and microgrooves (Optical (a) and SEM (b,c) images). Delaminated PI structure indicated by red arrow and original position of the PI structure indicated by yellow arrow. Scale bars: (b) 200 µm and (c) 100 µm.

The surface modification is done with an Ar^+ ion plasma (Ar^+ sputter-etch) [14]. Two mechanisms that explain the improved adhesion after an argon plasma etch have been proposed. In the first place, the roughened PI surface was suggested to initiate a PI-PDMS mechanical interlocking. Secondly, the treatment of the PI surface increases the amount of –OH groups [30].

To test the effect of the plasma treatment, a new batch of test wafers was fabricated with the Ar^+ sputter etch. The fabrication of the test devices followed the same steps as the full device except for the omission of the electrodes and the interconnect structures. The fabrication process for these test structures is summarized in Appendix A.1. The treatment was done after the curing of the PI film prior to the deposition of the PDMS layer. Test devices with and without plasma etching treatment were fabricated to compare and assess the effectiveness of the treatment.

The adhesion of the PI to PDMS membrane was evaluated by immersing the test device in a range of wet chemicals that are used in the fabrication of the Cytostretch device (Acetone, N-Methyl Pyrrolydone, TMAOH). As an example, the results for the acetone immersion test are shown in the Figure 4.9. In Figure 4.9, an untreated sample before (a) and after (b) the immersion test is shown. As indicated by the yellow arrow in Figure 4.9b, the PI detached from the PDMS layer. The treated sample before (c) and after (d) the immersion are shown in Figure 4.9. No signs of detachment were identified in this case as well as the other chemicals (N-Methyl Pyrrolydone and TMAOH). From the results of the immersion test, it can be concluded that the plasma etching treatment significantly improves the adhesion between the PI and PDMS layers. Therefore, sputter etch treatment of the PI was permanently included in the fabrication flow of the Cytostretch device.

As an alternative to the treatment here presented, our group also developed and tested the use of an carbide-oxide (SiC–SiO_2) interfacial bilayer. The SiC–SiO_2 bilayer

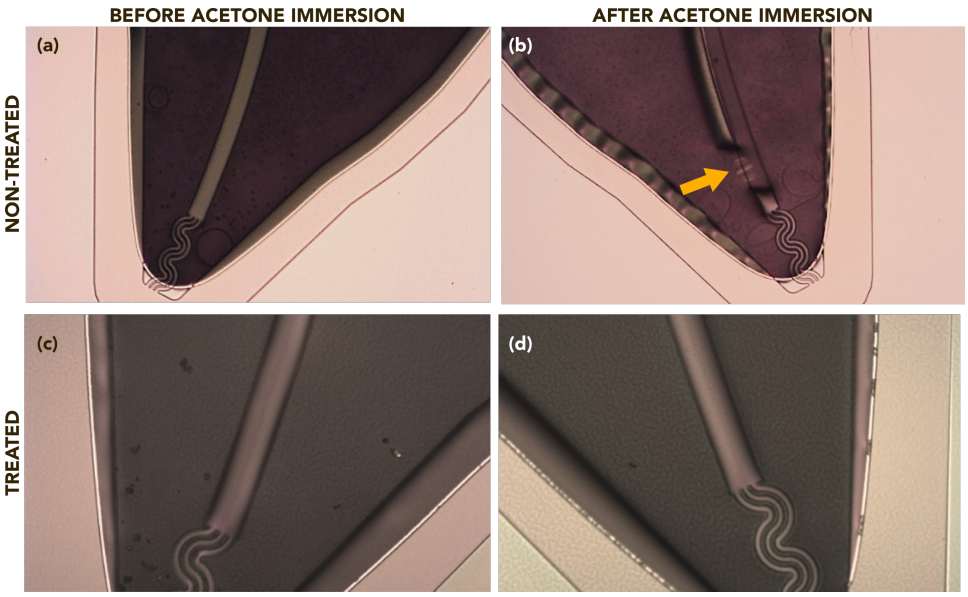

Figure 4.9: The delamination of PI film from PDMS after immersion in acetone at 40 °C for 5 minutes, as observed under an optical microscope (a,b). The result of plasma etching treatment showing no delamination of the PI film after immersion in the same solvent for 20 minutes (c,d). Delaminated PI structure indicated by yellow arrow.

solely relies on chemical bonding [29] and it involves a strong bonding of the PDMS to the oxide through silanol groups, a Si-Si bonding at the carbide-oxide interface, and a bonding through carbon chains in the SiC-PI interface [29].

The final fabrication process for the Cytostretch device, including the treatments to guarantee sufficient adhesion among the polymer layers stack, is summarized in Appendix A.2.

4.5. FROM PDMS SPINNING AND ETCHING TO MOLDING

An alternative to spin coating and photolitography for the deposition and patterning of PDMS on Si wafers was developed. This was not only done to expand the range of PDMS thicknesses achievable on a Si wafer, but also to remove the earlier mentioned problems regarding the cleaning of the etching equipment after PDMS processing.
The use of spin coating and etching processes has two main limitations:

First, the deposition of thick layers (> 200 µm) of PDMS is at the moment performed by manually dispensing a specific amount of uncured PDMS onto the wafer, making sure that the PDMS does not spill over the edge wafer. The PDMS is then cured by plac-

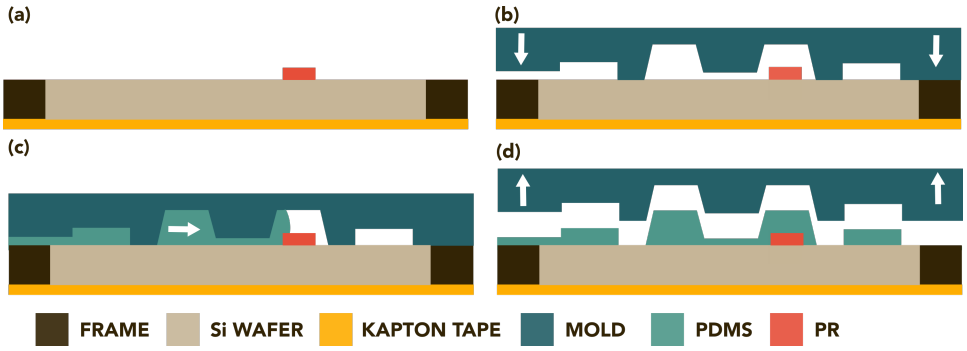

Figure 4.10: Process flow: (a) the wafer is loaded onto a customized holder and inserted into an MMS-LM molding system; (b) the mold, protected by a 50 µm Kapton foil, is brought in contact with the wafer; (c) the uncured PDMS is loaded inside the molding machine and is injected into the mold cavities; (d) the molding press opens and the wafer is unloaded. The figures are not drawn to scale.

ing the wafer in a vacuum chamber to remove air bubbles. This process is prone to mistakes and variability because the thickness of the layer is defined indirectly by the PDMS volume used, while the layer uniformity is dependent on how horizontally the wafer is placed in the oven and /or by the topographies on the wafer.

Secondly, it does not provide a way to pattern these thick layers. Degassing issues during subsequent sputtering of metal layers on top of the PDMS become more pronounced for thicker layers. Moreover, due to the low dry etch rate of PDMS, the etching of thick PDMS layer is not practical.

These limitations can be overcome by combining standard silicon fabrication processes with automated 3D molding techniques using a commercially available molding system. The process is applied in the fabrication of two components: (a) a molded microfluidic channel providing high control over the thickness of the PDMS, and (b) the Cytostretch PDMS membranes including 3D topography without the need for lithography or etching.

The 3D PDMS molding on Si wafers is performed using a commercially available BESI MMS-LM molding system. For this proof-of-concept, the wafer was diced and reshaped into an 7x9 cm^2 rectangle to fit in a pre-existing holder (Figure 4.10a). The loading of the wafer is currently performed manually, but other BESI B.V. tools (e.g. an AMS-LMmolding system) perform this step automatically. The wafer can be either pristine or pre-processed to embed MEMS or electrical components and structures into the PDMS [31]. A pre-designed mold, with the negative image of the desired PDMS structure, is automatically brought in contact with the wafer (Figure 4.10b). During the process, the mold is protected from the injected polymer by means of a 50 µm thick Ethylene Tetra

Fluoro Ethylene (ETFE) foil that is pulled and fixated to the inner surfaces of the mold by special vacuum channels (ETFE foil not shown in Figure 4.10).

Next, PDMS (Sylgard 182 with a 1:10 elastomer/curing agent ratio) is injected into the cavities of the mold creating the desired structures (Figure 4.10c). The pressure between the wafer and the mold is kept constant, preventing any damage to the wafer. Moreover, the injection speed is controlled to smoothly fill the mold with a transfer speed starting at 2 mm/s, slowing down to 1 mm/s and finally to 0.5 mm/s. The molding tool is equipped with a venting mechanism that mechanically closes as soon as the cavity is completely filled. After that, the temperature (100 °C) and the pressure (5 MPa) are kept constant for the time needed for the pre-curing of the PDMS (10 min). After curing, the mold opens, and the molded sample is removed (Figure 4.10d). Finally, the wafer is removed from the holder, and fully cured (120 °C, 4 hours). The automatic molding prevents PDMS residues and particles on the backside and edges of the wafer, allowing for further processing of the wafer in a CR environment. The mold cleaning is automatically performed by removing the ETFE foil from the mold.

In order to verify whether this technique allow for the deposition and patterning of PDMS in a uniform and conformal way, two different test structures were fabricated with the presented process. The first one consists of 100 µm PR structures embedded in a uniform 200 µm thick PDMS layer. The second structure is a Cytostretch membrane with 3D topography surrounding the membrane.

4.5.1. TEST STRUCTURE 1

For this structure a flat mold was used to deposit a uniform layer of PDMS on top of 100 µm-thick structures made of THB-151N negative PR. The PR was conformally covered by the PDMS without any bubble or void formation as shown in Figure 4.11a,b.

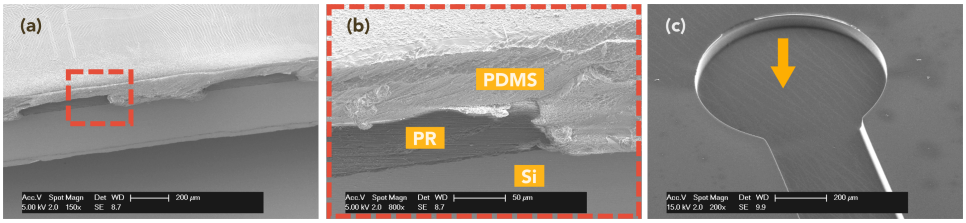

Figure 4.11: (a) SEM images of the 100 µm thick PR structures embedded in a 200 µm thick PDMS layer. (b) Close-up of the PR structures covered with PDMS. The PDMS conformally covers the vertical walls of PR, thus retaining the predefined geometry. The microchannels (indicated by yellow arrow) were created by peeling off the PDMS layer ending up with the PR pattern imprinted into the backside of the PDMS layer (c). Scale bars: (a) 200 µm, (b) 50 µm and (c) 200 µm.

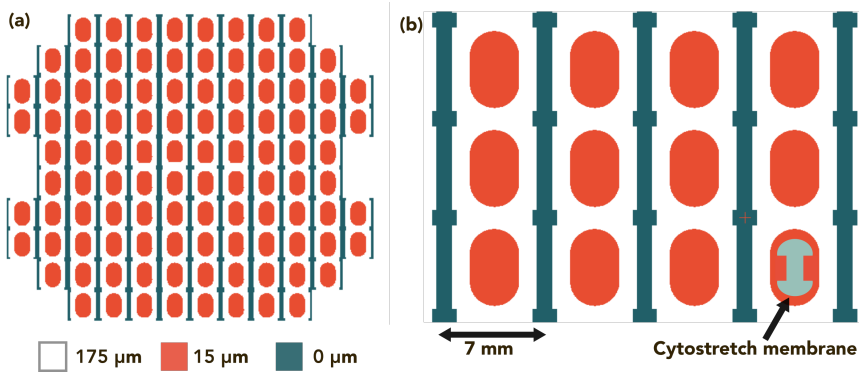

Figure 4.12: Mold design - white area: 175 µm, red: 15 µm, blue: 0 µm. (a) Full wafer and (b) close-up of 12 chips.

The thickness of the PDMS can be changed by tuning the distance between the mold and the wafer in the machine. This guarantees a high control over the thickness of the molded layer across the wafer. By adjusting the distance between the wafer and the mold to 200 µm, it is possible to obtain a 200.8 µm layer with only ±4 µm variations, as measured with a Dektak 8 surface profilometer. The thickness of the PDMS layer can be easily increased up to 1 mm. The 100 µm high PR structures did not affect the uniformity of the deposition both when the PDMS was injected against or along the PR lines.

The 200 µm thick PDMS layer was detached from the wafer leaving the PR pattern transferred into the bottomside of the PDMS film (Figure 4.11c). This step can be made easier by means of the scalable releasing technique presented by Quirós-Solano at al. [32, 33] and introduced in Section 2.3.4. Even though this was not the goal of this test, this process might eventually be used to improve the fabrication process of the microfluidic components of the OOC presented by Hu et al. [34].

4.5.2. TEST STRUCTURE 2 (CYTOSTRETCH)

Furthermore, the process was also employed to fabricate the stretchable membranes included in the Cytostretch device [31]. The process allows for the fabrication of the membranes in one single step, without any need for lithography and etching steps to pattern the PDMS at the location of the bondpads. The design of the mold employed for this test is shown in Figure 4.12a,b.

The process was used for the deposition and patterning of 3D PDMS structures with thicknesses ranging from 15 to 175 µm (Figure 4.13a,b). With the mold covering the bond pads (colored in blue in Figure 4.13), these areas are left free from PDMS. The thickness of the layer was characterized with a VK-X250 3D Laser Scanning Confocal

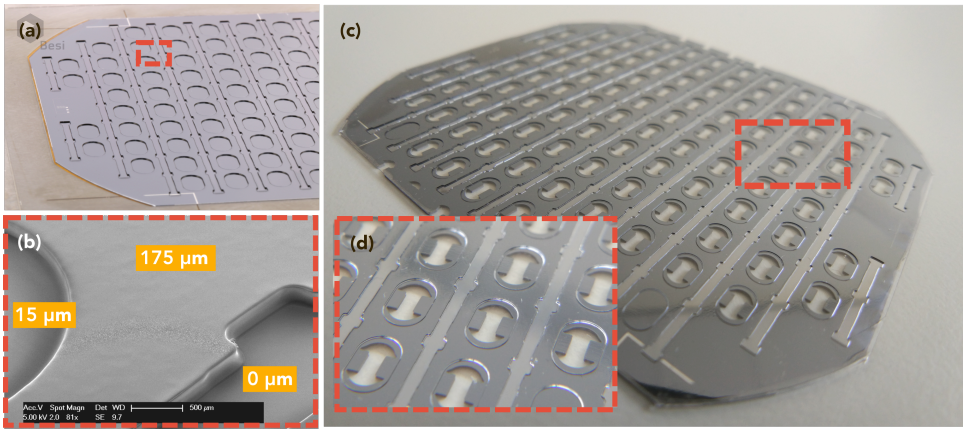

Figure 4.13: (a) Si wafer with 3D PDMS molded structures customized for the Cytostretch Heart-on-Chip. (b) Structures with different heights in a single step (ranging between 15 µm and 175 µm). Designated areas of the wafer are left completely clean from PDMS, making etching steps unnecessary. Scale bar: 500 µm. (c,d) Suspended PDMS areas/membranes were then released by locally etching the Si from the back of the wafer with deep-reactive ion etching.

Microscope, showing variations of only ±1.3 µm on the 15 µm-thick membrane areas across the wafer (colored in red in Figure 4.13). The 15 µm PDMS membranes were then released by etching the Si supporting the PDMS membrane (Figure 4.13c) by means of DRIE. In order to do this, the molded wafer was placed upside down and loaded on a transport wafer in the DRIE etcher. The fabrication of thinner membranes was not attempted as filling of narrower gaps during the molding process was not considered feasible because of the PDMS viscosity and the injection pressure required.

4.6. CONCLUSIONS

In this chapter, the limitations of the original Cytostretch, presented in Chapter 3, were highlighted. These are related to three main areas: manufacturability, performance, and ease of use. Next, the chapter focuses on the manufacturability, addressing two main fabrication issues: the use of parylene and the need to dry etch PDMS.

In order to remove parylene from the Cytostretch, the TiN interconnects were isolated with PI. A deposition and patterning process for this material was successfully defined and optimized. In order to integrate PI into the Cytostretch device, the adhesion between the two layers of PI and between PI and PDMS was improved by means of oxygen plasma and argon plasma treatments, respectively. By replacing parylene with PI, the fabrication of the MEA module presented in Chapter 3 became compatible with a standard CR environment. The new process flow was employed for the fabrication of

the Cytostretch chips used in the next chapters (Chapter 5-7).

To pattern PDMS without dry etching, automated 3D molding techniques and a commercially available molding system was employed to deposit and pattern the PDMS. A 200 µm-thick PDMS layer was conformally deposited on 100 µm-thick PR structures without any voids or bubble formation. By adjusting the distance between the wafer and the mold to 200 µm, it is possible to obtain a 200.8 µm thick layer with variations of only ±4 µm. The process also allowed for the deposition and patterning of 3D PDMS structures with thicknesses ranging from 15 to 175 µm, showing variations of only ±1.3 µm on the 15 µm-thick membranes across the wafer. These results clearly indicate that this process can be effectively used in the microfabrication of multiple 2D and 3D structures, showing its versatility, uniformity and robustness. It is important to highlight the potential of this new technique to create PDMS structure, as it could be used for a wide range of structures and applications. It is worthwhile to investigate maximum and minimum thickness and molding feature sizes. Moreover, these structures can be employed in combination with of prefabricated thick PR structures, similar to those presented in Chapter 8.

REFERENCES

[1] N. Gaio, S. Kersjes, W. Q. Solano, P. Sarro, and R. Dekker, *Versatile and automated 3d polydimethylsiloxane (pdms) patterning for large-scale fabrication of organ-on-chip (ooc) components,* in *2018 EUROSENSORS*, Vol. 2 (2018) p. 873.

[2] I. J. Onakpoya, C. J. Heneghan, and J. K. Aronson, *Post-marketing withdrawal of 462 medicinal products because of adverse drug reactions: a systematic review of the world literature,* BMC medicine **14**, 10 (2016).

[3] J. Lexchin, *Drug withdrawals from the canadian market for safety reasons, 1963–2004,* Cmaj **172**, 765 (2005).

[4] S. R. Braam, L. Tertoolen, A. van de Stolpe, T. Meyer, R. Passier, and C. L. Mummery, *Prediction of drug-induced cardiotoxicity using human embryonic stem cell-derived cardiomyocytes,* Stem cell research **4**, 107 (2010).

[5] S. K. Pakazad, A. Savov, A. Van de Stolpe, and R. Dekker, *A novel stretchable micro-electrode array (smea) design for directional stretching of cells,* Journal of Micromechanics and Microengineering **24**, 034003 (2014).

[6] S. Khoshfetrat Pakazad, *Stretchable micro-electrode arrays for electrophysiology,* (2015).

[7] E. Ghafar-Zadeh, J. R. Waldeisen, and L. P. Lee, *Engineered approaches to the stem cell microenvironment for cardiac tissue regeneration,* Lab on a Chip **11**, 3031 (2011).

[8] A. Marsano, C. Conficconi, M. Lemme, P. Occhetta, E. Gaudiello, E. Votta, G. Cerino,

A. Redaelli, and M. Rasponi, *Beating heart on a chip: a novel microfluidic platform to generate functional 3d cardiac microtissues,* Lab on a Chip **16**, 599 (2016).

[9] A. Stett, U. Egert, E. Guenther, F. Hofmann, T. Meyer, W. Nisch, and H. Haemmerle, *Biological application of microelectrode arrays in drug discovery and basic research,* Analytical and bioanalytical chemistry **377**, 486 (2003).

[10] T. Meyer, K.-H. Boven, E. Günther, and M. Fejtl, *Micro-electrode arrays in cardiac safety pharmacology,* Drug Safety **27**, 763 (2004).

[11] M. E. Spira and A. Hai, *Multi-electrode array technologies for neuroscience and cardiology,* Nature nanotechnology **8**, 83 (2013).

[12] D. C. Rodger, A. J. Fong, W. Li, H. Ameri, A. K. Ahuja, C. Gutierrez, I. Lavrov, H. Zhong, P. R. Menon, E. Meng, *et al.*, *Flexible parylene-based multielectrode array technology for high-density neural stimulation and recording,* Sensors and Actuators B: chemical **132**, 449 (2008).

[13] J. Charmet, J. Bitterli, O. Sereda, M. Liley, P. Renaud, and H. Keppner, *Optimizing parylene c adhesion for mems processes: potassium hydroxide wet etching,* Journal of Microelectromechanical Systems **22**, 855 (2013).

[14] P. Rezai, P. R. Selvaganapathy, and G. R. Wohl, *Plasma enhanced bonding of polydimethylsiloxane with parylene and its optimization,* Journal of Micromechanics and Microengineering **21**, 065024 (2011).

[15] S. Joshi, *Free standing interconnects for stretchable electronics,* Ph.D. thesis, Delft University of Technology (2018).

[16] M. Ochoa, P. Wei, A. J. Wolley, K. J. Otto, and B. Ziaie, *A hybrid pdms-parylene subdural multielectrode array,* Biomedical microdevices **15**, 437 (2013).

[17] J. Flueckiger, V. Bazargan, B. Stoeber, and K. C. Cheung, *Characterization of postfabricated parylene c coatings inside pdms microdevices,* Sensors and Actuators B: Chemical **160**, 864 (2011).

[18] D.-J. Liaw, K.-L. Wang, Y.-C. Huang, K.-R. Lee, J.-Y. Lai, and C.-S. Ha, *Advanced polyimide materials: syntheses, physical properties and applications,* Progress in Polymer Science **37**, 907 (2012).

[19] S. Diaham, M.-L. Locatelli, and R. Khazaka, *Bpda-pda polyimide: synthesis, characterizations, aging and semiconductor device passivation,* in *High Performance Polymers-Polyimides Based-From Chemistry to Applications* (IntechOpen, 2012).

[20] T. Stieglitz, M. Schuetter, and K. P. Koch, *Implantable biomedical microsystems for neural prostheses,* IEEE engineering in medicine and biology magazine **24**, 58 (2005).

[21] M. Kotera, B. Samyul, K. Araie, Y. Sugioka, T. Nishino, S. Maji, M. Noda, K. Senoo, T. Koganezawa, and I. Hirosawa, *Microstructures of bpda-ppd polyimide thin films with different thicknesses,* Polymer **54**, 2435 (2013).

[22] J. S. Ordonez, C. Boehler, M. Schuettler, and T. Stieglitz, *Silicone rubber and thin-film poly-*

imide for hybrid neural interfaces—a mems-based adhesion promotion technique, in *2013 6th International IEEE/EMBS Conference on Neural Engineering (NER)* (IEEE, 2013) pp. 872–875.

[23] B. Mimoun, H. T. Pham, V. Henneken, and R. Dekker, *Residue-free plasma etching of polyimide coatings for small pitch vias with improved step coverage,* Journal of Vacuum Science & Technology B, Nanotechnology and Microelectronics: Materials, Processing, Measurement, and Phenomena **31**, 021201 (2013).

[24] S. Joshi, S. Yazadi, V. Henneken, R. Dekker, and R. Sanders, *Conformable body patches for ultrasound applications,* in *2015 IEEE 17th Electronics Packaging and Technology Conference (EPTC)* (IEEE, 2015) pp. 1–4.

[25] J. Salem, F. Sequeda, J. Duran, W. Lee, and R. Yang, *Solventless polyimide films by vapor deposition,* Journal of Vacuum Science & Technology A: Vacuum, Surfaces, and Films **4**, 369 (1986).

[26] R. D. Kornbluh, D. S. Flamm, H. Prahlad, K. M. Nashold, S. Chhokar, R. Pelrine, D. L. Huestis, J. Simons, T. Cooper, and D. G. Watters, *Shape control of large lightweight mirrors with dielectric elastomer actuation,* in *Smart Structures and Materials 2003: Electroactive Polymer Actuators and Devices (EAPAD)*, Vol. 5051 (International Society for Optics and Photonics, 2003) pp. 143–159.

[27] J. S. Ordonez, C. Boehler, M. Schuettler, and T. Stieglitz, *Silicone rubber and thin-film polyimide for hybrid neural interfaces—a mems-based adhesion promotion technique,* in *2013 6th International IEEE/EMBS Conference on Neural Engineering (NER)* (IEEE, 2013) pp. 872–875.

[28] Y. Nakamura, Y. Suzuki, and Y. Watanabe, *Effect of oxygen plasma etching on adhesion between polyimide films and metal,* Thin Solid Films **290**, 367 (1996).

[29] S. Joshi, R. Bagani, L. Beckers, and R. Dekker, *Novel method for adhesion between pi-pdms using butyl rubber for large area flexible body patches,* in *Multidisciplinary Digital Publishing Institute Proceedings*, Vol. 1 (2017) p. 307.

[30] S. Joshi, A. van Loon, A. Savov, and R. Dekker, *Adhesion improvement of polyimide/pdms interface by polyimide surface modification,* MRS Advances **1**, 33 (2016).

[31] N. Gaio, B. van Meer, W. Quirós Solano, L. Bergers, A. van de Stolpe, C. Mummery, P. Sarro, and R. Dekker, *Cytostretch, an organ-on-chip platform,* Micromachines **7**, 120 (2016).

[32] W. Quirós-Solano, N. Gaio, O. Stassen, Y. Arik, C. Silvestri, N. Van Engeland, A. Van der Meer, R. Passier, C. Sahlgren, C. Bouten, *et al.*, *Microfabricated tuneable and transferable porous pdms membranes for organs-on-chips,* Scientific reports **8**, 13524 (2018).

[33] W. Quiros-Solano, N. Gaio, C. Silvestri, Y. Arik, O. Stassen, A. Van Der Meer, C. Bouten, A. Van Den Berg, R. Dekker, and P. Sarro, *A novel method to transfer porous pdms membranes for high throughput organ-on-chip and lab-on-chip assembly,* in *2018 IEEE Micro Electro Mechanical Systems (MEMS)* (IEEE, 2018) pp. 318–321.

[34] D. Huh, H. J. Kim, J. P. Fraser, D. E. Shea, M. Khan, A. Bahinski, G. A. Hamilton, and D. E. Ingber, *Microfabrication of human organs-on-chips,* Nature protocols **8**, 2135 (2013).

5

ALTERNATIVE MATERIALS FOR CYTOSTRETCH ELECTRODES

This chapter is based on:

- Gaio, C. Silvestri, B. van Meer, S. Vollebregt, C.L. Mummery, R. Dekker. "Fabrication and characterization of an upside-down carbon nanotube microelectrode array". IEEE Sensor Journal, 16, n. 24 (2016): 8685-8691 [1].
- A. Waafi*, N. Gaio*, W.F. Quirós-Solano, P. Dijkstra, P.M. Sarro, R. Dekker. "Low-impedance PEDOT:PSS MEA integrated in an Organ-on-Chip Device". Under reviews in IEEE Sensor Journal. *These authors should be regarded as joint first author [2].

5.1. INTRODUCTION

Microelectrode arrays (MEAs) are widely employed to monitor and stimulate *in vitro* and *in vivo* biological systems composed of electrically active cells e.g. neurons or cardiomyocytes [3–7]. The membrane of these cells contains ion channels that actively exchange ions with the surrounding extracellular matrix (ECM), generating a difference in ionic concentration [8, 9]. By doing so, the electrical potential of the intra-cellular matrix is altered with respect to the ECM. The combination of these chemical and electrical phenomena gives rise to electrical signals [8, 10, 11] that can be detected with a microelectrode [12–15]. The electrode functions as charge transfer interface between the cells ECM and a read-out system [16, 17].

The charge transfer between the electrode surface and the ECM is affected by var-

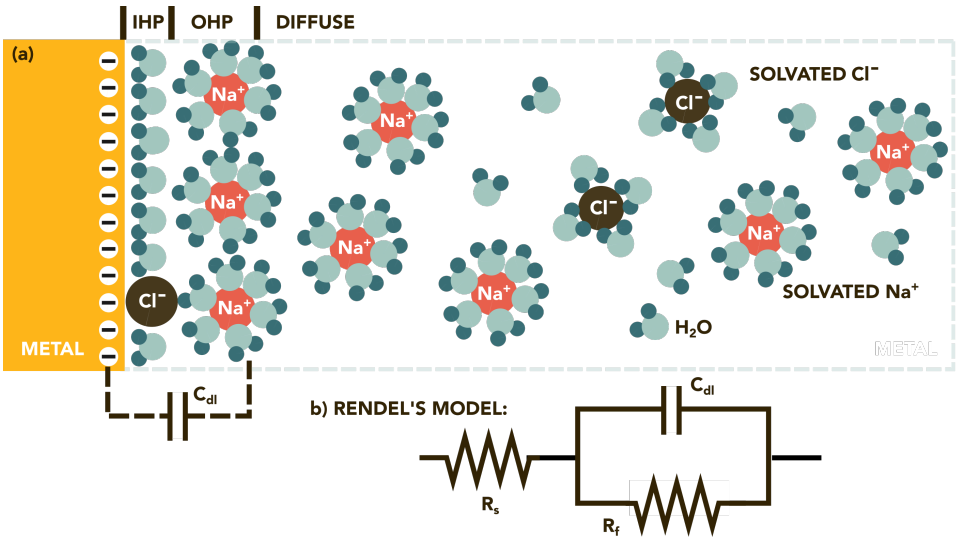

Figure 5.1: (a) The double layer capacitance (C_{dl}) at the electrode-electrolyte interface. The double layer area, extends from the high charge concentration area near the metal surface to the diffuse area in the electrolyte. (b) Equivalent circuit of a metal electrode-electrolyte interface (Randle's circuit). Figures adapted from [18–21].

ious electrical and chemical phenomena at the interface [18–20, 22, 23]. Electrodes are in general made of metals or alloys (s.a. platinum (Pt), platinum alloys and gold). These materials conduct electricity by means of free electron movement driven by an electrical field [22]. Meanwhile, electrolyte solutions in the ECM conduct electricity by means of ion movement and redox reactions among ions [24, 25]. At the interface between these two materials, charge transfer happens by redox reactions between the electrode surface and the ions in the solution. These reactions are known as faradaic charge transfer. In parallel to charge transfer, two compact layers of opposite charge form at the electrode-electrolyte interface immediately after immersion [20, 22, 23]. This structure is caused by the redistribution of charge carriers on the metal surface (electrons in Figure 5.1a), which subsequently attracts ions with opposite polarity (Na^+ in Figure 5.1a). This structure behaves as a parallel plate capacitor and it is known as double-layer capacitance (C_{dl}).

The solution side of the C_{dl} is composed of several layers as shown in Figure 5.1a. The inner layer (known as inner Hemholtz plane - IHP) consists of strongly oriented water molecules and other ions absorbed on the surface of the electrode. Next to the IHP, a highly concentrated layer of ions (with opposite polarity to the electrode) can be found (outer Hemholtz plane - OHP region). The rest of the charges are distributed in the dif-

fuse region extending toward the ECM bulk.

The impact of all the electrical and chemical phenomena described above are collectively known as electrochemical impedance. The electrode-electrolyte interface and the electrochemical impedance can be represented with an equivalent circuit, known as Randle's circuit [21]. In Figure 5.1b, the Randle's circuit used for metallic electrodes is reported. This circuit includes the double layer capacitor, shunted by a Faradaic resistance (R_f). The parallel of the two elements is in series with a resistance that represents the metal interconnects and the solution (R_s).

5.1.1. CYTOSTRETCH MEA WITH TIN ELECTRODES

The microelectrodes and electrical interconnects of the Heart-on-Chip developed with the Cytostretch platform are made of titanium nitride (TiN). This capacitive material has several advantages for bioelectrode applications [15]:

- sputtered TiN presents a highly porous geometry called fractal which guarantees a low electrode-electrolyte impedance;
- TiN can be easily patterned using standard lithography and dry etching;
- TiN guarantees mechanical and chemical stability and a good biocompatibility;
- room temperature deposition; and
- easy sterilization.

The electrochemical impedance spectroscopy (EIS) of Cytostretch was reported in [26]. The impedance measurement was performed using a Metrohm Autolab instrument with a PGSTAT12 module and a three electrode set-up. The measured impedance amplitude at 1 kHz was equal to ~ 4.5 MΩ.

This impedance is too high for a device meant to detect low voltage bio-signals (with amplitudes of few µV). This can be also seen from the electrical signals recording shown in Section 3.2.3. In comparison, the conventional MEA device from Multi-Channel Systems GmbH (MCS) has an impedance two orders of magnitude lower than the Cytostretch device [27]. This problem is mainly due to the "polymer last approach" technique used to fabricate the electrodes, as TiN presents a fractal geometry only on the side facing the target during sputter deposition, while, on the substrate side the TiN layer has a less porous surface. In the Cytostretch device, cells are in contact with this smooth surface rather than the fractal one. The flat surface of those electrodes, combined with their small dimensions, results in a high impedance.

5.1.2. TOWARDS ADVANCED MATERIALS FOR THE CYTOSTRETCH MEA

Recently, non standard materials such as PEDOT:PSS and CNTs have been considered as a replacement for more commonly used materials such as Pt, platinum alloys, Iridum oxide, and TiN, due to their superior electrochemical performances. These materials guarantee sufficiently high SNR during the detection of cellular action potential [15, 27], a crucial requirement for several applications such as cardiotoxicity studies where the extracellular field potential generated by the cells' action potential needs to be studied in details to identify possible QT intervals prolongations often associated with safety-pharmacological risks [28]. Apart from the lower SNR during *in vitro* cell monitoring, the chemical surface of these materials can be modified to improve their biocompatibility. Last but the least, the intrinsically 3D and porous nature of these materials has often been exploited to promote the mechanical anchoring of cells to the electrodes [15].

Even though previous work has shown that CNT and PEDOT:PSS outperform conventional materials, their integration in a standard microfabrication process is not trivial. The growth of CNTs on Si wafers is not uniform and often based on non-CMOS-compatible catalysts. Moreover, its intrinsic 3D nature makes the use of standard lithography almost impossible. On the other hand, PEDOT:PSS is not compatible with standard lithography since the electrical properties are altered by developers and standard etching and cleaning processes [29]. This issue limits the use of PEDOT:PSS to local electrochemical deposition. This process reduces deposition throughput and yield as PEDOT:PSS needs to be deposited on each electrode sequentially. Nevertheless, this issue has not discouraged MEA suppliers to provide proof-of-concepts and prototypes with CNT and PEDOT:PSS electrodes [27], as the highly competitive market requires companies to constantly innovate.

This chapter reports on the work done to improve the electrochemical performance of the Cytostretch electrodes by using CNTs and PEDOT:PSS. By integrating CNT and PEDOT:PSS in the Cytostretch MEA, the aim was to reduce the impedance of the electrodes, but also promoting the convergence between MEA and OOC devices. Cytostretch is in fact the only OOC platform able to provide MEA monitoring and could potentially be the device that brings these two fields together. However, to achieve this goal, researchers and users need OOC equipment with high performance MEAs. For this reason, the integration of CNTs and PEDOT:PSS in OOC can be considered as an essential step towards their commercialization.

For both CNT and PEDOT:PSS, a new fabrication process was developed. Extensive characterization was performed to prove that the two materials are indeed providing

better electrochemical performance and to assess the quality of the two materials. In this work, the focus was on the integration of these materials rather than material optimization.

5.2. CNT

CNTs are an allotrope form of Carbon (C): the structure of a single CNT can be seen as a graphene layers rolled up forming an allow tube. Graphene consists of a monoatomic layer composed by sp^2 hybridized C atoms displaced in an hexagonal net. A CNT can be either composed by a single layer of graphene (single walled CNT), or more concentric layers (multi walled CNT). A microelectrode can be coated by synthesizing CNTs directly on top of it, creating a conductive forest-like structure composed of thousand of these allow tubes [30].

Previous work [31] has shown how CNT coatings and their forest-like structure can drastically improve the SNR of the recorded cell potentials. Unlike flat electrodes, the contact area between the electrolyte and the electrodes (electrochemical surface area - ESA) of CNTs is higher than the area of the electrode itself (geometric surface area - GSA), as shown in Figure 5.2. Consequently, CNT coatings provides large ESA, increasing the C_{dl} of the electrodes and decreasing its electrochemical impedance. Furthermore, CNTs provide additional advantages such as high mechanical and electrical stability, good electrical conductance, and stable cell-electrode coupling [32, 33].

However, CNTs cannot be easily grown on surfaces made of common biocompatible polymers like PDMS etc., due to the high thermal budget required for their synthetization. For this reason, previously presented CNT MEAs are usually fabricated on rigid supports, e.g. Si wafers. Consequently, CNT MEAs cannot be employed in applications like Organ-on-Chip devices [26, 34], where the MEA needs to be integrated on a stretchable or a flexible surface.

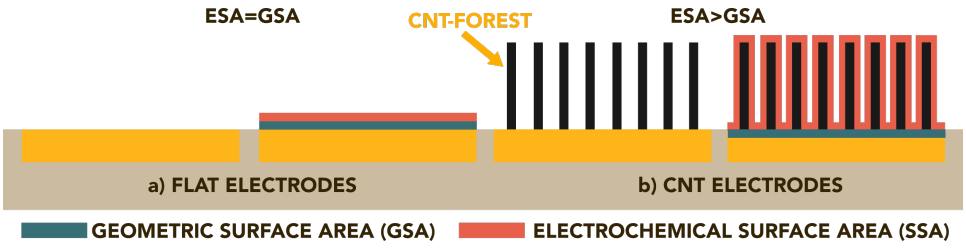

Figure 5.2: (a) Flat electrode with a geometric surface area (GSA) equal to the electrochemical surface area (ESA). (b) The forest-like structure of CNTs guarantees a large contact surface between the electrolyte and the electrode (ESA>GSA). The figures are not drawn to scale.

This problem has been overcome by first growing and patterning the CNT electrodes on a rigid Si substrate, and then transferring them onto the flexible/stretchable polymer film, followed by a partial isolation with a second polymer film [34]. However, this process contains intensive manual procedures that may drastically reduce the device yield.

To overcome this, we developed a novel fabrication process to include CNT MEAs in the Cytostretch technology, which does not require manual assembly and sample handling. Like in [34], the polymer membrane is deposited after CNT growth, however, in our case the electrodes are released by etching the support Si wafer from the backside rather than peeling-off the membrane. In order to be able to focus on the fabrication of this upside-down MEA itself, without the additional complications of a stretchable membrane, the fabrication and the characterization of a prototype upside-down CNT MEA was demonstrated on a rigid membrane.

5.2.1. FABRICATION

Besides the upside-down CNT MEA, two other reference MEAs were fabricated (a reference TiN MEA and a reference CNT MEA). In all cases the devices were fabricated starting with polished 4-inch monocrystalline Si wafers with a thickness of 525 µm thickness.

UPSIDE-DOWN CNT MEA

The upside-down CNT MEA consists of a 12 µm thick membrane provided with CNT based electrodes. The electrodes are connected to aluminum (Al) interconnects embedded in the membrane. The process starts by growing 2 µm of thermal oxide (SiO_2). Next, a layer stack consisting of 5 nm of titanium (Ti), 50 nm of TiN and 100 nm of Ti is sputter deposited. The purpose of the Ti bottom layer is to improve the adhesion between the TiN and the SiO_2, while the TiN layer acts as support layer for the CNT growth.

On top of the Ti/TiN/Ti stack a 1 µm thick layer of Tetraethyl Orthosilicate (TEOS) is deposited. The PECVD TEOS layer is patterned using reactive ion etching (RIE) to define an array of holes with a depth of 1 µm and a diameter of 12 µm, landing on the Ti/TiN/Ti disks. The top Ti layer prevents the fluorine-chemistry plasma, used to etch the TEOS layer, from entering in contact with the TiN support layer and affecting CNT alignment [35]. The 100 nm Ti layer is subsequently removed by soaking the wafer in a 1% Hydrofluoric acid (HF) solution.

Next, a 5 nm thick layer of Cobalt (Co) is evaporated and patterned using lift-off to be used as catalyst for CNT growth in the cavities (Figure 5.3a). The enclosed CNTs are grown by low-pressure chemical vapor deposition (LPCVD) at 500 °C for 38 seconds reaching an height of 1 µm (Figure 5.3b). The growth temperature is chosen to promote vertical CNT growth as well as to preserve CMOS compatibility. The resulting CNTs have

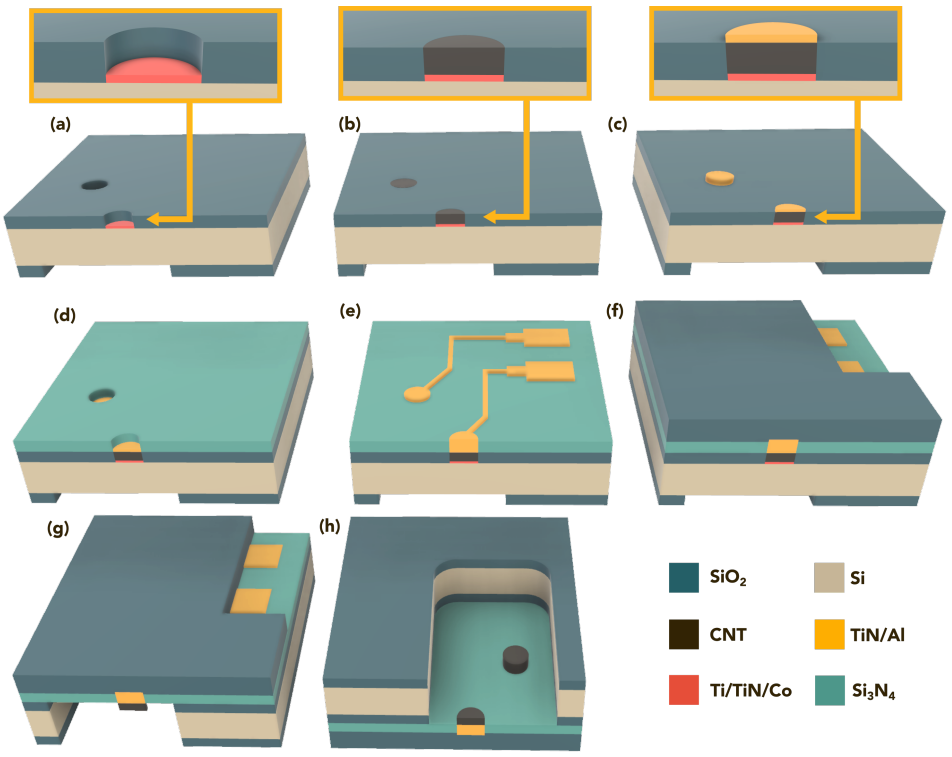

Figure 5.3: Process flow for the fabrication of upside-down CNT MEA: (a) hole array patterning; (b) CNT growth and electrode definition; (c) lids fabrication; (d,e,f) membrane definition; (g,h) membrane releasing. The figures are not drawn to scale.

a bamboo-like structure in contrast to the more fluffy structure obtain at lower temperature. More details can be found in the CNTs characterization section (Section 5.2.2). After growing the CNTs, the CNT tips are sealed with a 100 nm TiN and 1 µm Al layer (Figure 5.3c).

The last process sequence is the fabrication of the membrane that embeds the metal lines connecting the CNT electrodes to the contact pads (Figure 5.3e). This membrane can be either a PDMS-based stretchable membrane [26], or a rigid membrane consisting of a stack of 2 µm plasma-enhanced CVD (PECVD) silicon nitride (Si_3N_4), and 10 µm thick layer of PECVD SiO_2 (Figure 5.3d-f). The membrane release process starts by etching the wafer from the backside using DRIE and landing on the etch stop layer, and ends by etching the SiO_2 etch-stop layer in BHF (Figure 5.3g,h). The TiN disks embedded in the SiO_2 are automatically removed during BHF etching and subsequent DI rinsing. The fabrication process of the upside-down CNT MEA is summarized in Appendix A.3.

REFERENCE MEAS

The fabrication of the reference MEA device starts by growing 2 µm of thermal SiO_2. Metal lines, contact pads and electrodes are fabricated by deposition and patterning of 100 nm of TiN, 500 nm of Ti and 50 nm of TiN. The metal lines are isolated with a 1 µm thick TEOS layer, which is subsequently dry etched to open the electrodes and contact pads. This is the last process step of the reference TiN electrodes. The fabrication of the reference CNT MEA continues with the evaporation and patterning of 5 nm of Co and by growing the CNTs under the same condition as the upside-down CNTs. The fabrication process of the reference MEAs is summarized in Appendix A.4.

5.2.2. CHARACTERIZATION PROCEDURE

The combination of the barrier and catalyst layers is an essential requirement for the growth of vertically aligned carbon nanotubes using LPCVD. The CNT morphology and quality crucially depends on the composition of these two layers. Although different barrier materials and catalyst nanoparticles have been reported in literature [36, 37], one of the aims of this work was to maintain CMOS compatibility to allow for wafer-scale integration and transfer of the process to standard foundries. These led us to combine TiN and Co nanoparticles as barrier and catalyst layers, respectively. In particular, Co guarantees CMOS compatibility because it does not result in deep-level traps and additionally because of the lower diffusion coefficient compared to copper and iron.

As mentioned earlier, the CNTs were grown with LPCVD in a commercially available deposition system (AIXTRON Blackmagic). After loading the wafer in the reactor, the entire system is pumped down to < 0.1 mbar. 700 sccm of hydrogen (H_2) are then injected into the reactor, while the temperature and pressure are ramped to 500 °C and 80 mbar, respectively. This step is followed by a three minutes anneal to stabilize the chamber to the required deposition temperature. Next 50 sccm of acetylene (C_2H_2) are added and the CNTs are synthesized on top of the catalyst particles. A more detailed description of the CNT deposition process can be found in [30].

CNT QUALITY AND MORPHOLOGY

The morphology and quality of CNT dense arrays are strongly dependent on the deposition temperature. Four different temperatures have been investigated: 350, 400, 500 and 650 °C.

A temperature of 350 °C is extremely low for CNT growth by CVD but very attractive from a standpoint of CMOS compatibility. In fact, the low activation energy of the Co catalyst (0.4-0.43 eV) allows for a low temperature process while achieving a sufficiently high growth rate [30]. To determine the dependence of the growth rate on the process

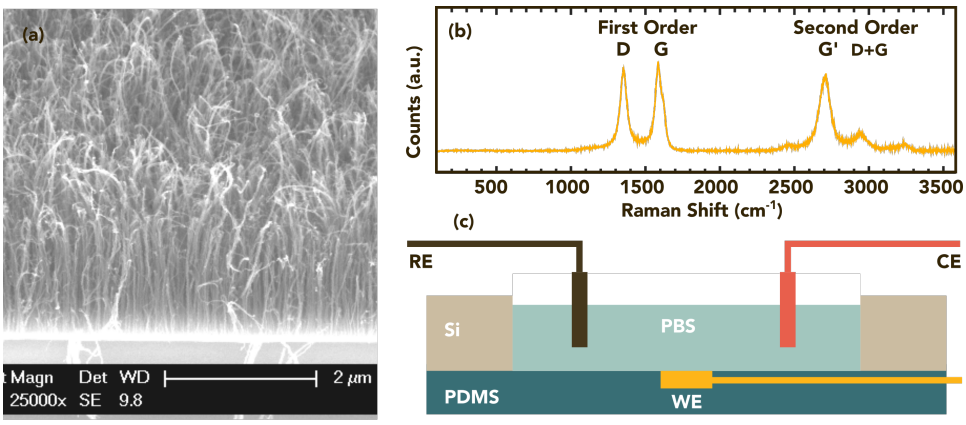

Figure 5.4: (a) SEM image of 1 µm high CNTs grown at 650 °C. (b) Raman spectrum of 1 µm high CNTs grown at 650 °C, showing the two regions and the characteristic peaks. (c) Schematic of a three-electrodes setup.

temperature, a sequence of time-progressive images was taken at different deposition times and analyzed by SEM. Figure 5.4a shows the SEM images of 1 µm-high CNT forests grown at 650 °C.

To determine whether the Co nanoparticles are lifted up (tip-growth mechanism) or pinned down (root-growth mechanism), a double temperature growth test has been performed [38]. The first step consisted of 2 minutes CNT growth at 500 °C; then the second step was performed by increasing the reactor temperature to 600 °C at which temperature the CNTs were grown for 2 minutes.

A widely used technique to assess CNT quality is Raman spectroscopy. This is a vibrational spectroscopy based on inelastic scattering of a monochromatic laser. The light, interacting with molecular vibrations, is shifted in frequency; these phenomena can be studied by analysing the spectrum of the signal after interfacing with the sample. Intensity and full width at half maximum (FWHM) of the peaks in the spectrum can be analyzed to assess CNT crystallinity.

As can be seen in Figure 5.4b, two regions can be identified in CNT Raman spectra: first order and second order region. In the first order region two strong bands can be found: D band around 1350 cm^{-1} and G band around 1582 cm^{-1}. The first originates from defect vibrations; the second one originates from the stretching modes in the graphite plane. The third feature of the first order region is called D' and is also disorder generated; this is weaker than the other two and can be found as a shoulder of G. In the second-order region only one sharp band, called G' band, can be found. This

is placed around 2700 cm^{-1} and is generated by two inelastic phonon scattering processes.

Absolute and relative amplitudes (I) and bandwidths of these peaks provide information about CNT crystallinity. CNTs grown at higher temperature present higher crystallinity: this change in CNT quality can be verified by studying the variations in Raman spectrum (peaks and bandwidths) at different temperatures. $I_{D/G}$, $I_{D'/IG'}$ and $I_{G'/G}$ are commonly used to assess CNT quality. I_D and I'_D are influenced by the disorder in CNT crystal: as a consequence, $I_{D/G}$ and $I_{D'/IG'}$ decrease for increasing crystallinity. $I_{G'/IG}$ ratio increases for increasing quality. Last but not least, also the FWHM can be used to assess sample quality: wider bands correspond in fact to lower-quality CNTs.

The spectral response of all samples, with a spectra coverage of 3550 cm^{-1}, was recorded with a Renishaw inVia Raman spectroscope with 514 nm laser wavelength. For each sample three Raman spectra were acquired.

BIOCOMPATIBILITY ASSESSMENT

The biocompatibility of the cobalt-grown CNTs was tested by plating human pluripotent stem cell derived cardiomyocytes on top of the CNT forests. Co-grown CNT samples were sterilized in ethanol and then coated with Matrigel (Invitrogen) to induce cell attachment. Next, the cells were plated and cultured on the CNT samples for 3 days in a CO_2 incubator at 37 °C. The cells were then fixed using 2% paraformaldehyde for 30 minutes and stained with an anti-alpha-actinin antibody and 4,6-diamidino-2-phenylindole (DAPI) to reveal the sarcomeric structures and cell nuclei, respectively.

ELECTROCHEMICAL CHARACTERIZATION

The electrochemical performance of all MEAs was studied by EIS in a phosphate buffered saline (PBS) solution. In order to perform EIS on both the reference electrodes and the upside-down devices, plastic cylinders were glued to the surface of the device. These cylinders were used to contain the PBS solution during electrochemical characterization, and to guarantee complete isolation of the solution from the bondpads of the device. The EIS measurements were performed with a potentiostat and a three-electrode setup (shown in Figure 5.4c). A silver/silver chloride (Ag/AgCl) electrode electrode (supplied by EDAQ) and a Pt strip were used as reference (RE) and counter electrode (CE), respectively. The potentiostat accurately produces an excitation voltage (potential difference) between one of the Cytostretch microelectrodes (working electrode - WE) and the RE. The potential difference is set up by adjusting the current from the WE to the CE until the desired potential value is reached. This current is measured by the potentiostat to determine the impedance of the working electrode. The EIS tests were per-

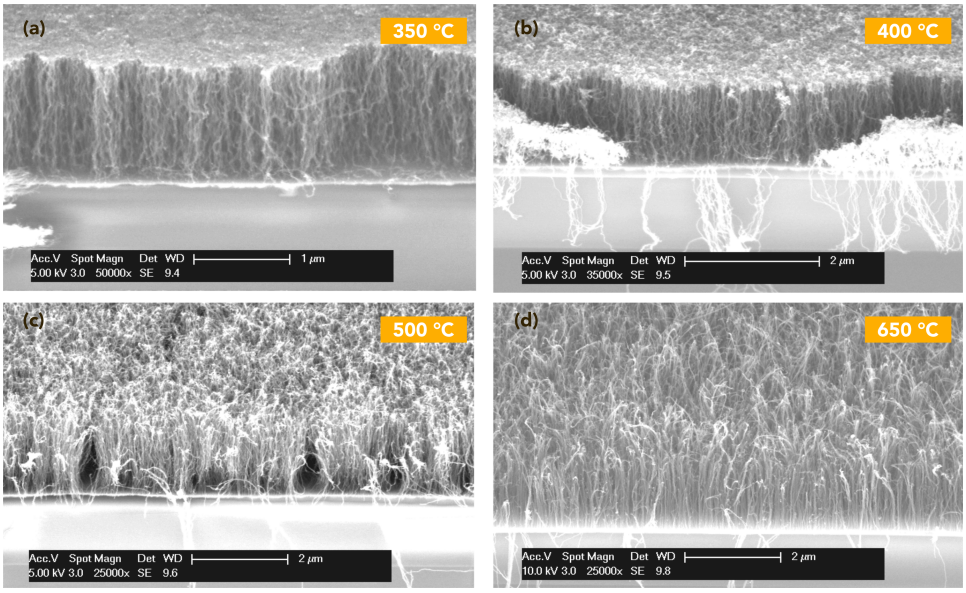

Figure 5.5: CNT forests (1 µm high) grown at (a) 350, (b) 400, (c) 500 and (d) 650 °C. Scale bars: (a) 1 and (b,c,d) 2 µm.

formed with an Autohom Metrolab potentiostat with FRA2 module. In correspondence to previous studies [26], the EIS measurements were performed in the frequency range of 0.01 Hz - 10 kHz, with an amplitude of 20 mV (RMS). The output current signal has been checked during measurements to detect eventual non-linearities caused by high-amplitude stimulation.

5.2.3. Results and Discussion

CNT quality assessment and biocompatibility

CNT growth rates of 0.285, 1.977, 30.83, 163 nm/sec for 350 °C, 400, 500 and 650 °C, respectively, were achieved. Figure 5.5 shows the SEM images of a 1 µm long CNTs grown at different temperatures. The height of these forests is similar to the CNTs in the final upside-down MEA. A careful inspection of the obtained morphologies indicates that CNTs grown at 650 °C show a better alignment compared to the ones synthesized at lower temperatures. However, higher growth temperatures result in less uniformity in height across the CNT forest. CNTs grown at 350 and 400 °C showed a similar morphology.

Figure 5.6 shows the results obtained from the double temperature growth test. As highlighted by the red dotted line, CNTs grown at two different temperature present two

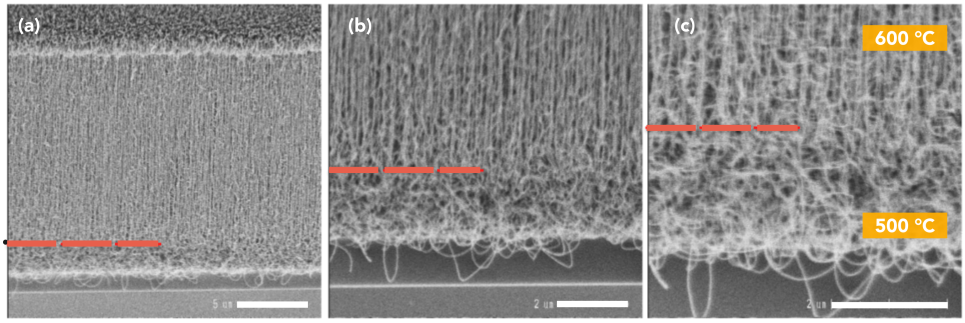

Figure 5.6: SEM images of CNTs synthesized at a two growth temperatures (2' at 500 °C and 2' 600 °C). The top segment of the CNT forest, grown at 600 °C, is well aligned as opposed to the bottom one, grown at a lower temperature (500 °C), showing that the employed catalyst/support combination results in a tip-growth process. Scale bars: (a) 5 µm, (b) 2 µm and (c) 2 µm.

distinct phases: the top segment of the CNT forest, grown at 600 °C, is well aligned as opposed to the bottom one, grown at a lower temperature (500 °C). In contrast to what is claimed in [30], these results demonstrate that the employed catalyst/support combination results in a tip-growth process. This is probably due to a weak interaction between TiN surface and Co particles. Moreover, the tip-growth mechanism implies that Co nanoparticles are enclosed in the TiN/Al during the metallization step described in Figure 5.3c.

Figure 5.7a shows the first and second order bands of the Raman spectrum obtained from CNT forests grown at different temperatures. The spectrum deconvolution was made with a combination of eight Lorentzian and two Gaussian distributions [30]. The obtained ratio between the amplitudes of the D and G peaks ($I_{D/G}$) is equal to 1.11, 1.14, 1.27 and 1.02 for the CNTs grown at 350, 400, 500 and 650 °C, respectively. The $I_{D/G}$ ratio of the CNTs grown at 350 °C reveals a crystallinity degree comparable to the ones reported in other works [32], in which the CNT growth temperature was even higher.

With respect to CNT biocompatibility, after three days the stem cell derived cardiomyocytes plated on the CNT electrodes were beating spontaneously, demonstrating their viability and functionality. In Figure 5.7b a fluorescent image of the cells on the CNTs is shown. The cells exhibit the characteristic striated sarcomeric structures found in functional cardiomyocytes. This demonstrates the short term biocompatibility of CNTs for culturing stem cell derived cardiomyocytes.

FABRICATION

Figure 5.8 shows scanning electron microscopy (SEM) images of all three types MEAs. The BHF etching, performed as the last fabrication step in the upside-down CNT MEA,

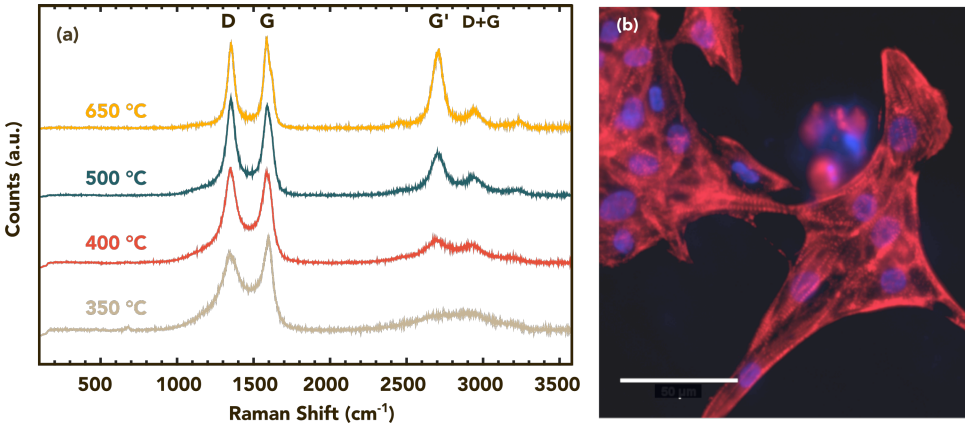

Figure 5.7: (a) Raman spectra of CNTs grown on 5 nm Co at four different growth temperatures. To obtain insights about CNT properties like purity and structural quality, the ($I_{D/G}$) ratio is calculated. The ($I_{D/G}$) ratio decreases as the CNT growth temperature increases. (b) Merged fluorescent images of fixed human stem cells derived cardiomyocytes plated in on top of CNTs for 3 days: nucleus are stained in blue (stain: DAPI) and alpha-actinin in red (stain: CY3). Scale bar: (b) 50 µm.

causes a buckling phenomenon in the CNT arrays. Consequently, the ESA of the CNT array is reduced, increasing the impedance.

ELECTROCHEMICAL CHARACTERIZATION

The EIS spectrum of a representative electrode of the upside-down CNT MEA is shown in Figure 5.9 a,b. The impedance amplitude and phase over the investigated frequency range are compared to the reference TiN electrode. In particular, at 1 kHz the upside-down CNT electrode shows a marked impedance reduction of one order of magnitude compared to a flat TiN electrode: 230 ± 13 kΩ and 2.1 ± 0.08 MΩ, respectively (Figure 5.9). However, the previously observed CNT buckling phenomenon severely increases the upside-down CNT MEA impedance. This is shown by the fact that the reference CNT

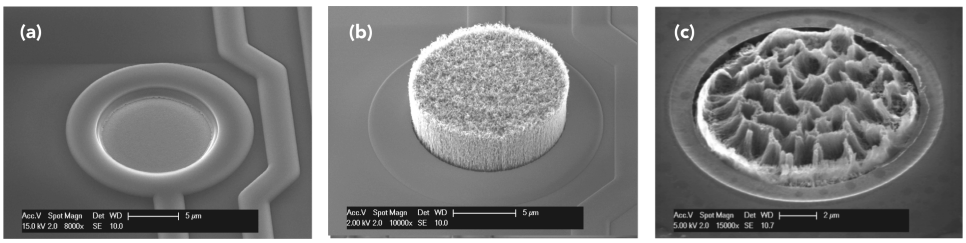

Figure 5.8: SEM pictures of the fabricated electrodes: (a) reference TiN electrode, (b) reference CNT electrode (not affected by CNT buckling) and (c) upside-down CNT electrode (showing severe CNT buckling due to BHF etching). Scale bars: (a) 5 µm, (b) 5 µm and (c) 2 µm.

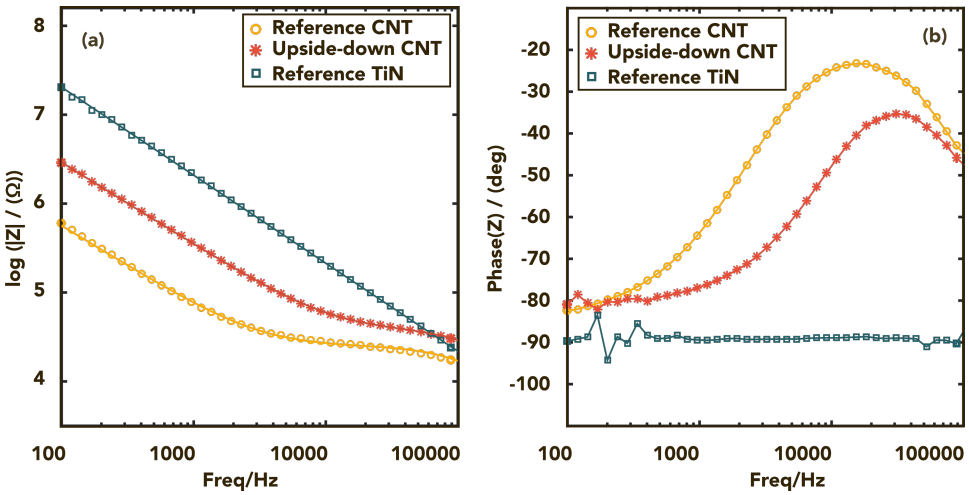

Figure 5.9: (a,b) Bode plot ((a) amplitude and (b) phase) of impedance spectra of a reference CNT electrode (not a affected by CNT buckling), an upside-down CNT electrode and a reference TiN electrode (diameter: 12 µm). The average EIS at 1 kHz are equal to 2.1 MΩ, 230.5 kΩ and 83.4 kΩ for reference CNT, upside-down CNT and reference TiN, respectively.

electrodes, which are not affected by buckling, have a significantly lower impedance then the upside-down MEAs. At 1 kHz the reference CNT electrodes have an impedance as low as 83.4 ± 5 kΩ. The measured TiN electrodes showed a constant phase behaviour over the investigated frequency range indicating a smooth electrode surface [15].

The correlation between CNT buckling and the resulting impedance increase has been further studied by inducing the phenomenon on a CNT reference electrode. The reference CNT MEA was covered with isopropyl alcohol (IPA) for 5 minutes and then rinsed with PBS 3 times. Figure 5.10 shows a SEM image of a CNT forest before (a) and after (b) IPA treatment. As shown, IPA causes the same buckling effect as induced by BHF. In particular, the impedance amplitude of the CNT electrodes increased from 83.4 kΩ up to 367 ± 51 kΩ at 1 kHz after IPA treatment, demonstrating that CNT buckling severely affects the electrochemical performance of CNT electrodes. Therefore, to overcome this limitation it is necessary to prevent or reduce the CNT buckling. A valuable option is to make use of HF vapor etching for the CNT electrode release instead of conventional BHF etching.

The reported impedance values were recorded 30 minutes after immersion in the PBS solution. In fact, during reference CNT MEA characterization a remarkable drop in impedance is observed as time passes, from 160 kΩ right after the PBS immersion, to 83.4 kΩ after 30 minutes. This decrease is related to the wettability transition phenomenon occurring in the CNT forest, called Cassie-Baxter to Wenzel transition [39].

To verify if a wettability transition occurs in the CNT forest, the hydrophobicity of the Co-grown CNTs was monitored. Data was collected by measuring the contact angle and the contact area of a water droplet on top of the CNT forest as a function of time. As shown in Figure 5.10c-e, during water evaporation the contact line remains pinned while the contact angle decreases, proving that the water is penetrating into the CNT forest voids [39]. By taking advantage of this phenomenon, it is possible to reduce the electrochemical impedance of a MEA without any plasma treatment, known to deteriorate CNT conductivity. In fact, the obtained impedance value is of the same order of magnitude as compared to a similar CNT MEA subjected to plasma treatment [31].

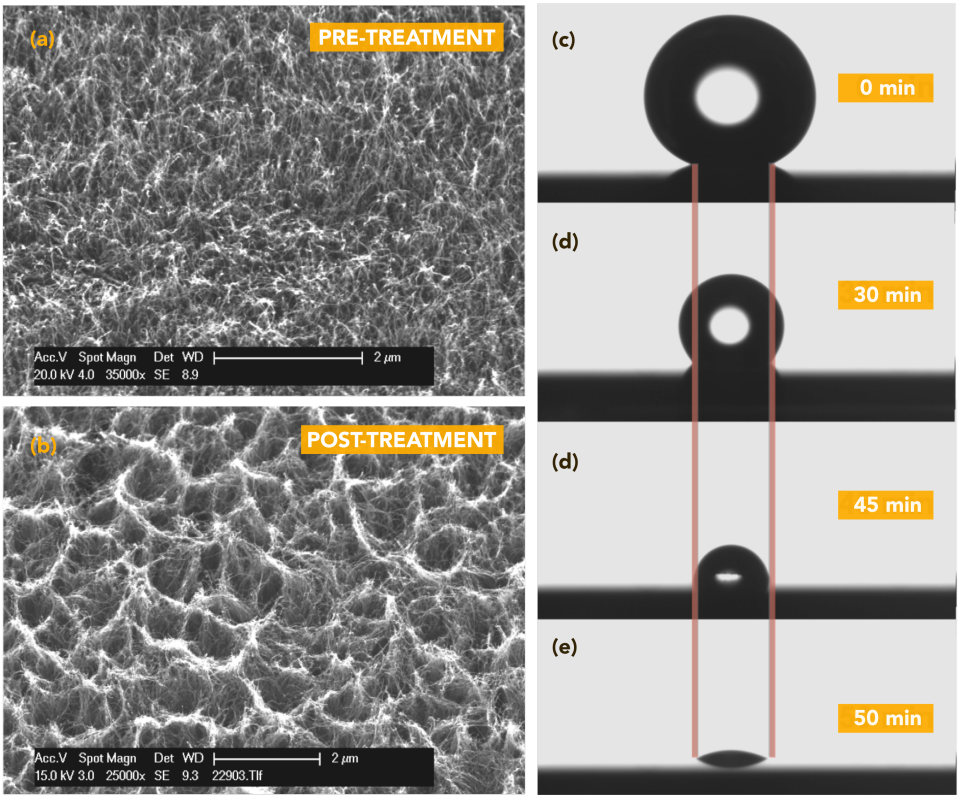

Figure 5.10: Effect of IPA on 1 µm high CNT forest: sample SEM (a) before and (b) after IPA treatment. (c-e) Evaporation process of a 7 µL drop of water deposited on top of a CNT forest. The contact area between water and CNTs remains pinned, as indicated by the two vertical lines, while the contact angle is reduced strongly (decreasing from 150 °, measured at the initial time, to 25 ° after 50 minutes).

5.2.4. CONCLUSIONS

A novel fabrication process has been presented to embedded CNT MEA on the backside of the Cytostretch membrane. In contrast to previously reported fabrication schemes, the newly presented procedure completely avoids manual assembly such as membrane peeling and alignment, and thereby increases device reliability and yield, while at the same time it opens the way towards high-volume production. The fully automated procedure has been tested by fabricating the upside-down CNT MEA on a Si_3N_4 membrane.

By using EIS, the impedance response of different MEAs was measured. The increase of the electrode surface area with CNTs resulted in an impedance reduction of 96% at 1 kHz, compared to reference TiN electrodes. Moreover, the morphology and quality of CNT forests grown at different process temperature were investigated. It can be concluded that CNTs grown at 500 °C represent the best compromise between quality, packing density, surface to volume ratio and thermal budget. Moreover, the possibility to lower the temperature to 350 °C to make the entire process more CMOS compatible is still a valuable option. Finally, the biocompatibility of the CNT electrodes was assessed by plating human pluripotent stem cell-derived cardiomyocytes. The upside-down CNT fabrication method presented in this paper is a first step towards the high-volume production of stretchable CTN MEA devices with low impedance electrodes.

5.3. PEDOT:PSS

As mentioned in Section 5.1.1, also Poly(3,4-ethylenedioxythiophene) polystyrene sulfonate (PEDOT:PSS) can be used to obtain a low-impedance MEA [15]. This conductive organic polymer guarantees a sufficiently low noise-to-signal ratio for the detection of cellular action potentials [15], a crucial requirement for several applications such as cardiotoxicity studies.

Beside providing low-impedance, PEDOT:PSS is considered extremely promising for the OOC field [15, 40] since it is known for its biocompatibility and long-term stability in a biological environment [41, 42]. The use of PEDOT:PSS also allows for the integration of new sensors in OOC devices as PEDOT:PSS electrodes have previously proved to be useful for *in vitro* pH [43], humidity [44] and DNA [45] measurements, and to characterize the electrostatic interaction between the cells and the PEDOT:PSS surface [46]. This could provide an efficient way to monitor multiple parameters, such as cells oxygen consumption of tissues, in OOC devices.

In order to integrate the PEDOT:PSS electrodes in the Cytostretch device, the fabrication process was improved by covering the TiN electrodes with a Pt layer to allow the *in situ* electrochemical deposition of PEDOT:PSS [47]. The Pt electrodes were then

coated with PEDOT:PSS and fully characterized with SEM, Raman spectroscopy, EIS and cyclic voltammetry (CV) to confirm the correct PEDOT:PSS deposition and quantify the corresponding electrochemical impedance improvement. The deposition parameters of the PEDOT:PSS were then tuned to optimize the impedance of the electrode.

5.3.1. FABRICATION

The fabrication of the Cytostretch device equipped with the low-impedance PEDOT:PSS MEA, can be divided in two steps. First, starting from the Cytostretch platform, an Heart-on-Chip with Pt MEA is fabricated. In order to fabricate this device, the process previously presented in Section 3.2.3 was modified to coat the TiN electrodes with a Pt layer. Secondly, the PEDOT:PSS is deposited directly on top of the Pt electrodes by electrochemical polymerization.

PLATINUM MEA

The wafer-scale fabrication of the new Heart-on-Chip device with the Pt-coated MEA is illustrated in Figure 5.11. The process starts with the deposition of 2 and 6 µm of SiO_2 by plasma-enhanced chemical vapor deposition (PECVD) on the front and backside of a 4" wafer, respectively. The SiO_2 layer on the backside is patterned by dry-etching to define the membrane area. The process continues by sputtering a 1.5 µm-thick Al layer on the front side of the wafer. The Al is then patterned by dry-etching to define the contact pads (Figure 5.11a).

Next, a 100 nm-thick Pt layer, preceded by a 20 nm Ti adhesion layer, is evaporated onto the wafer and patterned by lift-off to form the electrodes of the MEA (Figure 5.11b). In the next step, the interconnects extending from the contact pads to the MEA are fabricated. For this, a 700 nm thick photosensitive polyimide (PI) (Fujifilm LTC 9305) layer is deposited by spin coating, patterned and cured at 350 °C for 1 hour in atmospheric-pressure nitrogen (N_2) atmosphere (Figure 5.11c). Subsequently, a 200 nm thick layer of TiN, preceded by a 10 nm Ti adhesion layer, is sputtered on the front side of the wafer at room temperature, and patterned by dry etching (Figure 5.11d). A second layer of 800 nm-thick PI is spin coated and patterned to provide electrical insulation for the metal lines (Figure 5.11e). An oxygen plasma treatment (Tepla Plasma 3000 - Power: 600 W - Pressure: 250 ml/min - Time: 1 min) is first performed to promote the adhesion between the two PI layers as presented in Chapter 4 [48]. Subsequently, a Polydimethylsiloxane (PDMS) layer is deposited by spin coating on the front side of the wafer, at a spin speed of 6000 RPM for 30 seconds and cured for 30 min at 90 °C, resulting in a layer thickness of 10 µm. The adhesion of the PDMS to the PI was improved by performing an argon plasma treatment (Trikon Sigma 204 - Power 120 W - Pressure: 40 sccm - Time: 15 sec),

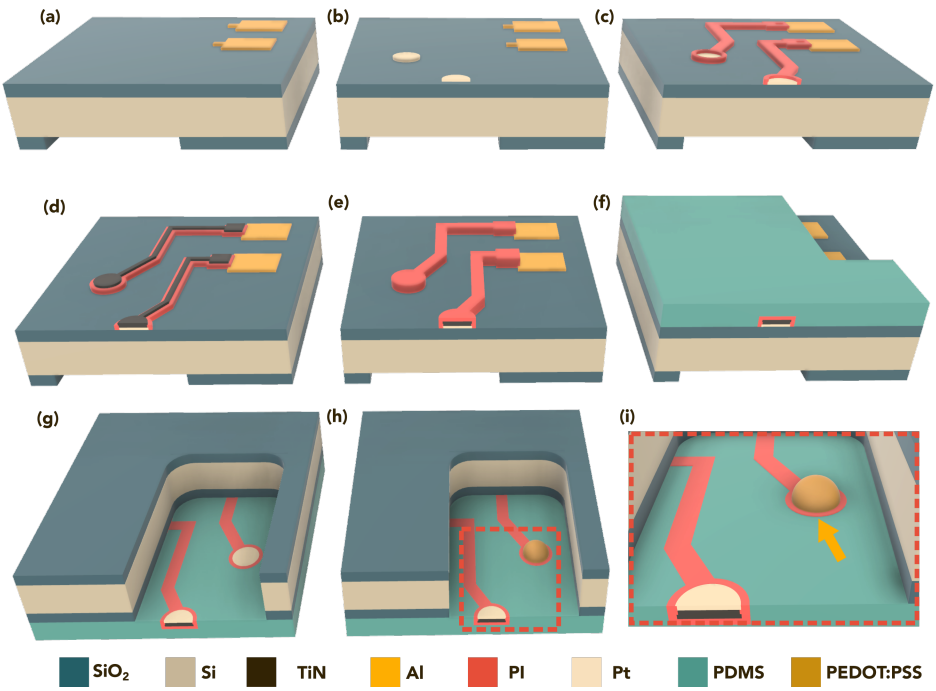

Figure 5.11: Process flow for the fabrication of the Heart-on-Chip with PEDOT:PSS MEA: (a) contact pads and Pt electrodes are fabricated on top of a 2 µm SiO_2 layer. A 5 µm-thick SiO_2 layer is deposited and patterned on the backside of the wafer. (b) The Pt electrodes are fabricated. (c) A 1 µm layer of polyimide (PI) is deposited and patterned. (d) The 200 nm thick titanium nitride (TiN) metal lines are fabricated. (e) The second layer of PI is deposited and patterned to isolate the metal lines. (f) A Polydimethylsiloxane (PDMS) layer is deposited and patterned to access the contact pads. (g) The PDMS membrane is released by etching the Si from underneath the PDMS layer making the electrodes accessible. (h,i) PEDOT:PSS is deposited on the Pt electrodes via electrochemical polymerization. The figures are not drawn to scale.

as previously reported Chapter 4. The contact pads are then opened by patterning the PDMS layer by means of RIE using an Al layer as hard etch mask (Figure 5.11f). Finally, the membrane is released by removing the Si and the SiO_2 layers from underneath the membrane by means of DRIE and BHF, respectively (Figure 5.11g). The fabrication process of the Pt MEA is summarized in Appendix A.5.

The Pt MEA was packaged following the procedure presented in details in Chapter 6. The procedure starts by dicing the 4-inch wafer with an automatic dicing saw. More than 100 Cytostretch chips can be obtained from each 4-inch wafer. Four chips are mounted on a printed-circuit board (PCB) with a fully-automatic pick-and-place system. The PCB is designed to fit into a MCS *in vitro* recording devices (MEA2100-System). The Al contact pads on the chip are subsequently wire-bonded to the PCB. The packaging is then finished by mounting a glass cylinder on top of each die on the PCB with epoxy glue

(EPO-TEK 353ND-T) cured at 75 °C for 90 minutes in a nitrogen ambient at atmospheric pressure. This glass cylinder creates an open well structure on top of each chip, where the cells can be seeded. The PDMS membrane can then be stretched by connecting the PCB to an external system that applies pneumatic pressure to the backside of the device.

This well will be used as the electrochemical cell for the PEDOT:PSS deposition on top of the Pt electrodes embedded in the stretchable membrane of the Cytostretch. The well can be also directly molded on top of the chips by an automated and monolithic molding technique presented in [49] and Chapter 7.

PEDOT:PSS MEA

The next step is to cover the Pt electrodes of the Cytostretch MEA with a PEDOT:PSS layer (Figure 5.11g). The *in situ* deposition of PEDOT:PSS coating was performed from an aqueous solution containing a mixture of 0.001 M of EDOT monomers, 0.1 M of Sodium Poly(Styrene Sulfonate) (NaPSS, Mw: 70.000) as the dopant material as well as a surfactant, and 0.005 M of Tetrabutylammonium Tetrafluoroborate (TBABF4) as secondary doping to increase the conductivity of the solution. The electrochemical procedures were performed with an Autolab Potentiostat (Metrohm), with a Pt strip and a miniaturized Ag/AgCl reference electrode (supplied by EDAQ) as the counter and reference electrodes, respectively. The CV deposition method with a three electrodes cell setup (Figure 5.4), was utilized to increase the deposition rate by exploiting the capacitive current. In this procedure, the voltage on the working electrode is scanned over a 0.2 - 1.3 V (vs. Ag/AgCl reference electrode) range with a scan rate of 0.5 V/s. The amount of charge delivered during the deposition is 3 µC.

After each deposition, the MEA was drained of the remaining solution and rinsed with DI water. After rinsing, vacuum drying was performed at room temperature for 30 minutes to remove all liquid residues.

5.3.2. Characterization procedure

PEDOT:PSS deposition

The deposition of the PEDOT:PSS was verified by comparing the SEM images of the electrodes before and after the electrochemical deposition and by performing Raman spectroscopy on the electrodes. This analysis was performed with a Renishaw inVia Raman Spectroscope, with 488 nm wavelength and 300 to 1900 cm^{-1} spectrum coverage.

The electrical performance of the MEA is investigated by means of EIS to determine the impedance of the electrodes over a certain frequency range, and CV measurements to estimate the amount of charge that can be delivered within a certain voltage scan.

ELECTROCHEMICAL CHARACTERIZATION

The improvement provided by the PEDOT:PSS was measured by characterizing the electrodes before and after the electrochemical deposition of the polymer.

All of the electrochemical characterization procedures were done with a three electrodes set-up in PBS medium (by Sigma Aldrich), similar to the one presented in Section 5.2.2. The electrochemical characterization, i.e. EIS and CV measurements, was performed in a single run for each microelectrode type without changing the PBS medium.

In correspondence to similar studies [15], the EIS measurements in this study were performed in the frequency range of 0.01 Hz - 10 kHz, with an amplitude of 50 mV (RMS). The output current signal has been checked during measurements to detect eventual non-linearities caused by high-amplitude stimulation. The CV measurements were performed over a voltage range of -0.6 V to 0.8 V, which also corresponds to the electrochemical window of water [50]. The starting potential was 0 V, with a scan rate of 0.5 V/s (forward scan first). Each CV measurement consisted of 5 repetitive scans.

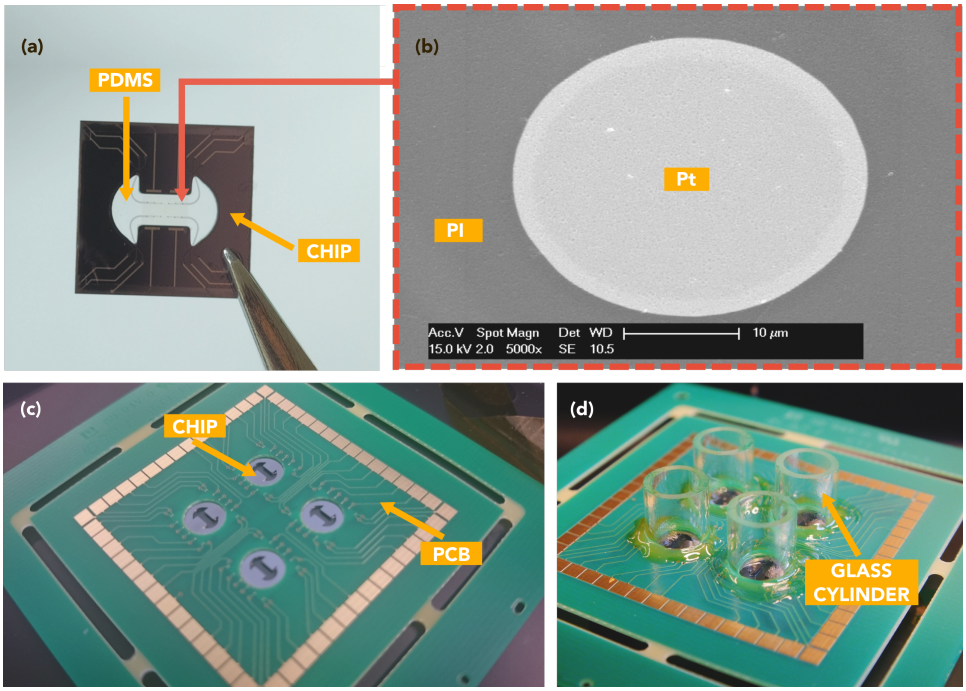

Figure 5.12: (a) Optical image of one Cytostretch chips including the Pt MEA embedded in a stretchable PDMS membrane. The chip includes 12 Pt circular electrodes (diameter: 30 µm). b) SEM image of Pt MEA. (c,d) Optical image of the multi-well plate consisting of four Cytostretch chips mounted on a PCB before (c) and after (d) attaching the glass cylinders on the chips.

5.3.3. RESULTS AND DISCUSSIONS

FABRICATION

Figure 5.12a shows a successfully fabricated OOC device with Pt electrodes before being mounted on the PCB. The SEM image (top view) of one of the Pt electrodes (with a diameter of 30 µm) embedded in the stretchable membrane is shown in Figure 5.12b. The Ti layer in between the TiN and the Pt layers successfully promoted the adhesion, since none of the fabricated electrodes showed Pt detachment after the membranes were released, as confirmed by SEM analysis. The chips mounted and wirebonded on the PCB, and the glass cylinders glued on the PCB are shown in Figure 5.12c,d, respectively.

PEDOT:PSS DEPOSITION AND CHARACTERIZATION

The deposition of a PEDOT:PSS layer on top of the Pt electrodes was successfully achieved. The material was easily identified on the electrodes by the change of color observed on the Pt electrodes (Figure 5.13a,b) in agreement with what has been previously observed [42], and was also confirmed by SEM imaging. The SEM images of two PEDOT:PSS electrodes are shown in Figure 5.13c,d. The PEDOT:PSS was locally deposited only on the electrodes, proving that the adhesion between the two layers of PI (improved in Chapter 4), was sufficient to prevent any current leakage during the deposition. The well and the PEDOT:PSS MEA on its bottom were rinsed 5 times with PBS using a pipette. No PEDOT:PSS peeling was detected, indicating sufficient adhesion of the PEDOT:PSS to the electrodes.

The results of the Raman spectroscopy measurements on the PEDOT:PSS coated microelectrodes are shown in Figure 5.14. The Raman spectrum presents a similar trend as observed by Kayinamura et al. [47] and Lapkowski et al. [51]. The maximum peak

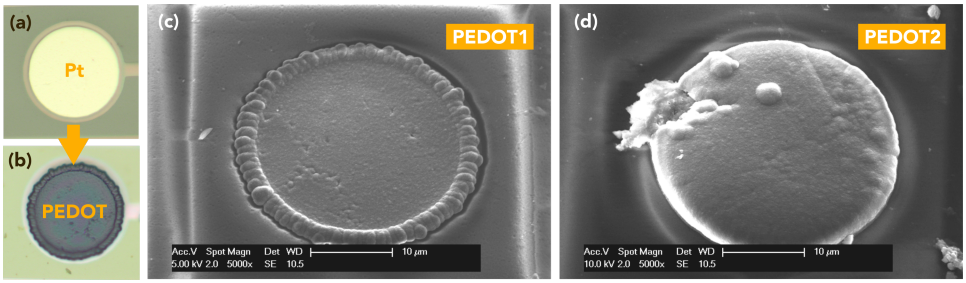

Figure 5.13: (a) Optical image of one of the electrodes embedded in a stretchable PDMS membrane before (a) and after (b) the electrochemical deposition of PEDOT:PSS. (c) SEM image of the PEDOT:PSS electrode deposited with CV deposition, scanning the voltage on the working electrode between 0.2 - 1.3 V (vs. Ag/AgCl) with a scan rate of 0.5 V/s (**PEDOT1**). (d) SEM image of the PEDOT:PSS electrode deposited with CV deposition, scanning the voltage on the working electrode between 0.2 - 1 V (vs. Ag/AgCl) with a scan rate of 0.5 V/s (**PEDOT2**). Scale bars: 10 µm.

appears at 1436 cm^{-1}, which corresponds to the symmetric vibration of C–C bonds in the oxidized polymer chain [47]. Several minor peaks around 1249 cm^{-1} are also visible, which corresponds to the bonds in the doped PEDOT:PSS polymer [51]. These results confirm the successful deposition of a PEDOT:PSS film.

During the CV deposition of the PEDOT:PSS, the charge response and current response were recorded (Figure 5.15a). Five of the CV cycles are depicted in Figure 5.15b (Cycle 01,20,40,60 and 80). As can be inferred from the current response (Figure 5.15a in blue), the deposition rate of the PEDOT:PSS was not constant during the process. In fact, the charge delivered by the electrode during the deposition shows an abrupt increase during the first cycles. This phenomenon is due to the high current peaks caused by the PEDOT:PSS oxidation [52–54] appearing between 1 and 1.3 V. This oxydation in the first deposition cycles (Cycle 01) is shown in Figure 5.15b. As previously suggested by Kayinamura et al. [47], a high deposition rate causes rapid movement of ions in the solution, which results in a less ordered polymer chain and eventually in a high impedance.

In order to avoid these current peaks while minimizing the deposition time, the potential range was narrowed down to 0.2 - 1 V (vs. Ag/AgCl). The current response (Figure 5.15a in red) and the charge delivery plot (Figure 5.15c) after this optimization, confirmed that the deposition rate was now almost constant during the first few cycles. Moreover, the deposition rate was progressively increasing, due to the increasing current as a result of the decrease in the electrode impedance.

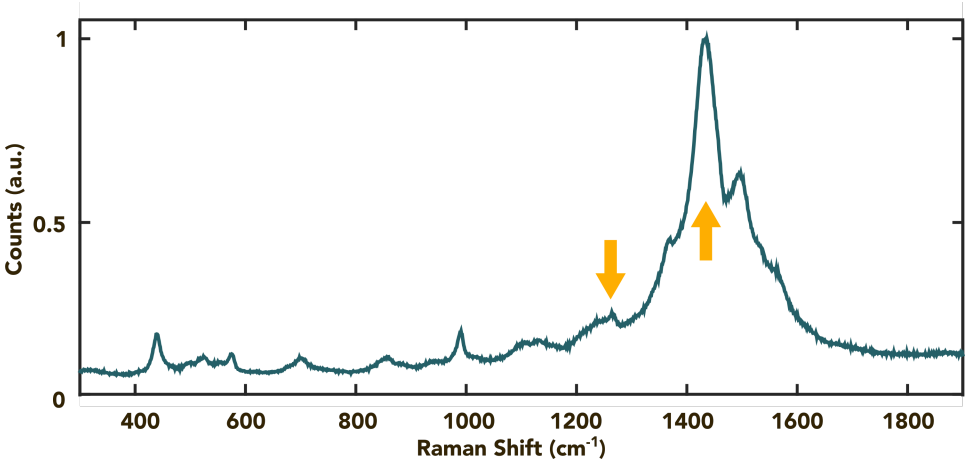

Figure 5.14: Raman spectra of PEDOT:PSS grown on the Pt electrodes showing a similar trend with the results observed by Kayinamura et al. [47] and Lapkowski et al. [51]. The maximum peak appears at 1436 cm^1 and several minor peaks can be seen around 1249 cm^{-1}.

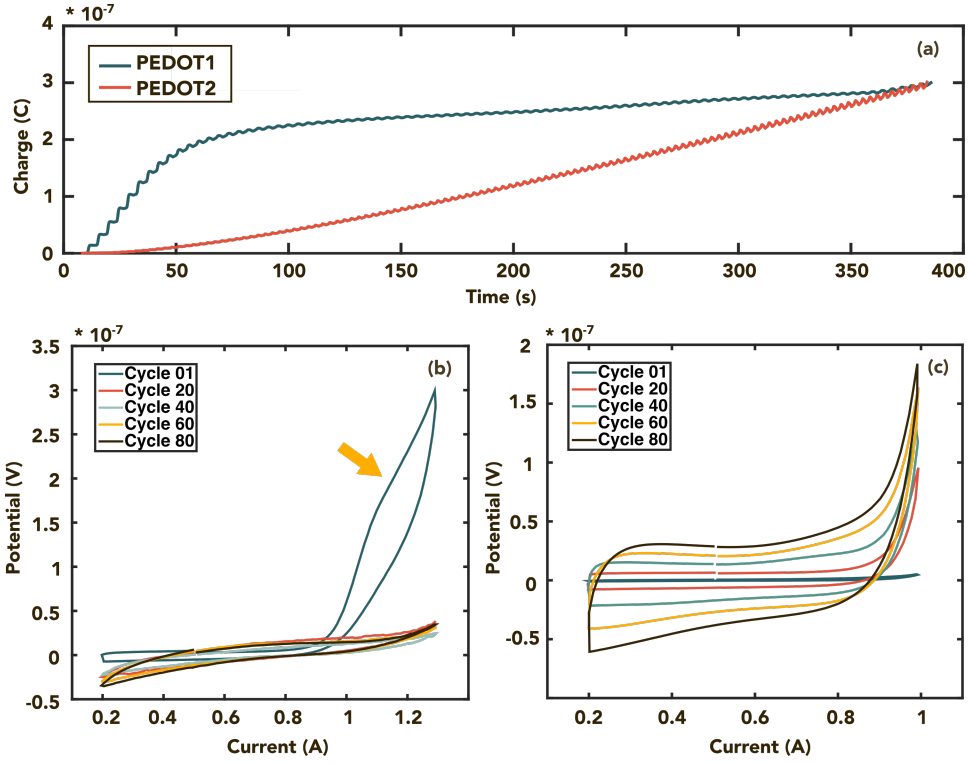

Figure 5.15: (a) Charge delivered through the electrode during of **PEDOT1** (in blue) and **PEDOT2** (in red) depositions. (b) Current response during cycle 01,20,40,60 and 80 for **PEDOT1** deposition. (c) Current response during cycle 01,20,40,60 and 80 for **PEDOT2** deposition.

ELECTROCHEMICAL CHARACTERIZATION

The EIS and CV measurements results are shown in Figure 5.16a,b and Table 5.1. A significant change was observed in both the impedance, as well as the phase characteristics of the PEDOT:PSS electrodes. The reference Pt electrodes exhibit an electrode impedance of 865 ± 35 kΩ (1 kHz). The electrode impedance of the PEDOT:PSS electrodes strongly depends on the deposition conditions. The deposition with voltage range between 0.2 and 1.3 V (referred to here as **PEDOT1**) only yields a small improvement in term of the electrochemical impedance, 705 ± 21 kΩ at 1 kHz. On the other hand, the PEDOT:PSS deposition with a voltage range between 0.2 and 1 V (**PEDOT2**) significantly reduced the impedance to 55.2 ± 2 kΩ, which is in the same range of PEDOT:PSS electrodes integrated in non stretchable surfaces [27]. This corresponds to a 93.3% impedance reduction compared to the Pt electrodes. The phase plot of **PEDOT2** electrodes also showed a more ohmic behavior for frequencies higher than 100 Hz.

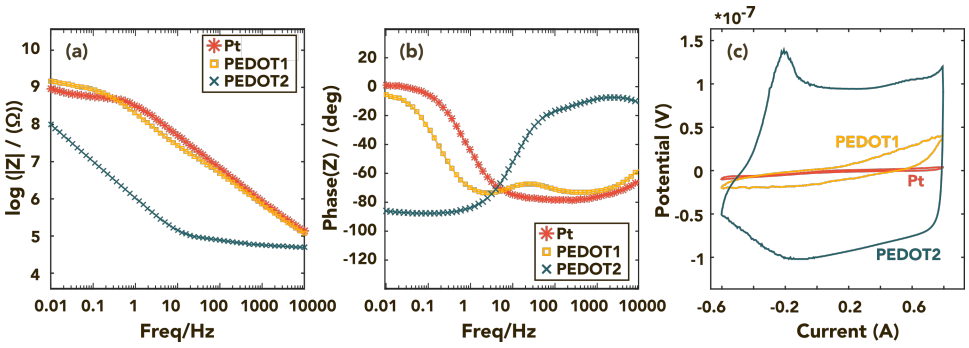

Figure 5.16: (a,b) Bode plot ((a) amplitude and (b) phase) of impedance spectra of a TiN electrode, a Pt electrode and two PEDOT:PSS electrodes (deposited with **PEDOT1** and **PEDOT2** programs) (diameter: 30 µm). EIS at 1 kHz are equal to 856 kΩ, 705 kΩ and 55 kΩ for Pt, **PEDOT1** and **PEDOT2** electrodes, respectively. (c) CV measurement from three types of the microelectrodes combined in one graph.

5

Compared to Pt, an improvement of the electrochemical impedance and the change of phase characteristics with the PEDOT:PSS coating are due to the inherent faradaic activity of the PEDOT:PSS film, attributed to the faradaic doping/undoping reactions, which allow ions to react at a faster rate [55, 56]. This value is even higher than the value reported in earlier studies [57], proving that a slow and ordered deposition of the PEDOT:PSS can even further improve the electrochemical properties of this material.

The significant difference between **PEDOT1** and **PEDOT2** characteristics is mainly caused by the fact that the slower deposition rate results in more orderly structured polymer chains.

The CV curves from each of the microelectrodes types are shown in Figure 5.16c. The CV curves of the PEDOT:PSS coating, particularly **PEDOT2**, shows very large capacitive currents, compared to Pt, both in the forward and the reverse scans. This is caused by the large double layer capacitance of the PEDOT:PSS coating. This proves once again that PEDOT:PSS provides a better performance than Pt in the Cytostretch MEA. Furthermore, the charge delivery capacity (*CDC*) value for each microelectrode type was derived from this measurement to qualitatively evaluate the microelectrode

	Material	Voltage Range (V)	Charge (µC)	|Z| 1 kHz (kΩ)
Reference	Pt	/	/	865 ± 35
PEDOT1	PEDOT:PSS on Pt	0.2-1.3	3	705 ± 21
PEDOT2	PEDOT:PSS on Pt	0.2-1	3	55 ± 2

Table 5.1: Electrodes overview and impedance values (at 1 kHz).

surface area. The values of CDC are calculated with Equation 5.1, separately for the cathodic and anodic scans:

$$CDC = \frac{1}{\nu \cdot A} \int_{E_c}^{E_a} I \cdot dE \tag{5.1}$$

where I is the measured current (A), ν is the scan rate (V/s), A is the area of the electrode (cm^2), and E_a and E_c are the peak anodic and cathodic potentials, respectively [58]. The anodic and cathodic CDC values of PEDOT:PSS coated microelectrodes are 30.88 and 33.45 mC/cm^2 respectively. On the contrary, the anodic and cathodic CDC values of the reference electrode are 0.364 and 0.532 mC/cm^2. This result confirms the superior electrochemical performance of PEDOT:PSS coated microelectrodes in comparison to the Pt and TiN microelectrodes.

5.3.4. Conclusions

In this second part of the chapter the fabrication, characterization and optimization of the first OOS device equipped with a PEDOT:PSS coated electrode were presented.

The fabrication of the OOC device was successfully improved by coating its TiN electrodes with a Pt layer to guarantee the adhesion between the PEDOT:PSS and the electrodes. The optimized Cytostretch devices were then packaged and assembled on a PCB. After that, the conducting polymer was locally deposited on the electrodes. The deposition was verified by means of optical and SEM imaging. Moreover, the material was analyzed with Raman spectroscopy, and the results compared to previous work so as to prove that the deposited material was indeed PEDOT:PSS.

The electrochemical performance of the MEA embedded in the novel device was characterized before and after the PEDOT:PSS deposition, and compared to a reference Pt MEA. After tuining the potential range of the CV deposition, the PEDOT:PSS electrodes showed an electrochemical impedance reduction of 93.3% when compared to Pt electrodes. Moreover, the CV characterization of PEDOT:PSS electrodes confirmed a higher capacitive current, compared to Pt. In fact, the CDC values for the PEDOT:PSS electrodes were 2 orders of magnitude higher that the Pt electrodes.

The results presented in this Chapter are a first step toward the integration of low impedance CNT and PEDOT:PSS MEAs in an OOC, which could eventually allow for low-noise and on-line monitoring of cells in these *in vitro* models, and promote their use in cardiotoxicity tests during the preclinical phase of medicine development.

REFERENCES

[1] N. Gaio, B. van Meer, C. Silvestri, S. Pakazad, S. Vollebregt, C. Mummery, and R. Dekker, *Upside-down carbon nanotube (cnt) micro-electrode array (mea),* in *2015 IEEE SENSORS* (IEEE, 2015) pp. 1–4.

[2] N. Gaio, C. Silvestri, B. van Meer, S. Vollebregt, C. L. Mummery, and R. Dekker, *Fabrication and characterization of an upside-down carbon nanotube (cnt) microelectrode array (mea),* IEEE Sens. J , 1 (2016).

[3] H.-B. Zhou, G. Li, X.-N. Sun, Z.-H. Zhu, Q.-H. Jin, J.-L. Zhao, and Q.-S. Ren, *Integration of au nanorods with flexible thin-film microelectrode arrays for improved neural interfaces,* Journal of microelectromechanical systems **18**, 88 (2009).

[4] D. E. Arreaga-Salas, A. Avendaño-Bolívar, D. Simon, R. Reit, A. Garcia-Sandoval, R. L. Rennaker, and W. Voit, *Integration of high-charge-injection-capacity electrodes onto polymer softening neural interfaces,* ACS applied materials & interfaces **7**, 26614 (2015).

[5] L. Wang, L. Liu, X. Li, N. Magome, K. Agladze, and Y. Chen, *Multi-electrode monitoring of guided excitation in patterned cardiomyocytes,* Microelectronic Engineering **111**, 267 (2013).

[6] I. Kehat, L. Khimovich, O. Caspi, A. Gepstein, R. Shofti, G. Arbel, I. Huber, J. Satin, J. Itskovitz-Eldor, and L. Gepstein, *Electromechanical integration of cardiomyocytes derived from human embryonic stem cells,* Nature biotechnology **22**, 1282 (2004).

[7] S. Rajaraman, S.-O. Choi, M. A. McClain, J. D. Ross, M. C. LaPlaca, and M. G. Allen, *Metal-transfer-micromolded three-dimensional microelectrode arrays for in-vitro brain-slice recordings,* Journal of Microelectromechanical Systems **20**, 396 (2011).

[8] A. L. Hodgkin and B. Katz, *The effect of sodium ions on the electrical activity of the giant axon of the squid,* The Journal of physiology **108**, 37 (1949).

[9] A. L. Hodgkin, *The ionic basis of electrical activity in nerve and muscle,* Biological Reviews **26**, 339 (1951).

[10] D. Curtis, J. Phillis, and J. Watkins, *Chemical excitation of spinal neurones,* Nature **183**, 611 (1959).

[11] D. Kenshalo Jr, G. Giesler Jr, R. Leonard, and W. Willis, *Responses of neurons in primate ventral posterior lateral nucleus to noxious stimuli,* Journal of Neurophysiology **43**, 1594 (1980).

[12] N. Gaio, B. van Meer, W. Quirós Solano, L. Bergers, A. van de Stolpe, C. Mummery, P. Sarro, and R. Dekker, *Cytostretch, an organ-on-chip platform,* Micromachines **7**, 120 (2016).

[13] A. Stett, U. Egert, E. Guenther, F. Hofmann, T. Meyer, W. Nisch, and H. Haemmerle, *Biological application of microelectrode arrays in drug discovery and basic research,* Analytical and bioanalytical chemistry **377**, 486 (2003).

[14] S. F. Cogan, P. R. Troyk, J. Ehrlich, and T. D. Plante, *In vitro comparison of the charge-injection limits of activated iridium oxide (airof) and platinum-iridium microelectrodes,* icEE Transactions on Biomedical Engineering **52**, 1612 (2005).

[15] S. F. Cogan, *Neural stimulation and recording electrodes,* Annu. Rev. Biomed. Eng. **10**, 275 (2008).

[16] A. Perestrelo, A. Águas, A. Rainer, and G. Forte, *Microfluidic organ/body-on-a-chip devices at the convergence of biology and microengineering,* Sensors **15**, 31142 (2015).

[17] D. Huh, B. D. Matthews, A. Mammoto, M. Montoya-Zavala, H. Y. Hsin, and D. E. Ingber, *Reconstituting organ-level lung functions on a chip,* Science **328**, 1662 (2010).

[18] J. Bockris, M. Devanathan, and K. Müller, *On the structure of charged interfaces,* in *Electrochemistry* (Elsevier, 1965) pp. 832–863.

[19] B. JO'M and K.-T. Jeng, *Water structure at interfaces: the present situation,* Advances in colloid and interface science **33**, 1 (1990).

[20] S. Srinivasan, *Electrode/electrolyte interfaces: Structure and kinetics of charge transfer,* in *Fuel Cells* (Springer, 2006) pp. 27–92.

[21] K. Yang, S. Yiacoumi, and C. Tsouris, *Electrical double-layer formation: Dekker encyclopedia of nanoscience and nanotechnology,* (2004).

[22] J. O. Bockris, A. K. Reddy, and M. Gamboa-Aldeco, *The electrified interface,* Modern Electrochemistry 2A: Fundamentals of Electrodics , 771 (2000).

[23] Z. Stojek, *The electrical double layer and its structure,* in *Electroanalytical methods* (Springer, 2010) pp. 3–9.

[24] J. O. Bockris and A. K. Reddy, *Ion-ion interactions,* Modern Electrochemistry 1: Ionics , 225 (1998).

[25] J. O. Bockris and A. K. Reddy, *Ion transport in solutions,* in *Modern Electrochemistry* (Springer, 1970) pp. 287–460.

[26] S. K. Pakazad, A. Savov, A. Van de Stolpe, and R. Dekker, *A novel stretchable micro-electrode array (smea) design for directional stretching of cells,* Journal of Micromechanics and Microengineering **24**, 034003 (2014).

[27] R. Gerwig, K. Fuchsberger, B. Schroeppel, G. S. Link, G. Heusel, U. Kraushaar, W. Schuhmann, A. Stett, and M. Stelzle, *Pedot–cnt composite microelectrodes for recording and electrostimulation applications: Fabrication, morphology, and electrical properties,* Frontiers in neuroengineering **5**, 8 (2012).

[28] T. Meyer, C. Leisgen, B. Gonser, and E. Günther, *Qt-screen: high-throughput cardiac safety pharmacology by extracellular electrophysiology on primary cardiac myocytes,* Assay and drug development technologies **2**, 507 (2004).

[29] W. Quiros-Solano, N. Gaio, C. Silvestri, G. Pandraud, and P. Sarro, *Pedot: Pss: a conductive and flexible polymer for sensor integration in organ-on-chip platforms,* Procedia Engineering **168**, 1184 (2016).

[30] S. Vollebregt and R. Ishihara, *Carbon nanotubes as vertical interconnects for 3d integrated circuits,* in *Carbon Nanotubes for Interconnects* (Springer, 2017) pp. 195–213.

[31] K. Wang, H. A. Fishman, H. Dai, and J. S. Harris, *Neural stimulation with a carbon nanotube microelectrode array,* Nano letters **6**, 2043 (2006).

[32] A. O. Fung, C. Tsiokos, O. Paydar, L. H. Chen, S. Jin, Y. Wang, and J. W. Judy, *Electrochemical properties and myocyte interaction of carbon nanotube microelectrodes,* Nano letters **10**, 4321 (2010).

[33] Y. Hanein and L. Bareket-Keren, *Carbon nanotube-based multi electrode arrays for neuronal interfacing: progress and prospects,* Frontiers in neural circuits **6**, 122 (2013).

[34] M. David-Pur, L. Bareket-Keren, G. Beit-Yaakov, D. Raz-Prag, and Y. Hanein, *All-carbon-nanotube flexible multi-electrode array for neuronal recording and stimulation,* Biomedical microdevices **16**, 43 (2014).

[35] S. Vollebregt, R. Ishihara, J. Derakhshandeh, J. van der Cingel, H. Schellevis, and C. Beenakker, *Integrating low temperature aligned carbon nanotubes as vertical interconnects in si technology,* in *2011 11th IEEE International Conference on Nanotechnology* (icEE, 2011) pp. 985–990.

[36] C. Silvestri, B. Morana, G. Fiorentino, S. Vollebregt, G. Pandraud, F. Santagata, G. Q. Zhang, and P. M. Sarro, *Cnt bundles growth on microhotplates for direct measurement of their thermal properties,* in *2014 IEEE 27th International Conference on Micro Electro Mechanical Systems (MEMS)* (icEE, 2014) pp. 48–51.

[37] W. Zhou, Z. Han, J. Wang, Y. Zhang, Z. Jin, X. Sun, Y. Zhang, C. Yan, and Y. Li, *Copper catalyzing growth of single-walled carbon nanotubes on substrates,* Nano letters **6**, 2987 (2006).

[38] T. Iwasaki, G. Zhong, T. Aikawa, T. Yoshida, and H. Kawarada, *Direct evidence for root growth of vertically aligned single-walled carbon nanotubes by microwave plasma chemical vapor deposition,* The Journal of Physical Chemistry B **109**, 19556 (2005).

[39] K. Gjerde, R. R. Kumar, K. N. Andersen, J. Kjelstrup-Hansen, K. B. Teo, W. I. Milne, C. Persson, K. Mølhave, H.-G. Rubahn, and P. Bøggild, *On the suitability of carbon nanotube forests as non-stick surfaces for nanomanipulation,* Soft Matter **4**, 392 (2008).

[40] R. Kim, S. Joo, H. Jung, N. Hong, and Y. Nam, *Recent trends in microelectrode array technology for in vitro neural interface platform,* Biomedical Engineering Letters **4**, 129 (2014).

[41] T. D. Kozai, K. Catt, Z. Du, K. Na, O. Srivannavit, M. H. Razi-ul, J. Seymour, K. D. Wise, E. Yoon, and X. T. Cui, *Chronicin vivoevaluation of pedot/cnt for stable neural recordings,* IEEE Transactions on Biomedical Engineering **63**, 111 (2016).

[42] A. Schander, T. Teßmann, S. Strokov, H. Stemmann, A. K. Kreiter, and W. Lang, *In-vitro evaluation of the long-term stability of pedot: Pss coated microelectrodes for chronic recording and electrical stimulation of neurons,* in *2016 38th annual international conference of the IEEE engineering in medicine and biology society (EMBC)* (IEEE, 2016) pp. 6174–6177.

[43] P. Lin and F. Yan, *Organic thin-film transistors for chemical and biological sensing,* Advanced materials **24**, 34 (2012).

[44] D. Nilsson, T. Kugler, P.-O. Svensson, and M. Berggren, *An all-organic sensor–transistor based*

on a novel electrochemical transducer concept printed electrochemical sensors on paper, Sensors and Actuators B: Chemical **86**, 193 (2002).

[45] K. Krishnamoorthy, R. S. Gokhale, A. Q. Contractor, and A. Kumar, *Novel label-free dna sensors based on poly3, 4-ethylenedioxythiopheneelectronic supplementary information esi available: Experimental details and sensor response for various sensors listed in table 2. cyclic voltammograms confirming the increase in resistance due to the duplex formation between the probe and target dna in conducting polymer matrix. see http: www. rsc. orgsuppdat-accb3b316794a,* (2004).

[46] P. Lin, F. Yan, J. Yu, H. L. Chan, and M. Yang, *The application of organic electrochemical transistors in cell-based biosensors,* Advanced Materials **22**, 3655 (2010).

[47] Y. P. Kayinamura, M. Ovadia, D. Zavitz, and J. F. Rubinson, *Investigation of near ohmic behavior for poly (3, 4-ethylenedioxythiophene): A model consistent with systematic variations in polymerization conditions,* ACS applied materials & interfaces **2**, 2653 (2010).

[48] Y. Nakamura, Y. Suzuki, and Y. Watanabe, *Effect of oxygen plasma etching on adhesion between polyimide films and metal,* Thin Solid Films **290**, 367 (1996).

[49] N. Gaio, A. Waafi, M. Vlaming, E. Boschman, P. Dijkstra, P. Nacken, S. Braam, C. Boucsein, P. Sarro, and R. Dekker, *A multiwell plate organ-on-chip (ooc) device for in-vitro cell culture stimulation and monitoring,* in *2018 IEEE Micro Electro Mechanical Systems (MEMS)* (IEEE, 2018) pp. 314–317.

[50] T. Rose and L. Robblee, *Electrical stimulation with pt electrodes. viii. electrochemically safe charge injection limits with 0.2 ms pulses (neuronal application),* IEEE Transactions on Biomedical Engineering **37**, 1118 (1990).

[51] M. Łapkowski and A. Proń, *Electrochemical oxidation of poly (3, 4-ethylenedioxythiophene)—"in situ" conductivity and spectroscopic investigations,* Synthetic Metals **110**, 79 (2000).

[52] A. J. Bard, L. R. Faulkner, J. Leddy, and C. G. Zoski, *Electrochemical methods: fundamentals and applications*, Vol. 2 (wiley New York, 1980).

[53] G. A. Mabbott, *An introduction to cyclic voltammetry,* Journal of Chemical education **60**, 697 (1983).

[54] H. Yamato, M. Ohwa, and W. Wernet, *Stability of polypyrrole and poly (3, 4-ethylenedioxythiophene) for biosensor application,* Journal of Electroanalytical Chemistry **397**, 163 (1995).

[55] H. J. Ahonen, J. Lukkari, and J. Kankare, *n-and p-doped poly (3, 4-ethylenedioxythiophene): two electronically conducting states of the polymer,* Macromolecules **33**, 6787 (2000).

[56] J. Bobacka, A. Lewenstam, and A. Ivaska, *Electrochemical impedance spectroscopy of oxidized poly (3, 4-ethylenedioxythiophene) film electrodes in aqueous solutions,* Journal of Electroanalytical Chemistry **489**, 17 (2000).

[57] Z. A. King, C. M. Shaw, S. A. Spanninga, and D. C. Martin, *Structural, chemical and electro-*

chemical characterization of poly (3, 4-ethylenedioxythiophene)(pedot) prepared with various counter-ions and heat treatments, Polymer **52**, 1302 (2011).

[58] E. Slavcheva, R. Vitushinsky, W. Mokwa, and U. Schnakenberg, *Sputtered iridium oxide films as charge injection material for functional electrostimulation,* Journal of the Electrochemical Society **151**, E226 (2004).

6

FROM CHIP TO SYSTEM

This chapter is based on:

- N. Gaio, A. Waafi, M. Vlaming, E. Boschman, P. Dijkstra, P. Nacken, S. Braam, C. Boucsein, P. Sarro, and R. Dekker, A multiwell plate organ-on-chip (ooc) device for in-vitro cell culture stimulation and monitoring, in 2018 IEEE Micro Electro Mechanical Systems (MEMS) (IEEE, 2018) pp. 314–317 [1].

6.1. INTRODUCTION

Since the first publications in this field [2], OOC development has been a multidisciplinary effort involving biology and engineering. This approach has promoted and stimulated the awareness for this class of devices in both the biological as well as the engineering worlds. This cross fertilization character has been one the causes for the "OOC hype" mentioned in Chapter 1 [3, 4]. The initial work in this field has mainly focused on the development of microfabricated chips and the validation of their functionality with simple proof of concept rather than performing full biological qualification of the models. As the technology became more and more mature, the OOC field moved towards a new stage, where biology became the focus of attention. As defined by Junaid et al. [5], the OOC world is becoming "the realm of biologists". Consequently, publications have more and more focused on qualifying physiologically relevant models and/or integrating stem cell cultures [6].

As the OOC field will continue following this trend, engineers will need to re-define their research goals. Beside focusing on technological advancements or developing new devices, engineers will need to focus on improving the adoptability of the current tech-

nologies and devices [5]. This should be done taking in consideration that this kind of activities might be a critical factor to guarantee the success of OOCs since "the commercial success of a technology not only depends on the degree of innovation, but also its adoptability" [7].

Promoting the adoption of OOC technology is not a trivial task. Adoption of new technologies that replace or complement existing methods is often a slow process [8]. Moreover, drug R&D is generally conservative in adopting new tools and technologies. On the bright side, biologists are currently showing an increasing interest in this class of products. However, at the moment it is generally felt that there is a significant gap still existing between the desired system and the available models [9]. Three main aspects that need to be be considered to make OOC a success in drug R&D were identified in [5, 10]: ease of use, throughput and compatibility:

- **Ease of use**:
  To increase the OOC acceptance in pharmaceutical R&D it is necessary to eliminate the need for external pumps or, at least, simplify their use. Moreover, it is essential to adapt the system to pipette operations, open well structures and multiwell plate and high-throughput formats. Last but not the least, it is required to develop systems that are compatible with small volumes handling.

- **Manufacturability:**
  Qualification and validation of OOC models usually requires a considerable number of devices. It is necessary to optimize fabrication processes to guarantee that a sufficient number is available for qualification. For this, not only the chip fabrication is important, but also a reliable and robust packaging system should be developed.

- **Compatibility:**
  The next generation of OOC devices needs to be compatible with previously developed analysis systems, which are already available in biological labs to reduce investments for labs and the time required to learn how to use them.

As a result, technical universities that in general focus more on technology push rather than the above mentioned aspects will likely lose their central stage in the development and fabrication OOC devices. Technological advancements should primarily come from the needs identified by biologists. OOC start-ups might be able to take the lead in the development and finalisation of robust and easy-to-use OOC systems focusing on costumer-oriented R&D. Spin-offs have already begun to spawn from academic research trying to fill this commercial space and are attracting investment to transform the drug

discovery industry with OOC devices [7]. Companies like Mimetas B.V. have thrived on this trend. The Mimetas B.V. product was indeed developed by focusing on user experience, and its unique selling point is ease of use [11]. This strategy has clearly paid off, as their product was quickly adopted among academia, allowing Mimetas to gain 14% percent of the OOC market share in only a few years [10].

6.1.1. CYTOSTRETCH EASE OF USE

As the InForMed project aimed at developing an Heart-on-Chip device suitable to be commercialized, the aspects above mentioned were taken in consideration to promote the adoption of the system and consequently increase its chances of success in the market. The definition of this target was possible only thanks to the unique InForMed consortium, including academia, silicon and packaging foundries, and end-users. The initial prototype of the Cytostretch device presented in Chapter 3 [12] was improved to satisfy the three aspects pointed out in [5, 10]:

- The original Cytostretch package required the user to perform several manual handling steps [13], which was making the device difficult to use and was negatively affecting the reproducibility as pointed out by the early adopters. Moreover, the device was not included in a complete system. Last but not the least, the original version was not compatible with a multi-well plate format and thus only useful for low throughput experiments.
- The original device was not manufacturable due to the cumbersome parylene processing and PDMS etching (Chapter 4).
- Last but no least, even though the original developed device was compatible with a Multi-channel System GmbH (MCS) MEA reader, it was not fully exploiting the potential of the system, using only 12 of the 60 signal channels available in the MEA1060 model [14].

This chapter will focus on a re-desing of the system around the Heart-on-Chip, taking into consideration ease of use, manufacturability, and compatibility. The system was adapted to reduce as much as possible the manual steps required from the user. Moreover, the system is developed not only focusing on the packaging of the chips, but also considering the pneumatic components to obtain a robust and complete system. The packaging of the device is performed with commercially available packaging equipment. The fabrication throughput is already guaranteed by the POS guidelines (Chapter 2) and the optimizations presented in Chapter 4. The device is compatible with inverted microscopes and the MCS read out system by design.

6.2. SYSTEM OVERVIEW

The Heart-on-Chip system is composed of multiple elements as represented in Figure 6.1. In order to be used, the chips presented in Chapter 4 are packaged in a compact and robust multi-well plate. Each plate houses four chips. The plate is designed with an open well structure that allows for pipette cardiomyocyte cells seeding. The plate is used in combination of a costume-made lid, that avoids contamination with particles and bacteria. In order to stretch the membranes, a pneumatic system was developed. This is composed of a peristaltic pump and a conditioning box. The pump is controlled by a PC and custom made software. The peristaltic pump and the software were designed to handle up to six plates in parallel. To apply the pressure generated by the pump to the chips, a conditioning box was developed.

A schematic drawing of the connected system is shown in Figure 6.2. The conditioning box can be placed in any standard incubator and is pneumatically connected to the pump via a tube inserted into the incubator through an opening at the backside. The plate can easily be loaded and unloaded in and out from the conditioning box without any need to disassemble the system (Figure 6.2b). While using the pump, the air injected in the conditioning box does not affect the temperature, humidity and the oxygen content since the conditioning box is leak tight. The air injected into the conditioning box is not in contact with the cell cultures, so the pump can be easily placed outside of the incubator without any risk of contamination and/or infection.

The cells on the plate can be analyzed with standard inverted microscopes (Figure 6.2c). The transparent optical windows of the chip and the plate makes Cytostretch compatible with various imaging systems. The minimum accepted working distance is 0.3 mm. The plate was designed to be compatible with the MCS MEA1060 family [14], so that this system can be used to monitor the electrical activity of the cardiomyocytes.

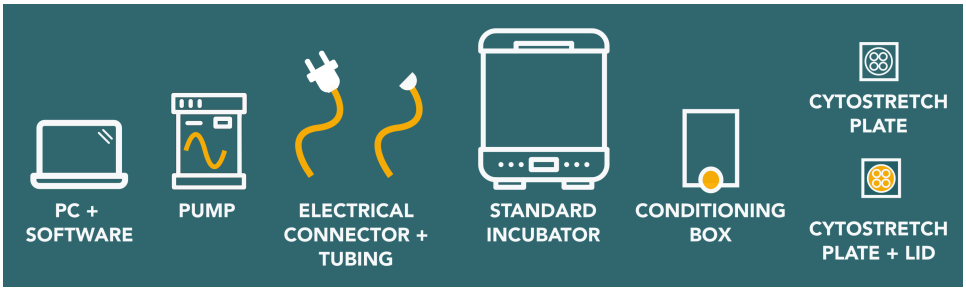

Figure 6.1: Schematic drawing of the different elements of the Cytostretch system: PC and software, pneumatic pump, electrical connectors and tubing, standard incubator, conditioning box, and the Cytostretch plate with a lid.

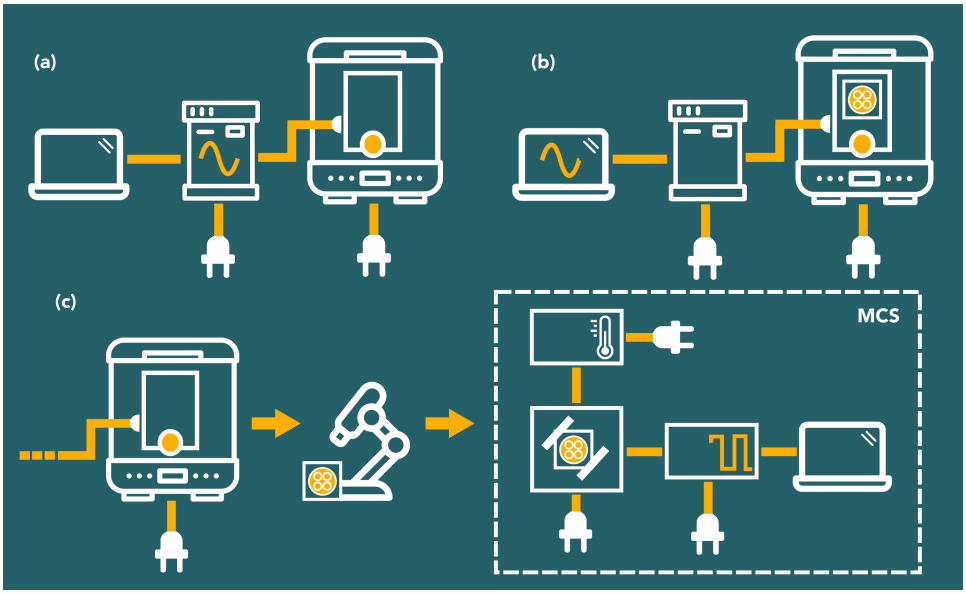

Figure 6.2: Schematic drawings of the pneumatic set up before (a) and after (b) loading the Cytostretch plate. (c) The Cytostretch plate can be simply detached from the pneumatic system during the test for microscopic analysis or to be placed in a MCS reader to monitor the electrical signals generated by the cardiac cells.

6.3. HEART-ON-CHIP PLATE

In this section the integration of multiple Cytostretch chips on a novel multi-well plate is discussed, taking into account the requirements mentioned in Section 6.1. The chips and the package together form the so called Cytostretch plate. The plate consists of a set of separated chips assembled on a customized PCB and packaged on PCB level using film assisted molding (FAM) [15].

6.3.1. ASSEMBLY

Before assemblying the Cytostretch chip on the PCB, the aluminum (Al) contact pads of the chips are provided with an under bump metallization (UBM) process. This makes the bondpads compatible with wirebonding as well solderbumping. To this end, the wafers were shipped to PacTech. Even though more than 10% of the wafer area consisted of membranes, none of the wafers broke during this transport. A protective foil was laminated on the backside of the wafers. This foil served to protect the backside of the wafers from the chemicals used for the electroless UBM deposition. This precaution was taken to avoid any biocompatibility issues or unwanted deposition and/or contamination on the membranes. The lamination of the foil is performed without applying

vacuum to the backside of the wafer to prevent unnecessary deformation of the PDMS membranes.

After this, an electroless UBM process was performed. This step was tuned to deposit a metallic stack composed of 5 µm Ni, 0.2 µm Pd and 0.05 µm Au (ENEPIG - Electroless Nickel Electroless Palladium Immersion Gold). The full procedure is performed in an automatic fashion composed of multiple steps. During the process, the Al of the contact pads is cleaned by etching away 250 nm of the top layer. The cleaning steps were performed without water spraying to avoid uncontrolled water jet pressure directly on the membranes. The process resulted in a Ni layer with an average thickness of 4.41 µm, a Pd layer with an average thickness of 0.2 µm, and an Au layer with an average thickness of 0.03 µm. The backside foil was then removed manually to avoid breaking of the wafer and/or membrane deformation.

After the UBM, the wafer is diced. Before dicing, a UC-353-EP-110 Furukawa foil is applied on the backside of the wafer with a by Ultron System USI Model UH114-8

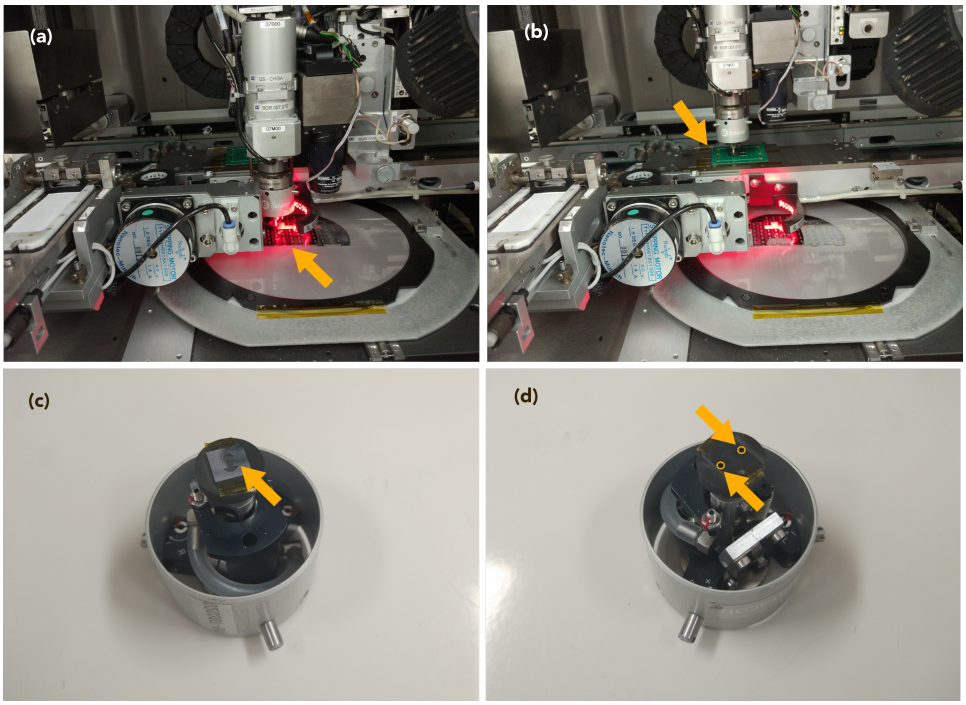

Figure 6.3: Datacon APM 220 Pick and Place tool moving four chips from the wafer (a) to the PCB (b). Wafer and PCB indicated by yellow arrows in (a) and (b), respectively. (c) Adaptor for Datacon APM 220 Pick and Place tool to pick up the Cytostretch chips without deforming the membranes (Cytostretch chip indicated by the yellow arrow). This is possible thanks to the two vacuum holes located far from the membrane and indicated by the yellow arrows in (d).

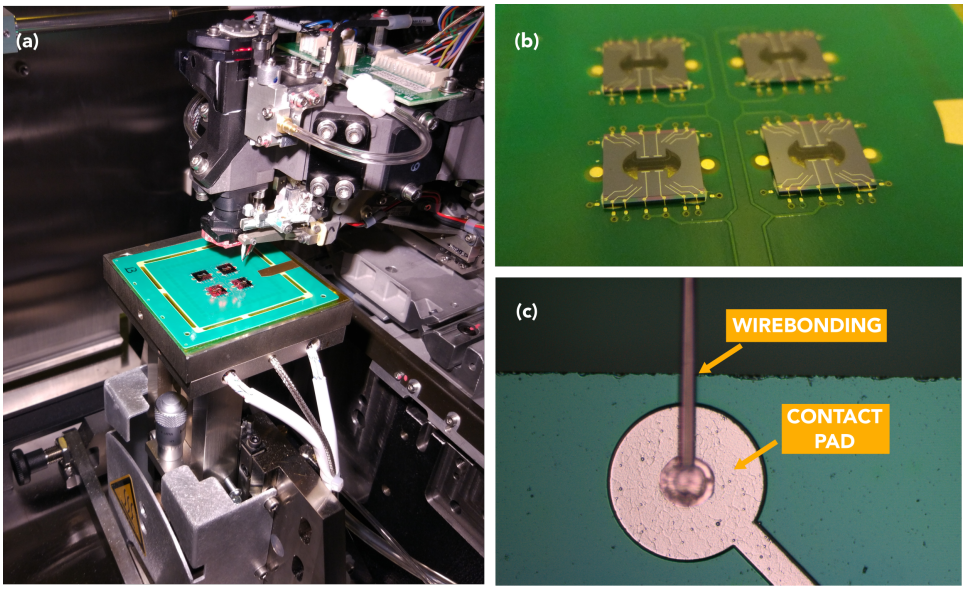

Figure 6.4: (a) PCB in the Kulicke Soffa (IConn PLUS power series) wire bonder. (b) Photograph of the PCB after the wirebonding. (c) Optical image of one gold wire applied to a contact pad on a Cytostretch chip.

system. The lamination is applied without vacuum and is free of bubbles. In order to promote the adhesion between the wafer and the foil, they are placed in an Heraeus oven at 50 °C for 30 minutes. The wafer, loaded on the dicing frame, is then moved in a fully automatic DISCO DFD63400 dicing tool, to separate the four inch wafer into 100 7x7 mm^2 dies.

After this step, a Datacon APM 220 Pick and Place tool is used to bring the dies from the foil to the PCBs. The PCB can be equipped with up to four chips. The pick and place machine first applies a solid pallet of Locatie Ablestik QMI536NB glue on four corners of the die, then picks up the chips and places them in the right position. In Figure 6.3 the moments when the chip is picked up (a) and then located on the PCB (b) are shown. In order to prevent any membrane damage, the chips were picked up with a customized vacuum holder (Figure 6.3c), with vacuum only applied on two parts of the chip far from the membrane, as highlighted in Figure 6.3d.

The PCBs are then loaded in a Memmert oven at 150 °C for one hour for fixating the chips. After this, the PCBs are cleaned with a March Instrument oxygen plasma Asher with ENI RF Generator for 2 minutes at 174 W power to remove possible organic residues from the contact pads. The contact pads of the chips are then electrically connected to the PCB with 20 µm diameter Au wires using a fully automatic Kulicke Soffa (IConn PLUS

power series) wire bonder (Figure 6.4). The samples are finally delivered to Boschman Technologies B.V. for the final step of the packaging, the molding.

6.3.2. MOLDING

Finally, the PCB and the chips are encapsulated with an epoxy compound by means of FAM, using a Boschman Unistar Innovate 2-FF system. FAM is a proprietary technology of Boschman Technologies B.V. [15], which guarantees a molding process without physical contact between the mold and the epoxy. This is achieved by two Teflon foils (Figure 6.5a) that are fixed to the inner surfaces of the mold (Figure 6.5b) by vacuum. The PCB is inserted in the tool (Figure 6.5c,d) and the epoxy material, liquefied by heat and pressure, is then forced into the closed mold, and held there until the epoxy is solidified (Figure 6.5e). A Sumitomo G700 series epoxy was used with a process temperature of 175 °C and an end-cure pressure of 45 bar. The in-mold cure time used for this process was 80 sec. The mold and epoxy pressures, injection temperature and cure time

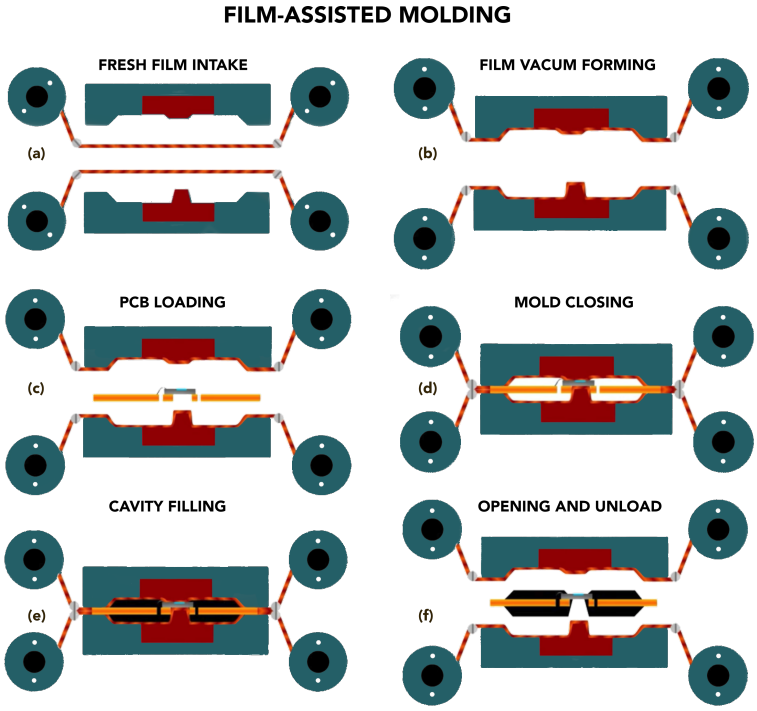

Figure 6.5: Process flow for the Film-Assisted Molding of the plate: (a) two Teflon films are rolled inside the mold; (b) the films are sucked into the inner surface of the mold; (c) the PCB is loaded inside the mold; (d) the mold is closed; (e) the liquefied epoxy material is injected in the mold and cured; (f) the mold is opened and the plate is unloaded. The figures are not drawn to scale. Figure adapted from [15].

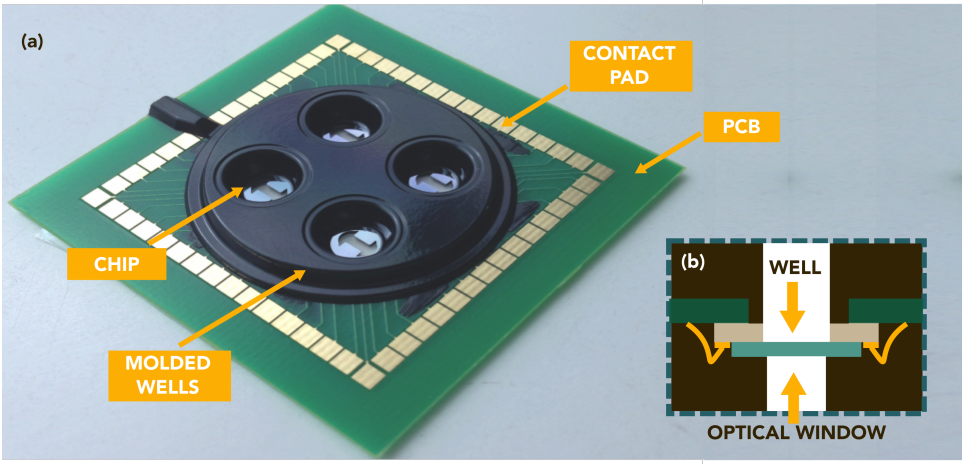

Figure 6.6: Optical image of the multi-well plate consisting of four Cytostretch chips mounted on a PCB and encased by the molded wells. (b) 2D sketch of the plate cross-section.

were optimized to result in void free encapsulation and to prevent damage to the chips.

The mold was customized to create the open-wells on top of the four chips, where the cells will be seeded, and to protect the wirebonds from the humid environment in a cell culture incubator. After opening of the mold, the encapsulated products are unloaded (Figure 6.5f). Next, the vacuum is removed, and the foils are transported and renewed so that a new cycle can start without the need for manual cleaning.

6.3.3. PLATE CHARACTERIZATION

Figure 6.4b shows a photograph of the four chips mounted on the PCB before molding. Figure 6.4c shows the Au wires connecting the chip to the PCB. The final plate after FAM is shown in Figure 6.6. The FAM molding resulted in a clean chip surface without epoxy residues on the chip surface or on the optical window. After optimization of the clamping pressure, both sides of the chip were clamped with high precision to avoid damage to the chips.

IN LINE CHARACTERIZATION - TEST 1

In order to study the continuity of the electrical connections between the chips and the PCB after the molding, a first batch of devices was fabricated using a test design, which contained test devices with bondpads that were daisy-chain connected with interconnects adjacent to the membranes. Figure 6.7a shows the schematic of the test chip. The metal lines were fabricated in Al (2 µm thick, 500 µm wide) and were placed on the Si

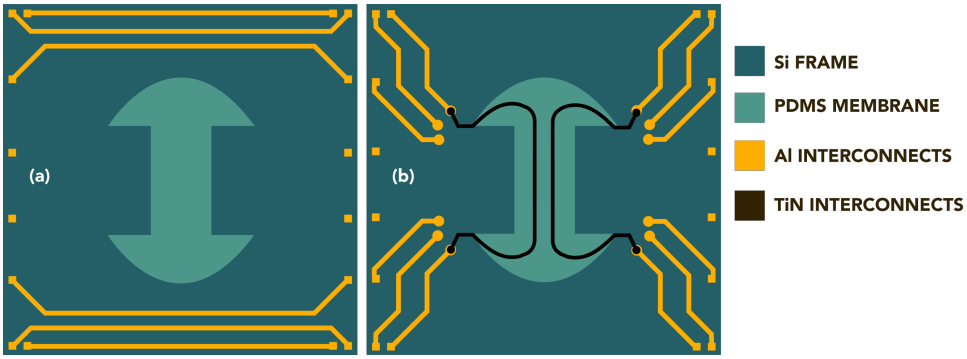

Figure 6.7: Layout of the test structures used in **Test 1** (a) and **Test 2** (b). The figures are not drawn to scale.

frame, avoiding the membrane area. The series connection of the copper PCB traces, the wirebonds, and the Al chip interconnects were characterized using two point probing. The yield on 65 interconnects distributed over 12 chips on 3 plates was 99%. The only open circuits found may be caused by a detachment of the bondwires from the bondpads, probably due to organic residues on the bondpads. The same test was performed on a plate that was placed in an incubator for 10 days. The incubation test did not result in any additional failures, proving that the epoxy mold protects the connections from the humid environment in the incubator and prevents corrosion.

The plate was then loaded on an inverted microscope to identify the compatibility with standard optical microscopy. The 0.3 mm working distance allowed to focus on the membrane with a magnification of 100X, showing that the epoxy mold underneath the chip does not obstruct the imaging of cells on the membrane.

FULL PROCESS TEST - TEST 2

The process was then repeated using a second test structure including metal lines consisting of Al and TiN, where the TiN lines were transversing the membrane (Figure 6.7b). In this case all the connections showed to be not conductive. After a thorough microscopic inspection of the samples, cracks in the TiN lines were identified (Figure 6.8a). It appeared that the automatic segmentation of the curvy interconnects resulted in unwanted corners. The high stress field at these corners apparently initiated the cracks, since no cracks were found in areas distant from these corners.

In order to identify which step of the assembly process caused the cracking of the interconnects, the assembly process was repeated, with an electrical characterisation of the metal lines performed after every step. This showed that the metal lines broke during the dicing step. Multiple attempts to reduce the pressure applied to the membranes

during this step were performed by testing multiple foils, but no apparent improvement was achieved.

FULL PROCESS TEST - TEST 3

Regardless of the problem identified in **Test 2**, a batch of chips equipped with platinum (Pt) electrodes was assembled and packaged onto the PCBs. This was done considering that the metal lines in these chips are shorter than those used in **Test 2**, so that the risk of cracks should be smaller. The electrodes in the plate were then tested one by one with a set up similar to that one presented in Chapter 5. Working electrodes were identified by performing a narrow bandwidth EIS around 1 kH to verify whether the electrochemical impedance was showing EIS values similar to those presented in Chapter 5. Almost all the electrodes in the three tested plates showed an impedance in the order of GΩ at 1 kHz. These open circuits are most likely again caused by the cracks originating from the dicing of the chips. Nevertheless, it was possible to characterize three electrodes with same EIS set-up used in Chapter 5. In Figure 6.8b,c the Bode plot of the impedance spectra of one of the Pt electrode is shown. At 1 kHz the average impedance calculated from the three Pt microelectrodes is 870 kΩ. The impedance trend and the recorded value is comparable to the values measured in Chapter 5, proving that the assembly is not affecting the performance of the electrodes itself.

6.4. PNEUMATIC SYSTEM

The burden of using pumps and external microfluidic systems to control the environment in an OOC device, has always been linked to the slow proliferation of OOCs in bi-

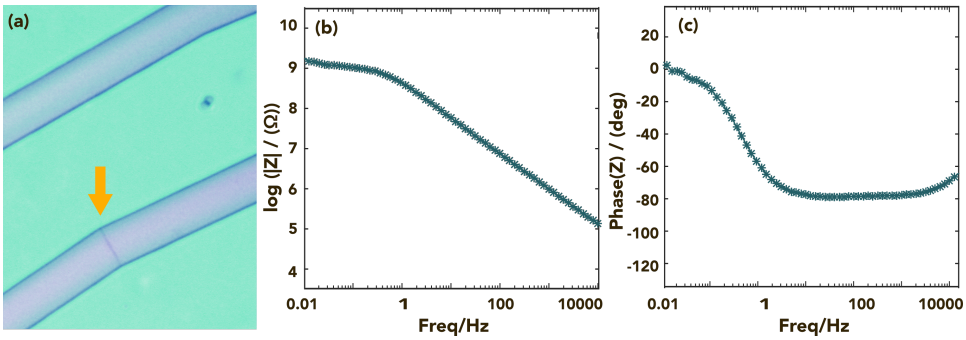

Figure 6.8: (a) TiN metal lines with a crack indicated by the yellow arrow. (b,c) Bode plot ((b) amplitude and (c) phase) of impedance spectra a Pt electrodes (diameter 30 µm), showing a similar behaviour than the electrodes presented in Chapter 5. At 1 kHz the average impedance calculated over the three Pt microelectrodes is 870 kΩ.

ological labs. Most pump systems are not particularly user friendly, which can be seen as an obstacle in their deployment. Moreover, the use of pumps in high throughput microfluidic tests requires a large amount of tubing, and consequently a long time to set up. Last but not least, the use of microfluidic tubing and connections often results in the formation of bubbles, which can eventually affect the results.

Recently, multiple companies have tried to avoid these problems with different approaches:

- **Removing the pump:**
  Companies like Mimetas B.V. [11] have completely abandoned the use of pumps, to maximize the ease of use. This solution provides the best user experience at the lowest price, even though it results in simple models and lack of functionality.

- **Reducing the amount of tubing by handling multiple chips in parallel:**
  Companies like Alveolix A.G. [16] and CN BIO Innovations Ltd [17] are still using a pump but only to stretch multiple membranes in parallel. Limiting the number of pump for these applications allows for several chips to be handled in parallel, which consequently reduces the tubing and the step-up time required. This choice provide a good user experience despite higher R&D costs and again a limited functionality.

- **Adapt the pump to the chips and the chips to the pump:**
  Companies like Emulate Inc. [18] and partially Micronit B.V. with Fluigent S.A. [19] are trying to improve the ease of use of their device by optimizing and adapting the perfusion systems to their device. This choice provides a good user experience combined with high functionality at the expense of high development costs.

As the Heart-on-Chip model developed in this work does not require microfluidics, we opted for the second approach having one single pump stretching multiple chips on the plate in parallel.

6.4.1. CONDITIONING BOX

The mechanical actuation of the Cytostretch device is required in two different phases of its use: in the first phase the cells are conditioned for extended periods of time within the incubator by periodically stretching them to promote growth and maturation, while in the second phase the cells are stretched during the acquisition of the electrophysiological signals to simulate exercise. For both phases, different mechanical holders were developed by MCS.

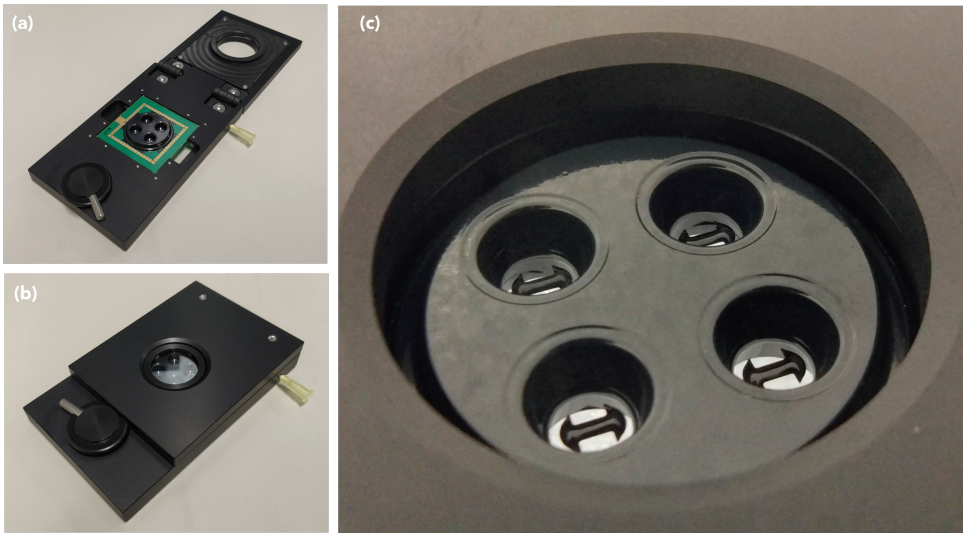

Figure 6.9: Photographs of an open (a) and closed (b) conditioning box containing one Cytostretch plate. (c) Photograph of the inflated PDMS membrane of a Cytostretch plate inside the conditioning box.

For the first phase, a conditioning box was developed. Figure 6.9 shows an open conditioning box with a Cytostretch plate, before (a) and after (b,c) being closed. This tool requires only a very small footprint, and it does not need to contain recording electronics or stimulation circuitry. The materials that were used are resistant against the conditions within the incubator, i.e. high humidity (95% rel. humidity) and temperatures of 37 °C. This conditioning box clamps the plate with the required force to ensure a tight seal between holder and MEA, and thus allows for stretching of the membranes. The conditioning box, besides being compatible with the plate, also allows for placing and removing the lid on top of the plate without disassembling the box. Moreover, it guarantees the exchange of oxygen between the incubator and the cell culture environment in the plate wells.

To perform electrophysiological measurements during stretching, an adaptation of the existing acquisition systems is necessary. For this, the heating plate of a commercial MCS MEA amplifier, which also serves as a mechanical support for the MEA, was replaced by a custom-designed pressure chamber insert. The tubing necessary to supply negative and positive air pressure can be placed into an existing cavity inside the base plate of the amplifier, which also carries cables for the heating plate.

6.4.2. PERISTALTIC PUMP AND SOFTWARE

In addition to the conditioning boxes, a pressure controller was developed. In order to run different experiments at the same time, this controller includes multiple independent pressure generators for each channel. The pressure cycles should be applied for extended periods of time to influence maturation of cells, i.e. several weeks of periodic stretching. The system is able to provide sinusoidal stimulation with frequencies from 1 to 5 Hz, and pressures up to 2000 Pa.

In order to meet these specifications, MCS developed and array of peristaltic pumps mounted in one common housing. Each of the pumps can be controlled independently. For this application, peristaltic pumps are advantageous since they are durable by design. Moreover, it is easy to replace damaged tubing, and they can easily meet the specifications. The pump array with and without a conditioning boxes is shown in Figure 6.10a,b.

For an easy control of the pneumatic system, custom made software was developed by MCS (Figure 6.10c). This allows the user to set pressure cycle parameters for each channel independently, stop and start them, and display the pressures for all channels.

6

6.5. PRELIMINARY TESTS OF THE SYSTEM

Before the biological tests presented in Chapter 7, the whole system composed of plate, conditioning box and pump was mechanically tested. First, the relation between the applied pressure and the resulting strain in the membrane was characterized. This was done by geometrically calculating the strain in the rectangular area of the dogbone

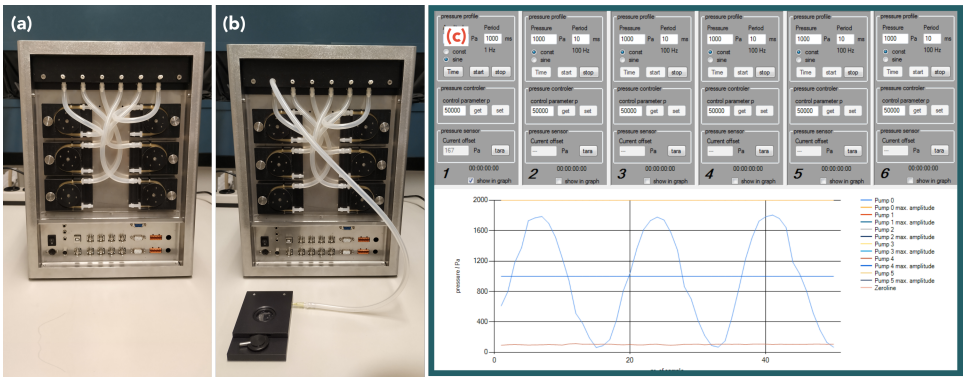

Figure 6.10: Photographs of the peristalitic pump with (a) and without (b) a conditioning box attached to it. The peristaltic pump can be connected to 6 conditioning boxes in parallel. (c) Screenshot of the custom made software developed to control the pump.

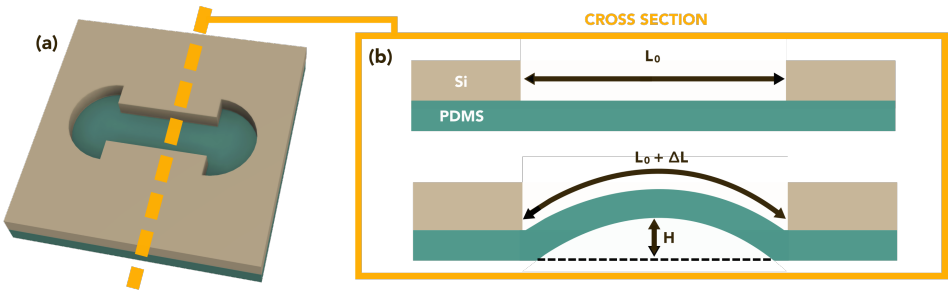

Figure 6.11: (a) 3D rendering of the Cytostretch chip. (b) Schematic cross-section of the PDMS membrane of the Cytostretch chip (inflated and non-inflated), with the geometrical parameters used in Equation 6.1.

membrane, by simply measuring the vertical displacement of the membrane for multiple pressures applied on the backside of the chip, as previously done in [12, 20]. The vertical displacement can be converted into strain using Equation 6.1:

$$\varepsilon = \frac{\Delta L}{L_0} = \frac{h^2+1}{2h} \arcsin \frac{2h}{h^2+1} - 1, h = \frac{H}{R} \tag{6.1}$$

where H is the vertical displacement at the center of membrane in the rectangular region obtained by microscopic inspection, L_0 denotes the original width of the membrane and $R = L_0/2$ (Figure 6.11). This formula can be used up to the point where the membrane cross-section has semicircular shape.

The deflation distance was obtained by measuring the vertical movement of the microscope stage when the focus is shifted from the edge to the centre of the membrane. The stage displacement was measured with a vertical height measurement instrument (Mitutoyo Absolute - resolution 1 µm). The tests were performed with empty wells as well as wells filled with deionized water. No difference in deflection was observed. Table 6.1 shows the strain values for 700, 1600 and 2000 Pa pressure values.

The system was also evaluated in a long term test under the same conditions to which the device would be exposed in a realistic biological experiment involving car-

Pressure (Pa)	Displacement (µm)	Strain
700	118±15	2.5%±0.6
1600	174±4	5.4%±0.25
2000	205±8	7.6%±0.6

Table 6.1: Pressure-Strain relation.

diomyocytes. Three plates were stretched with 2000 Pa pressure with 1 Hz frequency over a period of one month with medium in the well. No membrane breakage or leakages were identified, demonstrating the robustness of the system.

6.6. CONCLUSIONS

This chapter focused on the development of a system to use the Cytsotretch Heart-on-Chip presented in Chapter 4 and 5. The system was developed taking in consideration the following requirements: ease of use, manufacturability and compatibility.

The system is composed of two elements: a plate that encases multiple Cytostretch chips and a pneumatic system. The development of the first element resulted in a novel multi-well plate that can be used to simultaneously mechanically stimulate, and electrically monitor *in vitro* cell cultures. The plate includes four Cytostretch Chips mounted on a PCB. The wells and the insulation of the wirebonding were directly molded on top of the PCBs using a fully automatic FAM technology. This is the first time that such a packaging technique is employed for an OOC device. This work demonstrates that FAM can be a valuable option for directly molding a cell culture environment on top of OOC devices, creating a muti-well plate platform. The dimensions of the PCB and the mold can easily be re-defined to fit more Cytostretch chips in one plate, which will eventually be fabricated with a high-throughput format.

The new version of the Cytostretch chip was electrochemically characterized and the presented results showed an impedance in line with the electrodes presented in Chapter 5. During the characterization of the plate, cracks in the TiN lines connecting the contact pads and the electrodes were identified. This problem was attributed to a design flaw that resulted in breakage of the metal lines during the wafer dicing. In order to avoid the issue, and prevent other open circuits in the metal interconnects, it is necessary to optimize the mask design and eventually opt for meandering interconnects [13].

A new pneumatic system composed of a pump, condition boxes and software was successfully developed. A preliminary test of the complete system was performed to define the relation between the applied pressure and the resulting strain in the membrane and assess the robustness of the system. In the next chapter (Chapter 6), the functionality of the system will be tested even further by applying it to the mechanical stimulation of hiPSC-CMs.

REFERENCES

[1] N. Gaio, A. Waafi, M. Vlaming, E. Boschman, P. Dijkstra, P. Nacken, S. Braam, C. Boucsein, P. Sarro, and R. Dekker, *A multiwell plate organ-on-chip (ooc) device for in-vitro cell culture stimulation and monitoring,* in *2018 IEEE Micro Electro Mechanical Systems (MEMS)* (IEEE, 2018) pp. 314–317.

[2] D. Huh, B. D. Matthews, A. Mammoto, M. Montoya-Zavala, H. Y. Hsin, and D. E. Ingber, *Reconstituting organ-level lung functions on a chip,* Science **328**, 1662 (2010).

[3] M. Mastrangeli, S. Millet, and J. van den Eijnden-van Raaij, *Organ-on-chip in development: Towards a roadmap for organs-on-chip,* (2019).

[4] Gartner Inc., *5 trends emerge in the gartner hype cycle for emerging technologies, 2018,* (accessed: 06.03.2019).

[5] A. Junaid, A. Mashaghi, T. Hankemeier, and P. Vulto, *An end-user perspective on organ-on-a-chip: assays and usability aspects,* Current Opinion in Biomedical Engineering **1**, 15 (2017).

[6] V. van Duinen, S. J. Trietsch, J. Joore, P. Vulto, and T. Hankemeier, *Microfluidic 3d cell culture: from tools to tissue models,* Current opinion in biotechnology **35**, 118 (2015).

[7] B. Zhang and M. Radisic, *Organ-on-a-chip devices advance to market,* Lab on a Chip **17**, 2395 (2017).

[8] E. K. Sackmann, A. L. Fulton, and D. J. Beebe, *The present and future role of microfluidics in biomedical research,* Nature **507**, 181 (2014).

[9] Y. Liu, E. Gill, and Y. Y. Shery Huang, *Microfluidic on-chip biomimicry for 3d cell culture: a fit-for-purpose investigation from the end user standpoint,* Future science OA **3**, FSO173 (2017).

[10] Yole Développement, *Organs-on-chips 2017 report,* (accessed: 01.09.2018).

[11] Mimetas BV, *Easy-to-use,* (accessed: 06.03.2019).

[12] S. K. Pakazad, A. Savov, A. Van de Stolpe, and R. Dekker, *A novel stretchable micro-electrode array (smea) design for directional stretching of cells,* Journal of Micromechanics and Microengineering **24**, 034003 (2014).

[13] S. Khoshfetrat Pakazad, *Stretchable micro-electrode arrays for electrophysiology,* (2015).

[14] MultiChannel Systems GmbH, *Mea 1060,* (accessed: 06.03.2019).

[15] Boschman BV, *Fam,* (accessed: 06.03.2019).

[16] J. D. Stucki, N. Hobi, A. Galimov, A. O. Stucki, N. Schneider-Daum, C.-M. Lehr, H. Huwer, M. Frick, M. Funke-Chambour, T. Geiser, *et al.*, *Medium throughput breathing human primary cell alveolus-on-chip model,* Scientific reports **8**, 14359 (2018).

[17] CNBio, *Streamlined organs-on-a-chip solutions,* (accessed: 06.03.2019).

[18] Emulate Inc., *Platform & products,* (accessed: 01.01.2018).

[19] Fluigent, *Organ-on-chip platform,* (accessed: 06.03.2019).

[20] S. Rosset, M. Niklaus, P. Dubois, and H. R. Shea, *Metal ion implantation for the fabrication of stretchable electrodes on elastomers,* Advanced Functional Materials **19**, 470 (2009).

7

IT'S BEATING!

7.1. INTRODUCTION

As presented in Chapter 3, 5 and 6, in this thesis multiple hardware solutions for OOC applications were developed, by employing the POS guidelines and similar microfabrication technologies [1–5]. In most cases, the main challenge in the development of new devices is the identification of early adopters willing to test new materials, structures, and devices. In discussions with biologists in small pharma and biotech companies, as well as in academia, they confirmed their reluctance to work with untested and new OOC technologies. For the adoption of new OOC technology, it is thus necessary to execute a set of preliminary biological tests that assess its biocompatibility, tissue compatibility and its basic functionalities.

The development of new OOC technologies is complicated by the fact that technical universities are usually not equipped with the necessary facilities to perform these preliminary studies. In order to overcome this issue and guarantee a beta testing phase for new OOC technologies, technical universities can participate in biological projects, acting as hardware suppliers. In this case, the technological advancements come from the needs specified by biologists, encouraging the necessary biological testing. An example of this approach is the Gravitation project Netherlands Organ-on-Chip Initiative (NOCI) [6], in which TU Delft and the ECTM group provide OOC devices to biological groups of other universities.

As we focused on bringing the Cytostretch Heart-on-Chip a step closer to the market, the above mentioned requirements were taken in consideration. A biocompatibility assay of the device was performed in collaboration with Ncardia B.V. In particular a ro-

bust protocol for seeding cardiomyocytes on the device was defined. Last but not the least, the beta-testing of the basic functionalities of Cytostretch Heart-on-Chip, started by Pakazad et al. [7], was continued. Previous work has shown that the Cytostretch Heart-on-Chip can be used to detect electrical activities of cardiac cells both in a static environment as well as during a mechanical stimulation. However, the device was never used to mechanically stimulate cardiac cells in an assay lasting multiple days. The results of these tests, in combination with the results previously reported by Pakazad et al. [8], should be convincing evidence to persuade early adopters to start experiments with the Heart-on-Chip device in their assays.

7.2. PRELIMINARY TESTS OF THE CYTOSTRETCH DEVICE

Cytostretch chips, fabricated according the process presented in Section 3.2.1, were employed to test and optimize the seeding and culturing of human iPSC derived cardiomyocytes (hiPSC-CM). For these preliminary tests, a 1x1 cm^2 chip design with a circular PMDS membrane (diameter: 5 mm) was employed. In order to optimize the cell culturing, different parameters were tuned. Fibronectin and matrigel were evaluated as membrane coating. For both materials, different concentrations were used. Moreover, different cell densities were seeded onto the chips. These parameters were tuned by monitoring the corresponding cell and cell monolayer morphology by means of microscopy.

7.2.1. PROCEDURE

The chips were first placed in a 12 well plate, sterilized with 80% ethanol and dried under sterile laminar flow. The coating of the membranes, as well as the seeding of the cardiomyocyte were carried out accordingly to optimized protocols developed by Ncardia B.V.. The fibronecting was diluted 50 and 100 times in PBS. A droplet of 40 µL was carefully pipetted onto the membrane of each chip. The chips were then incubated at 37 °C and 5% CO_2 for 3 hours. The matrigel was diluted 50 and 100 times in Dulbecco's Modified Eagle Medium: Nutrient Mixture F-12 (DMEM/F12). Also in this case, a droplet of 40 µL of matrigel was carefully pipetted on the membranes. The chips with matrigel were incubated at room temperature for 45 minutes.

One vial of Pluricyte cardiomyocytes was thawed according to Ncardia protocol. The Cardiomyocytes were diluted in Pluricyte Cardiomyocyte Medium (PCM) to a density of ~30k/40 µL and ~50k/ 40 µL (corresponding to a cell density of ~750k/mL and ~1250k/mL respectively). After coating of the membranes, the excess coating solution was carefully removed using a vacuum powered suction system, and a droplet of 40 µL

cell suspension was carefully pipetted on each membrane. The chips were then incubated for 1 hour at 37 °C and 5% CO_2. After this initial seeding step, each well was filled with 500 µL pre-warmed PCM and then incubated at 37 °C and 5% CO_2. On day 1, 4, 6 and 8 the cells were monitored/inspected and the medium in each well was replaced with 500 µL of fresh pre-warmed PCM.

7.2.2. RESULTS AND DISCUSSIONS

Both fibronectin and matrigel functioned well as cell culturing matrix. However, matrigel showed a higher presence of areas without cells (i.e. in day 4) as can be seen in Figure 7.1a,b. In the particular case of fibronectin, seeding of either 30k and 50k cells per membrane resulted in conformal stable beating monolayers. Based on this result, fibronectin was chosen for consecutive tests. The culturing of 30k cells/membrane allowed the cells to spread out more (Figure 7.1c,d). Compared to standard polycarbonate well plates, the PDMS did not seem to affect the cell culture.

It is worth to notice that during this test, no plasma treatment was performed on the membranes, but this did not result in major issues. Even though in this phase a conformal monolayer was achieved, the poor wettability of the PDMS might have affected the cell adhesion at the edges of the membranes with both coatings, as shown in Figure 7.1e,f.

7

7.3. PRELIMINARY TESTS ON PACKAGED CYTOSTRETCH DEVICES

7.3.1. TEST 1

In order to verify whether the Cytostretch plate material affects the biocompatibility of the device, the protocol defined in Section 7.2.1 was applied to the wells of the plate. The cell numbers and medium volumes were adapted to the bottom area and the volume of the well. In this test, two different plates were tested: one with a molded well made of an optically transparent silicone (OE-6370 HF - Compound 1) and one made of an epoxy compound (EME-G770HP - Compound 2). The cell and monolayer morphology were analysed with optical microscopy. Moreover, the beating of cardiomyocytes was verified using calcium dye.

PROCEDURE

First, the wells of the plate were sterilized with 80% ethanol and dried under sterile laminar flow. On day zero, cardiomyocytes were thawed and counted according to the protocol of Ncardia. After this, the cells were diluted to ~196k cells/mL in PCM and 100 µL cell suspension was added to each well. This volume results in ~19.600 cells on a sur-

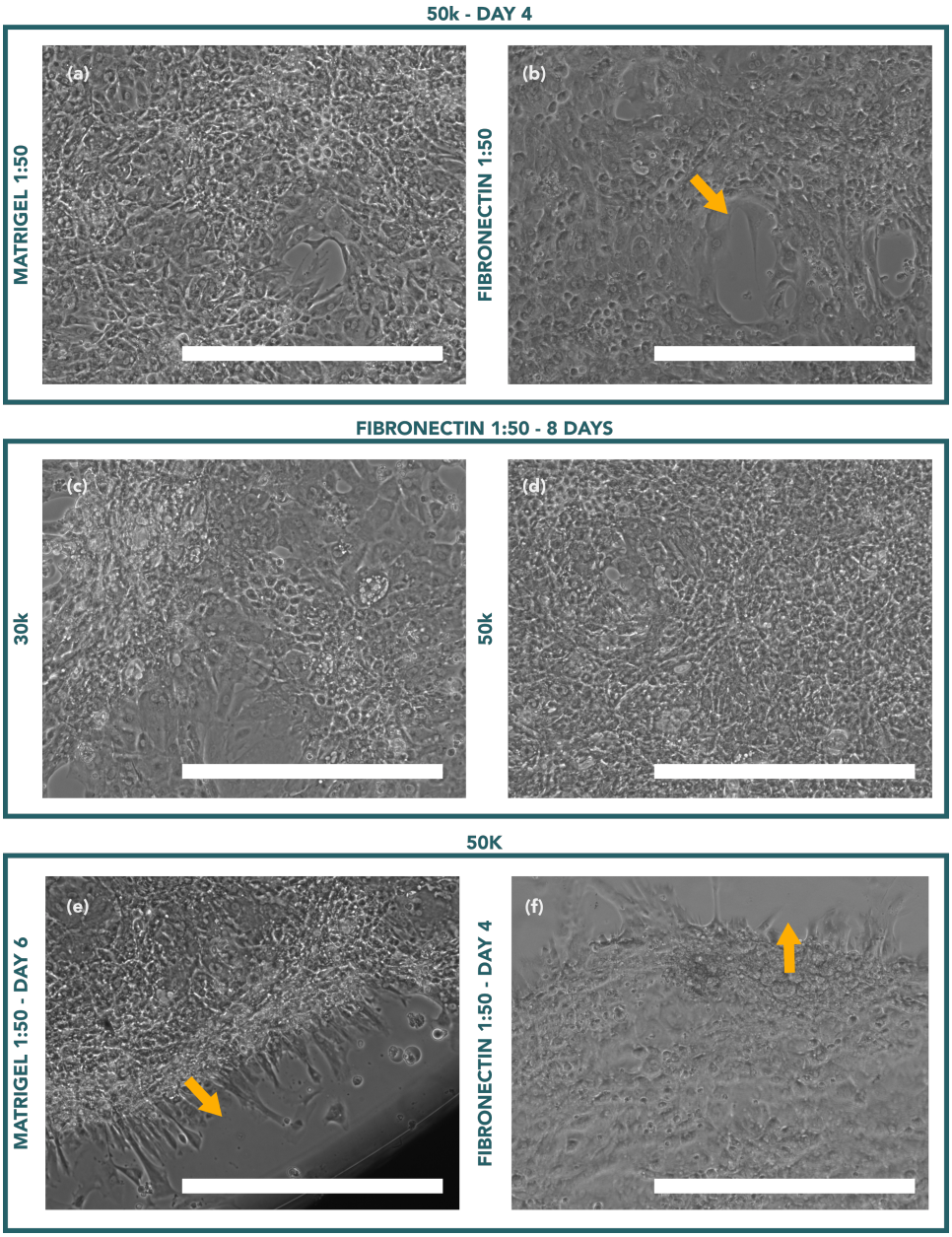

Figure 7.1: Representative images of cardiac monolayers cultured onto the Cytostretch chip. (a,b) Cell monolayers on matrigel and fibronectin with a 50k cells/membrane after 4 days. (b) Matrigel showed a higher presence of areas without cells (indicated by yellow arrow). (c,d) Cells monolayers on fibronectin (diluted 50 times) with 30k cells/membrane and a 50k cells/membrane densities. The culturing with 30k cells/membrane (c) allowed the cells to spread out more compared to (d). (e,f) Cells monolayers on fibronectin and matrigel, both showing poor cell adhesion on the edges of the membranes (indicated by yellow arrows). Scale bars: 500 µm.

face of 0.196 cm^2 (100k cells/cm^2). Unlike the previous test, the membranes placed at the bottom of the molded wells were dog-bone shaped described in Chapter 3 and had a smaller surface area. Consequently, in this case the added cell suspension covered not only the PDMS, but also the silicon around the membrane. The plates were covered with a lid to prevent dehydratation and were then incubated at 37 °C and 5% CO_2.

The wells were re-filled on day 1, 3, 4 with 100 µL fresh pre-warmed PCM per well. To monitor and document the culture, microscopy pictures were regularly taken. On day 7, calcium fluxes were visualised by adding Molecular Devices Calcium-6 dye.

RESULTS AND DISCUSSIONS

On day 2, cells were checked with phase contrast microscopy. Healthy and stretched cells attached to the membrane were observed (Figure 7.2a,b). Moreover, dead cells with a more rounded profile were found floating or loosely attached. Cells were monitored also on day 4 (Figure 7.2c,d). No particular change from day 2 to 4 was noticed. The whole membrane area was covered, even though the density of the cells per area of the well plate bottom was smaller as compared to the standard well plate. On day 7, the cells were checked with phase contrast microscopy, but no major changes were observed (Figure 7.2e,f). However, a pattern on the surface of the cells in Figure 7.2f affected the imaging of the cell culture with Compound 2. This was probably due to the membrane deflection or water condensation underneath the membrane.

On day 7, calcium dye was added to the cells to visualize calcium transients in the cells (Figure 7.3). While the cardiomyocytes appeared normal, no calcium transients were observed (no changes in fluorescence intensity were seen), suggesting the cells were not beating with both compounds. The possible cause for this could be connected to the molding materials. Moreover, the cell density did not seem to be uniform and reproducible among chips. This was attributed to the fact that in this case the cells were seeded directly on top of a dogbone shaped membrane. The smaller area, a shape that includes multiple corners, and the hydophobic surface of the PDMS, might have limited the wetting of the surface and eventually reduced the amount of cells on the bottom of the well. To improve wettability, a plasma treatment of the chips was implemented before the cell seedings [9].

During cell culturing, no leakage was observed, indicating adequate adhesion at the interface between the Cytostretch chips and the molded epoxy material.

7.3.2. TEST 2

As a consequence of the lack of spontaneous beating of the cardiac cells in **Test 1**, a new epoxy material was considered, Sumitomo G700LTD (Compound 3). The material

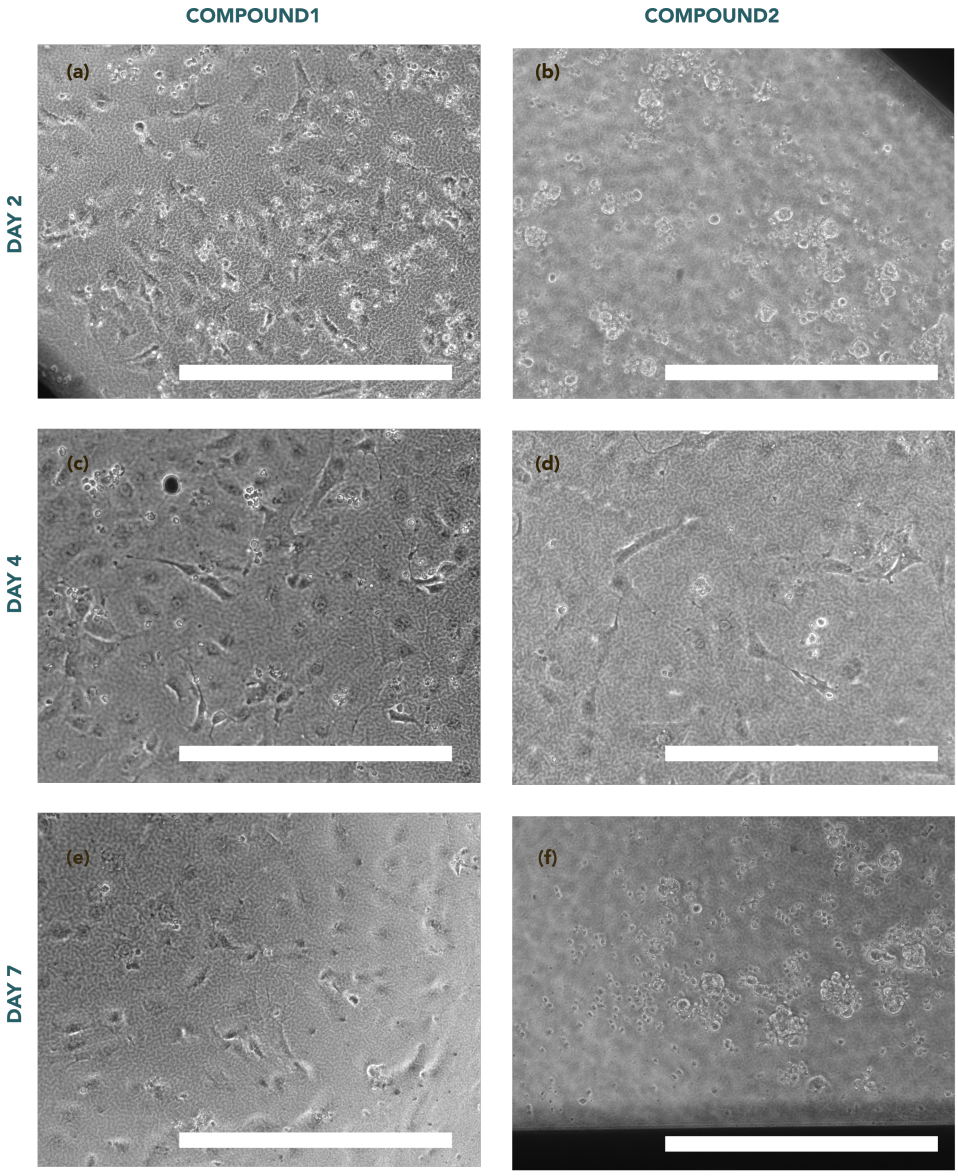

Figure 7.2: Representative images of cardiac monolayers cultured onto two Cytostretch plates fabricated with OE-6370 HF - Compound 1 and EME-G770HP - Compound 2 on day 2 (a,b), day 4 (c,d) and day 7 (e,f). Scale bars: 250 µm.

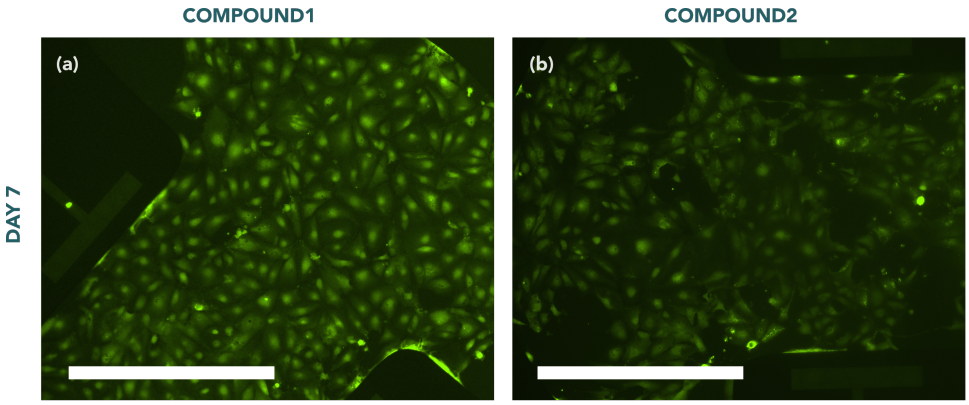

Figure 7.3: Microscopic image of hiPSC-CM cultured on the stretchable membrane for 7 days. The cells were stained with Calcium 6 dye (Molecular Devices). The Cardiomyocytes continue to appear normal and viable under fluorescent imaging even after seven days. No calcium transients were observed (no changes in fluorescence intensity were seen), suggesting the cells were not beating with both compounds. Scale bars: 2000 µm.

was previously used by InForMed partners in tests not presented in this work, and it was chosen here since it did not show biocompatibility issues. Before fabricating a plate with this material, a preconditioned medium test was performed.

PROCEDURE

Pieces of cured molding compound material (Compound 3) were cut and placed in a 12-well plate. The pieces were flushed with milliQ water and then sterilized with 80% ethanol. Using a vacuum powered suction system the fluid was removed. The residual liquid was left to evaporate under sterile laminar flow. PCM was added to the samples. The samples and the medium volumes were chosen to be in same range of the cell-culture surface area/volume ratio as in the Cytostretch device. The plates were sealed and incubated at 37 °C and 5% CO_2 for 10 days to obtain the preconditioned medium.

Pluricyte Cardiomyocytes were thawed and counted according the protocol of Ncardia. For the control plate, cells were diluted to ~340k cells/mL in PCM. 100 µL cell suspension was added per well, resulting in a cell density of ~100k cells/cm^2. The plate was then incubated at 37 °C and 5% CO_2 for 10 days. The PCM was replaced on day 1, 3, 4 with 100 µL of PCM per well. The cells cultured with preconditioned medium were tested in triplicates and they were compared to cells cultured in PCM that was incubated (named here incubated medium) in the same way as the medium that was exposed to the pieces of packaging material, to eliminate the effect of incubation on the medium itself.

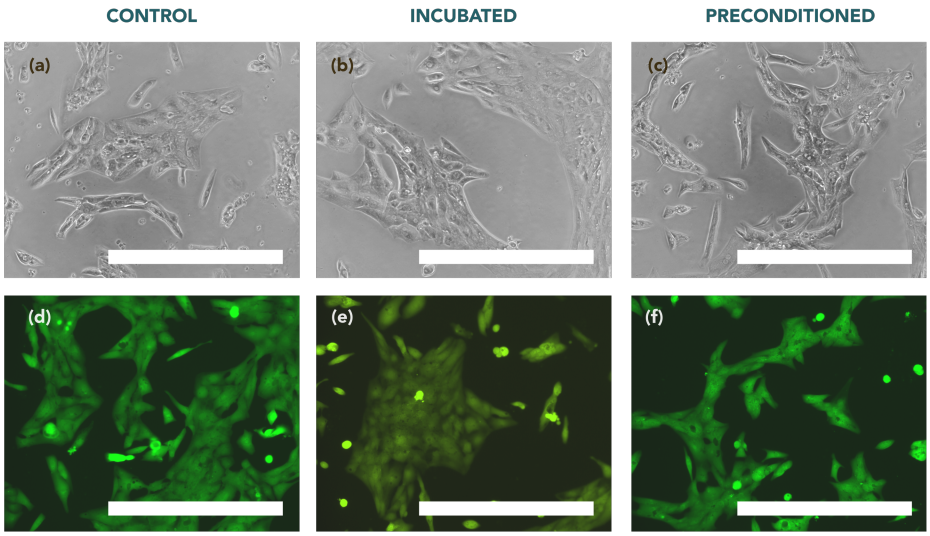

Figure 7.4: Representative images of cardiac cells cultured for 10 days in PCM (a,d), in incubated PCM (b,e) and in medium preconditioned with Sumitomo G700LTD - Compound 3 (c,f). Scale bars: 250 µm.

RESULTS AND DISCUSSIONS

On day 7, cells were inspected by microscopy. The cells incubated with the preconditioned medium showed more empty areas in the culture than the controls as can be seen in Figure 7.4.

On day 7, calcium dye was added to the cells to visualize calcium transients in the cells (Figure 7.4d,e,f). Calcium transients were observed in all cases suggesting that the cells are beating. Cells and groups of cells beat independently as cell-cell contact was not always present yet. Consequently, to achieve this, a higher seeding density of cells is required. The islands of cells seemed to be smaller in the samples with the preconditioned medium.

Based on these results, Compound 3 was chosen for consecutive tests. The cell seeding was adapted to the well plate format, and the resulting protocol is presented in Section 7.4.

7.4. PROTOCOL FOR CELL SEEDING ON THE FINAL CYTOSTRETCH PLATE

The surface of the packaged Cytostretch chips is first plasma-treated. This step makes the PDMS surface hydrophilic to allow for stronger cell-adhesion, which will improve

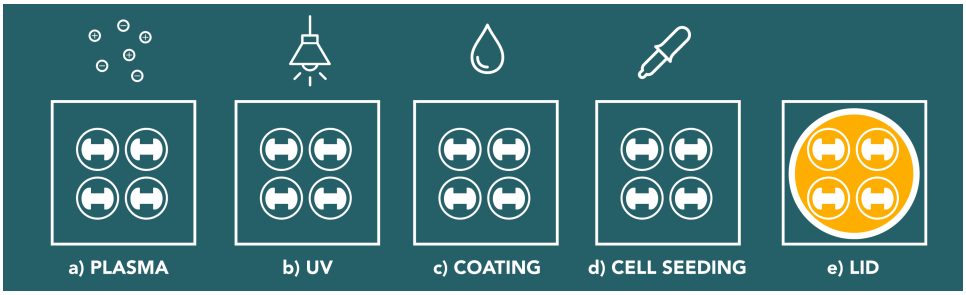

Figure 7.5: Schematic drawing presenting the protocol steps.

the reproducibility of the cell culture. The chips are treated with plasma for 1 min at 20-30 mA with a $2x10^{-1}$ mbar pressure. The chips are then sterilized for 40 minutes with an UV lamp (Philips TUV 30 8T lamp). After this, each well is covered with a 50 µl droplet of 1:100 fibronectin in PBS and is left for 3 hours at 37 °C and 5% CO_2.

One vial of Pluricyte Cardiomyocytes is thawed on day zero according to the protocol of Ncardia. After placing the vial in the incubator for 4 minutes, the content is gently transferred to a large 50 ml Falcon tube. The vial is rinsed with 1 ml PCM which is added to the 50 ml tube in a dropwise motion. Another 10 ml are added to the 50 ml tube in the same manner after which the cells of the homogeneous re-suspension are counted using a hemocytometer. After centrifugation the cardiomyocytes are suspended in PCM to a cell density of ~1k cell/µl. Upon aspiration of the fibronectin solution, a droplet of 40 µL of cell suspension is carefully pipetted at the centre of each well to achieve a coverage of ~2k cells/mm^2.

The plates are placed in the incubator for 1 hour (37 °C, 5% CO_2) after which 60 µl of PCM is added to each well. For the following 3 days, the medium is refreshed daily with 100 µl of PCM. After 3 days of static culturing the cell culture is ready to be mechanically stimulated with the Cytostrech system introduced in Chapter 6. The presented protocol is summarized in Figure 7.5 and the optical images of the stably beating and conformal cell culture obtained with it are shown in Figure 7.6 .

7.5. CARDIAC MONOLAYER MORPHOLOGY AFTER STRETCHING

This section reports the tests performed with the Cytostretch System, to identify the effects of the mechanical stimulation, at different frequencies and strain amplitudes, on the morphology of the cardiac monolayer.

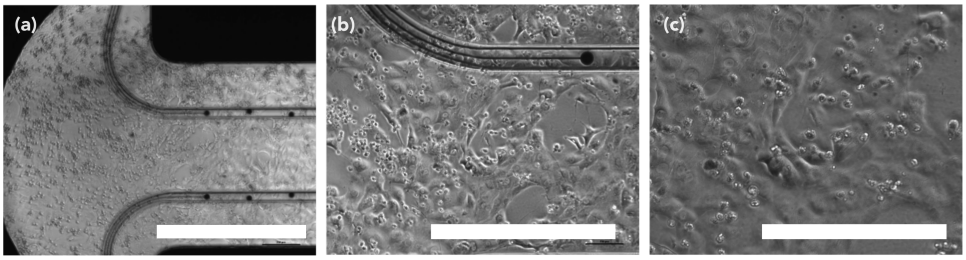

Figure 7.6: Representative images of the stably beating and conformal cell culture obtained following the presented protocol. Scale bars: (a) 2000 µm, (b) 500 µm), (c) 250 µm.

7.5.1. PROCEDURE

The protocol presented in Section 7.4 was followed to obtain an hiPSC-CM monolayer. Two different cell densities were tested, ~40k cells per well and ~60k cells per well.

Previous work [10–12] suggests that cardiomyocyte functionality and maturation can be improved by applying cyclic stress with i) frequencies of 1 Hz to 3 Hz, ii) elongation percentages up to 15%, and iii) over a duration of 2 days to 3 weeks. Taking into consideration previous work regarding mechanical stimulation of cardiac tissues [12–16], three conditions were chosen to evaluate the effect of cyclic stretching on the viability and morphology of the cardiac monolayer.

- **Condition 1:** 2.5% elongation percentage at 1 Hz;
- **Condition 2:** 7.5% elongation at 1 Hz;
- **Condition 3:** 7.5% elongation at 1.4 Hz.

The morphology of the cardiac monolayer was evaluated for all three conditions at day 0, day 3, day 5 and day 7 after application of the cyclic stretch. The cardiac monolayer of the different cell densities was evaluated in all conditions. Each condition was repeated in two wells.

7.5.2. RESULTS AND DISCUSSIONS

Representative images of the cardiac monolayer stimulated with **Condition 1** are shown in Figure 7.7a,b (40k cells/well density) and Figure 7.7c,d (60k cells/well density). The cardiac monolayer of the 40k cells/well condition kept a good morphology from day 0 until day 7. The monolayer with a 60k cells/well condition starts detaching from day 5 onwards as indicated by the yellow arrow in Figure 7.7c.

Representative images of the cardiac monolayer stimulated with **Condition 2** are shown in Figure 7.8a,b (40k cells/well density) and Figure 7.8c,d (60k cells/well density).

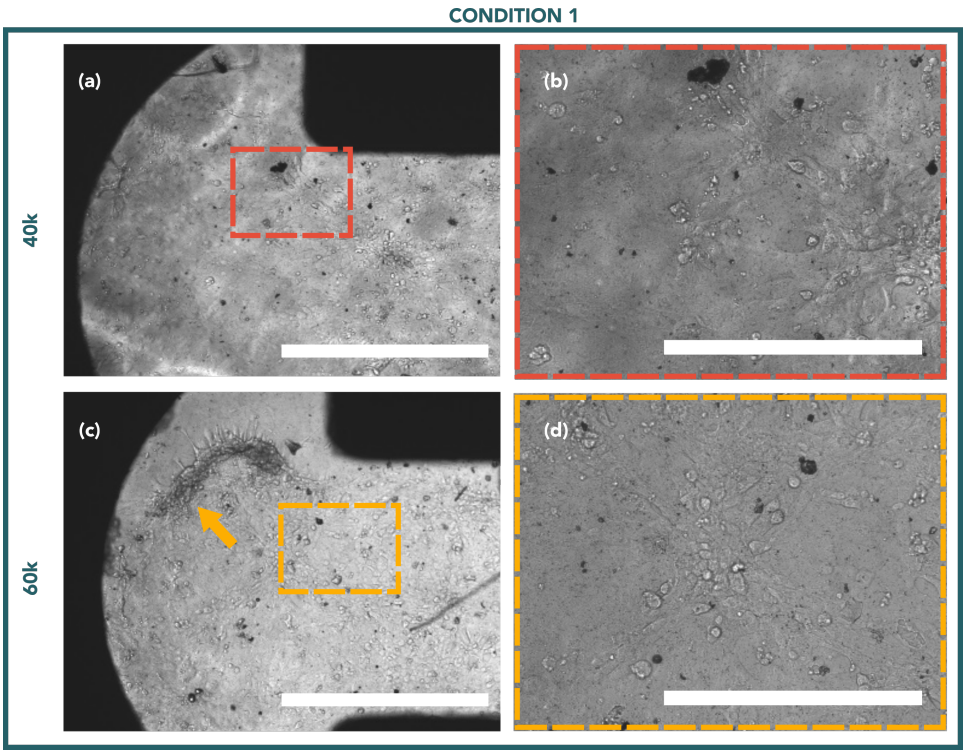

Figure 7.7: Representative images of the cardiac monolayer with a 40k (a,b) and 60k (c,d) cells/well density, stimulated with **Condition 1**. The monolayer with a 60k cells/well density shows cell detachment as indicated by the yellow arrow in (c). Scale bars: (a,c) 2000 µm, (b,d) 500 µm.

Cell detachment is evident in both cases from day 5 onwards. For the 60k cells/well condition the monolayer has detached considerably at day 7.

Representative images of the cardiac monolayer stimulated with **Condition 3** are shown in Figure 7.8e (40k cells/well density) and Figure 7.8f (60k cells/well density). The cardiac monolayer of the 40k cells/well condition kept a good morphology from day 0 until day 7 with some gaps in the cell layer forming after day 5 onwards, as indicated by the yellow arrows in Figure 7.8a. The monolayer with 60k cells/well density started detaching from day 5 onwards.

Although the experiments are limited in number and variations considered, a first observation can be that a 40k cells/well density leads to the formation of a more resilient cell monolayer. Additionally, increasing the strain seems to increase the detachment of the monolayer. The monolayer detachment is more prevalent from day 5 onwards, although in some cases the monolayer remains intact even up to day 7. Last but not the least, increasing the frequency from 1 Hz to 1.4 Hz does not have an impact on mono-

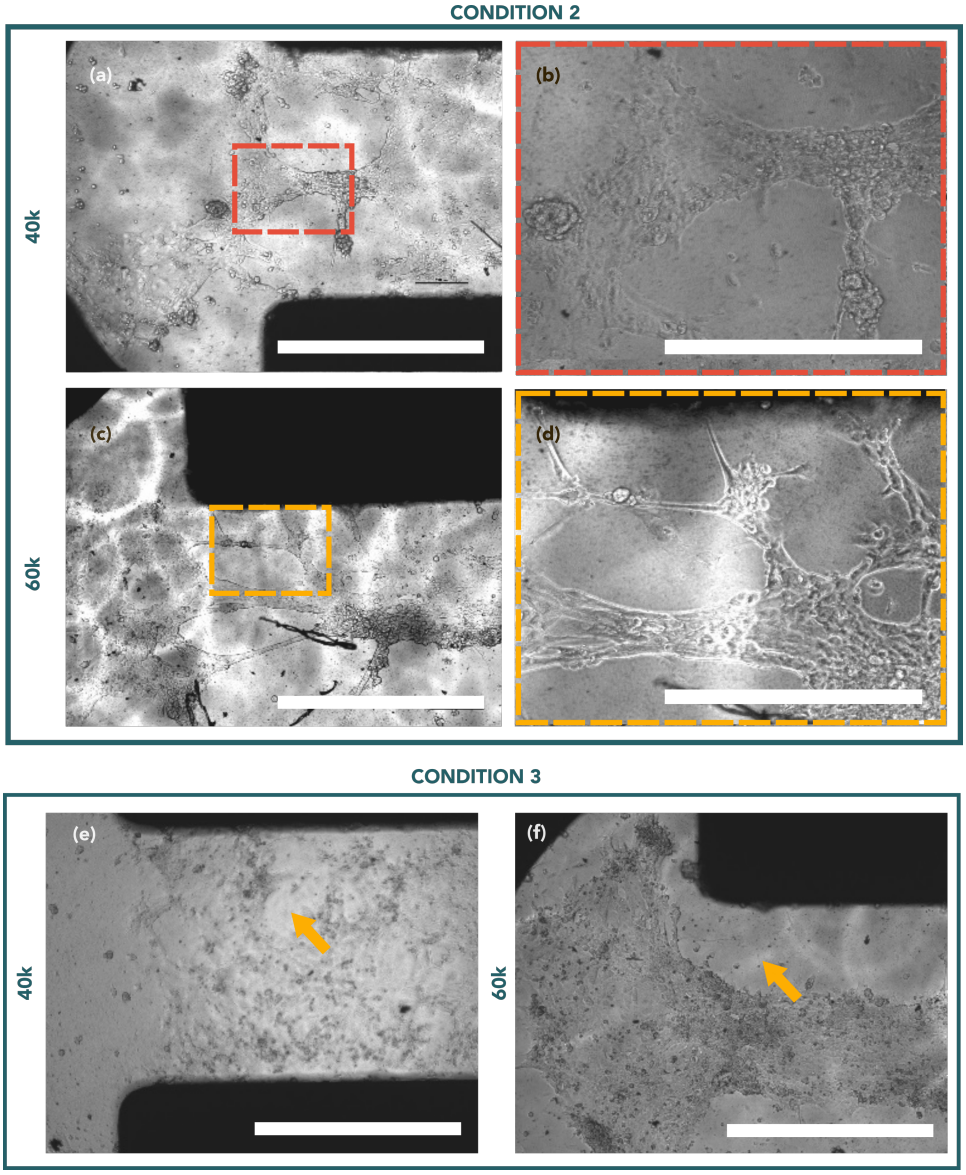

Figure 7.8: Representative images of the cardiac monolayer with a 40k (a,b) and 60k (c,d) cells/well density, stimulated with **Condition 2**. Both monolayers show severe cell detachment. (e,f) Representative images of the cardiac monolayer with a 40k (e) and 60k (f) cells/well density, stimulated with **Condition 3**. The monolayer with 40k cells/well density showed multiple gaps indicated by the yellow arrow in (e). The monolayer with a 60k cells/well density shows cell detachment as indicated by the yellow arrow in (f). Scale bars: (a,c,e) 2000 µm, (b,d,f) 500 µm.

layer morphology. Consequently, from this set of stimulation conditions, **Condition 1** (2.5% elongation - 1 Hz frequency) was selected because it resulted in a good monolayer and higher cell-attachment.

7.6. STRETCHING AND GENE EXPRESSION

This section reports the tests performed to determine whether the mechanical stimulation of the cardiac cells plated on the Cytostretch device has an impact on the gene expression of various markers associated with cardiac maturity.

7.6.1. PROCEDURE

For this test the protocol presented in Section 7.4 was followed. The following settings were chosen:

- Cell density: ~40k cells per well;
- Strain: 2.5% elongation;
- Frequency: 1 Hz; and
- 5 days stimulation.

Using this protocol, after 5 days no cell detachment and/or gaps were observed. As a control condition, cells were plated on Cytostretch plates that were not stimulated and kept in static condition for 5 days. Figure 7.9 shows the cell monolayers in static (control samples) and dynamic (simulated sample) conditions.

To ensure proper RNA yield in our experiment, two Cytostretch plates were used per condition (dynamic and static). After 5 days of cyclic stretch stimulation, the cells were collected from each well by enzymatic passaging and lysed. RNA was subsequently isolated and reverse transcribed to cDNA. Real time PCR (qPCR) was performed on various genes associated with cardiac maturity. Results were analyzed using the Livak method ($2^{-\Delta Ct}$). GAPDH was used as the housekeeping gene. The fold change data extrapolated were normalized to the control set.

7.6.2. RESULTS AND DISCUSSIONS

The qPCR results are shown in Figure 7.10. A clear upregulation was observed for genes SCN5A (sodium channel), KCNJ12 (IK1 current), PGC-1a (metabolism), MYL2 (sarcomere structure-beta light chain myosin), MYL7 (sarcomere structure-alpha light chain

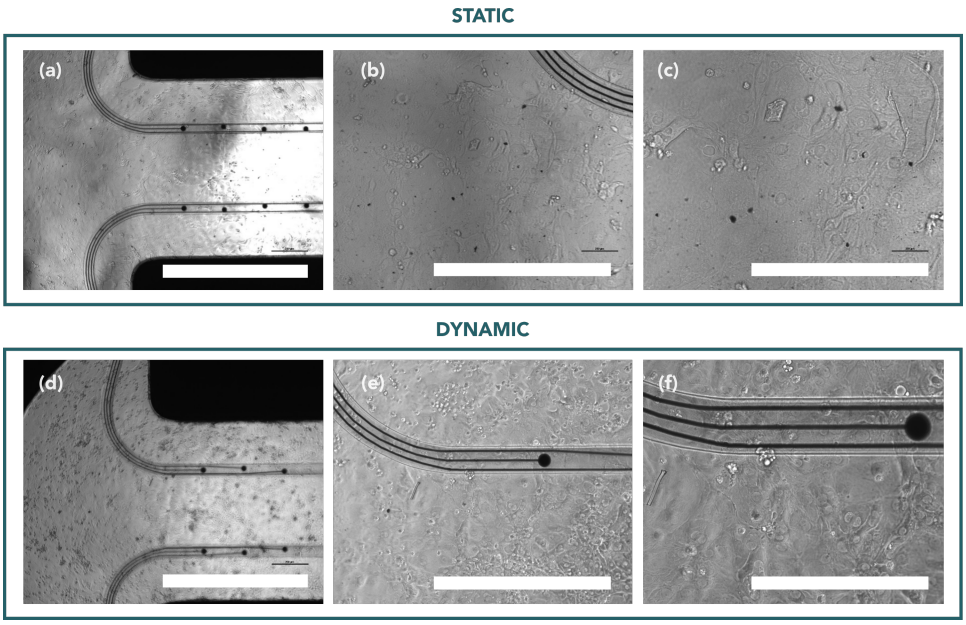

Figure 7.9: Representative images of the cardiac monolayer cultured with the protocol defined in Section 4.4 without (a,b,c) and with (c,d,e) cyclic mechanical stimulations (**Condition 1**). Scale bars: (a,d) 2000 µm, (b,e) 500 µm, (c,f) 250 µm.

myosin), MYH7 (sarcomere structure-beta-heavy chain myosin), SERCA (calcium handling), CASQ2 (calcium handling), RYR2 (calcium handling) and CACNA1C (calcium handling-L-type calcium ion channel) in the hiPSC-CMs that were under cyclic stress. A minor upregulation for genes KCNH2 (IKr current), NPPB (Natriuretic Peptide B) and TNNT2 (cardiac troponin) was also observed. Genes KCNQ1 (IKs current), MYH6 (sarcomere structure-alpha-heavy chain myosin), HCN4 (If current) were not upregulated (Figure 7.10).

These preliminary results showed that the cyclic stretch conditions chosen (1 Hz frequency - 2.5% elongation - 5 days stimulation) might have an impact on the expression of various genes associated with cardiomyocyte differentiation, in line with the results previously obtained by Mihic et al. [12]. However, it should be emphasized that these results are based on a single culture experiment, and that for a definite conclusion of the effect of cyclic stretching on the maturation of the cardiomyocytes this experiment should be repeated independently.

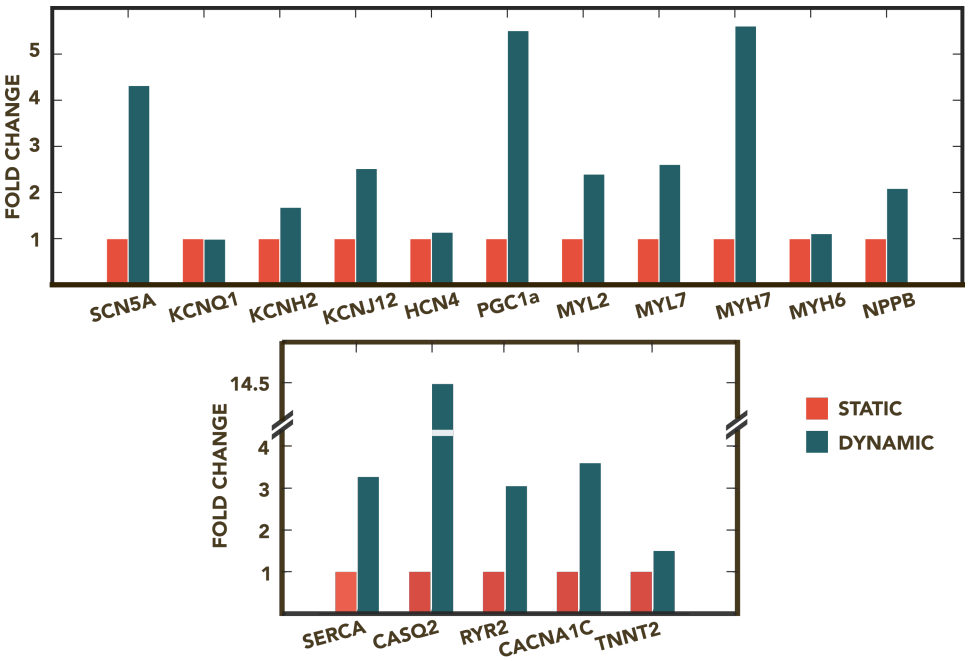

Figure 7.10: Qualitative PCR (qPCR) performed on various genes associated with cardiac maturity. Red: static control - blue: cyclically stretched sample.

7.7. CONCLUSIONS

In conclusion, this chapter aimed at encouraging the adoption of the system among early adopters, by performing a set of preliminary biological tests which assess its biocompatibility, tissue compatibility and its basic functionality. The biocompatibility of the chips was assessed by culturing hiPSC-CMs on the PDMS membranes before being packaged. Compared to standard polycarbonate well plates, the PDMS did not seem to affect the cell cultures, guaranteeing a uniform monolayer. The biocompatibility of the package material was addressed by culturing hiPSC-CMs onto the well of the plates and with preconditioned media tests. After these tests, an epoxy compound (Sumitomo G700LTD) was selected as the most optimal material for the package.

A robust and easy-to-follow protocol for seeding hiPSC cardiomyocytes into the wells of the Cytostretch wells was developed and optimized. Before seeding the cells in the wells, it is necessary to treat the PDMS membrane with an oxygen plasma treatment. A cell density of 40k cells/well and fibronectin as substrate coating are chosen. The protocol guarantees a conformal and reproducible healthy monolayer. The morphology of this monolayer was then studied during mechanical stimulations in a 5-days test. Ap-

plying a 7.5% strain resulted in the formation of gaps and detachment of the monolayer. A 2.5% strain did not result in any visible change in the morphology of the layer. The basic functionality of the device was then tested by applying a cyclic stretch (2.5% - 1 Hz) to the monolayer for 5 days. This resulted in a clear and visible impact on the expression of various genes associated with cardiomyocyte maturity. These experiment should be repeated and expanded to confirm that the mechanical stretch is affecting the maturation of the cardiomyocytes. Nevertheless, these tests, in combination with the results previously reported by Pakazad et al. [8], are convincing evidence to persuade early adopters to start experiments with the Heart-on-Chip device in their assays.

REFERENCES

[1] W. Quirós-Solano, N. Gaio, O. Stassen, Y. Arik, C. Silvestri, N. Van Engeland, A. Van der Meer, R. Passier, C. Sahlgren, C. Bouten, *et al., Microfabricated tuneable and transferable porous pdms membranes for organs-on-chips,* Scientific reports **8**, 13524 (2018).

[2] N. Gaio, B. van Meer, C. Silvestri, S. Pakazad, S. Vollebregt, C. Mummery, and R. Dekker, *Upside-down carbon nanotube (cnt) micro-electrode array (mea),* in *2015 IEEE SENSORS* (IEEE, 2015) pp. 1–4.

[3] N. Gaio, S. Kersjes, W. Q. Solano, P. Sarro, and R. Dekker, *Versatile and automated 3d polydimethylsiloxane (pdms) patterning for large-scale fabrication of organ-on-chip (ooc) components,* in *Multidisciplinary Digital Publishing Institute Proceedings*, Vol. 2 (2018) p. 873.

[4] N. Gaio, A. Waafi, M. Vlaming, E. Boschman, P. Dijkstra, P. Nacken, S. Braam, C. Boucsein, P. Sarro, and R. Dekker, *A multiwell plate organ-on-chip (ooc) device for in-vitro cell culture stimulation and monitoring,* in *2018 IEEE Micro Electro Mechanical Systems (MEMS)* (IEEE, 2018) pp. 314–317.

[5] N. Gaio, B. van Meer, W. Quirós Solano, L. Bergers, A. van de Stolpe, C. Mummery, P. Sarro, and R. Dekker, *Cytostretch, an organ-on-chip platform,* Micromachines **7**, 120 (2016).

[6] T. N. O. on Chip Initiative, *Noci website,* (accessed: 06.03.2019).

[7] S. K. Pakazad, A. Savov, A. Van de Stolpe, and R. Dekker, *A novel stretchable micro-electrode array (smea) design for directional stretching of cells,* Journal of Micromechanics and Microengineering **24**, 034003 (2014).

[8] S. Khoshfetrat Pakazad, *Stretchable micro-electrode arrays for electrophysiology,* (2015).

[9] D. Bodas and C. Khan-Malek, *Hydrophilization and hydrophobic recovery of pdms by oxygen plasma and chemical treatment—an sem investigation,* Sensors and Actuators B: Chemical **123**, 368 (2007).

[10] E. Ghafar-Zadeh, J. R. Waldeisen, and L. P. Lee, *Engineered approaches to the stem cell microenvironment for cardiac tissue regeneration,* Lab on a Chip **11**, 3031 (2011).

[11] A. Marsano, C. Conficconi, M. Lemme, P. Occhetta, E. Gaudiello, E. Votta, G. Cerino,

A. Redaelli, and M. Rasponi, *Beating heart on a chip: a novel microfluidic platform to generate functional 3d cardiac microtissues,* Lab on a Chip **16**, 599 (2016).

[12] A. Mihic, J. Li, Y. Miyagi, M. Gagliardi, S.-H. Li, J. Zu, R. D. Weisel, G. Keller, and R.-K. Li, *The effect of cyclic stretch on maturation and 3d tissue formation of human embryonic stem cell-derived cardiomyocytes,* Biomaterials **35**, 2798 (2014).

[13] W.-H. Zimmermann, K. Schneiderbanger, P. Schubert, M. Didie, F. Munzel, J. Heubach, S. Kostin, W. Neuhuber, and T. Eschenhagen, *Tissue engineering of a differentiated cardiac muscle construct,* Circulation research **90**, 223 (2002).

[14] N. L. Tulloch, V. Muskheli, M. V. Razumova, F. S. Korte, M. Regnier, K. D. Hauch, L. Pabon, H. Reinecke, and C. E. Murry, *Growth of engineered human myocardium with mechanical loading and vascular coculture,* Circulation research **109**, 47 (2011).

[15] G. Kensah, I. Gruh, J. Viering, H. Schumann, J. Dahlmann, H. Meyer, D. Skvorc, A. Bär, P. Akhyari, A. Heisterkamp, *et al.*, *A novel miniaturized multimodal bioreactor for continuous in situ assessment of bioartificial cardiac tissue during stimulation and maturation,* Tissue Engineering Part C: Methods **17**, 463 (2011).

[16] V. F. Shimko and W. C. Claycomb, *Effect of mechanical loading on three-dimensional cultures of embryonic stem cell-derived cardiomyocytes,* Tissue Engineering Part A **14**, 49 (2008).

8

BI/OND CYTOSTRETCH

This chapter is based on:

- N. Gaio and W. Quirós-Solano, Versatile 3D stretchable micro-environment for Organ-on-Chip devices fabricated with standard silicon technology, Patent NL2017 227B1 [1].

8.1. INTRODUCTION

The previous chapters discussed important steps necessary to bring the fabrication of OOC devices towards a more manufacturable and scalable process, using the upgraded version of the Cytostretch Platform. The resulting microfabricated Heart-on-Chip, showed the advantages of the directions taken by the ECTM group. The high degree of control on the fabrication and packaging provides a scalable stretchable MEA for high throughput screening.

As already mentioned in Chapter 1, OOCs are often defined as microfluididc chips. The term microfluidic system narrows down the definition of OOC, by not including the Cytostretch Heart-on-Chip presented in this thesis and other previously developed OOCs such as the Alveolix Lung on Chip [2], the Tara Bioscience Heart-on-Chip [3] and the Heart-on-Chip presented in [4]. Even though these models do not include a microfluidic channel per se, they recapitulate the microarchitecture and functions of living human organs with human tissues cultured on a chip, and should be consequently regarded as an OOC.

Nevertheless, several organs require microfluidic channels to be properly modelled. This can limit the range of applications of the Cytostretch platform and the OOS field.

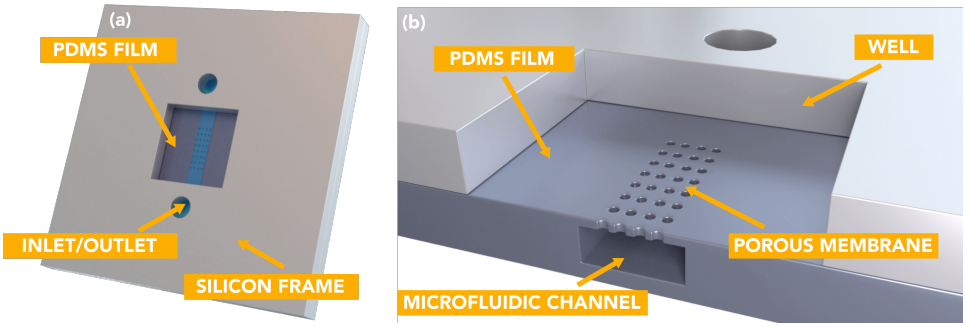

Figure 8.1: 3D rendering of a chip fabricated with the BI/OND platform. The figures are not drawn to scale.

For instance, microchannels have been used to recreate the microvasculature of tissues to provide cell cultures with better mechanical and biochemical stimulation, or to supply nutrients [5–7]. However, none of these functionalities is included in Cytostretch device.

This chapter proposes a microfluidic OOC device designed and fabricated following the POS guidelines. This device can be considered a novel platform, here named BI/OND platform, for the creation of microfluidic OOS[1].

Here, the technical aspects of its development are detailed, focusing on its fabrication. The platform is presented as an alternative to replace soft-lithography based OOC devices, combining their functionalities with potential additional features and applications. The platform opens the possibility for future research focused on introducing state-of-the-art silicon-based microfabrication technologies for monitoring and stimulating, e.g. sensors and actuators [8–11] in microfluidic channels, resulting in the convergence between OOC devices and *in situ* monitoring.

The BI/OND platform was employed to develop a microfluidic OOS compatible with macroscopic 3D tissues, such as organoids as illustrated by the perfusion of mid-brain organoids [12]. The chip was packaged and combined with an external perfusion system. In order to promote the adoptability of the system among early users, also for this device a validation of the basic functionalities is demonstrated.

8.2. BI/OND MICROFLUIDIC PLATFORM

The BI/OND platform consists of a microfluidic system embedded in a PDMS film (Figure 8.1). The PDMS film with the microfluidic system is supported by a Si frame, which

[1] The platform, patented in 2016 [1], was transferred from TU Delft to the company BIOND Solution B.V. (known as BI/OND) in January 2019 and was lately named BI/OND platform.

includes a well facing the PDMS layer. The frame also includes openings (inlet and outlet) to the channels in the film. The dimensions and the shape of the well, the channels and the openings can be adapted to a specific application. The channel can be fully isolated and confined in the PDMS film, or it can be brought in contact with the open well via a single opening or an array of micropores.

The fabrication procedure of the BI/OND platform is shown in Figure 8.2. A 500 µm Si wafer is used as a starting substrate. The process begins by the PECVD SiO_2 on the frontside (1 µm) and backside (5 µm) of the wafer. The backside is patterned to create a hard mask that later will be used to pattern the Si bulk (Figure 8.2a). Next, the wafer is coated with a first layer of PDMS, which will be the porous membrane of the microfluidic channels. The PDMS layer is then patterned, as presented in Chapter 2 (Figure 8.2b), to connect the microfluidic system with the well through opening and/or arrays of pores and to connect the microfluididc system to the Si inlet and outlet openings.

Subsequently, the wafer is coated with a sacrificial material that is patterned to form the microfluidic channel (Figure 8.2c). A second layer of PDMS is dispensed to form the bottom of the channel (Figure 8.2d). The thickness of the second PDMS layer is around 200 µm.

Finally, the PDMS film is released by etching the Si substrate and the SiO_2 etch stop layer from underneath the film, using DRIE and BHF etching, respectively (Figure 8.2e).

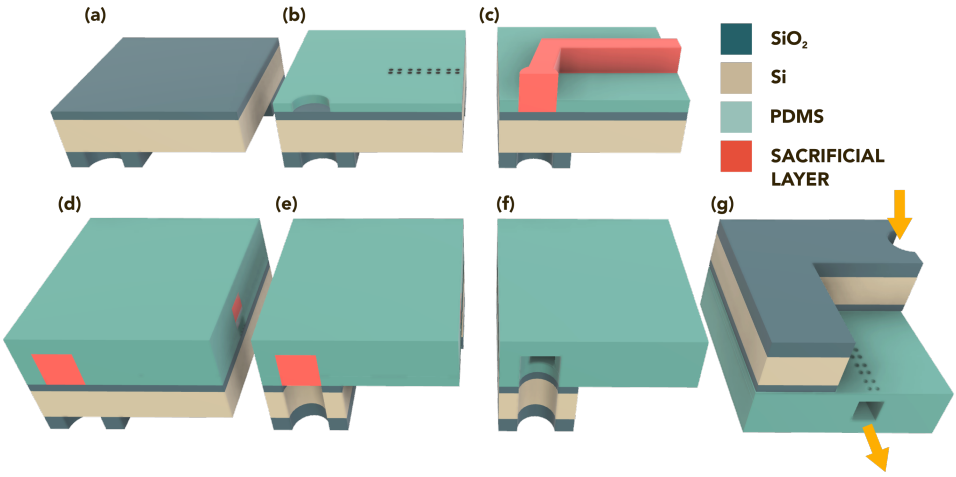

Figure 8.2: Process flow for the product platform: (a) 2 and 6 µm of PECVD SiO_2 are deposited on the backside and the front of the wafer; the backside of the wafer is patterned; (b) the PDMS is spin coated on the wafer and patterned; (c) the sacrificial layer is deposited and patterned, forming the microfluidic channel; (d) the second layer of PDMS is spin coated; (e) the Si and the SiO_2 under the film are etched; (f,g) the channel is then released. The figures are not drawn to scale.

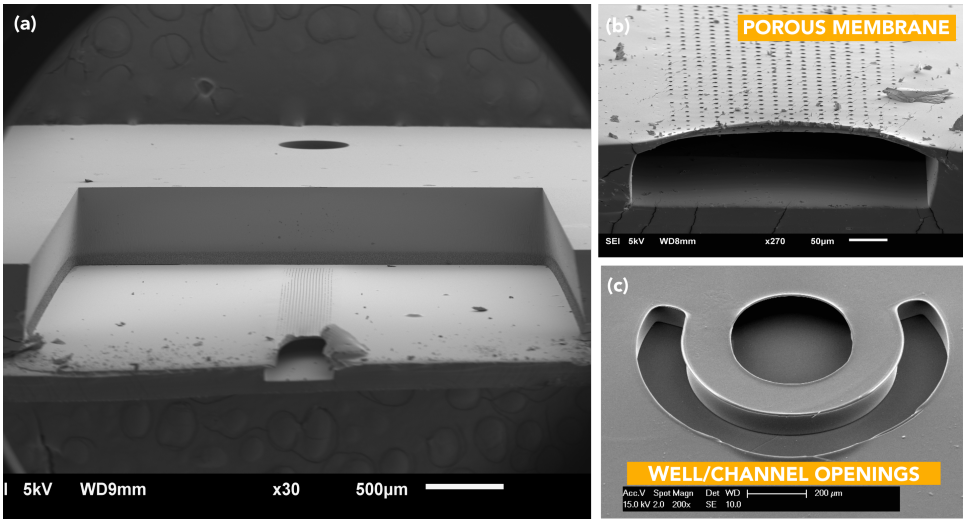

Figure 8.3: (a) SEM images of a chip fabricated with the BI/OND platform. The microfluidic channel can be connected to the top well through an array of pores (b) or single openings (c) as those presented by Tang et al. [13]. Scale bars: (a) 500 µm, (b) 50 µm and (c) 200 µm.

This step creates the well and the microfluidic inlet and outlet. The microchannel is opened by removing the sacrificial layer from the inside of the channel (Figure 8.2f,g). Figure 8.3a shows the cross section of a chip fabricated with the BI/OND platform. The channel and the well can be connected via a porous membrane, shown in Figure 8.3b, or via single and macroscopic openings as those shown in Figure 8.3c. The latter can be used to locally deliver drugs and compounds, as presented by Tang et al. [13].

8

8.3. MICROFLUIDIC OOS FOR ORGANOIDS PERFUSION

As mentioned in Chapter 1, over the past 8 years more than 30 start-up worldwide entered the OOC market, each with their own devices [14, 15]. The large number of new companies and universities working in the field, combined with the wide range of technologies, appears overwhelming for early-users, who might not see the unique advantages of each individual OOC technology. Under these circumstances, it is important to find a niche where the BI/OND chips can stand out and have a clear advantage over similar hardware solutions, such as the Wyss OOC [16, 17].

Previous work has focused on recapitulating 3D tissues by stacking 2D cell cultures, for example by seeding cells on the opposite sides of a porous membrane. On the contrary, little effort has been done to include complex 3D tissues such as organoids [18], cell bundles [3] and ex-vivo tissues [19] directly inside microfluidic OOCs [20]. 3D tis-

sues are essential for studying diseases affecting complex human tissues and organs, such as the brain. Indeed, the traditional models based on 2D tissues have shown strong limitations [12], as they cannot mimic specific *in vivo* phenomena.

In particular organoids have attracted increasing interest in the biology field [18, 21]. Organoids are 3D structures composed of self-organized cells (for example iPSC). These tissues, are created under specific environmental conditions that promote the differentiation and the arrangement of the cells to obtain structures that resemble *in vivo* tissue arrangement and function. Among others, muscle, skin, gut and brain organoids have been created, showing the wide range of application of this technology [22]. Organoids, like other 3D cell cultures, have shown the potential to model central nervous system diseases [12, 18].

OOC and organoids are often presented as competitive tools for the development of human tissues models. The main biological difference between these two technologies is related to the way how the tissues are formed. In the case of an OOC, a tissue is artificially constructed by arranging multiple cells cultures in different locations of the chip, thus, the cell arrangement is fully designed by the user. This feature provides a high degree of flexibility and control over the model, even though it limits the level of complexity achieved in the tissue [21]. In the case of an organoid, the organization of the tissue is mainly induced and controlled by the self-organization of cells [22, 23]. Consequently, organoids provide less flexibility, even though they results in more biologically relevant tissues. Despite these differences, these two technologies have the potential to be combined to obtain an even more predictive model.

Replacing the standard 2D cell cultures included in OOCs with organoids is likely to provide better *in vitro* tissues and disease models, while improving their ease of use. The seeding of cells in complex OOC such as the Lung-on-Chip presented by Hu et al. [24] strongly relies on manual pipetting of cells in small, closed and flexible chips, resulting in failure such as imperfect cells seeding, membrane fractures and/or cells waste. This step becomes even more complex when a 3D cell culture needs to be formed directly inside the chip. Organoids, on the other hand, can be cultured and grown outside the OOC, and then be transferred into the OOC to include phisiological factors such as flow and stretch to obtain an even more biologically relevant environment.

At the same time, OOCs can be used to improve organoids models. OOCs have the potential to promote differentiation and long-term culturing [21]. The large dimensions of the organoids, often results in poor nutrient and oxygen delivery due to gradients around the organoid. This can result in undesired differentiation, limited maturation of some of the cell types and necrotic regions [12, 18, 25]. These problems can be

addressed by simply exploiting the perfusion capabilities intrinsically available in microfluidic OOCs [21]. Brain organoids are additionally lacking endothelial cells. Here OOCs could offer a solution, since they have often been used to induce vascularization of tissues. [18, 21]. Moreover, OOCs will improve nutrient supply and refreshing to enhance the growth and long term viability of organoids [18, 21].

Because of the huge potential of organoids, it was decided to direct the development of the BI/OND platform towards the use of the microfluidic OOC environment for organoid perfusion.

The BI/OND platform, is by design, compatible with 3D tissue such as organoids and biopsies. As can be seen in Figure 8.1, the open well can be used as to host 3D tissues. This well has a depth in the same order of magnitude of an organoid after its maintenance period [12], resulting in a natural confinement of the tissue. The shape and dimensions of the well can be easily adapted to the specific shape of the 3D tissue or for a specific application. For example the well shape can be designed specifically to align the tissues with other structures on the chip. As the chip is fabricated following the POS guidelines, the PDMS layers and the Si frame are fabricated and processed with standard and robust processes that guarantee high interlayer adhesion, and prevents leakages [26]. Last but not the least, the intrinsically hydrophobic surface provided by the PDMS gives the perfect environment for culturing organoids and to preserve their architecture in a ultra-low-adhesion well plate [12].

8.3.1. THE BI/OND CHIP

The Organoid-on-Chip developed with the BI/OND platform is shown in Figure 8.4, depicting a 1x1 cm^2 chip with a 3x3 mm^2 well. The microfluidic system embedded in the PMDS film consists of a 500 µm wide and 90 µm high channel that connects the in- and outlet. The channel is connected to the well by a porous membrane composed of 4 µm diameter pores placed in a regular matrix to achieve a 2% porosity. In order to maximize the contact area between the microfluididc channel and the tissue, the channel was branched out into three subchannels (Figure 8.4c,d), providing a 40% coverage of the bottom area of the well, while still maintaining structural integrity of the membrane.

Throughput and yield data were tracked during the fabrication of 3 different batches of 5 wafers each. Even in a research environment, a reasonable device yield of 75% ±5% was obtained. Because the devices are made according to the POS guidelines, scaling of the device to high volume production should be straightforward.

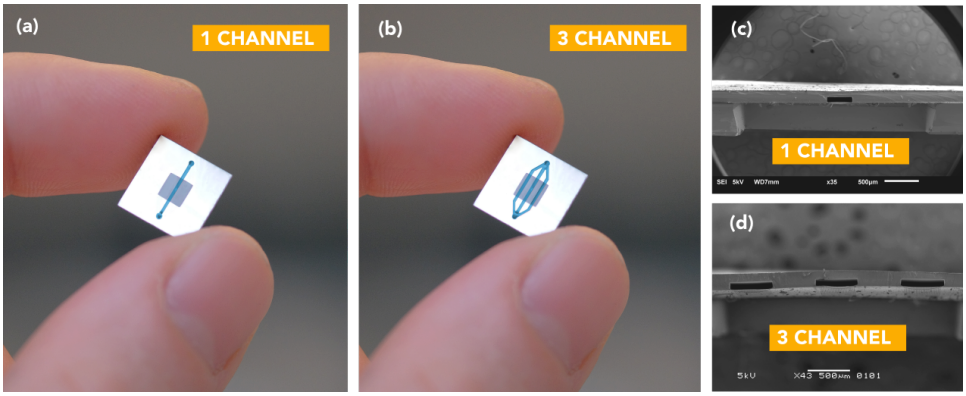

Figure 8.4: (a) Photograph of the standard chip fabricated with the BI/OND platform. (b) Photograph of the chip optimized for organoids perfusion applications. The channel branches out into three subchannels to maximize the contact area between the microfluididc channel and the tissue. (c) SEM cross section of the standard chip. (d) SEM cross section of the chip optimized for the organoid application. Scale bars: (c,d) 500 µm.

8.3.2. FROM CHIP TO SYSTEM

In order to use the BI/OND chip, the BI/OND plate was developed[2]. The plate was designed taking into consideration multiple factors:

- First, the plate needs to be compatible with 3D tissues (in particular organoids) and their handling during long term assays.
- Secondly, considering the fact the organoids can be quite expensive [22], the system should prevent any kind of leakage and/or waste.
- Thirdly, the plate and the chip are used in combination with an external pump. In order to simplify its use and to make the device as compatible as possible with standard workflow biological labs, the plate needs be easily assembled and connected to the pump.

The plate, shown in Figure 8.5, can house up to 6 chips in parallel. The throughput of the plate was considered sufficient for the validation of the device, also taking into consideration that the plate is used in combination with an external pump. Six chips are located on the bottom plate and each of them is covered by a top-plate. In order to guarantee a leak tight connection between the chip, the bottom plates and the top plate a ring that can be easily closed with a jar-like motion was employed. Since, each chip is sealed in between the bottom plate and a top plate, it is possible to individually take out one of

[2]The BI/OND plate was developed by BIOND Solution B.V. under the NWO Take-off 1 project "Design, fabrication and testing of an user-friendly interface for organ on chips".

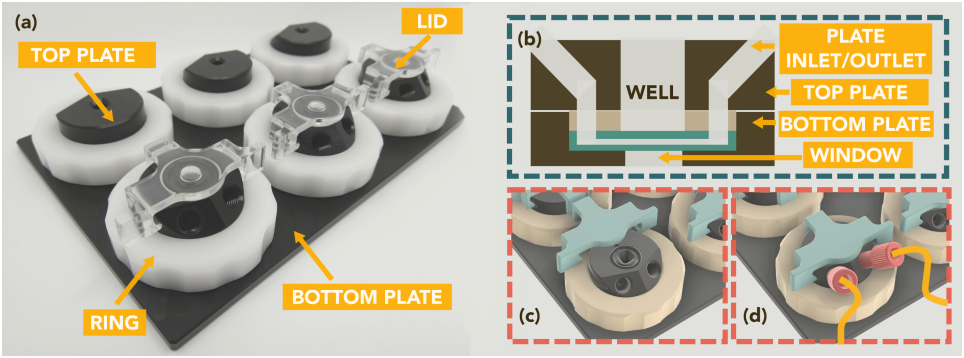

Figure 8.5: (a) Photograph of the BI/OND plate. (b) 2D sketch of the cross section of the plate and its microfluidic system. (c) 3D rendering of the plate with a open lid. (d) 3D rendering of the plate with perfusion tubing connected to one of the chip.

the chips during the test without affecting the others.

The top plate has two main functionalities. First, it increases the volume of the well of the chip from 10 µl to 300 µl. This allows to accomodate thicker tissues and it increases the amount of medium on top of the tissue. Secondly, the top plate provides an interface between the inlet and outlet of the chip to the tubing attached to the external pump (Figure 8.5b,c). The top plate connects standard 1/4" microfluidic fittings to the chip. Loading the chip inside the plate, assembling the plate and connecting the pump to it is straightforward. Different users have successfully assembled and used the system after only one tutorial of 2-3 hours.

In order to avoid contamination of the well with particles and bacteria, and to prevent the evaporation of medium, a lid was developed (Figure 8.5a,c). Unlike the lid developed for Cytostretch, this provides a leak tight environment that prevents the medium leaking from the channel up into the well. Without the lid, the medium would simply flow into the well instead of moving towards the outlet. The cells and/or 3D tissues can be inserted in the device by pipetting them inside the well and through the

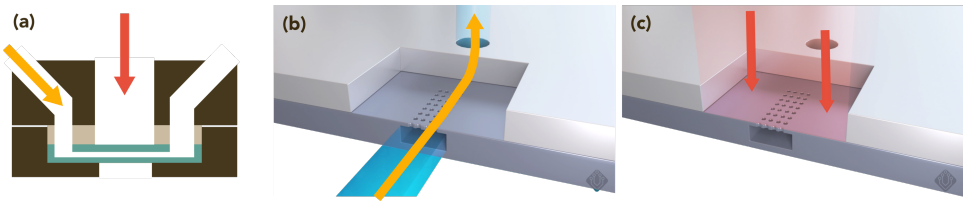

Figure 8.6: (a) Cells can be inserted with pipetting in two ways: through the top well of the plate (yellow arrows) or through the inlet and outlet of the plate (red arrows). This allows for seeding of cells directly in the chip channels (b) and into the chip well (c).

inlet and outlet of the top plate (Figure 8.6).

To image the tissue inside the device, an optical window provided in the bottom plate in combination with a transparent lid, allows the imaging of a tissue inside the device using an inverted optical microscope. The plate is currently compatible with multiple microscopes. Using the AMEX1000 LifeTechnologies microscopy, a magnification up to 20X can be easily employed to image a tissue on top of the PDMS film. The optical window, which is the thick layer of PDMS covering the channel, additionally provides oxygen to the tissue, as a result to the high diffusion rate of the elastomer [27].

The complete system is introduced in Section 8.3.3 with the testing of the basic functionality of the device.

The well and the microchannel form a microfluidic system similar to those presented in [28, 29]. A steady flow inside the channel allows to continously perfuse the well (Figure 8.7a). The inlet flow is distributed between the microchannel and the well. This distribution is consequence of the given geometric characteristics of the membrane, the microchannel, the well and the overall mass conservation of the medium in the device

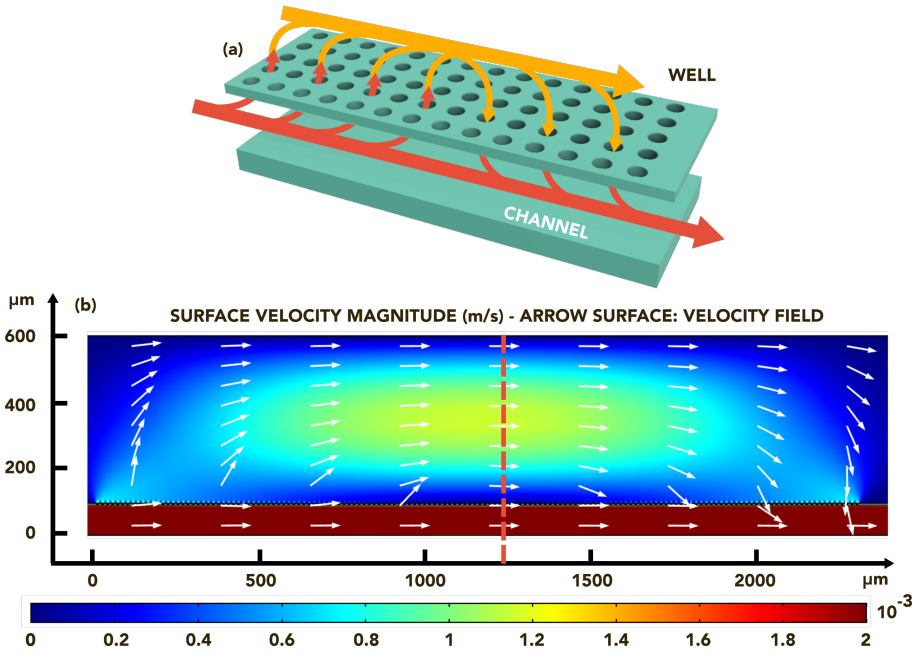

Figure 8.7: (a) 3D sketch of the porous membrane separating the channel and the well in the BI/OND device and the distribution of flow. The figure is not drawn to scale. (b) Velocity field in the microchannel and well in the BI/OND device (surface, arrow) obtained with Comsol Multiphysics for Q=30 µl/min.

[28].

A finite element (Comsol Multiphysics) simulation was used to provide 2D flow visualization. The 2D simulation was conducted with the actual channel and membrane geometries. However, due to the three orders-of-magnitude differences between the dimensions of the well and the pores, the well was replaced with a 500 µm high channel. In Figure 8.7c, the velocity field in the channel and the well are shown. To calculate the actual flowrate in the well, the velocity field was integrated over a cross section at the mid point of the geometry (red line in Figure 8.7c). The corresponding flowrate is 31% of the input flowrate.

8.3.3. BI/OND CHIP BASIC FUNCTIONALITIES

As mentioned above, the BI/OND device applied to organoids has the potential to: (a) improve how nutrients are supplied and refreshed, (b) promote maturation and vascularization of mid-brain organoids and (c) enhance growth and long term viability. As in the case of Cytostretch, this thesis does not aim at developing biological models, but instead, it aims to develop hardware and tools and promote their use among early adopters. To achieve this, the compatibility of the device with organoids was assessed. In particular, a protocol to perfuse organoid for 26 days inside the BI/OND device was defined. Using the BI/OND plate and chips, the medium around the organoids is continuously refreshed as explained in Section 8.3.2. At the end of the test, the organoid's shape and viability was assessed to verify whether the culture environment provided by the BI/OND device is suitable for these 3D tissues. Moreover, the effect of flow on Human Midbrain-Specific Organoids from Neuroepithelial Stem Cells with and without PINK1 gene mutation was studied. These tests were performed in a collaboration between BI/OND Solutions B.V. and the Developmental and Cellular Biology Group of the Luxembourg University.

PRELIMINARY TESTS

Preliminary biological assessment was performed to verify whether the chips are compatible with organoids, a preliminary test was performed. The first step consisted in placing 6 organoids, that had already gone through their maintenance period, on 6 different chips covered with a differentiation medium in a static environment (Figure 8.8a). The organoids were left inside the well for 7 days, and their shape was monitored at the end of this phase. The organoids did not stick to the chips and could be easily taken out of the wells with a pipette at the end of the test. More importantly, the organoids did not disaggregated, showing that the PDMS surface on the bottom of the well is not affecting their shape or structure, as can be seen in Figure 8.8b.

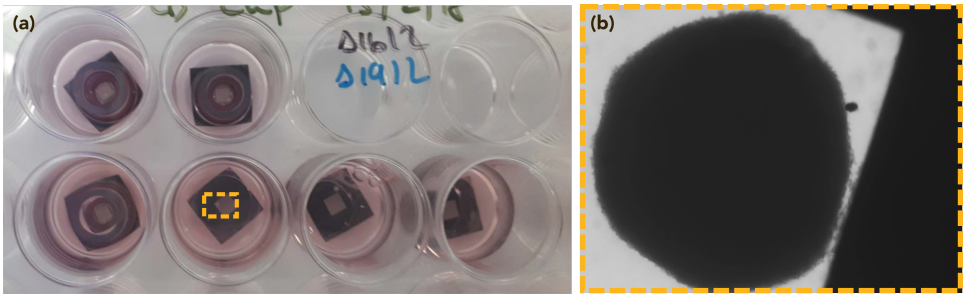

Figure 8.8: (a) Photograph of the six chips with organoids in a multi well plate. (b) Optical image of one organoid left for 7 days on top of the BI/OND chip.

PERFUSION TESTS

Six additional organoids were provided by the same group of the Luxembourg University. Three of them were carrying the PINK1 mutation, known to be a cause of autosomal recessive Parkinson's disease [30], and three of them were composed of the same cell line, but with the mutation corrected back to the wilde type sequence. The organoids were kept under maintenance medium for 1 week before proceeding with the differentiation and maturation protocol in the dynamic environment provided by the BI/OND device. The different elements composing the system and how to assemble it are shown in Figure 8.9 and Figure 8.10, respectively. The set up was prepared by first sterilising all the components (tubing, chip, adaptors reservoirs and plate) with 80% ethanol, and then rising them with DI water and medium. The set up was then assembled by connecting the reservoir of a Harvard syringe pump (Reservoir 1) to the plate with Polytetrafluoroethylene (PTFE) Tubing (1/16" OD X 1/32" ID), and the plate to a final reservoir (Reservoir 2) at ambient pressure (isolated with a filter).

Before loading the organoids inside the plate, the whole microfluididc system was

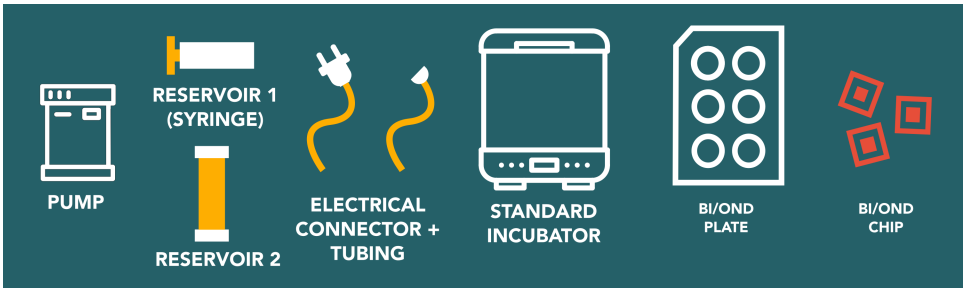

Figure 8.9: Schematic drawing of the different elements composing the BI/OND system: Syringe pump, syringes (Reservoir 1 and Reservoir 2), standard incubator, BI/OND plate and BI/OND chips.

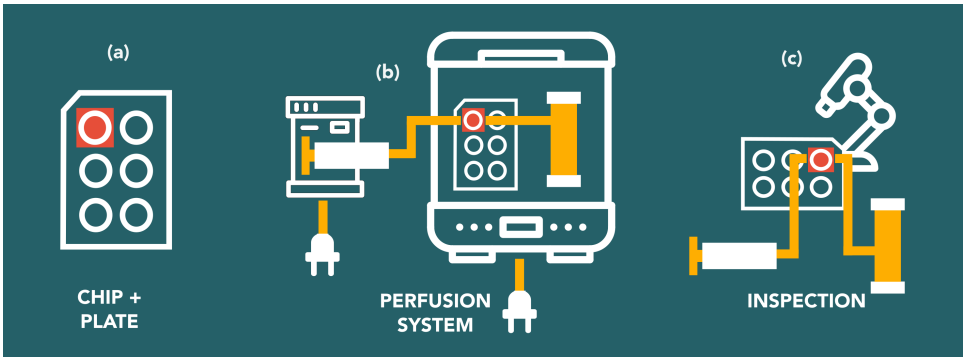

Figure 8.10: (a) Schematic drawing of the pneumatic set up with the BI/OND plate. The plate can be detached from the pneumatic system (with the reservoirs) during the test for microscopic analysis and refreshing the medium in the reservoirs.

filled with medium. This was done to reduce bubbles created during the assembly of the device and to test the integrity of the flow setup. The organoids were then inserted in the upper well by means of pipetting and additional medium was injected in the well. Before applying flow to the microfluidic system, the wells were properly sealed with the lids.

The pump chosen for the setup guarantees a recirculation of the medium (back and forth) between the two reservoirs. Even though this pump does not allow for unidirectional flow during the recirculation, this feature is not necessary since there are no cells cultured in the channel. A moderate flow rate of 30 µl/min was used. The tests started with 2.5 ml of medium in Reservoir 1 and 2.5 ml in Reservoir 2.

After setting up the system, the organoids were perfused for 26 days inside an incubator (Figure 8.11a). The perfusion was stopped every 4 days to replace the differentiation and the maturation medium inside the two reservoirs, following the protocol timeline presented in [12]. The medium inside the tubing is not replaced as it contains only 10% percent of the total medium volume in the system. During every replacement, the organoids are inspected under the microscope.

The full 26 day protocol was successfully completed for 5 out of the 6 organoids with one organoid disintegrating after few days. Figure 8.11 shows an organoid on day 0 (b), and day 26 (c). During the differentiation protocol, an enlargement of the organoids was observed in accordance with previous results. The organoids reached a mean core size of 1.089±0.11 mm after 12 days of perfusion and 1.2 ±0,08 mm after 19 days of perfusion. The lid provided by BI/OND never caused unwanted leakages during the entire test. The organoids showed similar morphology than those presented by [12], proving that the device is not negatively affecting the organoids.

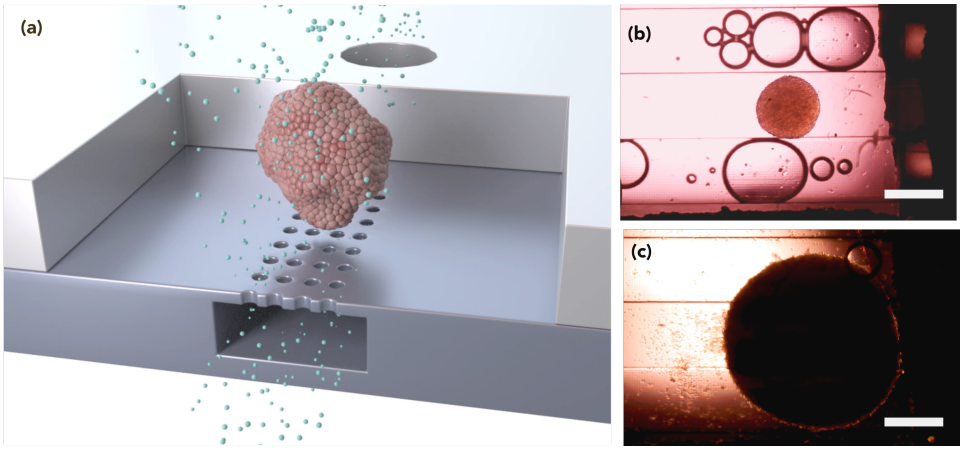

Figure 8.11: (a) 3D rendering of an organoid in the well. The figure is not drawn to scale. (b) Midbrain organoid in the microfluidic device (day 0). (c) Midbrain organoid in the microfluidic device (day 26). Scale bars: 500 µm.

To image the cells inside the organoids, two of the 6 organoids (one with the PINK1 mutation and one with the corrected gene) were fixed with 4% paraformaldehyde overnight at 4 °C and washed for three times with PBS for 15 min. After treatment, the organoids were embedded in 3-4% low-melting point agarose in PBS. The solid agarose block was sectioned with a vibratome (Leica VT1000s) into 50 µm sections. The sections were blocked on a shaker with 0.5% Triton X-100, 0.1% sodium azide, 0.1% sodium citrate, 2% BSA and 5% serum in PBS for 90 min at RT. Primary antibodies were diluted in the same solution but with only 0.1% Triton X-100 which was applied for 48 h at 4 °C.

After incubation with the primary antibodies, sections were washed three times with PBS and subsequently rinsed for 30 min at RT on a shaker. Then, the sections were incubated with the secondary antibodies in 0.05% Tween-20 in PBS for 2 h at RT and washed with 0.05% Tween-20 in PBS and Milli-Q water before they were mounted in Fluoromount-G mounting medium (Southern Biotech).

After fixation, immunofluorescence was performed to visualize neurons and in particular dopaminergic neurons. The image analysis was performed with Matlab using algorithms developed by Bolognin et al. [31]. The confocal pictures show that the morphology of the neurons was well preserved and there was no negative effect of the flow (Figure 8.12a,b,c,d). Moreover, organoids carrying PINK1 mutation showed a dramatic decreased percentage of dopaminergic neurons as compared to the same cell line where the mutation was corrected back to the wilde type sequence. The neurons showing a co-localization of the two midbrain dopaminergic markers TH and FOXA2 also decreased

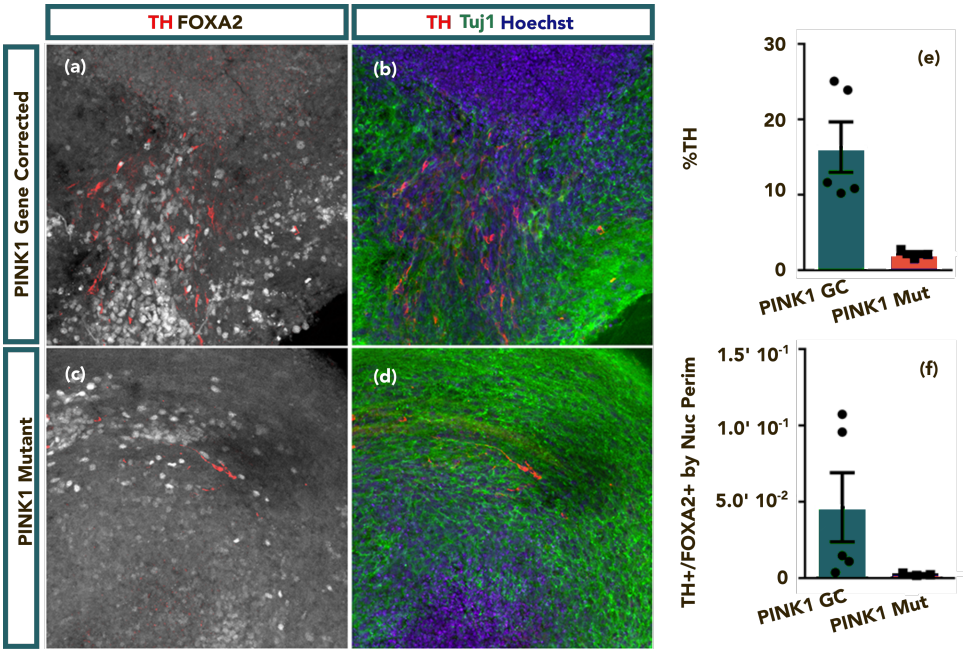

Figure 8.12: Midbrain organoids carrying the PINK1 mutation show decreased dopaminergic neurons compared to gene corrected oragnoids. (a,b,c,d) Representative confocal images showing the expression of the midbrain dopaminergic markers TH (red), and FOXA2 (gray) in PINK1 gene corrected and mutant organoids. The general neuronal marker Tuj1 (green) and nuclear marker Hoechst are also shown. (e,f) Quantification of the percentage of TH expressing cells and of the double positive TH+/FOXA2+ cells in the PINK1 gene corrected and mutant organoids. The image analysis was performed with Matlab using the algorithms presented in [31].

8

in PINK1 Mut compared to PINK1 GC (Figure 8.12e,f). This further confirms that there is an impairment of dopaminergic neurons in the PD-model, consistent to the phenotype observed in autoptic brain patient samples [32, 33]. In previous and not published tests performed at the Luxemburg University, it was not possible to observe the same extent of dopaminergic differentiation with organoids in static conditions. However, it should be emphasized that these results are based on two single organoids and for a definite conclusion of the effect of perfusion on the number of domaninergic neurons in healthy and the PD models, the test should be repeated.

8.4. CONCLUSIONS

This chapter presented a novel platform for the fabrication of microfluidic OOS. By developing and testing this platform, we proved that POS guidelines are not limited to the fabrication of PDMS membranes (such as the Cytostretch platform presented in

Chapter 3) but they can be also used to fabricate microfluidic chips, which are often used to replicate a minimal functional unit of an organ. The platform was successfully employed to fabricate a microfluidic chip suitable for the perfusion of organoids. The platform was adapted to this application by branching the main channel into three sub-channels and maximize the contact area between the microfluididc channel and the tissue. The chip was then combined with a plate that allows for handling of 6 chips in parallel. This tool provides an interface between the chips and the perfusion system employed to perfuse the channels in the chips.

After a preliminary biocompatibility assay of the chips, the basic functionality of the device (the perfusion of organoids) was tested with two types of mid-brain organoids, one carrying the PINK1 mutation and one with the corrected gene. The two groups of organoid, were perfused for 26 days in the device. At the end of the tests, the midbrain organoids carrying the PINK1 mutation showed decreased dopaminergic neurons compared to gene corrected oragnoids. The quantification of the percentage of TH expressing cells and of the double positive TH+/FOXA2+ cells in the PINK1 gene corrected and mutant organoids, confirmed that there is an impairment of dopaminergic neurons in the PD-model, consistent with patient samples [34]. Also in this case, these tests should be repeated and expanded to confirm these promising results. Nevertheless, we proved that it is possible to combine OOCs and organoids, by employing the open well OOS presented in this chapter.

REFERENCES

[1] N. Gaio and W. Quiros, *Versatile 3d stretchable micro-environment for organ-on-chip devices fabricated with standard silicon technology,* Patent **NL2017227B1**.

[2] A. O. Stucki, J. D. Stucki, S. R. Hall, M. Felder, Y. Mermoud, R. A. Schmid, T. Geiser, and O. T. Guenat, *A lung-on-a-chip array with an integrated bio-inspired respiration mechanism,* Lab on a Chip **15**, 1302 (2015).

[3] J. W. Miklas, S. S. Nunes, B. Zhang, and M. Radisic, *Design and fabrication of biological wires,* in *Cardiac Tissue Engineering* (Springer, 2014) pp. 157–165.

[4] A. Marsano, C. Conficconi, M. Lemme, P. Occhetta, E. Gaudiello, E. Votta, G. Cerino, A. Redaelli, and M. Rasponi, *Beating heart on a chip: a novel microfluidic platform to generate functional 3d cardiac microtissues,* Lab on a Chip **16**, 599 (2016).

[5] A. Queval, N. R. Ghattamaneni, C. M. Perrault, R. Gill, M. Mirzaei, R. A. McKinney, and D. Juncker, *Chamber and microfluidic probe for microperfusion of organotypic brain slices,* Lab on a Chip **10**, 326 (2010).

[6] D. Kim, X. Wu, A. T. Young, and C. L. Haynes, *Microfluidics-based in vivo mimetic systems for*

the study of cellular biology, Accounts of chemical research **47**, 1165 (2014).

[7] T. Das and S. Chakraborty, *Perspective: Flicking with flow: Can microfluidics revolutionize the cancer research?* Biomicrofluidics **7**, 011811 (2013).

[8] S. K. Pakazad, A. Savov, A. Van de Stolpe, and R. Dekker, *A novel stretchable micro-electrode array (smea) design for directional stretching of cells,* Journal of Micromechanics and Microengineering **24**, 034003 (2014).

[9] A. K. H. Achyuta, A. J. Conway, R. B. Crouse, E. C. Bannister, R. N. Lee, C. P. Katnik, A. A. Behensky, J. Cuevas, and S. S. Sundaram, *A modular approach to create a neurovascular unit-on-a-chip,* Lab on a Chip **13**, 542 (2013).

[10] A. Gaitas, R. Malhotra, T. Li, T. Herron, and J. Jalife, *A device for rapid and quantitative measurement of cardiac myocyte contractility,* Review of Scientific Instruments **86**, 034302 (2015).

[11] Q. Hamid, C. Wang, Y. Zhao, J. Snyder, and W. Sun, *A three-dimensional cell-laden microfluidic chip for in vitro drug metabolism detection,* Biofabrication **6**, 025008 (2014).

[12] A. S. Monzel, L. M. Smits, K. Hemmer, S. Hachi, E. L. Moreno, T. van Wuellen, J. Jarazo, J. Walter, I. Brüggemann, I. Boussaad, *et al., Derivation of human midbrain-specific organoids from neuroepithelial stem cells,* Stem Cell Reports **8**, 1144 (2017).

[13] Y. T. Tang, J. Kim, H. E. López-Valdés, K. Brennan, and Y. S. Ju, *Development and characterization of a microfluidic chamber incorporating fluid ports with active suction for localized chemical stimulation of brain slices,* Lab on a Chip **11**, 2247 (2011).

[14] B. Zhang and M. Radisic, *Organ-on-a-chip devices advance to market,* Lab on a Chip **17**, 2395 (2017).

[15] Y. Développement, *Organs-on-chips 2017 report,* (accessed: 01.09.2018).

[16] D. Huh, B. D. Matthews, A. Mammoto, M. Montoya-Zavala, H. Y. Hsin, and D. E. Ingber, *Reconstituting organ-level lung functions on a chip,* Science **328**, 1662 (2010).

[17] D. Huh, H. J. Kim, J. P. Fraser, D. E. Shea, M. Khan, A. Bahinski, G. A. Hamilton, and D. E. Ingber, *Microfabrication of human organs-on-chips,* Nature protocols **8**, 2135 (2013).

[18] N. D. Amin and S. P. Paşca, *Building models of brain disorders with three-dimensional organoids,* Neuron **100**, 389 (2018).

[19] T. G. Meijer, K. A. Naipal, A. Jager, and D. C. van Gent, *Ex vivo tumor culture systems for functional drug testing and therapy response prediction,* Future science OA **3**, FSO190 (2017).

[20] F. Piccinini, I. D. Santis, and A. Bevilacqua, *Advances in cancer modeling: fluidic systems for increasing representativeness of large 3d multicellular spheroids,* BioTechniques **65**, 312 (2018).

[21] X. Yin, B. E. Mead, H. Safaee, R. Langer, J. M. Karp, and O. Levyx, *Engineering stem cell organoids,* Cell stem cell **18**, 25 (2016).

[22] C. Tachibana, *Stem-cell culture moves to the third dimension.* Nature **558**, 329 (2018).

[23] A. Skardal, T. Shupe, and A. Atala, *Organoid-on-a-chip and body-on-a-chip systems for drug*

screening and disease modeling, Drug discovery today **21**, 1399 (2016).

[24] Q. Yang, Q. Lian, and F. Xu, *Perspective: Fabrication of integrated organ-on-a-chip via bioprinting,* Biomicrofluidics **11**, 031301 (2017).

[25] E. Berger, C. Magliaro, N. Paczia, A. S. Monzel, P. Antony, C. L. Linster, S. Bolognin, A. Ahluwalia, and J. C. Schwamborn, *Millifluidic culture improves human midbrain organoid vitality and differentiation,* Lab on a Chip **18**, 3172 (2018).

[26] K.-S. Koh, J. Chin, J. Chia, and C.-L. Chiang, *Quantitative studies on pdms-pdms interface bonding with piranha solution and its swelling effect,* Micromachines **3**, 427 (2012).

[27] M. D. Brennan, M. L. Rexius-Hall, L. J. Elgass, and D. T. Eddington, *Oxygen control with microfluidics,* Lab on a Chip **14**, 4305 (2014).

[28] H. H. Chung, M. Mireles, B. J. Kwarta, and T. R. Gaborski, *Use of porous membranes in tissue barrier and co-culture models,* Lab on a Chip **18**, 1671 (2018).

[29] H. H. Chung, C. K. Chan, T. S. Khire, G. A. Marsh, A. Clark, R. E. Waugh, and J. L. McGrath, *Highly permeable silicon membranes for shear free chemotaxis and rapid cell labeling,* Lab on a Chip **14**, 2456 (2014).

[30] S. Gandhi, A. Wood-Kaczmar, Z. Yao, H. Plun-Favreau, E. Deas, K. Klupsch, J. Downward, D. S. Latchman, S. J. Tabrizi, N. W. Wood, *et al., Pink1-associated parkinson's disease is caused by neuronal vulnerability to calcium-induced cell death,* Molecular cell **33**, 627 (2009).

[31] S. Bolognin, M. Fossépré, X. Qing, J. Jarazo, J. Ščančar, E. L. Moreno, S. L. Nickels, K. Wasner, N. Ouzren, J. Walter, *et al., 3d cultures of parkinson's disease-specific dopaminergic neurons for high content phenotyping and drug testing,* Advanced Science , 1800927 (2018).

[32] E. M. Valente, P. M. Abou-Sleiman, V. Caputo, M. M. Muqit, K. Harvey, S. Gispert, Z. Ali, D. Del Turco, A. R. Bentivoglio, D. G. Healy, *et al., Hereditary early-onset parkinson's disease caused by mutations in pink1,* Science **304**, 1158 (2004).

[33] A. Domanskyi, H. Alter, M. A. Vogt, P. Gass, and I. A. Vinnikov, *Transcription factors foxa1 and foxa2 are required for adult dopamine neurons maintenance,* Frontiers in cellular neuroscience **8**, 275 (2014).

[34] A. Domanskyi, H. Alter, M. A. Vogt, P. Gass, and I. A. Vinnikov, *Transcription factors foxa1 and foxa2 are required for adult dopamine neurons maintenance,* Frontiers in cellular neuroscience **8**, 275 (2014).

9

CONCLUSIONS AND RECOMMENDATIONS

9.1. CONCLUSIONS

Organ-on-Chip devices have the potential to disrupt the way pharmaceutical products are being developed and tested. This thesis aims at bringing the OOC field a step closer to mainstream adoption, by re-designing their fabrication processs through a combination of polymer processing and silicon microfabrication. In particular, this thesis demonstrates that a material commonly used for the fabrication of OOCs devices, PDMS, can be processed with silicon based fabrication techniques. In order to achieve this, a set of guidelines for PDMS processing on silicon, called here PDMS on Silicon (POS) guidelines, was defined and reported in Chapter 2. These guidelines were then employed for the development of two OOC platforms: Cytostretch and the BI/OND platform (Chapter 3-5 and 8, respectively). For each platform one prototype product was realized and its basic functionalities were tested (Chapter 6, 7 and 8). In order to differentiate these devices from OOCs fabricated with soft-lithography, the term Organ-on-Silicon (OOS) was created. The main contribution to the field are stated below.

Contribution 1: POS Guidelines

In this thesis robust and reproducible techniques are defined to deposit, pattern, and transfer PDMS layers onto silicon. This guarantees that the wafers can be further processed in conventional CR tools, without damaging or altering the PDMS structures or contaminating the machines used.

The deposition process was developed and characterised. This resulted in a uniform

deposition process that guarantees variations of only ±0.1 and ±0.2 µm measured across the wafer and across a batch of wafers, respectively. Additionally, an automated lithography process on PDMS was presented. Features down to 2 µm were achieved without critical issues.

A dry etching recipe to pattern PDMS was presented and tested. The recipe guarantees an etching rate of around 0.4 µm/min and it was used to pattern standard porous membranes with a wide range of porosity and 3D scaffolds.

Contribution 2: Cytostretch platform

The first OOS platform consists of a microfabricated PDMS membrane with four different modules that can be independently inserted into the main fabrication flow without affecting other features and by adding functionality depending on the requirements of a particular application. The limitations of this platform, and in particular the Heart-on-Chip developed with it, were highlighted and addressed in this work. The identified issues relate to: manufacturability, performance, and ease of use.

- **Manufacturability**

  The fabrication of the Cytostretch Heart-on-Chip is affected by two process steps: the use of parylene, and the need to dry etch the PDMS. In this thesis we successfully eliminated parylene from the device by insulating the TiN interconnects with polyimide. The deposition and patterning process for this material were successfully defined and optimized. In order to integrate this material into the Cytostretch device, the adhesion of the new polymer stack included in the device was improved.

  In order to avoid PDMS dry etching, this thesis presents a new way to deposit and pattern a PDMS layer with automated 3D molding techniques, and a commercially available molding system. Different 3D PDMS structures were created. In particular a 200 µm-thick PDMS layer was conformally deposited on 100 µm-thick PR structures without voids or bubble formation. This proved the high uniformity of the PDMS deposition, with variations of ±4 µm on the 200 µm-thick PDMS layer. Moreover, the process also allowed for the deposition and patterning of 3D PDMS structures with thicknesses ranging from 15 to 175 µm, showing variations of only ±1.3 µm on the 15 µm-thick membrane areas across the wafer.

- **Performance**

  In order to reduce the impedance of the electrodes included in the Cytostretch Heart-on-Chip, this thesis presented and successfully implemented the fabrication of CNT and PEDOT:PSS MEA on the backside of the Cytostretch membrane.

Both materials resulted in a drastic reduction of the electrode impedance, more than 90% lower than the electrodes fabricated with standard materials such as Pt and TiN. The PEDOT:PSS electrodes were also characterized with CV measurements, confirming a higher capacitive current, compared to Pt. The materials were also characterized by performing morphology, quality and biocompatibility studies.

- **Ease of use**
  This thesis presents a new system to use the Cytsotretch Heart-on-Chip. The system was developed focusing on its ease of use. The system is composed of two elements: a plate that encases multiple Cytostretch chips and a pneumatic system. The first element is assembled and packaged with standard techniques used in the IC and MEMS industry. In particular, for the first time a fully automated film assisted molding technology was employed for an OOC device. A new pneumatic system composed of a pump, condition boxes and software was successfully developed. The complete system was tested to define the relation between the applied pressure and the resulting strain in the membrane, and to assess the robustness of the system.

In order to promote the use among early adopters, preliminary biological tests to assess the biocompatibility, tissue compatibility and basic functionalities were performed. The biocompatibility of the chips was assessed by culturing hiPSC-derived cardiomyocytes on the PDMS membranes before and after being packaged. A robust and easy-to-follow protocol for seeding hiPSC cardiomyocytes into the wells of the Cytostretch device was developed and optimized to guarantee a conformal and reproducible monolayer of cells. The morphology of this monolayer was then examined over a 5-day period with different cyclic strain stimulations. A 2.5% cyclic strain was chosen as optimal as it preserves the monolayer morphology. Last but not the least, the basic functionality of the device was tested by applying a cyclic stretch (2.5% - 1 Hz) to a monolayer for 5 days. This resulted in a clear and visible impact on the expression of various genes associated with cardiomyocyte maturation.

Contribution 3: BI/OND platform

In this work a novel platform for the fabrication of microfluidics OOS with POS guidelines was presented. The platform was successfully employed to fabricate a microfluidic chip suitable for perfusion of organoids. The chip was then combined with a plate that allows for handling of 6 chips in parallel.

After a preliminary biocompatibility assay of the chips, the basic functionality of the

device was tested with two kinds of mid-brain organoids, one carrying the PINK1 mutation and one with the corrected gene. The two groups of organoids, were perfused for 26 days in the BI/OND device. At the end of the test, the midbrain organoids carrying a PINK1 mutation showed decreased dopaminergic neurons compared to gene corrected organoids. The quantification of the percentage of TH expressing cells and of the double positive TH+/FOXA2+ cells in the PINK1 gene corrected and mutant organoids, confirmed that there is an impairment of dopaminergic neurons in the PD-model, consistent to the patient samples.

9.2. SUGGESTIONS FOR FUTURE WORK

The results achieved in this thesis are a first step towards the large scale fabrication of PDMS based OOCs. Moreover, this work has shown that exchanging soft-lithography for silicon based fabrication process does not result in any limitations by developing two products and testing their basic functionalities. While the silicon based fabrication and the use of automated packaging systems have resulted in robust prototypes, more development will be required to commercialize them.

- The POS guidelines need to be completed and optimized by automating the remaining manual steps, such as deposition of PDMS and/or the wafer cleaning. Moreover, each steps needs to be analyzed and studied to define the range of dimensions achievable. In particular, the PDMS molding technique should be tested in combination with PR structures and other sacrificial layers, to prove the wide range of 3D PDMS structures that can be realized with this technology.

- The use of CNT and PEDOT:PSS resulted in electrodes with drastically lower impedances. However, these novel electrodes should be tested in a biological relevant environment to prove that the lower impedances does result in a lower SNR during signal detection. The robustness of these electrodes should be also tested to study the effect of long-term culturing on their performance and the effect of cyclic stretching on their adhesion. Moreover, these two materials and their unique properties should be fully exploited by inducing cell anchoring, local drug delivery etc.

- The Cytostretch system should be finalized and thoroughly tested. The fabrication of the plate should be repeated with chips without cracks in the metallic interconnects. The metal lines and the electrode performance should then be studied in combination with the system. The up-regulation of genes related to cardiac maturation identified after the stimulation performed with the Cytostretch needs

to be confirmed by repeating the tests. The mechanical stimulation provided by the chip, and the monitorning provided by the electrodes needs to be then evaluated in a cardiotoxicity test.

- With regard to the BI/OND platform and the developed product, it is necessary to improve the usability of the system by simplifying the assembly and disassembly. In particular the handling of multiple tubes should be addressed. Moreover, the tests performed with the mid-brain organoids needs to be repeated to confirm the promising results.

A

APPENDIX

A.1 FABRICATION PROCESS OF TEST STRUCTURE FOR ADHESION TEST

Main steps required for the fabrication of the tests structures used to test PDMS-PI adhesion.

- Si substrate (4 inch-diameter, 525 μm thick, double side polished, monocrystalline silicon wafers).
- Full cleaning line - Tepla + HNO_3 100% and 65%.
- Lithography - Alignment markers - Spin coat 1.4 μm thick Shipley SPR3012 positive photoresist with EVG 120 coater - Expose masks COMURK and FWAM, with job "20X20COMURK0.0"+ "FWAM" and the correct exposure energy 150 mJ - Develop with EVG 120 developer (Backside).
- Dry etching - Alignment markers - Trikon Ωmega 201 plasma etcher (Backside).
- Full cleaning line - Tepla + HNO_3 100% and 65%.
- Deposition SiO_2 PECVD: 2 μm - Novellus PECVD reactor - 400 °C (Frontside).
- Full cleaning line - Tepla + HNO_3 100% and 65%.
- Deposition SiO_2 PECVD: 6 μm - Novellus PECVD reactor - 400 °C (Backside).

- Lithography - SiO_2 patterning - Hard Mask - Spin coat 4 μm thick Shipley SPR3027 positive photoresist with EVG 120 coater - Expose masks with correct exposure energy 500 mJ - Develop with EVG 120 developer (Backside).
- Dry etching - SiO_2 patterning - Hard Mask - Drytek Triode 384T (Backside).
- Full cleaning line - Tepla + HNO_3 100% and 65%.
- PI coating: 700 nm - Insulation layer - FUJIFILM 9305 Polyimide - Pre-baked to dry the solvent at 105 °C - Single-wafer coater (Frontside).
- Expose masks with correct exposure energy 100 mJ - Develop manually in HTRD2 (Frontside).
- PI curing - Koyo Oven 350 °C.
- Argon treatment - TRIKON SIGMA sputter coater (Frontside).
- PR Coating - Backside protection - Spin coat 4 μm thick Shipley SPR3027 positive photoresist with EVG 120 coater (Backside).
- PDMS spinning: 10 μm - Single-wafer coater.
- PDMS curing - 90 °C, 30 min - Memmert over.
- Cleaning backside- Acetone - Single-wafer coater.
- LUR test - TRIKON SIGMA sputter coater.
- Al deposition: 250 nm - TRIKON SIGMA sputter coater (Frontside).
- DRIE etching Si - Rapier Omega i2L (Backside).
- Wet etching Al - PES 15 min at RT.
- Wet etching - SiO_2: BHF - 20 min.
- Adhesion tests in acetone.

A.2 FABRICATION PROCESS OF THE CYTOSTRETCH DEVICE EQUIPPED WITH TIN MEA AND MICROGROOVES

Main steps for the fabrication of Cytostretch chips equipped with TiN electrodes and microgrooves.

- Si substrate (4 inch-diameter, 525 μm thick, double side polished, monocrystalline silicon wafers.
- Full cleaning line - Tepla + HNO_3 100% and 65%.
- Lithography - Alignment markers - Spin coat 1.4 μm thick Shipley SPR3012 positive photoresist with EVG 120 coater - Expose masks COMURK and FWAM, with job "20X20COMURK0.0"+ "FWAM" and the correct exposure energy 150 mJ - Develop with EVG 120 developer (Backside).
- Dry etching - Alignment markers - Trikon Ωmega 201 plasma etcher (Backside).
- Full cleaning line - Tepla + HNO_3 100% and 65%.
- Deposition SiO_2 PECVD: 1 μm - Novellus PECVD reactor - 400 °C (Frontside).
- Ti sputter deposition: 100 nm - TRIKON SIGMA sputter coater (Frontside).
- Lithography - Ti patterning - Mirror - Spin coat 1.4 μm thick Shipley SPR3012 positive photoresist with EVG 120 coater - Expose masks with correct exposure energy 300 mJ - Develop with EVG 120 developer (Frontside).
- Dry etching - Ti patterning - Mirror - Trikon Ωmega 201 plasma etcher (Frontside).
- Cleaning line - Tepla + HNO_3 100%.
- Deposition SiO_2 PECVD: 1 μm - Novellus PECVD reactor - 400 °C (Frontside).
- Cleaning line - Tepla + HNO_3 100%.
- Deposition SiO_2 PECVD: 6 μm - Novellus PECVD reactor - 400 °C (Backside).
- Lithography - SiO_2 patterning - Hard Mask - Spin coat 4 μm thick Shipley SPR3027 positive photoresist with EVG 120 coater - Expose masks with correct exposure energy 500 mJ - Develop with EVG 120 developer (Backside).
- Dry etching - SiO_2 patterning - Hard Mask - Drytek Triode 384T (Backside).
- Cleaning line - Tepla + HNO_3 100%.
- Al deposition: 1.5 μm - TRIKON SIGMA sputter coater (Frontside).
- Lithography - Al patterning - Contact pads - Spin coat 3.1 μm thick Shipley SPR3027 positive photoresist with EVG 120 coater - Expose masks with correct exposure energy 300 mJ - Develop with EVG 120 developer (Frontside).

- Wet etching Al - PES 5 min at 40 °C.
- Cleaning line - Tepla + HNO_3 100%.
- PI coating: 700 nm - Insulation layer - FUJIFILM 9305 Polyimide - Pre-baked to dry the solvent at 100 °C - Single-wafer coater (Frontside).
- Expose masks with correct exposure energy 100 mJ - Develop manually in HTRD2 (Frontside).
- PI curing - Koyo Oven 350 °C (Frontside).
- Ti and TiN deposition: 10 nm and 200 nm respectively - Metal interconnects - TRIKON SIGMA sputter coater (Frontside).
- Lithography - Ti and TiN patterning - Spin coat 2 μm thick Shipley SPR3012 positive photoresist with EVG 120 coater - Expose masks with correct exposure energy 200 mJ - Develop with EVG 120 developer - Metal interconnects (Frontside).
- Dry etching - Ti and TiN patterning - Metal interconnects - Trikon Ωmega 201 plasma etcher (Backside).
- Oxygen plasma treatment - Tepla Plasma 3000 - Power: 600 W - Pressure: 250 ml/min - Time: 1 min.
- PI coating: 700 nm - Insulation layer - FUJIFILM 9305 Polyimide - Pre-baked to dry the solvent at 100 °C - Single-wafer coater (Frontside).
- Expose masks with correct exposure energy 100 mJ - Develop manually in HTRD2 (Frontside).
- PI curing - Koyo Oven 350 °C (Frontside).
- Argon treatment - TRIKON SIGMA sputter coater (Frontside).
- Lithography - Microgrooves - Spin coat 3.1 μm thick Shipley SPR3027 positive photoresist with EVG 120 coater - Expose masks with correct exposure energy 300 mJ - Develop with EVG 120 developer (Frontside).
- PR Coating - Backside protection - Spin coat 4 μm thick Shipley SPR3027 positive photoresist with EVG 120 coater (Backside).
- PDMS spinning: 10 μm - Single-wafer coater.

- PDMS curing - 90 °C, 30 min - Memmert over.
- Cleaning backside - acetone - Single-wafer coater.
- LUR test - TRIKON SIGMA sputter coater.
- Al deposition: 250 nm - TRIKON SIGMA sputter coater (Frontside).
- Lithography - Al patterning - Contact pads opening - Spin coat 1.4 μm thick Shipley SPR3012 positive photoresist with EVG 120 coater - Expose masks with correct exposure energy 150 mJ - Develop with EVG 120 developer (Frontside).
- Dry etching - Al patterning - Al contact pads - Trikon Ωmega 201 plasma etcher (Frontside).
- DRIE etching Si - Rapier Omega i2L (Backside).
- PR Coating - Frontside protection (Frontside).
- Wet etching - SiO_2: BHF - 20 min (Backside).
- Cleaning wafer in acetone - 5 min.
- Wet etching Al - PES 15 min at RT.
- Releasing microgrooves.

A.3 Fabrication process of Upside-Down CNT MEA

Main steps required for the fabrication of an Upside-Down CNT MEA.

- Si substrate (4 inch-diameter, 525 μm thick, double side polished, monocrystalline silicon wafers.
- Full cleaning line - Tepla + HNO_3 100% and 65%.
- Lithography - Alignment markers - Spin coat 1.4 μm thick Shipley SPR3012 positive photoresist with EVG 120 coater - Expose masks COMURK and FWAM, with job "20X20COMURK0.0"+ "FWAM" and the correct exposure energy 150 mJ - Develop with EVG 120 developer (Backside).
- Dry etching - Alignment markers - Trikon Ωmega 201 plasma etcher (Backside).
- Full cleaning line - Tepla + HNO_3 100% and 65%.

- Thermal oxidation (wet): 2 μm - 8 h - 800 °C.
- Ti, TiN and Ti sputter deposition (Frontside): 10 nm, 50 nm and 100 nm respectively - TRIKON SIGMA sputter coater.
- Lithography - Ti, TiN and Ti patterning - Disks - Spin coat 1.4 μm thick Shipley SPR3012 positive photoresist with EVG 120 coater - Expose masks with correct exposure energy 200 mJ - Develop with EVG 120 developer - Disk (Frontside).
- Dry etching - Ti, TiN and Ti patterning - Disk - Trikon Ωmega 201 plasma etcher (Backside)
- Cleaning line - Tepla + HNO_3 100%.
- Deposition TEOS PECVD: 1 μm - Novellus PECVD reactor - 350 °C (Frontside).
- Lithography - TEOS patterning - Electrodes - Spin coat 1.4 μm thick Shipley SPR3012 positive photoresist with EVG 120 coater - Expose masks with correct exposure energy 200 mJ - Develop with EVG 120 developer (Frontside).
- Dry etching - TEOS patterning - Electrodes - Drytek Triode 384T (Frontside).
- Wet etching Ti in 0.55% HF - 1 min.
- Lithography - Lift-off - Spin coat 1 μm thick NLOF 2020 negative photoresist with EVG 120 coater - Expose masks with correct exposure energy 110 mJ - Develop with EVG 120 developer (Frontside).
- Catalyst evaporation: 5 nm - Evaporator (CR class 10000).
- Lift-off - NMP 70 °C in ultrasonic bath (SAL).
- CNT growth - 500 °C (CR class 10000).
- TiN and Al sputter deposition - 100 nm and 2 μm respectively - TRIKON SIGMA sputter coater (Frontside).
- PR Coating - Frontside protection - Spin coat 1.4 μm thick Shipley SPR3012 positive photoresist with Single-wafer coater (Frontside).
- Backside contamination cleaning: 1 μm of SiO_2 - BFH - 3 min (SAL).
- Cleaning line - HNO_3 100% (SAL).
- Deposition SiO_2 PECVD: 4 μm - Novellus PECVD reactor - 400 °C (Backside).

- Lithography - SiO_2 patterning - Hard Mask - Spin coat 4 μm thick Shipley SPR3027 positive photoresist with EVG 120 coater - Expose masks with correct exposure energy 400 mJ - Develop with EVG 120 developer (Backside).
- Dry etching - SiO_2 patterning - Hard Mask - Drytek Triode 384T (Backside).
- Cleaning line - HNO_3 100% (SAL).
- Lithography - Al and TiN patterning - Metal lids - Spin coat 2 μm thick Shipley SPR3012 positive photoresist with EVG 120 coater - Expose masks with correct exposure energy 250 mJ - Develop with EVG 120 developer (Frontside).
- Dry etching - Al and TiN patterning - Metal lids - Trikon Ωmega 201 plasma etcher (Frontside).
- Cleaning line - HNO_3 100% (SAL).
- Deposition Si_3N_4 PECVD: 2 μm - Novellus PECVD reactor - 400 °C (Backside).
- Lithography - Si_3N_4 patterning - Electrode cavity - Spin coat 2 μm thick Shipley SPR3012 positive photoresist with EVG 120 coater - Expose masks with correct exposure energy 250 mJ - Develop with EVG 120 developer (Frontside).
- Dry etching - Si_3N_4 patterning - Electrode cavity - Drytek Triode 384T (Frontside)
- Cleaning line - HNO_3 100% (SAL).
- Al sputter deposition: 4 μm - Metal interconnecs - TRIKON SIGMA sputter coater (Frontside)
- Lithography - Al patterning - Metal interconnects - Spin coat 4 μm thick Shipley SPR3027 positive photoresist with EVG 120 coater - Expose masks with correct exposure energy 500 mJ - Develop with EVG 120 developer (Frontside).
- Dry etching - Al patterning - Al interconnects - Trikon Ωmega 201 plasma etcher (Frontside)
- Cleaning line - HNO_3 100% (SAL).
- Deposition SiO_2 (low-stress) PECVD: 10 μm - Novellus PECVD reactor - 400 °C (Backside).

- Lithography - SiO_2 patterning - Contact pads - Spin coat 12 μm thick AZ9260 positive photoresist with EVG 120 coater - Expose masks with correct exposure energy - Develop with EVG 120 developer (Frontside).
- Dry etching - Low-stress SiO_2 patterning - Contact pads - Drytek Triode 384T (Frontside).
- Cleaning line - HNO_3 100% (SAL).
- DRIE etching Si - Rapier Omega i2L (Backside).
- PR Coating - Frontside protection (Frontside).
- Wet etching - SiO_2: BHF - 20 min (Backside).
- Cleaning wafer in acetone - 5 min.

A.4 FABRICATION PROCESS OF TIN AND CNT REFERENCE MEA

Main steps required for the fabrication of the reference TiN and CNT MEAs.

- Si substrate (4 inch-diameter, 525 μm thick, double side polished, monocrystalline silicon wafers.
- Lithography - Alignment markers - Spin coat 1.4 μm thick Shipley SPR3012 positive photoresist with EVG 120 coater - Expose masks COMURK and FWAM, with job "20X20COMURK0.0"+ "FWAM" and the correct exposure energy 150 mJ - Develop with EVG 120 developer (Backside).
- Dry etching - Alignment markers - Trikon Ωmega 201 plasma etcher (Backside).
- Full cleaning line - Tepla + HNO_3 100% and 65%.
- Thermal oxidation (wet): 2 μm - 8 h - 800 °C.
- Ti, TiN and Ti sputter deposition (Frontside): 500 nm, 50 nm and 100 nm respectively - Electrodes and metal interconnects - TRIKON SIGMA sputter coater (Frontside).
- Lithography - Ti, TiN and Ti patterning - Electrodes and metal interconnects - Spin coat 2 μm thick Shipley SPR3012 positive photoresist with EVG 120 coater - Expose masks with correct exposure energy 250 mJ - Develop with EVG 120 developer (Frontside).

- Dry etching - Ti, TiN and Ti patterning - Electrodes and metal interconnects - Trikon Ωmega 201 plasma etcher (Frontside).
- Cleaning line - Tepla + HNO_3 100%.
- Deposition TEOS PECVD: 1 μm - Novellus PECVD reactor - 350 °C (Frontside).
- Lithography - TEOS patterning - Electrodes and contact pads - Spin coat 2 μm thick Shipley SPR3012 positive photoresist with EVG 120 coater - Expose masks with correct exposure energy 250 mJ - Develop with EVG 120 developer (Frontside).
- Dry etching - TEOS patterning - Electrodes and contact pads - Drytek Triode 384T (Frontside).
- Wet etching Ti - 0.5% HF - 1 min.
- Cleaning line - Tepla + HNO_3 100%.
- Lithography - Lift-off - Spin coat 1 μm thick NLOF 2020 negative photoresist with EVG 120 coater - Expose masks with correct exposure energy 110 mJ - Develop with EVG 120 developer (Frontside).
- Catalyst evaporation: 5 nm - Evaporator (CR class 10000).
- Lift-off - NMP 70 °C in ultrasonic bath (SAL).
- CNT growth - 500 °C (CR class 10000).

A.5 Fabrication process of the Cytostretch device equipped with Pt MEA

Main steps required for the fabrication of Cytostretch chips equipped with Pt electrodes.

- Si substrate (4 inch-diameter, 525 μm thick, double side polished, monocrystalline silicon wafers.
- Lithography - Alignment markers - Spin coat 1.4 μm thick Shipley SPR3012 positive photoresist with EVG 120 coater - Expose masks COMURK and FWAM, with job "20X20COMURK0.0"+ "FWAM" and the correct exposure energy 150 mJ - Develop with EVG 120 developer (Backside).
- Dry etching - Alignment markers - Trikon Ωmega 201 plasma etcher (Backside).

- Full cleaning line - Tepla + HNO_3 100% and 65%.
- Deposition SiO_2 PECVD: 1 μm - Novellus PECVD reactor - 400 °C (Frontside).
- Ti sputter deposition: 100 nm - Mirror and contamination barrier - TRIKON SIGMA sputter coater (Frontside).
- Deposition SiO_2 PECVD: 1 μm - Novellus PECVD reactor - 400 °C (Frontside).
- Deposition SiO_2 PECVD: 6 μm - Novellus PECVD reactor - 400 °C (Backside).
- Lithography - SiO_2 patterning - Hard Mask - Spin coat 4 μm thick Shipley SPR3027 positive photoresist with EVG 120 coater - Expose masks with correct exposure energy 500 mJ - Develop with EVG 120 developer (Backside).
- Dry etching - SiO_2 patterning - Hard Mask - Drytek Triode 384T (Backside).
- Full cleaning line - Tepla + HNO_3 100% and 65%.
- Al deposition: 1.5 μm - TRIKON SIGMA sputter coater (Frontside).
- Lithography - Al patterning - Contact pads - Spin coat 3.1 μm thick Shipley SPR3027 positive photoresist with EVG 120 coater - Expose masks with correct exposure energy 300 mJ - Develop with EVG 120 developer (Frontside).
- Wet etching Al - Contact pads - PES 5 min at 40 °C.
- Cleaning line - Tepla + HNO_3 100%.
- Lithography - Lift-off - Spin coat 1 μm thick NLOF 2020 negative photoresist with EVG 120 coater - Expose masks with correct exposure energy 110 mJ - Develop with EVG 120 developer (Frontside).
- Catalyst evaporation: Ti and Pt: 20 nm and 100 nm respectively - Evaporator (CR class 10000).
- Lift-off - NMP 70 °C in ultrasonic bath (SAL).
- Cleaning line - HNO_3 100% (SAL).
- PR Coating - Spin coat 4 μm thick Shipley SPR3027 positive photoresist with EVG 120 coater (Frontside).
- Backside contamination cleaning: 1 μm of SiO_2 - BHF (SAL).

- Cleaning line - HNO_3 100% (SAL).
- PI coating: 700 nm - Insulation layer - FUJIFILM 9305 Polyimide - Pre-baked to dry the solvent at 100 °C - Single-wafer coater (Frontside).
- Expose masks with correct exposure energy 100 mJ - Develop manually in HTRD2 (Frontside).
- PI curing - Koyo Oven 350 °C (Frontside).
- Ti and TiN deposition: 10 nm and 200 nm respectively - Metal interconnects - TRIKON SIGMA sputter coater (Frontside).
- Lithography - Ti and TiN patterning - Metal interconnects - Spin coat 2 μm thick Shipley SPR3012 positive photoresist with EVG 120 coater - Expose masks with correct exposure energy 200 mJ - Develop with EVG 120 developer (Frontside).
- Dry etching - Ti and TiN patterning - Metal interconnects - Trikon Ωmega 201 plasma etcher (Backside).
- Oxygen plasma treatment - Tepla Plasma 3000 - Power: 600 W - Pressure: 250 ml/min - Time: 1 min.
- PI coating: 700 nm - Insulation layer - FUJIFILM 9305 Polyimide - Pre-baked to dry the solvent at 100 °C - Single-wafer coater (Frontside).
- Expose masks with correct exposure energy 100 mJ - Develop manually in HTRD2 (Frontside).
- PI curing - Koyo Oven 350 °C (Frontside).
- Argon treatment - TRIKON SIGMA sputter coater (Frontside).
- Lithography - Microgrooves - Spin coat 3.1 μm thick Shipley SPR3027 positive photoresist with EVG 120 coater - Expose masks with correct exposure energy 300 mJ - Develop with EVG 120 developer (Frontside).
- PR Coating - Spin coat 4 μm thick Shipley SPR3027 positive photoresist with Single-wafer coater (Backside).
- PDMS spinning: 10 μm - Single-wafer coater.
- PDMS curing - 90 °C, 30 min - Memmert over.

- Cleaning backside - Acetone - Single-wafer coater.
- LUR test - TRIKON SIGMA sputter coater.
- Al deposition: 250 nm - RT - TRIKON SIGMA sputter coater (Frontside).
- Lithography - Al patterning - Contact pads opening - Spin coat 1.4 μm thick Shipley SPR3012 positive photoresist with EVG 120 coater - Expose masks with correct exposure energy 150 mJ - Develop with EVG 120 developer (Frontside).
- Dry etching - Al and PDMS patterning - Al contact pads - Trikon Ωmega 201 plasma etcher (Frontside).
- DRIE etching Si - Rapier Omega i2L (Backside).
- PR Coating - Frontside protection (Frontside).
- Wet etching - SiO_2: BHF - 20 min (Backside).
- Cleaning wafer in acetone - 5 min.
- Wet etching Al - PES 15 min at RT.

SUMMARY

The cost and the development time of pharamecutical products are often severely affected by the *in vitro* tests currently employed in pharmaceutical R&D. These assays are often failing to accurately recapitulate diseases and to predict human responses to new medicines. Organ-on-Chip (OOC) devices are designed to result in advanced *in vitro* assays that better replicate human responses. The increasing interest and demand for this new class of devices is pushing for a quick commercialization of these tools. However, the currently employed fabrication processes pose major technical hurdles towards large-scale manufacturing, higher throughput and robustness, which are important steps for industrial adoption. This thesis aims to address these challenges, by implementing conventional cleanroom-compatible microfabrication processes for their fabrication. The aim is to copy, in the OOC field, what has been done in the micro-electro-mechanical system (MEMS) field, where the standardization of surface patterning techniques using lithography and etching have been a major factor in their success. The OOCs resulting from this effort are named Organ-on-Silicon (OOS) devices in this thesis.

For the fabrication of an OOS device, PDMS and other polymers need to be processed on silicon wafers. In this thesis a set of guidelines for PDMS processing on silicon, named PDMS on Silicon (POS) guidelines, was defined. This includes robust and reproducible techniques to deposit, pattern, and transfer PDMS layers onto silicon. First a deposition process was developed and characterised, resulting in a high uniformity across wafers and from wafer to wafer. Next, an automated lithography and etching process for PDMS was presented and characterized. These fabrication steps were integrated in a standard microfabrication process, guaranteeing that PDMS structures can be further processed in standard CR tools, without damaging the PDMS structures or contaminating the CR equipment.

Using the above mentioned POS guidelines, two devices were fabricated, proving that the use of conventional cleanroom-compatible microfabrication processes in the OOC field does not limit the range of structures, functionalities and applications. The first OOS platform (Cytostretch) consists of a microfabricated PDMS membrane with four different modules that can be independently inserted into the main fabrication flow to

add functionality depending on the requirements of a particular application. One of the main application of Cytostretch is a Heart-on-Chip device. To bring the Heart-on-Chip a step closer to its commercialization, this thesis focuses on three main aspects: manufacturability, performance, and ease of use. With regard to the manufacturability, the previously presented Cytostretch Heart-on-Chip was limited by two process steps: the use of parylene and the need to dry etch the PDMS. To improve manufacturability, the parylene was replaced by polyimide. As an alternative to PDMS dry etching, this thesis presents a new way to deposit and pattern a PDMS layer with an automated 3D molding technique using a commercially available molding system.

With respect to the performance of the device, the impedance of the electrodes included in the original Cytostretch Heart-on-Chip was improved by coating them with CNT and PEDOT:PSS. Both materials resulted in a drastic reduction of the electrode impedance, more than 90% lower than the electrodes fabricated with standard materials such as Pt or TiN. To improve the ease of use, this thesis presents a new system to use the Cytostretch Heart-on-Chip. The system is composed of a plate that encases multiple Cytostretch chips and a pneumatic system. The system was developed taking in consideration its ease of use. The novel system, in combination with the novel Heart-on-Chip, was tested to assess its biocompatibility, tissue compatibility and basic functionality. A robust and easy-to-follow protocol for seeding hiPSC derived cardiomyocytes into the Cytostretch wells was developed and optimized to guarantee a conformal and reproducible monolayer of cardiomyocytes. The morphology of this monolayer was then studied during a 5-day test with different cyclic strain stimulations. Using a 2.5% cyclic strain stimulation, the cardiomyocyte monolayer was stimulated for 5 days to test the basic functionality of the device. This resulted in a clear and visible impact on the expression of various genes associated with cardiomyocyte maturation.

Finally, the POS guidelines where employed to fabricate a microfluidic OOC (BI/OND platform), suitable for the perfusion of organoids. The chip was combined with a plate that allows for handling of 6 chips in parallel. After a preliminary biocompatibility assay of the chips, the basic functionality of the device was tested with two kinds of mid-brain organoids, one carrying the PINK1 mutation and one with the corrected gene. The two groups of organoids were perfused for 26 days. At the end of the tests, the midbrain organoids carrying a PINK1 mutation showed decreased dopaminergic neurons compared to gene corrected oragnoids. The quantification of the percentage of TH expressing cells and of the double positive TH+/FOXA2+ cells in the PINK1 gene corrected and mutant organoids confirmed that there is an impairment of dopaminergic neurons in the PD-model, consistent to patient samples.

SAMENVATTING

De ontwikkelingstijd van nieuwe medicijnen en de daaraan verbonden kosten worden in aanzienlijke mate bepaald door de in-vitro modellen die bij het farmacologisch onderzoek worden gebruikt. Deze zogenaamde assays slagen er vaak niet in het effect van nieuwe medicijnen op menselijk weefsel te voorspellen. Organ-on-Chips (OOCs) zijn geavanceerde in-vitro assays die hier een aanzienlijk verbetering in zouden moeten brengen. De toenemende vraag naar betere ziektemodellen maakt een snelle commercialisatie van OOC noodzakelijk, echter de huidige fabricagemethodes staan een grootschalige robuuste productie in de weg. Dit proefschrift behandelt dit probleem door de implementatie van conventionele cleanroom compatibele microfabricage processen voor de fabricage van OOC. Dit proefschrift heeft tot doel voor OOC hetzelfde te bewerkstelligen als wat heeft plaatsgevonden bij de fabricage van micro electro mechanische systemen, waar het gebruik van standaard microfabricage technieken, zoals lithografie en etsen, in belangrijke mate heeft bijgedragen tot een succesvolle marktintroductie.

Voor de fabricage van OOC is het nodig PDMS en andere polymeren aan te brengen en te bewerken op silicium wafers. In dit proefschrift zijn een aantal richtlijnen voor de processing van PDMS op silicium wafers gedefinieerd. Deze omvatten technieken om op een robuuste en reproduceerbare manier PDMS op een silicium wafer aan te brengen en te patroneren. Als eerste is een depositieproces ontwikkeld dat resulteert in een zeer uniforme laagdikte over de wafer en van wafer tot wafer. Vervolgens is een geautomatiseerd lithografie- en etsproces ontwikkeld en getest. Deze fabricagestappen zijn vervolgens geïntegreerd in een standaard microfabricage proces waardoor de wafers met PDMS structuren bewerkt kunnen worden met standaard cleanroom apparatuur zonder kans op beschadiging of verontreiniging.

Volgens deze PAS richtlijnen zijn vervolgens twee OOC devices geproduceerd waarmee wordt aangetoond dat het gebruik van conventionele cleanroom compatibele microfabricage technieken geen beperking hoeft te vormen ten aanzien van de variatie in structuren, functionaliteit of toepassing. Het eerste OOC device (Cytostretch) bestaat uit een PDMS membraan waaraan vier verschillende functionele modules onafhankelijk van elkaar kunnen worden toegevoegd, afhankelijk van een bepaalde toepassing.

Om het Cytostretch hart-op-een-chip verder richting commercialisatie te ontwikkelen concentreert dit proefschrift zich op drie aspecten: maakbaarheid, prestaties en gebruikersgemak. Een verbetering in de maakbaarheid van het eerder gepresenteerde Cytostretch hart-op-een-chip werd beperkt door het gebruik van paryleen en het noodzakelijke droogetsen van PDMS. Om de maakbaarheid te verbeteren werd het paryleen vervangen door polyimide. Als een alternatief voor het droogetsen van PDMS wordt in dit proefschrift een nieuwe methode gepresenteerd om PDMS te deponeren en te patroneren waarbij gebruik wordt gemaakt van geautomatiseerde 3D spuitgiet-technieken met behulp van een commercieel verkrijgbaar systeem.
Met betrekking tot de werking van het device is de impedantie van de elektrodes verlaagd door de elektrodes te voorzien van een laagje CNT en PEDOT:PSS. Beide coatings resulteren in een aanzienlijk reductie van de elektrode impedantie, waarbij een reductie van meer dan 90% ten opzichte van de oorspronkelijk platina en TiN electrodes werd bereikt. Ter verbetering van het gebruikersgemak wordt in dit proefschrift een nieuw systeem om Cytostretch te gebruiken voorgesteld. Het systeem bestaat uit een plaat waarop meerdere Cytostretch chips zijn aangebracht alsmede de pneumatische aansluitingen. Dit nieuwe systeem is in combinatie met een nieuw hart-on-chip ontwerp getest met betrekking tot biocompatibiliteit, weefselcompatibiliteit en functionaliteit. Een eenvoudig en robuust protocol is ontwikkeld waarmee conforme en reproduceerbare monolagen iPSC cardiomyocyten kunnen worden aangebracht op het hart-on-chip membraan. De morfologie van deze monolagen is bestudeerd door middel van een test waarbij de cellen gedurende vijf dagen aan verschillende rek cycli werden blootgesteld. Nadat de cellen vijf dagen aan een cyclische rek van 2.5% waren blootgesteld was er duidelijk effect op de expressie van diverse genen die worden geassocieerd met de maturiteit van cardiomyocyten.
Tenslotte is er volgens de POS richtlijnen een microfluidisch OOC platform gerealiseerd dat geschikt is voor de perfusie van organoides. Deze chip is vervolgens gecombineerd met een plaat waarin 6 van deze chips tegelijk kunnen worden gebruikt. Na een eerste biocompatibiliteits test, is dit device getest met twee soorten mid-brain organoides waarvan er één een PINK1 mutatie had en de ander een gecorrigeerd PINK1 gen. De twee groepen organoides werden gedurende 26 dagen blootgesteld aan perfusie. Aan het eind van de test vertoonde de organoides met de PINK1 mutatie een afname in dopaminergieke neuronen in vergelijking met de gecorrigeerde organoides. Een kwantificering van het percentage cellen dat TH tot uitdrukking brengt en de dubbel positieve TH+/FOXA2+ cellen in de PINK1 gemuteerde en gecorrigeerde organoides bevestigde dat er een beschadiging is van de dopaminergieke neuronen in het PD-model.

BIOGRAPHY

Nikolas Gaio was born in Feltre, Italy in 1990. He received a BSc in electronic engineering from the Polytechnic University of Milan, Milan, Italy in 2012. In 2011 he was a visiting student at Tongji University, Shanghai, China, where he received a BSc. in Electronic Information in 2013. He then joined the Shenzhen Institute of Advanced Technology (Chinese Academy of Science) as guest researcher in 2013. In 2015 he received a MSc (cum laude) in Biomedical Engineering at the Faculty of Mechanical, Maritime and Materials Engineering at the Delft University of Technology (TU Delft), Delft, the Netherlands.

In 2015, Nikolas Gaio started his PhD at TU Delft in the Department of Microelectronics. His work was performed within the framework of the InForMed project, a European project that aims to bring medical devices to the market. During this experience, he collaborated with multiple companies (Philips, MultiChannel system and Ncardia, among others), focusing on improving the technology readiness level of a device for in-vitro electrophysiology assays. He also collaborated with multiple biology groups in the human Organ and Disease Model Technologies (hDMT) network on the development of novel Organ-on-Chip devices. He received the Best Student Paper Award at the 2015 IEEE Sensors, the Public Poster Award at the ICT Open Conference in 2016 and the Young Researcher Lush Prize in 2018.

Nikolas Gaio is the founder of BI/OND (BIOND Solution B.V.) where he is currently working. With the BI/OND team, he was awarded with the 12Startup prize in 2016, the Accenture Innovation Award in 2018 and the Philips Innovation Award in 2019.

List of Publications

Journal Papers and Patents

1. R. Martins da Ponte, **N. Gaio**, H. van Zeijl, S. Vollebregt, R. Dekker, V. Giagka and W.A. Serdijn. "MEMS-Electronics Co-fabrication: Monolithic Integration of a Real-time Smart Temperature Sensor for Silicon-based Heart-on-chip Platform". To be submitted to *Biosensors and Bioelectronics*.

2. W.F. Quirós-Solano, **N. Gaio**, C. Silvestri, G. Pandraud, R. Dekker and P.M. Sarro. "Metal and Polymer-based strain gauges for monolithically fabricated Organs-on-Chips". Submitted to *Micromachines*.

3. **N. Gaio***, A. Waafi*, W.F. Quirós-Solano, P. Dijkstra, P.M. Sarro, R. Dekker. "Low-impedance PEDOT:PSS MEA integrated in an Organ-on-Chip Device". Under review in *IEEE Sensor Journal*. *These authors should be regarded as joint first author.

4. W.F. Quirós-Solano, **N. Gaio**, O.M.J.A. Stassen, Y.B. Arik, C. Silvestri, N.C.A. Van Engeland, A. Van der Meer, R. Passier, C.M. Sahlgren, C.V.C. Bouten, A. van den Berg, R. Dekker, P.M. Sarro. "Microfabricated tuneable and transferable porous PDMS membranes for Organs-on-Chips". *Scientific reports*, 8, no. 1 (2018): 13524.

5. **N. Gaio**, W.F. Quirós-Solano. "Versatile 3D stretchable micro-environment for organ-on-chip devices fabricated with standard silicon technology". *Patent*, Pub. No.: WO/2018/021906.

6. **N. Gaio**, B. van Meer, W. Quirós-Solano, L. Bergers, A. van de Stolpe, C. Mummery, P.M. Sarro, R. Dekker. "Cytostretch, an organ-on-chip platform". *Micromachines*, 7, n.7 (2017): 120.

7. **N. Gaio**, C. Silvestri, B. van Meer, S. Vollebregt, C.L. Mummery, R. Dekker. "Fabrication and characterization of an upside-down carbon nanotube microelectrode array". *IEEE Sensor Journal*, 16, n. 24 (2016): 8685-8691.

CONFERENCE PROCEEDINGS PAPERS

1. **N. Gaio**, S. Kersjes, W.F. Quirós-Solano, P.M. Sarro, R. Dekker. "Versatile and Automated 3D Polydimethylsiloxane (PDMS) Patterning for Large-Scale Fabrication of Organ-on-Chip (OOC) Components". *Eurosensors 2018*, Graz, Austria, pp. 873, 2018.

2. **N. Gaio**, A. Waafi, M.L.H. Vlaming, E. Boschman, P. Dijkstra, P. Nacken, S.R. Braam, C. Boucsein, P.M. Sarro, R. Dekker. "A multiwell plate Organ-on-Chip (OOC) device for in-vitro cell culture stimulation and monitoring". *IEEE Micro Electro Mechanical Systems (MEMS 2018)*, Belfast, Northern Ireland, pp. 314-317, 2018.

3. W.F. Quirós-Solano, **N. Gaio**, C. Silvestri, Y.B. Arik, O.M.J.A. Stassen, A.D. Van Der Meer, C.V.C. Bouten, A. Van Den Berg, R. Dekker, P.M. Sarro. "A novel method to transfer porous PDMS membranes for high throughput Organ-on-Chip and Lab-on-Chip assembly". *IEEE Micro Electro Mechanical Systems (MEMS 2018)*, Belfast, Northern Ireland, pp. 318-321, 2018.

4. W.F. Quirós-Solano, **N. Gaio**, C. Silvestri, G. Pandraud, P.M. Sarro. "Polymeric strain gauges as pressure sensors for microfabricated organ-on-chips." *International Conference on Solid-State Sensors, Actuators and Microsystems (TRANSDUCERS 2017)*, Kaohsiung, Taiwan, pp. 1296-1299, 2017.

5. W.F. Quirós-Solano, **N. Gaio**, C. Silvestri, G. Pandraud, P.M. Sarro. "PEDOT: PSS: a Conductive and Flexible Polymer for Sensor Integration in Organ-on-Chip Platforms". *Eurosensors 2016*, Budapest, Hungary, pp. 1184-1187, 2016.

6. **N. Gaio**, B. van Meer, C. Silvestri, S. Pakazad, S. Vollebregt, C.L. Mummery, R. Dekker. "Upside-down carbon nanotube (CNT) micro-electrode array (MEA)". *IEEE Sensors 2015*, Busan, South Korea, pp. 1-4, 2015.

CONFERENCE PRESENTATIONS AND POSTERS

1. S. Chakrabarty, **N. Gaio**, W.F. Quirós-Solano, M. Kuijten, H. Odijk , Jos Jonkers, R. Dekker, R. Kanaar, D. van Gent. "Cancer-on-chip for personalized medicine". *EURoOC Conference*, Graz, Austria, 2019.

2. S. Chakrabarty, **N. Gaio**, W.F. Quirós-Solano, M. Kuijten, H. Odijk , Jos Jonkers, R. Dekker, R. Kanaar, D. van Gent. "Cancer-on-chip: optimizing models for personalized medicine". *3D-Culture, Organoids & Tox Screening Europe 2019 Exhibition*, Rotterdam, The Netherlands, 2019.

3. J. Stein, M. De Graaf, **N. Gaio**, W.F. Quirós-Solano, C. Silvestri, L. Van Den Hill, E. Giacomelli, B. van der Meer, R. van Helden, V. Orlova, M. Bellin and C. Mummery. "A multicellular approach to iPSC-derived myocardium on a microfluidic platform for human disease modelling". *EURoOC Conference*, Stuttgart, Germany, 2018.

4. M. Hanif, L. Bergers, **N. Gaio**, R. Dekker. "Polybutadiene Rubber (PBR) Membrane Microfabrication for Organ-on-Chip Applications". *International Organ-On-Chip Symposium (IOOCS) 2018*, Eindhoven, The Netherlands, 2018.

5. O.M.J.A. Stassen, N.C.A. Van Engeland, W.F. Quirós-Solano, **N. Gaio**, A. Pollet, J.M.J. Toonder, R. Dekker, P.M. Sarro, C.M. Sahlgren and C.V.C. Bouten. "Cardiovascular-tissue-on-a-chip to study crosstalk between hemodynamics and cell-cell signalling in tissue engineering outcome". *1st International Conference on Tissue Engineered Heart Valves*, Amsterdam, The Netherlands, 2018.

6. **N. Gaio**, C. Silvestri, W.F. Quirós-Solano. "Versatile Organ-on-Chip Platform". *International MicroNano Conference 2017*, Amsterdam, The Netherlands, 2017.

7. W.F. Quirós-Solano, **N. Gaio**, Y.B. Arik, A. Van der Meer, R. Passier, R. Dekker, A. van den Berg and P.M. Sarro. "Highly porous and transferable microfabricated PDMS membranes for Organ-on-Chip". *Design of Medical Devices Conference Europe (DMD 2017)*, Eindhoven, The Netherlands, 2017.

8. **N. Gaio**, W.F. Quirós-Solano, P. Dijkstra, T. van Weelden, E. Boschman, R. Dekker. "Cystostretch: A Multi-Well Plate Heart-on-Chip Device". *Design of Medical Devices Conference Europe (DMD 2017)*, Eindhoven, The Netherlands, 2017.

9. W.F. Quirós-Solano, **N. Gaio**, Y.B. Arik, C. Silvestri, A. Van der Meer, R. Passier, and P.M. Sarro. "Highly porous microfabricated PDMS foils for Organ-on-Chip applications". *International Organ-on-Chip Symposium*, Lausanne, Switzerland, 2017.

10. A. Waafi, **N. Gaio**, R. Dekker. "Platinum and Titanium-Nitride Microelectrodes Array on Flexible Substrate for Organ-on-Chip Application". *ICT OPEN Conference*, Amersfoort, The Netherlands, 2017.

11. **N. Gaio**, W.F. Quirós-Solano, C. Silvestri, P.M. Sarro, R. Dekker. "Cytostretch Platform: Towards the Industrialization of an Heart-on-Chip Device". *International Organ-on-Chip Symposium*, Lausanne, Switzerland, 2017.

12. **N. Gaio**, R. Dekker. "Cytostretch: a Versitile Silicon-Based Organ-on-Chip". *Advances in Cell & Tissue Culture 2017*, Manchester, UK, 2017.

13. **N. Gaio**, M.L.H. Vlaming, T. van Weelden, P. Nacken, S. Braam, E. Boschman, R. Dekker. "Cytostretch device: a Stretchable Micro-Electrode Array in Multi-Well Plate Format". *Organ-on-a-Chip World Congress & 3D-Culture 2017*, Boston, USA, 2017.

14. W.F. Quirós-Solano, **N. Gaio**, G. Pandraud and P.M. Sarro. "Sensing devices in Organ-on-Chip: Towards an integrated sensing microtechnology for heart cells study". *ICT OPEN Conference*, Amersfoort, The Netherlands, 2016.

15. **N. Gaio**, W.F. Quirós-Solano, R. Dekker. "Large-Scale fabrication of PDMS membranes for Organ-on-Chip applications". *ICT OPEN Conference*, Amersfoort, The Netherlands, 2016.

CO-SUPERVISED MASTER THESIS

- "Optimization of microporous PDMS membranes for Organ-on-Chips" - Bart Kootte
- "Integration of a local drug delivery system in a micro-fabricated Brain-on-Chip device" - Hanieh Mastyani
- "Fabrication and characterization of PEDOT coated microelectrodes array for Organ-on-Chip applications" - Affan Kaysa Waafi

PROPOSAL CONTRIBUTIONS

- "BI/OND the Versatile Organ-on-Chip Platform". Take-off phase 2. Funded by Netherlands Organisation for Scientific Research.
- "BIOND the lab: Versatile Organ on Chip Platform toward the market". EIT Proof of Concept. Funded by European Institute of Innovation and Technology.
- "Design, fabrication and testing of an user-friendly interface for organ on chips". Take-off phase 1. Funded by Netherlands Organisation for Scientific Research.
- "Developing a validated Cancer-on-Chip prototype for personalized medicine". High Risk Project KWF Kanker Bestrijding. Funded by KWF Kankerbestrijding.
- "Membranes for a Heart Valve on a Chip". NanoInside Pilot Project Proposal. Funded by NanoNextNL.

- "Towards realistic barriers: Bringing microfabrication and Organ-on-Chips technology together to model cellular barriers". NanoInside Pilot Project Proposal. Funded by NanoNextNL.
- "BIOND: A universal Organ on chip platform". Project Leader: Ronald Dekker. NanoNextNL Valorisation Programme. Founded by NanoNextNL.

HONORS AND AWARDS RELATED TO THIS THESIS

- **NanoLabNl Voucher 2019**
  BI/OND
- **Philips Innovation Award 2019**
  BI/OND - Best Startup
- **Accenture Innovation Award 2018**
  BI/OND - Best Startup in Heath category
- **Lush Prize 2018**
  Young Researchers Award - Europe and rest of the world
- **12Startup 2016**
  BI/OND - First Prize
- **Best Poster Award 2016**
  Public Prize, ICT.OPEN 2016, Amersfoort, The Netherlands.
- **Best Student Paper Award 2015**
  IEEE Sensor Conference 2015, Busan, South Korea